



**HAL**  
open science

# Experimental investigation of textural atomization processes : application to cavitating flows

Fakhry Abuzahra

► **To cite this version:**

Fakhry Abuzahra. Experimental investigation of textural atomization processes : application to cavitating flows. Fluid Dynamics [physics.flu-dyn]. Normandie Université, 2019. English. NNT : 2019NORMR028 . tel-02284934

**HAL Id: tel-02284934**

**<https://theses.hal.science/tel-02284934>**

Submitted on 12 Sep 2019

**HAL** is a multi-disciplinary open access archive for the deposit and dissemination of scientific research documents, whether they are published or not. The documents may come from teaching and research institutions in France or abroad, or from public or private research centers.

L'archive ouverte pluridisciplinaire **HAL**, est destinée au dépôt et à la diffusion de documents scientifiques de niveau recherche, publiés ou non, émanant des établissements d'enseignement et de recherche français ou étrangers, des laboratoires publics ou privés.



Normandie Université

## THÈSE

Pour obtenir le diplôme de doctorat

Spécialité Énergétique

Préparée au sein de l'Université de Rouen Normandie

### Experimental Investigation of Textural Atomization Processes: Application to Cavitating Flows

Présentée et soutenue par

Fakhry ABUZAHA

Thèse soutenue publiquement le 12 Juillet 2019 à 14h00  
devant le jury composé de

Mme. Françoise BAILLOT	Professeure, CORIA, Université de Rouen Normandie	Examinatrice
M. Christophe DUMOUCHEL	Directeur de Recherche, CNRS, CORIA	Directeur de thèse
M. Chaouki HABCHI	HDR, IFPEN	Rapporteur
Mme. Camille HESPEL	Maître de Conférences, PRISME, Université d'Orléans	Examinatrice
M. Luis LE MOYNE	Professeur, ISAT - Université Bourgogne	Rapporteur
M. Cyril MAUGER	Maître de Conférences, INSA Lyon -GM -LMFA	Examinateur

Thèse dirigée par Christophe DUMOUCHEL et Jean-Bernard BLAISOT, laboratoire UMR 6614 CORIA



PHD, UNIVERSITY OF ROUEN AND CORIA - FRANCE

This research was done under the supervision of Dr. Christophe Dumouchel and Prof. Jean-Bernard Blaisot with the financial support of European Union's Horizon 2020 research and innovation program under the Marie Skłodowska-Curie grant agreement N° 675676, from June 2016 to July 2019.

Edition date *September 9, 2019*

# Acknowledgments

This work has been accomplished at CORIA lab, so I would like to express my gratitude to the lab members at all levels of the hierarchy. The gratitude is also conveyed to Prof. Manolis Gavaises – City University of London, who coordinated the project (Holistic Approach of Spray injection (HAoS)) which this work is part of. Special thanks for the jury members who devoted their time, efforts and very thoughtful suggestions. It has been an honor to have Dr. HDR Chaouki Habchi and Pr. Luis Le Moyne as reporters. Prof. Françoise Baillot being the president of the jury, Dr. Cyril Mauger and Dr. Camille Hespel, thank you all for the great insights on my thesis. I should pay my profound gratitude towards my supervisors, Dr. Christophe Dumouchel and Assoc. Pr. Jean-Bernard Blaisot, for their selfless guidance and ideas they put forward to accomplish this work. They were patient with me during my testing times and I shall always cherish the acquaintance. During my experiments I worked closely with the workshop members who were very skillful and helpful. Implementing complex experiments requires certain expertise and that makes CORIA lab one of the unique labs thanks to the metrology department. I interacted with almost all of this team specially Gilles Godard. Special thanks to Said Idlahcen also with whom I worked closely and shared different topics. Not to forget my colleagues who encouraged me (Yacine, Michael, Petra, Anirudh, Aqeel, Noureddine Taguelmimt, Rafael) and with whom I shared nice moments. Christophe Tirel who was always catching me eating! Nathalie Vallee with Christophe Tirel both helped in the coding for image processing. Dilip with whom I enjoyed sharing the office for the last year of my PhD. It was an honor to collaborate with Prof. Akira Sou, Japan, in the context of simplified transparent atomizers. The list of people to thank is long. I would like to thank Dr. Fabien Thiesset and Dr. Michael Gauding for the fruitful discussions on the turbulence-related calculations. Finally, the support I got from my family and my wife is priceless. They were all the time in my side. Thanks for everything.

## List of Conference Papers

- **Abuzahra, F.** and Dumouchel, C. and Blaisot, JB. and Idlahcen, S. and Lisiecki, D. (2017). Cavitation in a Scaled-up 2D-Transparent Nozzle: Experimental Rig Realization and Preliminary Results. In the 5<sup>th</sup> Cavitation and Multi-phase flows Workshop, Chania Greece (poster), June 26-28.
- **Abuzahra, F.** and Dumouchel, C. and Blaisot, JB. and Idlahcen, S. and Sou, A. (2019). In the 6<sup>th</sup> Cavitation and Multi-phase flows Workshop, Chania Greece (poster), June 24-27.
- Blaisot, JB and **Abuzahra, F.** and Sou, A. and Dumouchel, C. (2019). Entropy-based cavitation and primary atomization analysis with a 2D transparent injector. In the 29th European Conference Liquid Atomization and Spray Systems, September 2-4.
- **Abuzahra, F.** and Dumouchel, C. and Blaisot, JB. and Sou, A. and Godard, G. (2018). Influence of Cavitation on Textural Atomization. In the International Conference on Liquid Atomization and Spray Systems, Chicago USA (Poster), July 22-26.

## List of Journal Papers

- Dumouchel, C. and Blaisot, JB. and **Abuzahra, F.** and Sou, A. and Godard, G. and Idlahcen, S. (2019). Analysis of a textural atomization process. Experimental in fluids (under press).

# Contents

<b>Symbols</b>	<b>16</b>
<b>1 Introduction</b>	<b>21</b>
<b>2 Literature Review</b>	<b>24</b>
<b>3 Mathematical Elements</b>	<b>35</b>
3.1 Diameter Distribution . . . . .	35
3.1.1 General Concept . . . . .	35
3.1.2 Ensemble of Spheres . . . . .	38
3.1.3 Ensemble of Cylinders . . . . .	39
3.1.4 Diameter Distribution . . . . .	41
3.2 Scale Distribution . . . . .	45
3.2.1 General Concept . . . . .	45
3.2.2 Ensemble of Spheres . . . . .	48
3.2.3 Ensemble of Cylinders . . . . .	51
3.2.4 Multiscale Description . . . . .	53
<b>4 Exp. Setup &amp; Optical Diag.</b>	<b>56</b>
4.1 Hydraulic Circuit . . . . .	56

---

4.2	The Atomizer . . . . .	57
4.3	Flow Regimes . . . . .	59
4.4	Operating Conditions . . . . .	61
4.5	Punctual Techniques . . . . .	64
4.5.1	Velocity Measurement . . . . .	64
4.5.2	Diameter Measurement . . . . .	65
4.5.3	LDV and PDPA Setup . . . . .	65
4.5.4	Seeding Particles . . . . .	66
4.6	Imaging techniques . . . . .	69
4.6.1	Still Visualization . . . . .	69
4.6.2	High-Speed Visualization . . . . .	71
4.6.3	Image Pre-processing . . . . .	72
4.7	Scale distribution . . . . .	78
4.8	Drop Size . . . . .	80
4.8.1	Image Modeling . . . . .	82
4.8.2	Image Parameters . . . . .	84
4.8.3	Drop Diameter Estimation . . . . .	85
4.8.4	Drop Size Distribution Estimation . . . . .	87
4.8.5	Morphological Analysis . . . . .	89
4.9	Statistical Image Entropy . . . . .	92
<b>5</b>	<b>Results</b>	<b>94</b>
5.1	Internal and External Flow Visualizations . . . . .	94
5.1.1	Internal Flow . . . . .	94
5.1.2	External Flow . . . . .	101

---

5.2	LDV Measurements . . . . .	110
5.3	PDPA Measurements . . . . .	113
5.4	Scale Distribution . . . . .	118
5.5	Image-Based Drop Diameter Measurements . . . . .	120
<b>6</b>	<b>Analysis</b>	<b>125</b>
6.1	Influence of Cavitation on Orifice Flow . . . . .	125
6.2	Internal and External Flow: Entropy Analyses . . . . .	131
6.3	Textural Atomization and Sprays . . . . .	134
6.3.1	Spray Drop Diameter Distribution Analysis . . . . .	141
6.3.2	Textural Atomization Analysis . . . . .	146
<b>7</b>	<b>Conclusions and Perspectives</b>	<b>161</b>

# List of Figures

2.1	Separation of the fluid flow due to abrupt change in the flow direction. . .	26
2.2	Images of a cylindrical transparent large-scale atomizer: upper row images are the internal flow where the cavitation appears along the axis of the orifice starting from developing cavitation regime; lower row is the emerged liquid jet; in-nozzle flow regime classification: a) no-cavitation b) developing cavitation, c) super-cavitation and d) hydraulic flip (Sou et al., 2008). $\sigma_c$ is the modified cavitation number. . . . .	27
2.3	Schematic of a valve covering orifice (VCO) injector (Sou et al., 2012). . .	31
3.1	3D-representation of a cylinder of a diameter $D$ and unit height (left), and its 2D projection (right). . . . .	40
3.2	Effect of the parameter $\alpha$ on the number-based drop diameter distribution given by Eq. (3.22) at $n = 0$ , $q = 10$ and $D_{q0} = 300 \mu\text{m}$ . . . . .	45
3.3	Illustration of the erosion principle performed on a system with arbitrary shape: a) system before erosion, b) system after an erosion operation at scale $d$ (the black region is the remaining surface area after erosion denoted by $S(d)$ ). . . . .	46
3.4	2D projection of a cylinder of diameter $D$ (left) and of a sphere of diameter $D$ (right). . . . .	47
3.5	Scale distribution of the 2D projection of a) a cylinder of diameter $D$ and b) a sphere of diameter $D$ (Eqs. (3.37 and 3.38), respectively.) . . . . .	48
4.1	Schematic of the hydraulic circuit of the experimental test bench. . . . .	57

4.2	a) Schematic of a VCO injector (Sou et al., 2012) and b) schematic of the atomizer that is inspired from the internal path of a VCO atomizer, the red rectangle on Fig. a. Left is the front view and right is the side view. Dimensions are in mm. . . . .	58
4.3	The atomizer with acrylic transparent material on the left (Sou et al., 2012), and BK7 glass on the right. . . . .	59
4.4	a) Preliminary front-view visualization using A1 atomizer: upper-row is the internal and external flow (the black pixels are cavitating structures for the internal flow and liquid for the external flow); bottom-row is the external flow captured at 57 mm downstream the nozzle-orifice exit. Brown-rectangle: no-cavitation flow regime; red-rectangle: cavitation inception flow regime; yellow-rectangle: super-cavitation flow regime; green-rectangle: partial-hydraulic flip regime; b) internal flow zoomed-in for representative operating conditions. . . . .	60
4.5	Discharge coefficient as a function of the injection differential pressure for A1, G1 and G2 atomizers. . . . .	62
4.6	Example of a probe volume (on the left) and a Doppler burst (on the right) (Albrecht et al., 2013). . . . .	67
4.7	Schematic of the LDV and PDPA systems. . . . .	67
4.8	PDPA arrangement. . . . .	68
4.9	Schematic of the seeding particles feeder system. $Q_{part}$ is the flow rate in particles line. . . . .	68
4.10	General schematic of the back-light illumination used in the present work for the visualization of: a) front view using the side view of the atomizer and b) side view using the front view of the atomizer (see Fig. 4.2b). $\bar{z}$ is the optical axis. . . . .	70
4.11	Illustration of the normalization process. a) raw image, b) background image, c) obscurity image, d) normalized image, e) grey level histogram of the background image, f) grey level histogram of the raw image and g) grey level histogram of the normalized image. . . . .	74
4.12	Illustration of the holes-filling process. a) raw image, b) labeled image with holes, c) inverted image and d) binarized image with holes-filled. . . .	78

4.13	Example of the holes-filling process on a portion delimited by a red rectangle in Fig. 4.12b: a) selecting the hole as an object after image inversion, b) projecting the object onto the raw image, c) projecting the object onto the background image and d) projecting the object on the holes-filled image. . . . .	79
4.14	Image treatment steps for scale distribution measurement: a) image without the detached liquid and b) EDM image. . . . .	80
4.15	Scale distribution principle: erosion is performed on the region delimited by the principal skeleton line (the longest skeleton path) of the jet and the right interface, i.e. the grey region. . . . .	81
4.16	Scale distribution for the image shown in Fig. 4.14b: a) is the cumulative distribution $E_2(d)$ , b) is the scale distribution $e_2(d)$ and c) $e_2(d)$ averaged over 500-images. . . . .	81
4.17	Illustration of the drop diameter measurement-steps: a) is the raw image, b) normalized image and c) labeled image. . . . .	82
4.18	Theoretical image profile $\tilde{i}(\tilde{r})$ as a function of $\tilde{r}$ for: $\tilde{a} = 1.13$ and $\tau = 0$ ( $\circ$ ); $\tilde{a} = 1.5$ and $\tau = 0$ ( $\square$ ); $\tilde{a} = 1.5$ and $\tau = 0.2$ ( $\blacksquare$ ); $\tilde{a} = 2.5$ and $\tau = 0$ ( $\diamond$ ); $\tilde{a} = 2.5$ and $\tau = 0.2$ ( $\blacklozenge$ ); $\tilde{a} = 3$ and $\tau = 0.05$ ( $\triangleright$ ) . . . . .	84
4.19	A theoretical image profile(line) and the object profile (dash-line). . . . .	85
4.20	Reference level $l_m$ as a function of the contrast $C$ . . . . .	86
4.21	Gradient at the reference level $l = 0.5$ as a function of the contrast $C$ . . . . .	88
4.22	Experimental PSF half-width $\chi$ determined at a reference level $l = 0.5$ on a series of razor-blade images: a) at different height locations and b) zoomed-in at mid-height level using the optical diagnostic system No. III and c) using the optical system No. II (see Table 4.6). $\bar{z}$ is the optical axis. . . . .	89
4.23	Definition of the object shape parameters: a) sphericity ( $S_p$ ), b) ellipticity ( $\epsilon_{ell}$ ), c) uniformity ( $\eta_{unif}$ ), d) convexity ( $\zeta_{conv}$ ). . . . .	91
5.1	Still images of the internal flow of A1 atomizer using the optical system No. III: a to f presents A1-2 to A1-7 (Table 4.2). Flow enters from the upper-right and emerges downwards. . . . .	95
5.2	Still images of the internal flow of G1 atomizer using the optical system No. III: a to f presents G1-3 to G1-8 (Table 4.3). Flow enters from the upper-right and emerges downwards. . . . .	96

5.3	Still images of the internal flow of G2 atomizer using the optical system No. II: a to f presents G2-1 to G2-8 (Table 4.4). Flow enters from the upper-right and emerges downwards . . . . .	97
5.4	Sequence of images of G2-1 from the left to right pictured over 13.92 ms (time delay between images 480 $\mu$ s) using the optical system No. II in Table 4.7. . . . .	100
5.5	Sequence of images of A1-3 (Regime II) pictured over 1.35 ms (time delay between images 150 $\mu$ s) using the optical system No. I in Table 4.7. . . . .	101
5.6	Sequence of images of G2-4 pictured over 13.92 ms (time delay between images 480 $\mu$ s) using the optical system No. I in Table 4.7. . . . .	102
5.7	Sequence of images of A1-6 (Regime IV) pictured over 4.35 ms (time delay between images 150 $\mu$ s) using the optical system No. I in Table 4.7. . . . .	103
5.8	Sequence of images of A1-7 (Regime IV) pictured over 5.85 ms (time delay between images 150 $\mu$ s) using the optical system No. I in Table 4.7. . . . .	104
5.9	Still images of the external, front view of A1 atomizer using the optical system No. III: a to g presents A1-1 to A1-7. . . . .	105
5.10	Still images of the external, front view of G1 atomizer using the optical system No. III: a to h presents G1-1 to G1-8. . . . .	106
5.11	Still images of the external, front view of G2 atomizer using the optical system No. II: a to f presents G2-1 to G2-8. . . . .	107
5.12	Still images of the side view of G1 atomizer at the nozzle-exit using the optical system No. III: a to h presents G1-1 to G1-8. . . . .	108
5.13	Still images of the side view of G2 atomizer at the nozzle-exit using the optical system No. II: a to h presents G2-1 to G2-8. . . . .	109
5.14	Working plan of the LDV measurements using G1 atomizer. . . . .	111
5.15	Experimental mean stream-wise velocity $\langle U_z \rangle$ for G1 atomizer. . . . .	112
5.16	Schematic of the PDPA measurement points performed at different distances from the nozzle exit; the measurements performed at $x=0$ (middle of the injector in the front view); the grid coordination and distances are indicated on the figure. . . . .	114

5.17	Validated data rate of the diameter-measurements for G1-8 as a function of the distance from the orifice axis for different distances $z$ from the orifice exit.	115
5.18	probability density function (pdf) of the drop diameter measured at the points of the highest and furthest from the atomizer axis at different distances (10 - 60 mm) from the nozzle orifice exit for G1-8. . . . .	116
5.19	Droplet velocity at the highest validation rate of the PDPA measurements performed using G1 atomizer: a to f corresponding to operating conditions G1-1 to G1-6 and g to G1-8. The vertical line refers to the mean bulk velocity $U_b$ . . . . .	117
5.20	Measured scale distribution of A1-1 to A1-7. The scale step $\Delta d = 7$ pixels (37 $\mu\text{m}$ ). . . . .	119
5.21	Measured scale distribution of G1-1 to G1-8. The scale step $\Delta d = 7$ pixels (35 $\mu\text{m}$ ). . . . .	119
5.22	Measured scale distribution of G2-2 to G2-8. The scale step $\Delta d = 7$ pixels (35 $\mu\text{m}$ ). . . . .	120
5.23	Experimental surface-based drop diameter distribution $f_2(D)$ for the atomizers: a) A1 and b) G2. . . . .	122
5.24	Experimental number-based drop diameter distribution $f_0(D)$ for the atomizers: a) A1 and b) G2. . . . .	122
5.25	Sauter mean diameter $D_{32}$ as a function of the flow rate $Q_m$ for both A1 and G2 atomizers. . . . .	124
5.26	Surface-based drop size distribution $f_2(D)$ for: a) A1-1 and G2-4, b) A1-4 and G2-7. . . . .	124
6.1	Comparison between the LDV and LES for the mean stream-wise mean velocity $\langle U_z \rangle$ of G1-1. . . . .	127
6.2	a) Normalized mean stream-wise velocity profile $\langle U_z \rangle / U_b$ ; b) fluctuations $\langle U_{z,rms} \rangle / U_b$ ; c) normalized span-wise velocity $\langle U_x \rangle / U_b$ ; d) fluctuations $\langle U_{x,rms} \rangle / U_b$ for G1-1. $U_b = 10.0$ m/s. White dashed-line is the position where the velocity profile is probed. Red-dot is the LDV measurement and the red-line is the LES simulation. . . . .	128

6.3	a) Normalized mean stream-wise velocity profile $\langle U_z \rangle / U_b$ ; b) fluctuations $\langle U_{z,rms} \rangle / U_b$ ; c) normalized span-wise velocity $\langle U_x \rangle / U_b$ ; d) fluctuations $\langle U_{x,rms} \rangle / U_b$ for G1-4. $U_b = 13.8$ m/s. White dashed-line is the position where the velocity profile is probed. Red-dot is the LDV measurement and the red-line is the LES simulation. . . . .	129
6.4	a) Normalized mean stream-wise velocity profile $\langle U_z \rangle / U_b$ ; b) fluctuations $\langle U_{z,rms} \rangle / U_b$ ; c) normalized span-wise velocity $\langle U_x \rangle / U_b$ ; d) fluctuations $\langle U_{x,rms} \rangle / U_b$ for G1-8. $U_b = 19.0$ m/s. White dashed-line is the position where the velocity profile is probed. Red-dot is the LDV measurement and the red-line is the LES simulation. . . . .	130
6.5	Entropy maps for the internal flow of A1 atomizer: a to f presents A1-2 to A1-7. . . . .	135
6.6	Entropy maps for the internal flow of G1 atomizer: a to f presents G1-3 to G1-8. . . . .	135
6.7	Entropy maps for the internal flow of G2 atomizer: a to g presents G2-2 to G2-8. . . . .	136
6.8	Normalized 3-state region area for internal flow of atomizers A1, G1 and G2. Colors indicate the cavitation regime: black for regime I ( <i>no cavitation</i> ), red for II ( <i>cavitation inception</i> ), green for III ( <i>super cavitation</i> ) and blue for IV ( <i>partial-hydraulic flip</i> ). . . . .	136
6.12	Primary atomization region normalized area for: a) A1, b) G1 and c) G2 atomizers. . . . .	140
6.13	Standard deviation of the scale distribution at the smallest scale $e_2(d_{min})$ as a function of the mean entropy at the nozzle exit for mainly cavitation-induced variability (Cav.) and mainly air sucking-induced variability (A.S). . . . .	141
6.14	Correlation between the $D_{peak}$ left and right for A1 and G2 atomizers as a function of $CN$ . . . . .	142
6.15	Example of the $f_2(D)$ fit for: a)A1-3 and b)G2-5. Good fit was obtained for the other conditions. . . . .	143
6.16	$\beta_f$ as a function of $CN$ for A1 and G2 atomizers. . . . .	144
6.17	$\Delta_2$ as a function of $CN$ for A1 and G2 atomizers. . . . .	145
6.18	a) $\alpha_L$ and b) $q_L$ as a function of $CN$ . . . . .	146

6.19	Example of the mathematical fit of the scale distribution: circle is the experimental data and the dashed line is the mathematical fit. Good agreement is obtained also for the other conditions. . . . .	149
6.20	Textural atomization process for A1 atomizer. . . . .	150
6.21	a) $\alpha_1$ , b) $q_1$ and c) $D_{q01}$ as a function of $CN$ . . . . .	150
6.22	$D_{peakR}$ VS $d_p$ . . . . .	152
6.23	$\Delta_{2R}$ VS $q_1$ . . . . .	152
6.24	$\alpha_R$ VS $-e'_{2,1}(d_p)$ . . . . .	153
6.25	$\alpha_L$ VS $\alpha_1$ for A1 atomizer. . . . .	154
6.26	$\alpha_1/\alpha_L$ VS $d_{p2}/d_p$ for A1 atomizer. . . . .	155
6.27	Textural atomization process extracted using following method II for: a) A1 and b) G2 atomizers. . . . .	157
6.28	a) $q_1$ , b) $\alpha_1$ and c) $D_{q01}$ as a function of $CN$ . . . . .	158
6.29	Correlation between the parameter $D_{peakR}$ and the parameter $d_p$ for A1 and G2 atomizers. . . . .	159
6.30	Correlation between $\alpha_L$ and $-e''_2(d_{p2})$ for A1 and G2 atomizers. . . . .	160
6.31	Ratio of $\alpha_1/\alpha_L$ as a function of $d_{p2}/d_p$ for A1 and G2 atomizers. . . . .	160

# List of Abbreviations

**S-HGS** silver coated hollow glass sphere

**3pGG** three-parameter generalized gamma

**EDM** Euclidean Distance Mapping

**LDV** Laser Doppler Velocimetry

**MEF** Maximum Entropy Formalism

**PDA** Phase Doppler Anemometry

**pdf** probability density function

**PDPA** Phase Doppler Particle Analyzer

**PSF** Point-Spread Function

**VCO** valve covering orifice

# Symbols

$K_1$	cavitation number according to Bergwerk (1959)
$K_2$	cavitation number according to Pearce and Lichtarowicz (1971)
$K_3$	cavitation number according to Nurick (1976)
$p_1$	absolute upstream pressure
$p_c$	pressure at the vena contracta
$C_D$	discharge coefficient
$Q_m$	mass flow rate
$\rho_l$	water density
$C_c$	contraction coefficient
$p_v$	vapor saturation pressure
$p_{amb}$	atmospheric pressure
$U_c$	flow velocity at the vena contracta
$L$	orifice length
$D_H$	hydraulic diameter
$D$	diameter
$D_i$	median diameter in class $i$
$\Delta D_i$	width of class $i$
$j$	number of classes in the distribution
$D_{min}$	minimum diameter encountered in a distribution
$D_{max}$	maximum diameter encountered in a distribution
$N_i$	number of droplets in a class
$N$	total number of droplets in a distribution
$L_i$	characteristic length of droplets in class $i$
$S_i$	characteristic surface area of droplets in class $i$
$V_i$	characteristic volume of droplets in class $i$
$n$	type of the distribution; 0 for number-based, 1 for length-based, 2 for surface-based and 3 for volume-based
$p_{ni}$	histogram probability of class $i$ for $n$ type distribution

$D_{i,min}$	minimum diameter in class $i$
$D_{i,max}$	maximum diameter in class $i$
$f_n$	$n$ type diameter distributions
$F_n$	$n$ type cumulative diameter distributions
$D_{ab}$	mean diameters; $a$ and $b$ can be any non-equal real numbers
$D_{32}$	Sauter mean diameter
$D_{n\eta}$	representative diameters; $\eta \in [0; 1]$
$\Gamma$	gamma function
$\alpha, q, D_{q0}$	parameter of the three-parameter generalized gamma function
$q_{RR}, D_{RR}$	parameters of the Rossin-Rammlar distribution
$q_{NT}, \alpha_{NT}, b_{NT}$	parameters of the Nukiyama-Tanasawa distribution
$D_{pn}$	modal diameter
$d$	scale of observation
$E_2(d)$	surface-based cumulative scale distribution
$P(d)$	perimeter of the system eroded at scale $d$
$S_T$	total surface area of the system
$e_2(d)$	surface-based scale distribution
$d_{max}$	maximum scale
$f_{0c}(D)$	number-based cylinder diameter distribution
$L_{ch}$	atomizer orifice length
$w_{ch}$	atomizer orifice width
$T_{tp}$	atomizer transparent material thickness
$Z_{ch}$	inlet channel height
$\Delta P_i$	differential injection pressure
$U_b$	bulk flow velocity
$\nu$	kinematic viscosity
$\rho_g$	air density
$\sigma$	surface tension of water with air
$A_0$	cross-sectional area of the orifice exit
$h_{noz}$	nozzle-orifice thickness
$\lambda$	wavelength of the laser
$\theta$	intersection angle between the laser beams
$f_D$	Doppler burst frequency
$V_z$	traversing particle velocity
$\delta_f$	inter-fringe distance
$\Delta\Phi$	phase difference between received signals at the photo-multipliers
$C_\Phi$	phase factor constant

---

$\Phi_r$	scattering angle
$D_p$	diameter of seeding particles
$Q_{part}$	flow rate at the seeding particles line
$L_c$	characteristic length of the flow used in Stokes number
$\rho_p$	density of seeding particles
$I_n(i, j)$	intensity of the pixel $(i, j)$ in the normalized image
$I_{im}(i, j)$	intensity of the pixel $(i, j)$ in the raw image
$I_{bg}(i, j)$	intensity of the pixel $(i, j)$ in the background image
$\alpha$	shot-to-shot correction factor
$N_F$	normalization factor to prevent overloaded grey levels
$GL_{max}$	digitization-based maximum grey level
$N_{thresh}$	threshold value
$N_{max}$	maximum populated grey level value
$N_{min}$	minimum populated grey level value
$R_{thresh}$	relative threshold
$\psi$	wavelet function
$W$	coefficients of wavelet function
$\vec{\chi}$	vector refers to the pixel in the image
$\vec{b}$	shifting parameter
$\vec{a}$	dilation parameter
$\Psi$	mother wavelet
$O_g(x, y)$	object geometric image
$\tau$	amount of transmitted light
$r$	radial coordinate in the image plane
$a_i$	geometrical object size
$\gamma_0$	magnification factor
$a_0$	real object size
$\Pi$	rectangle function
$\chi$	PSF haf-width
$s_0$	normalization constant
$\bar{z}$	optical axis
$\tilde{i}(\tilde{r})$	image profile
$\tilde{a}$	dimensionless object radius
$\tilde{r}$	dimensionless radial coordinate
$\tilde{I}_0$	modified Bessel function of the first kind
$C$	dimensionless image contrast
$\tilde{i}_{min}$	minimum image profile
$\tilde{i}_{max}$	maximum image profile
$h$	image profile height
$l$	relative level

$\tilde{i}_{Ref}$	image profile at reference level
$l_m$	Reference level
$r_{meas}$	measured drop radius
$A_{l_m}$	surface area at relative level $l_m$
$\tilde{g}_{0.5}$	non-dimensional grey level gradient at mid-level
$C_{max}$	contrast of opaque object
$S_{ph}$	sphericity shape parameter
$S_{obj}$	surface area of the object
$S_{sph}$	surface area of a circle whose the same area and barycenter of the object
$p$	perimeter
$\epsilon_{ell}$	ellipticity shape parameter
$l_{min}$	shortest length of the rectangle encompassing the object
$l_{max}$	longest length of the rectangle encompassing the object
$\phi_{irr}$	irregularity shape parameter
$\eta_{unif}$	uniformity shape parameter
$r_{min}$	shortest distance measured from the center-of-gravity of the object and the nearest contour point
$r_{max}$	longest distance measured from the center-of-gravity of the object and the farthest contour point
$\zeta_{conv}$	convexity shape parameter
$S_{conv}$	the smallest surface area encompasses the object without any concave part in the contour
$E$	statistical entropy
$p_s$	probability of a physical state
$s$	number of states
$N_{AP}$	number of active pixels
$E_3$	3-state statistical entropy criterion
$\Delta d$	scale step
$\dot{n}_p$	number of validated measurements per unit time
$N_T$	total number of measured droplets in image-based drop sizing
$N_{valid}$	validated number of droplets in image-based drop sizing
$D_{peakR}$	peak drop diameter of the right population
$D_{peakL}$	peak drop diameter of the left population
$\Delta y$	distance between two adjacent grid points in the PDPA measurement
$\langle U_z \rangle$	mean stream wise velocity

---

$\langle U_x \rangle$	mean span wise velocity
$U_{k,rms}$	root mean square of the velocity component in the k direction
$\sigma_{e_2(d_{min})}$	standard deviation of the scale distribution at the minimum resolved scale $d_{min}$
$E_{mean}$	mean statistical entropy of a defined region
$\beta_f$	weighting parameter used in the drop diameter distribution analysis
$\Delta_2$	non-dimensional variance of the surface-based drop diameter distribution
$\beta_e$	weighting parameter used in the scale distribution analysis
$d_p$	scale where the inflection point exists
$d_{p2}$	scale where the first inflection point of the first derivative of the scale distribution $e'_2(d)$ exists

# Chapter 1

## Introduction

The emission legislation imposed on internal combustion engine-cars incites the automotive industry to do further research to reduce pollutant emissions. Among the possible levers to reach these requirements, the fuel injection is probably one of the major steps that could be optimized provided that this mechanism is known and understood. Unfortunately, the understanding of liquid injection remains partial and the absence of fundamental knowledge in the literature has to be deplored. The fuel injection is a complex mechanism whose aim is to transform a quantity of liquid into a flow of droplets, i.e., a spray. Using the fuel under the form of a spray has two main motivations. First, having their own velocity, the droplets can invade the combustion chamber and fill it in a more or less homogeneous way. Second, since the liquid is divided into small droplets, the liquid-gas interface is increased and enhances the evaporation rate. It is known that the size of the drop is an important parameter for these two mechanisms. If the drops are big, they have a sufficient momentum to reach the combustion chamber wall where they spread as liquid films. The presence of such films is known to produce pollutant emissions. Furthermore, the evaporation of big droplets takes more time and combustion may start before all liquid has evaporated, which is also an important pollutant emission source. We understand here that an important progress could be made by controlling the fuel spray production step. This objective could be reached only if the injection step is fully understood which requires conducting specific investigations on this subject. The study presented in this PhD report is one of them.

The liquid injection can be presented in two steps: 1 – the development of the liquid flow in the injector, i.e., the internal flow, 2 – the atomization process that takes place on the issuing liquid flow and that produces the spray, i.e., the external flow. The development of the internal flow is an important step since it conditions the characteristics of the flow issuing from the injector. These characteristics constitute the initial conditions for the external flow evolution. Car injectors used to inject fuel have complex internal geometry that imposes complicated paths to the liquid. This characteristic coupled with the use

of small dimensions and high injection pressures favor the cavitation of the liquid. This mechanism is important and influences the atomization process and the spray. The multi-scale nature of the liquid flow atomization has received a limited attention so far in research. One of the reasons for that is the lack of appropriate tools to investigate such a multi-scale mechanism. It has to be admitted that the task is rather difficult since what is called an atomization process is often the concomitancy of several mechanisms. For instance, for rather energetic flows, primary and secondary atomization mechanisms may coexist. Another categorization is proposed in this work, i.e. structural and textural atomization mechanisms. Indeed, the primary atomization can be considered structural or textural depending on the scale at which the atomization process takes place. These mechanisms will be defined in the next chapter.

In the context of mechanical injection, this work proposes a targeted study on the textural atomization processes for cavitating injection conditions. The objectives of this study are to describe the textural atomization process and the spray it produces, to investigate the possible role of the cavitation on the textural atomization process characteristics and efficiency, to establish a connection between the atomization process and the produced spray, to approach the sensitivity of the atomizer geometry on these questions. Beside the addressed questions, the originality of this work lies in the tools that have been developed and applied to perform the analyses. As far as this point is concerned, it is worth mentioning that a specific attention is paid on the establishment of mathematical formulations to describe the atomization processes and the sprays. Such mathematical tools are ferociously missing in the literature.

This thesis is structured as follows. Chapter 2 presents a brief literature review about the cavitation in the context of automobile injectors. It also mentions the scale distribution developed at CORIA lab for characterizing the atomization process. Furthermore, it defines the questions to be addressed and the research methodologies. Chapter 3 reviews the construction of the size distribution and its application on spheres and cylinders. It further reviews the mathematical formalism used to represent the diameter distribution and the scale distribution using the 3-parameter generalized gamma function. The notion of equivalent system of ensemble of cylinders is also introduced and applied for the first time to represent the textural atomization process. Chapter 4 presents the experimental setup with the injectors used, the optical diagnostic systems and the image post-processing. It reviews the model developed at CORIA and used to measure the diameter of the pictured droplets. It shed the light on the statistical entropy introduced by Blaisot and Yon (2003) to characterize the primary atomization. This statistical approach is employed to identify the variability of the flow at the exit-section inside the orifice. Chapter 5 presents the experimental results in terms of instantaneous images, videos, velocity measurements issued from Laser Doppler Velocimetry (LDV), drop size and velocity measurements issued from Phase Doppler Anemometry (PDA). This chapter presents also the scale distribution

measurements and the drop diameter distribution measured on images. Chapter 6 is the analysis chapter which starts by comparing the velocity measured by LDV system and that issued from LES simulation. It employs the statistical entropy to investigate the variability of the internal and external flow and correlate the variability of the exit-section with that of the emerging liquid jet. It further proposes a model to correlate the textural deformations with the textural sprays. Finally, it investigates the influence of the needle lift (upstream channel height) on both the internal and external flows. Chapter 7 concludes the work presented in the precedent chapters and highlights some perspectives.

# Chapter 2

## Literature Review

Atomization process designates the deformation and the disintegration into liquid fragments of a liquid flow evolving in a gaseous environment. This process stops when all liquid fragments are small enough so that the surface tension forces ensuring their cohesion are able to oppose extra fragmentation. At this stage, the liquid fragments become spherical drops of different size and velocity. This flow of drops is what is called a spray. Liquid sprays are used in many industrial and domestic applications such as agriculture, pharmaceutical industry, cosmetic, coating, spray printing, combustion, fire extinction, food industry... to cite just a few of them. It is now recognized that the characteristic features of a liquid spray (among which the drop diameter distribution is the most important) always affect the efficiency of the application it is used for. It is therefore important to be able to produce calibrated sprays according to the applications in order to improve their efficiency. Such an objective would require a better knowledge of the connection between the free liquid flow characteristics and the spray it can produce. The present work intends to provide results on this very point.

The most frequent method to produce a liquid spray is to eject a liquid flow in a gaseous medium thanks to a device called an atomizer or an injector. Several concepts of atomizer and injector exist (Lefebvre, 1989). They differ by their internal geometry (that configures the exit flow characteristics), by their way of working (transient or continuous), as well as by the existence of an air flow to assist the atomization process. As the liquid flow emerges from the atomizer, perturbations deform it and some of these perturbations grow in such proportions that liquid fragments detach from the bulk flow. To their turn, these liquid fragments may deform and disintegrate in smaller fragments and this process continues until all liquid fragments are stable spherical drops. In the literature, the detachment of the first liquid fragments is referred to as the primary atomization process and the disintegration of these fragments is referred to as the secondary atomization process ((Dumouchel, 2008) and (Guildenbecher et al., 2009)).

---

The primary atomization process can be subdivided into two drop production processes. Numerous images of the literature report two sources for droplet production. Some liquid fragments and droplets may be peeled from the liquid gas interface while others result from the breakup of the liquid bulk. The first source depends on the *local* kinematic and geometrical characteristics of the liquid-gas interface whereas the second one depends on the *global* kinematic and geometrical characteristics of the liquid bulk. These two drop production mechanisms will be referred here as *textural* and *structural* atomization process, respectively. This designation is inspired by Kaye (1994) who introduced the textural and structural fractal dimension to differentiate the local boundary tortuosity of a system from its global shape. The textural atomization process is a near field mechanism, i.e., it is usually triggered soon after the liquid issues from the atomizer.

The Rayleigh-Taylor instability developing on an air-assisted laminar jet (Marmottant and Villermaux, 2004) and that produces streamwise ligaments, which eventually break up into droplets, can be seen as a textural atomization process. However, in most cases, textural atomization processes are imposed by the issuing flow characteristics. They manifest by an increase of tortuosity of issuing flow interface. The textural fractal dimension characterizing this tortuosity has been found to correlate with the issuing flow Reynolds number (Grout et al., 2007). This tortuosity is due to the emergence of rather ligamentary structures. A nice example of this was reported on laminar jets for which the vorticity distribution in the liquid near the interface, triggers the development of small ligaments from which droplets emanate (Wu et al., 1995). Manifested at small scales, the textural atomization processes are likely to be faster mechanisms than the structural atomization processes. Furthermore, the characteristic lengths of the textural ligaments are far smaller than the size of the flow, and the resulting droplets are small also. Being laterally ejected, these droplets induce an increase of the spray angle at the nozzle exit. Thus, an increase of the spray angle at the orifice exit is often a mark of a textural atomization process.

In applications that combine high injection pressures and small orifice dimensions, textural atomization processes may be energetic and produce dense sprays whose impact on the applications can not be ignored. This is the case, for instance, in fuel injection in engines. Therefore, the knowledge and understanding of the textural atomization processes are important. However, this specific mechanism has been barely investigated so far. Several questions arise: Which characteristics of the internal flow control the textural deformation of the liquid interface? Which characteristics of the textural tortuosity control the size distribution of the resulting sprays? On which bases these correlations could be established? How to mathematically represent an interface tortuosity, a spray drop size distribution? The last question is of interest in the context of atomization modeling and numerical simulations. The present work intends to shade more light on these points by experimentally investigate the textural atomization process in specific conditions, i.e., cavitating injection conditions. Liquid cavitation is an important mechanism in liquid

injection, and part of its influence could be precisely related to the textural atomization process.

Cavitation is a rupture in liquid continuum due to excessive stress and appears as soon as the pressure decreases below the liquid vapor pressure (Dumont et al., 2000). It is characterized by a phase change of the liquid. Many experimental works have reported the development of cavitation caused by sudden section change of the flow ((He and Ruiz, 1995), (Sato and Saito, 2001), (Stanley et al., 2011), (Mauger et al., 2012)) as illustrated in Fig. 2.1. The sudden section change may induce detachment of the boundary layer at the entrance of the downstream channel. Recirculation zones develop and the flow section area actually decreases (Payri et al., 2005). This region is called the "*vena contracta*". The pressure at the vena contracta is low and decreases when the flow rate increases. When it becomes smaller than the liquid vapor pressure, cavitation bubbles appear in the shear layer between the recirculation zones and the main flow (Mauger et al., 2012). Such a cavitation process is referred in the literature as geometrically induced cavitation.

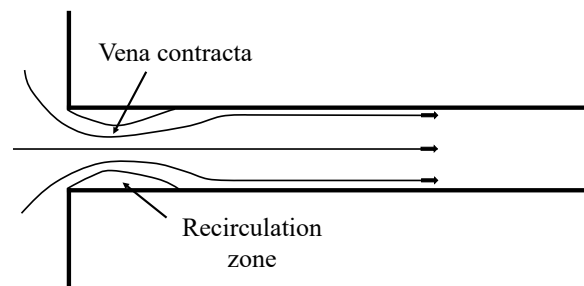


Figure 2.1: Separation of the fluid flow due to abrupt change in the flow direction.

Geometrically induced cavitation has been widely experimentally investigated owing to its dominance when the injection pressure is high and the discharge orifice diameter is small, such as for fuel injection in the car engine context ((Arai et al., 1985; Arai, 1988); (Hiroyasu, 1991); (Ohrn et al., 1991a,b); (Karasawa et al., 1992); (Tamaki et al., 1998); (Badock et al., 1999a); (Desantes et al., 2005); (Sou et al., 2007)); (Sou et al., 2008). For instance, Ohrn et al. (1991a) conducted parametrical study to investigate the effect of the internal geometry on the discharge coefficient in plain-orifice atomizer where cavitating operating conditions are considered. Desantes et al. (2005) considered cavitating condition in their characterization of the influence of the internal geometry (of nozzles diameter 115 to 200  $\mu\text{m}$ ) and the injection parameters on both the internal flow and the emerging flow downstream the nozzle exit. Badock et al. (1999a) also investigated the cavitation in real-size transparent nozzles and found out that the orifice inlet edge conditions the internal flow and affects the discharge coefficient to a greater extent than that of Reynolds number and length/diameter ratio. Hiroyasu (1991) observed an increase in the emerging

liquid coincided with the presence of cavitation inside the orifice. According to Sou et al. (2008), four internal-flow regimes have been identified: Regime I: no-cavitation, Regime II: developing cavitation, Regime III: super-cavitation, and Regime IV: hydraulic flip. They are illustrated in Fig. 2.2 (Fig. 8 in Sou et al. (2008)). This figure shows the internal flow in a transparent cylindrical orifice nozzle (top row) and the external flow just downstream the orifice (bottom row) as the injection pressure increases (from left to right). The presence of cavitation in the orifice is recognized by the appearance of dark regions along the axis of the orifice. The range of low injection pressure for which the cavitation phenomenon is not observed in the orifice corresponds to the no-cavitation regime (Regime I).

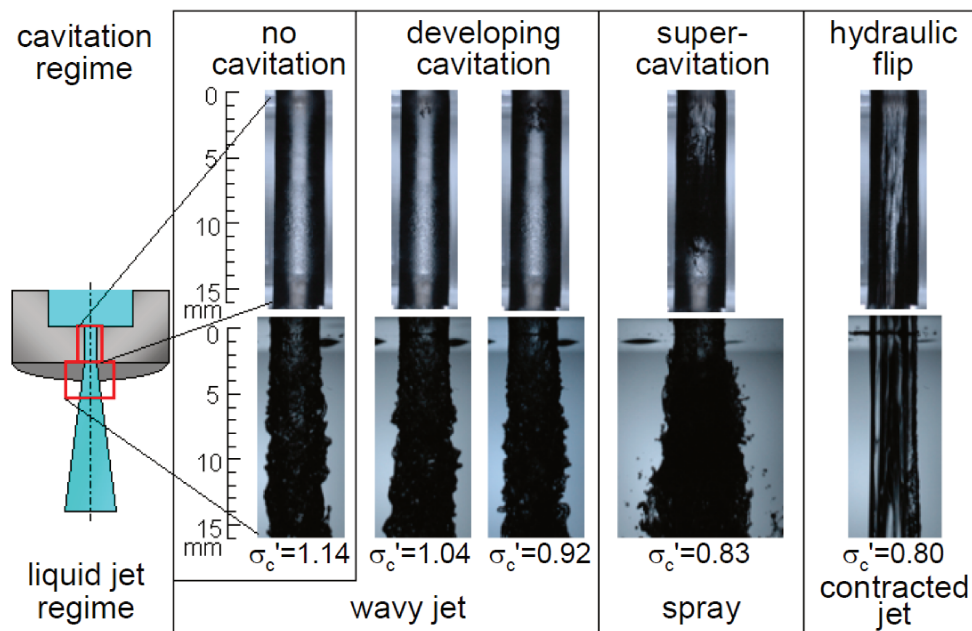


Figure 2.2: Images of a cylindrical transparent large-scale atomizer: upper row images are the internal flow where the cavitation appears along the axis of the orifice starting from developing cavitation regime; lower row is the emerged liquid jet; in-nozzle flow regime classification: a) no-cavitation b) developing cavitation, c) super-cavitation and d) hydraulic flip (Sou et al., 2008).  $\sigma_c$  is the modified cavitation number.

The appearance of cavitation bubbles at the entrance of the discharge orifice marks the beginning of the developing cavitation regime (Regime II). It has been often written that cavitation inception is triggered at the corner of the discharge entrance. However, a closer look indicates that the cavitation starts slightly downstream the orifice entrance in the shear layer between the main flow and recirculation zone (Mauger et al., 2012). Shedding of bubble clouds at a given frequency was reported in this regime (Stanley et al., 2011).

In the super-cavitation regime, the geometrically induced cavitation structure at the entrance of the orifice increases in length and may extend to the nozzle exit section. The variation of the cavitation region length is due to shedding of bubble clouds caused by the

shear forces imposed by the liquid flow core. The detached bubble clouds either reach the nozzle exit section or collapse before that. The shedding mechanism reports no specific frequency in this regime (Stanley et al., 2011). The interaction between the cavitation region front and the orifice wall modifies the turbulent characteristic of the downstream flow. LDV measurements reported by He and Ruiz (1995) showed an increase of turbulent intensity of 10-20% along the orifice wall behind the main cavitation cloud compared to an equivalent non-cavitating situation. Furthermore, the turbulence decay is slower in the cavitating case. Similarly, Sou et al. (2006, 2007) reported high velocity fluctuations downstream the reattachment of the boundary layer.

Finally, the hydraulic flip regime (Regime IV) occurs when the cavitation vanishes because downstream air moves upstream between the flow and the orifice wall (Dabiri et al., 2007). The limit between this regime and the previous one is not sharp, and a behavior, oscillating between these two regimes, has been reported (Chaves et al., 1995). As reported by Soteriou et al. (1995), the hydraulic flip might develop around a section of the cylindrical orifice wall only leading to an "imperfect" hydraulic flip regime or a "partial" hydraulic flip regime: the later being promoted by, mainly, the asymmetry of the atomizer. As a consequence, only part of the issuing liquid jet is smooth, the other part being ruffled due to internal parietal constraints. In real-size injectors, it is believed that the imperfect hydraulic flip is common because of geometry asymmetry (Soteriou et al., 1995), (Bergwerk, 1959).

Beside geometrically induced cavitation, dynamically induced cavitation has been reported in injectors close to real fuel injector geometry and equipped with a sac volume which feeds the discharge orifices ((Kim et al., 1997); (Arcoumanis et al., 2001); (Soteriou et al., 2001); (Payri et al., 2004, 2005); (Andriotis et al., 2008); (Andriotis and Gavaises, 2009); (Gavaises et al., 2009)). Dynamically induced cavitation designates string or column of cavitation structures produced in the sac volume where strong recirculations and vortex develop ((Kim et al., 1997); (Arcoumanis et al., 2001); (Soteriou et al., 2001)). This kind of cavitation has been found to originate from pre-existing cavitation sites formed at sharp corners inside the nozzle where the local pressure goes below the vapor saturation pressure. It might be originated also from the suction of the surrounding air downstream the nozzle exit ((Andriotis et al., 2008); (Andriotis and Gavaises, 2009); (Gavaises et al., 2009)). String cavitation favors cycle-to-cycle variations in transient injection conditions ((Andriotis and Gavaises, 2009), (Guo et al., 2018), Mitroglou et al. (2011)). Furthermore, it may reorganize the liquid flow issuing from the nozzle as a rather stable non atomizing cylindrical sheet of liquid (Dumouchel et al., 2013).

The propensity of a flow to develop cavitation structures is associated with a dimensionless number, i.e., the cavitation number, built as the ratio of two characteristic pressures. Bergwerk (1959) expressed a cavitation number as the ratio of the relative injection pressure on the ambient pressure, i.e.:

$$K_1 = \frac{p_1 - p_{amb}}{p_{amb}} \quad (2.1)$$

where  $p_1$  is the absolute upstream liquid pressure and  $P_{amb}$  is the absolute ambient pressure. Cavitation is promoted when this number increases since the relative injection pressure ( $p_1 - p_{amb}$ ) represents the available level of pressure, and the ambient pressure  $p_{amb}$  is an indication of the level of pressure to overcome to provoke cavitation. Another estimation of this pressure level incorporating the liquid vapor pressure  $p_v$  is suggested by Pearce and Lichtarowicz (1971) who established the cavitation number  $K_2$  (Ohrn et al., 1991a):

$$K_2 = \frac{p_{amb} - p_v}{p_1 - p_{amb}} \quad (2.2)$$

$K_2$  is the ratio of the pressure level to overcome cavitation on the available level of pressure to achieve it. Inversely constructed compared to  $K_1$ , flows with decreasing  $K_2$  are more prone to produce cavitation structures. Other propositions consider the fact that the available pressure level should consider the pressure drop in the injector. For this purpose, cavitation number including the discharge coefficient  $C_D$  have been suggested. For instance, Nurick (1976) used the cavitation number  $K_3$  defined as:

$$K_3 = \left( \frac{p_1 - p_c}{p_1 - p_{amb}} \right) \left( \frac{1}{C_D} \right)^2 \quad (2.3)$$

where  $p_c$  is the pressure at the vena contracta and the discharge coefficient  $C_D$  writes:

$$C_D = \frac{U_b}{\sqrt{\frac{2(p_1 - p_{amb})}{\rho_l}}} \quad (2.4)$$

where  $U_b$  is the average velocity of the issuing liquid flow and  $\rho_L$  is the liquid density. Because of the pressure drop, the discharge coefficient is less than 1. Therefore, a better estimation of the pressure available to produce cavitation is  $C_D^2(p_1 - p_{amb})$ . Using this expression in Eq. (2.2) leads to the following cavitation number  $CN$ :

$$CN = \frac{p_{amb} - p_v}{0.5\rho_l U_b^2} \quad (2.5)$$

This cavitation number has been used by Knapp et al. (1970); He and Ruiz (1995) and Sou et al. (2006, 2007). In this number, the available pressure level is expressed as the dynamic pressure of the flow issuing from the nozzle. Cavitating flows are associated with low  $CN$  number (less than 1). More sophisticated expressions for cavitation numbers have

been developed. For instance, Sou et al. (2009) constructed a cavitation number allowing measurements of cavitation region lengths obtained in a wide range of conditions in the super-cavitation regime to collapse into a single behavior. This cavitation number includes the flow contraction effect and the friction loss in the orifice:

$$\sigma_c = C_c^2 \left[ \frac{P_{amb} - P_v}{0.5\rho U_b^2} + \frac{\lambda L}{D_H} + 1 \right] \quad (2.6)$$

where  $C_c = U_b/U_c$  is the contraction coefficient,  $U_c$  is the flow velocity at the vena contracta,  $\lambda$  is the friction coefficient,  $L$  is the orifice length and  $D_H$  is the hydraulic diameter of the orifice.

The influence of cavitation on the deformation and atomization of the issuing liquid flow has been reported at several occasions ((Bergwerk, 1959), (Reitz and Bracco, 1982), (Soteriou et al., 1995)). An example of this is illustrated in Fig. 2.2 where the bottom row images visualize the flow issuing from the nozzle according to the Flow Regime. In the no-cavitation and developing cavitation regimes, wavy jets issue from the nozzle. The cavitation here seems to have a limited effect on the jet deformation at the nozzle exit. In the super-cavitation regime, the issuing liquid flow shows a wider angle and a textural atomization process clearly appears. This process involves the development of fine ligamentary structures and the production of few droplets. Finally, in the hydraulic flip regime, a smooth and stable cylindrical jet issues from the orifice. This configuration is due to the fact that the internal flow does not reattach to the discharge orifice wall before the exit section. The absence of parietal friction favors the development of a plug flow free of any interface perturbation as the external medium is reached. In similar situations, Arai et al. (1985) reported the same observations. The strong variation of the issuing flow deformation in the super-cavitation regime has been reported by several papers ((Stanley et al., 2011), (Abderrezzak and Huang, 2016), (Laoonual et al., 2001), (Sou et al., 2007), (Mauger et al., 2012)). As said above, the turbulent characteristics are increased near the orifice wall just downstream the main cavitation cloud. This inevitably impacts the initial perturbations responsible for the jet deformation at the nozzle exit. Furthermore, Ganippa et al. (2004) and Sou et al. (2007) consider that the cavitation shedding and collapse are the main contributors to the fluctuations of the spray produced by textural atomization. Experimental works due to Payri et al. (2004), Payri et al. (2012), Desantes et al. (2010) all agree on the fact that the increase of jet angle observed in the super-cavitation regime coincides with the presence of the cavitation bubbles in the exit section, which, beside this, is at the origin of the mass flow rate saturation often reported when the absolute injection pressure increases.

Real injectors often have complex internal geometries which, in transient injection conditions, vary in time. They constitute important factors as far as the development and

the impact of the cavitation are concerned. Figure 2.3 shows an example of the internal geometry of fuel injector. The needle ensures the opening and closing of the injector. Flow passages are small (orifice diameter of the order of 100 micrometers) and section and direction changes are numerous. Several experimental investigations performed with transparent injectors have revealed a complex internal flow with large-scale vortex, cavitation and turbulent structures in the sac volume ((Kim et al., 1997); (Badock et al., 1999b); (Arcoumanis et al., 2001) among others). The complex sac flow has a dominant impact on the flow in the discharge orifices and on the spray angle at the nozzle exit. Arcoumanis et al. (2001) revealed an interaction between dynamically induced cavitation strings or vortices in the sac volume and the geometrically induced cavitation at the orifice entrance.

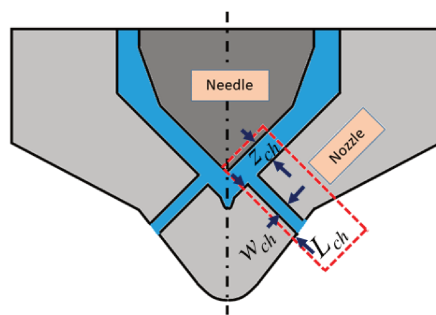


Figure 2.3: Schematic of a VCO injector (Sou et al., 2012).

The work series performed in Sou's group (2009-2015) on simplified transparent atomizers highlight the influence of the internal geometry on the cavitation processes and their subsequent impact on atomization. Sharp direction changes at the discharge orifice entrance favor the development of asymmetric geometrically-induced cavitation. At the nozzle exit, the flow on the side of the cavitation deviates outwards denoting the development of a textural atomization process and the production of droplets.

Within the context of this work which intends to provide a description of a textural atomization process, the question of the analysis of atomization processes and sprays is important and has to be addressed. The number of experimental studies on the atomization processes in the literature remains rather small. The classical approach for this task is to image the process and to analyze these images. For a long time, the most common atomization process characteristics measured by image analysis have been the spray angle at the nozzle exit and the break-up length defined as the distance between the nozzle-exit section and the position at which the atomization process is completed. Although these characteristics quantify the size of the spray, they do not provide any quantitative information on the atomization process itself. Today's images have reached such a high degree of quality that a fine description of the atomization process is accessible, all the more so since, the constant developments of computing capacities allows treating a high number of images in a reasonable time. Therefore, statistical image analyses, required for liquid

atomization process studies, are now reachable.

Images of the literature illustrate that, in all situations, atomizing liquid flows show complex shapes with many liquid structures of different sizes and shapes (see for instance (Dumouchel et al., 2008)). The question is: which quantity, providing a relevant description of the atomization process, should be measured on these images? In every application, the role of atomization is to increase the liquid-gas interface area and the efficiency of an atomization process includes the amount of interface per unit liquid volume of the produced spray (Evers, 1994). Therefore, characterizing an atomization process consists in characterizing the temporal evolution of the liquid-gas interface area and shape. The knowledge of the shape of the interface is important since it contains information on the way system deformations evolve, and therefore, on the evolution of the amount of interface. Image analysis may be used to approach this but it is important to keep in mind that such analyses are 2D whereas atomization processes are 3D. In atomization processes, the increase of the liquid-gas interface results from the appearance of perturbations whose development increase the tortuosity of the interface. The fractal dimension concept provides a way of quantifying such tortuosity and has been first used by Shavit and Chigier (1995) to investigate the atomization of co-axial cylindrical jets. They succeeded in measuring a fractal dimension whose downstream evolution reported a maximum in the breakup region. The fractal dimension concept was also applied to analyze the atomization process of a turbulent liquid sheet produced by a triple-disk nozzle ((Dumouchel et al., 2005b), (Dumouchel et al., 2005a), (Grout et al., 2007)). Such a nozzle produces a perturbed liquid sheet showing a textural atomization process at sufficiently high flow rate and a structural one that goes through the rearrangement of the liquid flow as a ligament network that eventually breaks up into droplets. Among other results, the tortuosity of the interface at the nozzle exit was associated with a textural fractal dimension whose value correlated with the flow Reynolds number. This result is a supplementary demonstration of the link between the flow in the discharge orifice and the textural atomization process. Furthermore, the tortuosity of the liquid system at the ligament network stage was associated with a structural fractal dimension that correlated to the liquid Weber number of the liquid flow. These behaviors demonstrate that, during liquid atomization processes, the interface evolution is controlled, first by the dynamic of the issuing flow and, second, by the surface tension forces. However, these works pointed out that atomizing liquid systems cannot be fully described by a single fractal dimension and that the scale range representative of the whole system is wider than the one for which self-similarity is observed. Thus, the traditional fractal concept must be replaced by a multiscale description approach where the fractal dimension becomes a scale-dependent function. The notion of scale distribution has been introduced for this purpose ((Dumouchel and Grout, 2009), (Dumouchel et al., 2015a), (Dumouchel et al., 2015b), (Dumouchel et al., 2017), (Tirel et al., 2017), (Vu and Dumouchel, 2018)).

The multiscale description tool developed in CORIA Lab is used in the present inves-

---

tigation and will be presented in details later. This method is an extension of the fractal dimension concept. From a technological point of view, both methods use the same image analyzing operation, i.e., Euclidean Distance Mapping. The multiscale tool provides a description of systems of any shape by assigning them a scale distribution. An atomization process is then described by the temporal evolution of the scale distribution whose analysis provides information on the representative liquid structure length scales and on their dynamic. The multiscale analysis method has been applied on stretched atomizing ligaments (Dumouchel et al., 2015a), highly perturbed liquid sheets ((Dumouchel and Grout, 2009), (Vu and Dumouchel, 2018)), turbulent jets produced by car fuel injectors (Dumouchel et al., 2015b), viscoelastic capillary jets ((Tirel et al., 2017)). The temporal aspect of the analyses has given access to fine description of atomization processes such as the impact of initial stretch of a liquid ligament on the size of the droplets it is going to disintegrate into, or the characteristic relaxation time of dilute viscoelastic solutions.

The possibility given by the multiscale method of conducting temporal analysis of atomization processes is not the motivation of its use in the present work. As explained above, textural atomization processes are local, rapid and involve very small structures, which complicates to temporally resolve the mechanism. In this work, it is rather decided to proceed to a global description of the textural deformation of the interfaces concerned textural atomization process. It is also intended to derive a mathematical representation of the textural atomization process and the notion of equivalent systems introduced by the multiscale method will help to this end. The scale distribution of a system is not a measurement of its shape and it has been demonstrated that different systems may report the same scale distribution. Such systems are referred to as *equivalent systems*. For instance, as detailed later in this text, it has been demonstrated that the scale distribution of a sphere is the same as the one of an ensemble of cylinders whose diameter are equiprobably distributed (Dumouchel et al., 2019). Furthermore, in 2D, which is the embedded dimension imposed by any image analysis approach, it has been shown that any system has an equivalent system of cylinders. Thus, giving a mathematical description for the equivalent system diameter distribution would give a mathematical formulation for the scale distribution of the actual system. This approach is very appealing in the present context where the textural tortuosity is expected to result from the development of more or less cylindrical ligaments whose 2D projections resemble cylinders. Therefore, the scale distribution of the textural atomization process will receive a mathematical representation from the mathematical diameter distribution of the equivalent system of cylinders. This process brings out the important question of the mathematical representation of the size distribution of ensembles of objects.

The question of a universal mathematical expression for the diameter distribution of liquid spray droplets has been largely debated in the community ((Lefebvre, 1989), (Babin-sky and Sojka, 2002), (Villermaux, 2007), (Dumouchel, 2009)) but it remains unanswered.

One of the reasons for that is that none of the approaches is based on a fine description of the atomization process. In the context of this work, the diameter distribution are represented by a three-parameter generalized gamma (3pGG) function. Presented in detail in the following, this function has been proven to cover a wide range of mathematical and empirical distributions of the literature. Furthermore, this function has modeling foundations (Dumouchel, 2006) which will help interpreting the results. The 3pGG function is going to be applied in the textural atomization process analysis to represent the diameter distribution of the cylinder equivalent system, and in the spray description to represent the drop diameter distribution.

# Chapter 3

## Mathematical Elements: Definitions and Concepts

### 3.1 Diameter Distribution

#### 3.1.1 General Concept

This section introduces the general concept of diameter distribution that will then be applied to sets of spheres and of cylinders in the two next sections. We consider an ensemble of  $N$  objects, each of them being fully defined by the quantity  $D$  called diameter. For the considered ensemble, the variable  $D$  is assumed to range in the interval  $[D_{min}, D_{max}]$ . The diameter distribution of this ensemble expresses the probability of occurrence associated with each value of the variable  $D$ . It can be constructed as follows. The interval  $[D_{min}, D_{max}]$  is divided into  $j$ -diameter classes, each of them being associated with a median diameter  $D_i$ , a class width  $\Delta D_i$  and an index  $i$ , ( $i = 1, 2, \dots, j$ ). Using these notations, the diameter interval corresponding to class  $i$  writes:

$$\left[ D_i - \frac{\Delta D_i}{2}, D_i + \frac{\Delta D_i}{2} \right] \quad (3.1)$$

for  $i = 1, 2, \dots, j$ . The diameter of the smallest and biggest objects,  $D_{min}$  and  $D_{max}$ , respectively, can then be expressed as:

$$D_{min} = D_1 - \frac{\Delta D_1}{2} \quad (3.2)$$

$$D_{max} = D_j + \frac{\Delta D_j}{2} \quad (3.3)$$

Each object of the ensemble is allocated in a class according to its diameter. If the number of objects belonging to class  $i$  is denoted  $N_i$ , the following equality can be written:

$$N = \sum_{i=1}^j N_i \quad (3.4)$$

The classes are constructed such that their widths are much smaller than their median diameters, i.e.  $\Delta D_i \ll D_i$ . Therefore, it is usually acceptable to assume that the objects of the same class have the same diameter equal to the median diameter  $D_i$ . Beside the median diameter  $D_i$ , each object in class  $i$  is associated with a characteristic length  $L_i$ , a characteristic surface area  $S_i$ , and a characteristic volume  $V_i$ . As for the diameter, all objects belonging to class  $i$  have the same length  $L_i$ , area  $S_i$  and volume  $V_i$ . The total length  $L$ , surface area  $S$ , and volume  $V$  of the whole ensemble can then be respectively expressed as:

$$\begin{aligned} L &= \sum_{i=1}^j N_i L_i \\ S &= \sum_{i=1}^j N_i S_i \\ V &= \sum_{i=1}^j N_i V_i \end{aligned} \quad (3.5)$$

The histogram probability of the number-weighted diameter distribution  $p_{0i}$ , length-weighted diameter distribution  $p_{1i}$ , area-weighted diameter distribution  $p_{2i}$ , and volume-weighted diameter distribution  $p_{3i}$  of the ensemble are respectively defined by:

$$\begin{aligned}
p_{oi} &= \frac{N_i}{N} \\
p_{1i} &= \frac{N_i L_i}{L} \\
p_{2i} &= \frac{N_i S_i}{S} \\
p_{3i} &= \frac{N_i V_i}{V}
\end{aligned} \quad i = 1, 2, \dots, j \quad (3.6)$$

By construction, Eqs. (3.4 - 3.6) indicate that:

$$\sum_{i=1}^j p_{ni} = 1 \quad n = 0, 1, 2, 3 \quad (3.7)$$

where  $n$  refers to the type of the distribution. Considering that the diameter is a continuous variable, it is more appropriate to use continuous diameter distributions  $f_n(D)$  defined by:

$$P_{ni} = \int_{D_{i,min}}^{D_{i,max}} f_n(D) dD \quad n = 0, 1, 2, 3 \quad (3.8)$$

where  $D_{i,min}$  and  $D_{i,max}$  are the minimum and maximum diameters of class  $i$ . The dimension of the diameter distributions  $f_n(D)$  is the inverse of a length. Furthermore, according to Eqs. (3.7 - 3.8) it is easy to show that the distributions  $f_n(D)$  are normalized, i.e.:

$$\int_0^{\infty} f_n(D) dD = 1 \quad n = 0, 1, 2, 3 \quad (3.9)$$

Furthermore, the cumulative diameter distributions,  $F_n(D)$  are also introduced:

$$f_n(D) = \frac{dF_n(D)}{dD} \quad F_n(D) = \int_0^D f_n(x) dx \quad n = 0, 1, 2, 3 \quad (3.10)$$

The cumulative distributions are monotonously increasing from 0 to 1. They express the number-fraction, length-fraction, surface-fraction and volume fraction of all the objects

that have a diameter less than or equal to  $D$ .

Finally, mean and representative diameters are defined from the distribution  $f_0(D)$  and the cumulative distributions  $F_n(D)$ , respectively. The series of mean diameters is built as the ratio of moments of  $f_0(D)$  of different orders (Mugele and Evans, 1951), i.e.:

$$(D_{ab})^{a-b} = \frac{\int_0^{\infty} f_0(D) D^a dD}{\int_0^{\infty} f_0(D) D^b dD} \quad (3.11)$$

where  $a$  and  $b$  can be any real number (providing that they are not equal). The sum  $a + b$  is called the order of the mean diameter (Lefebvre, 1989). The representative diameters  $D_{n\eta}$  are associated with a specific value of one of the cumulative distributions. They can be defined by the following equation:

$$F_n(D_{n\eta}) = \int_0^{D_{n\eta}} f_n(x) dx = \eta \quad n = 0, 1, 2, 3 \quad (3.12)$$

where  $\eta \in [0; 1]$ . The representative diameters are characteristics of the distribution type. Some of the representative diameters often encountered in the literature are  $D_{3, 0.1}$ ,  $D_{3, 0.5}$  and  $D_{3, 0.9}$ : 10%, 50% and 90% of the total volume of the ensemble is carried by objects with a diameter smaller than or equal to the representative diameter, respectively.

### 3.1.2 Application to an Ensemble of Spheres

This section applies the concept introduced in the previous section to an ensemble of spheres. Each sphere is associated with the median diameter  $D_i$  of the class it belongs to, as well as with a length  $L_i$  that is equal to the median diameter, with a surface area  $S_i$  that is the one of the circle of diameter  $D_i$ , this circle being the 2D projection of the sphere of the same diameter, and with a volume  $V_i$  that is the volume of the sphere of diameter  $D_i$ . These definitions give:

$$\begin{aligned} L_i &= D_i \\ S_i &= \frac{\pi}{4} D_i^2 \\ V_i &= \frac{\pi}{6} D_i^3 \end{aligned} \quad (3.13)$$

And Eqs (3.5), (3.6) and (3.13) lead to:

$$p_{ni} = \frac{p_{oi} D_i^n}{\sum_{i=1}^j p_{oi} D_i^n} \quad n = 0, 1, 2, 3 \quad (3.14)$$

Considering Eqs. (3.8) and (3.11), the previous equation (Eq. (3.14)) can be written as:

$$f_n(D) = \left( \frac{D}{D_{n0}} \right)^n f_0(D) \quad n = 0, 1, 2, 3 \quad (3.15)$$

Using Eq. (3.15), the equation of the mean diameters (Eq. (3.11)) can be reformulated as:

$$(D_{ab})^{a-b} = \frac{\int_0^{\infty} f_n(D) D^{a-n} dD}{\int_0^{\infty} f_n(D) D^{b-n} dD} \quad n = 0, 1, 2, 3 \quad (3.16)$$

Several mean diameters are frequently encountered among which the  $D_{10}$ ,  $D_{21}$ ,  $D_{32}$  and  $D_{43}$  that correspond to the arithmetic mean diameter of the distributions  $f_0(D)$ ,  $f_1(D)$ ,  $f_2(D)$  and  $f_3(D)$ , respectively (Sowa, 1992).  $D_{20}$  is the diameter of a sphere whose surface area multiplied by the total number of spheres equals the total surface area of the whole ensemble. Similarly,  $D_{30}$  is the sphere diameter whose volume multiplied by the total number of spheres equals the volume of the whole ensemble.

### 3.1.3 Application to an Ensemble of Cylinders

In this section, the concept of diameter distribution is applied to ensemble of cylinders. Considering all cylinders of the same length (for convenience we consider the length is one unit), they are all fully defined by their diameter  $D$ . Furthermore, the surface area of the cylinders is the cross-sectional one (i.e. the lateral surface area only without considering the one of both ends). In atomization, such cylinders may be seen as portions of liquid ligaments. The 2D projection of the cylinder is a rectangle as illustrated in Fig. 3.1.

On the basis of this definition, the characteristic length  $L_i$ , surface area  $S_i$ , and volume  $V_i$  of a cylinder of diameter  $D_i$  write:

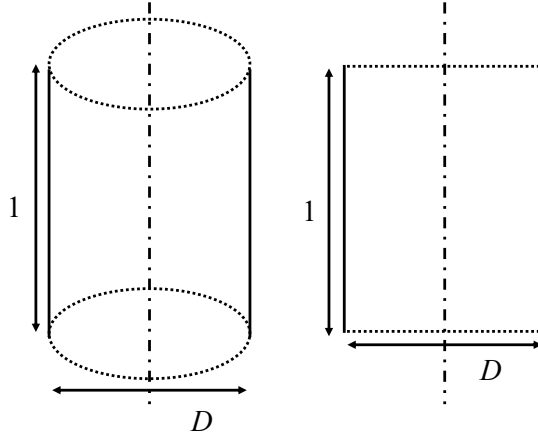


Figure 3.1: 3D-representation of a cylinder of a diameter  $D$  and unit height (left), and its 2D projection (right).

$$\begin{aligned}
 L_i &= D_i \\
 S_i &= D_i \\
 V_i &= \frac{\pi}{4} D_i^2
 \end{aligned}
 \tag{3.17}$$

Introducing these equations in Eqs.(3.5) and (3.6) leads to the following expression for the histogram series  $p_{ni}$ :

$$\begin{aligned}
 p_{ni} &= \frac{p_{oi} D_i^n}{\sum_{i=1}^j p_{oi} D_i^n} & n = 0, 1 \\
 p_{ni} &= \frac{p_{oi} D_i^{n-1}}{\sum_{i=1}^j p_{oi} D_i^{n-1}} & n = 2, 3
 \end{aligned}
 \tag{3.18}$$

In agreement with Eq. (3.17) we note that the histogram-probability length-weighted diameter distribution is equal to the surface-weighted diameter distribution, i.e.:

$$p_{1i} = p_{2i} \tag{3.19}$$

The same observation can be made between the distributions  $f_1(D)$  and  $f_2(D)$ , and between the cumulative distributions  $F_1(D)$  and  $F_2(D)$  when the diameter is considered as a continuous variable. In this case, the diameter distribution series writes:

$$\begin{aligned}
f_n(D) &= \left(\frac{D}{D_{n0}}\right)^n f_0(D) & n = 0, 1 \\
f_n(D) &= \left(\frac{D}{D_{n-1,0}}\right)^{n-1} f_0(D) & n = 2, 3
\end{aligned} \tag{3.20}$$

And the mean diameter series (Eq. (3.11)) is defined by:

$$\begin{aligned}
(D_{ab})^{a-b} &= \frac{\int_0^\infty f_n(D) D^{a-n} dD}{\int_0^\infty f_n(D) D^{b-n} dD} & n = 0, 1 \\
(D_{ab})^{a-b} &= \frac{\int_0^\infty f_n(D) D^{a-n+1} dD}{\int_0^\infty f_n(D) D^{b-n+1} dD} & n = 2, 3
\end{aligned} \tag{3.21}$$

The meaning of mean diameters has slightly changed compared to those characterizing an ensemble of spheres. Whereas  $D_{10}$  and  $D_{21}$  remains the arithmetic mean diameters of  $f_0(D)$  and of  $f_1(D)$  respectively, those of the distributions  $f_2(D)$  and  $f_3(D)$  are the mean diameters  $D_{21}$  and  $D_{32}$ . On the other hand  $D_{10}$  is the diameter of a cylinder whose surface multiplied by the total number of cylinders equals the total surface area of the ensemble of cylinders. Similarly  $D_{20}$  is the diameter of a cylinder whose volume multiplied by the total number of cylinders equals the total volume of the ensemble of cylinders.

### 3.1.4 Mathematical Representation of Spray Drop-Diameter Distribution

A universal mathematical distribution to represent spray drop diameter distribution has not been established so far despite the numerous investigations reported in the literature on this topic. According to Lefebvre (1989), such a mathematical distribution should have the following attributes:

1. Satisfactorily fit the drop size data.
2. Permit the extrapolation to droplet sizes outside the range of the measured data.
3. Allow easily calculating mean diameters and other parameters of interest.
4. Allow gathering large amount of data.

5. Ideally, provide some indications on the physical mechanisms involved in the atomization process.

Among the mathematical distributions of the literature, the three-parameter generalized Gamma (3pGG) function, introduced in previous works (Dumouchel (2006), Lecompte and Dumouchel (2008) for instance) fulfills these requirements. The 3pGG function is expressed as:

$$f_n(D) = \frac{q}{\Gamma\left(\frac{\alpha+n}{q}\right)} \left(\frac{\alpha}{q}\right)^{\frac{\alpha+n}{q}} \frac{D^{\alpha+n-1}}{D_{q0}^{\alpha+n}} \exp\left(-\frac{\alpha}{q} \left(\frac{D}{D_{q0}}\right)^q\right) \quad \text{with } n = 0, 1, 2, 3 \quad (3.22)$$

where  $\Gamma$  is the Gamma function and  $\alpha$ ,  $q$  and  $D_{q0}$  are the three parameters to be determined. The parameter  $n$  allows expressing all types of distributions, from the number-based to the volume-based representation. The 3pGG function provided sufficiently good representations of drop size distributions of very different sprays ((Lecompte and Dumouchel, 2008), (Fdida et al., 2018)). Furthermore, it covers a large range of empirical distributions of the literature. For instance:

- The Weibull distribution (Lindgren and Denbratt, 2000) writes:

$$f_0(D) = q \frac{D^{q-1}}{D_{q0}^q} \exp\left(-\left(\frac{D}{D_{q0}}\right)^q\right) \quad (3.23)$$

which is a 3pGG function when  $q = \alpha$ .

- The Rosin-Rammler distribution writes:

$$f_3(D) = q_{RR} \frac{D^{q_{RR}-1}}{D_{RR}^{q_{RR}}} \exp\left(-\left(\frac{D}{D_{RR}}\right)^{q_{RR}}\right) \quad (3.24)$$

where  $q_{RR}$  and  $D_{RR}$  are the parameters of the Rosin-Rammler distribution. This distribution is a 3pGG function when the parameters are related to each other by:

$$\begin{aligned} q &= q_{RR} \\ D_{q0} &= \left(\frac{q_{RR} - 3}{q_{RR}}\right)^{1/q_{RR}} D_{RR} \\ \alpha &= q_{RR} - 3 \end{aligned} \quad (3.25)$$

- The Nukiyama-Tanasawa distribution writes:

$$f_0(D) = a_{NT} D^{\alpha_{NT}} \exp(-b_{NT} D^{q_{NT}}) \quad (3.26)$$

where  $q_{NT}$ ,  $\alpha_{NT}$  and  $b_{NT}$  are the parameters of the Nukiyama-Tanasawa distribution and  $a_{NT}$  is the normalization parameter, i.e.:

$$a_{NT} = \frac{q_{NT}}{\Gamma\left(\frac{\alpha_{NT}+1}{q_{NT}}\right)} b_{NT}^{\frac{\alpha_{NT}+1}{q_{NT}}} \quad (3.27)$$

The Nukiyama-Tanasawa distribution is identical to a 3pGG function since distribution parameters are related to each other, i.e.:

$$\begin{aligned} q_{NT} &= q \\ b_{NT} &= \frac{\alpha}{q D_{q0}^q} \\ \alpha_{NT} &= \alpha - 1 \end{aligned} \quad (3.28)$$

Using Eq. (3.28), the normalization parameter (Eq. (3.27)) expresses as:

$$a_{NT} = q \left(\frac{\alpha}{q}\right)^{\alpha/q} \frac{1}{\Gamma\left(\frac{\alpha}{q}\right) D_{q0}^\alpha} \quad (3.29)$$

There is therefore no doubt that the 3pGG function is able to represent the drop-diameter distribution of many different sprays. This function presents also the advantage of allowing mathematical manipulations. For instance, the mean diameter series can be easily expressed as a function of the three parameters. It comes:

$$D_{kl}^{k-l} = \left(\frac{q}{\alpha}\right)^{\frac{k-l}{q}} \frac{\Gamma\left(\frac{\alpha+k}{q}\right)}{\Gamma\left(\frac{\alpha+l}{q}\right)} D_{q0}^{k-l} \quad (3.30)$$

The 3pGG function given by Eq. (3.22) has a bell shape showing one mode (one maximum) only. The mode appears for the modal diameter  $D_{pn}$  that depends on the type of the distribution (Dumouchel, 2006). It can be shown that:

$$D_{pn} = \left[ \frac{\alpha - 1 + n}{\alpha} \right]^{1/q} D_{q0} \quad (3.31)$$

In the context of spray drop-diameter distribution, the 3pGG function has been established from the application of the Maximum Entropy Formalism (MEF). This formalism has been widely used in the literature to establish drop diameter and velocity distributions of liquid sprays (Babinsky and Sojka, 2002). The MEF is a statistical tool allowing the determination of a probability density function or a probability distribution on the basis of partial information of the sought distribution. This information imposes a set of constraints the distribution has to satisfy. Among all distributions satisfying a set of constraints, the MEF suggests to take as solution the most objective one, i.e., the solution whose statistical entropy is maximum. In a previous investigation (Dumouchel, 2009) the MEF was used to derive a mathematical distribution for spray drop-diameter distribution on the basis of three constraints. The first constraint imposes the normalization of the diameter distribution. Since the diameter of the drops of any spray is always bounded by a maximum value, the second constraint states that all the moments of the distribution must be finite. This constraint is expressed as:

$$\int_0^{\infty} f_0(D) D^q dD = D_{q0}^q \quad (3.32)$$

This constraint introduces two parameters, i.e.,  $q$  and  $D_{q0}$ . In the following the parameter  $q$  is taken positive. Furthermore, in virtue of the surface tension effects, producing infinitely small droplets requires more energy than producing larger droplets. Therefore, larger droplets have more possibilities to be produced than small ones. The third constraint takes this into account and introduces a diameter accessibility distribution  $g(D)$  by:

$$g(D) = AD^{\alpha-1} \quad (3.33)$$

where  $A$  is a constant. As far as the surface tension efforts are concerned, the probability of producing a drop with a diameter equal to  $D$  is proportional to  $g(D)$ . The parameter  $\alpha$  is taken positive and greater than 1. The distribution  $g(D)$  indicates that the probability of producing a droplet with a diameter equals to zero is null. (This is coherent with the fact that the cohesion surface tension forces of such a drop would be infinity.) According to (Kapur, 1983) the statistical entropy of the sought distribution includes the distribution  $g(D)$  and writes:

$$S = -k \int_0^{\infty} f_0(D) \ln \left( \frac{f_0(D)}{g(D)} \right) dD \quad (3.34)$$

where  $k$  is a constant. The distribution that satisfies all constraints (Eqs. (3.32 and 3.33 plus the normalization) and that maximizes the statistical entropy  $S$  can be calculated. It is the 3pGG function given by Eq. (3.22). This short presentation of the origin of the

3pGG function reminds us the meaning of the parameter  $\alpha$ . It describes the population in the small diameter range: The smaller the parameter  $\alpha$ , the higher the propensity to disperse in the small diameter region. This is illustrated in Fig. 3.2 which shows the 3pGG number-based distribution ( $n = 0$ ) with  $q = 10$  and  $D_{q0} = 300 \mu\text{m}$  and a parameter  $\alpha$  ranging from 4 to 10. It can be seen that reducing  $\alpha$  allows the small diameter region to be more and more populated. This behavior is described as an increase of the dispersion in the small diameter range.

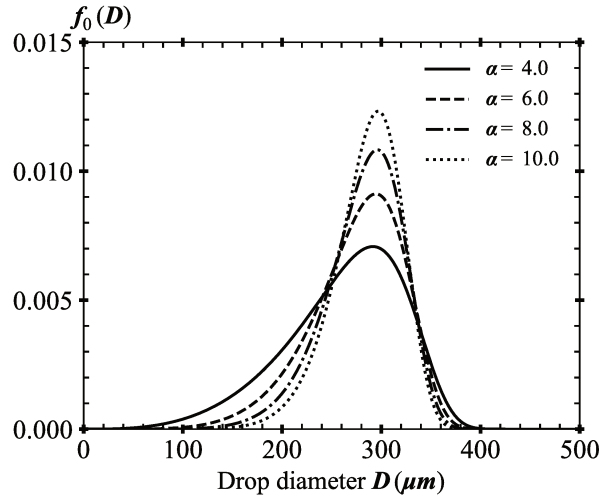


Figure 3.2: Effect of the parameter  $\alpha$  on the number-based drop diameter distribution given by Eq. (3.22) at  $n = 0$ ,  $q = 10$  and  $D_{q0} = 300 \mu\text{m}$ .

## 3.2 Scale Distribution

### 3.2.1 General Concept

The diameter distributions introduced in the previous section are convenient to ensembles of objects provided that these objects are fully defined by one variable, the diameter  $D$ . As shown above, this is the case for ensembles of spheres or of cylinders. However, such a representation does not suit sprays of non spherical drops for instance. For such situations, a multiscale description has been suggested in a previous investigation (Dumouchel et al., 2008). The ensemble of non spherical elements is described by the scale distribution. In Dumouchel et al. (2008) this distribution is measured on images of the 2D projections of the elements. Inspired from the fractal analysis, the scale distribution is based on the application of the Euclidean Distance Mapping (EDM) as follows. Let us consider a 2D system of arbitrary shape (see Fig. 3.3a) whose total surface area is noted  $S_T$ . This system

is eroded using a circular structuring element of diameter  $d$  (Soille, 2013). The diameter  $d$  is referred to as the *scale of observation*. The result of the erosion operation is illustrated in Fig. 3.3b. The surface area of the eroded system at scale  $d$  is noted  $S(d)$  (black region in Fig. 3.3b) and the cumulative (surface-based) scale distribution  $E_2(d)$  is defined as:

$$E_2(d) = \frac{S_T - S(d)}{S_T} \quad (3.35)$$

The distribution  $E_2(d)$  is determined for  $d$  varying from 0 to infinity. For  $d = 0$ ,  $S(d =$

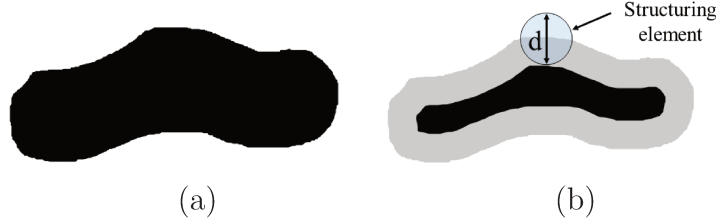


Figure 3.3: Illustration of the erosion principle performed on a system with arbitrary shape: a) system before erosion, b) system after an erosion operation at scale  $d$  (the black region is the remaining surface area after erosion denoted by  $S(d)$ ).

$0) = S_T$  and  $E_2(d = 0) = 0$ . When  $d$  tends toward infinity,  $S(d) \rightarrow 0$  and  $E_2(d) \rightarrow 1$ . Furthermore,  $E_2(d)$  keeps increasing when  $d$  increases. Therefore,  $E_2(d)$  is a cumulative scale distribution. The first derivative in the scale space of the cumulative distribution  $E_2(d)$  is the surface-based scale distribution  $e_2(d)$ :

$$e_2(d) = \frac{dE_2(d)}{dd} = \frac{P(d)}{2 \times S_T} \quad (3.36)$$

The unit of the distribution  $e_2(d)$  is the inverse of a length. As expressed by Eq.(3.36) the scale distribution  $e_2(d)$  is equal to the ratio of the perimeter  $P(d)$  of the system eroded at scale  $d$  divided by twice the surface area  $S_T$ .

Although the multiscale description has been developed for deformed objects, it can be applied on simple objects such as the 2D projections of a cylinder or of a sphere as defined in the previous subsection and reproduced in Fig. 3.4. For these two cases, the cumulative  $E_2(d)$  and the scale distribution  $e_2(d)$  can be analytically determined. Indeed, it can be shown that the scale distribution of the 2D projection of a cylinder of diameter  $D$  is given by:



Figure 3.4: 2D projection of a cylinder of diameter  $D$ (left) and of a sphere of diameter  $D$  (right).

$$e_2(d) = \begin{cases} \frac{1}{D} & \text{when } d < D \\ 0 & \text{Otherwise} \end{cases} \quad (3.37)$$

and the scale distribution of the 2D projection of a sphere of diameter  $D$  is equal to:

$$e_2(d) = \begin{cases} \frac{2}{D} \left(1 - \frac{d}{D}\right) & \text{when } d < D \\ 0 & \text{Otherwise} \end{cases} \quad (3.38)$$

These scale distributions are illustrated in Fig. 3.5. We note that the 2D scale distribution of a cylinder reports no dependence on the scale  $d$  except when it is equal to the diameter of the cylinder. The 2D scale distribution of a sphere shows a linear dependence on scale. The distributions in Fig. 3.5 show that the scale distribution allows differentiating objects according to the derivative of the distribution.

Fig. 3.5 shows that for the 2D projection of a cylinder or of a sphere, all characteristics of the scale distribution (value at  $d = 0$ , slope, maximum scale) are functions of the single characteristic  $D$ . Therefore, these objects are not multiscale. However, an ensemble of cylinders or of spheres of different sizes will be multiscale due to the size distribution of the objects. This size distribution can be represented by the functions introduced in the beginning of this chapter and the ensemble may also be described by its 2D scale distribution. Therefore, for ensembles of cylinders or of spheres, the diameter distribution and the scale distribution must be related to each other. This very point is presented in the two next subsections.

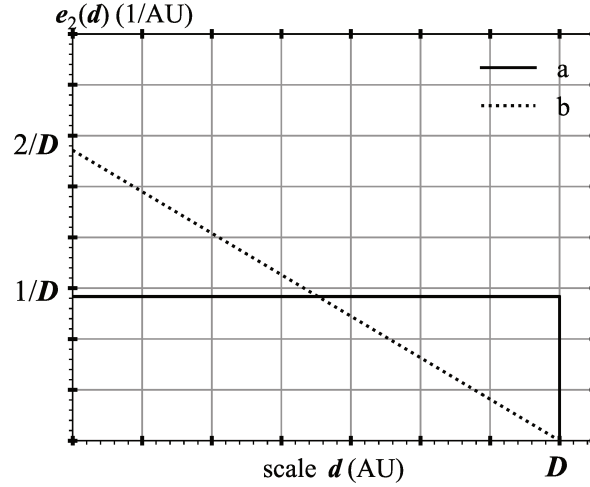


Figure 3.5: Scale distribution of the 2D projection of a) a cylinder of diameter  $D$  and b) a sphere of diameter  $D$  (Eqs. (3.37 and 3.38), respectively.)

### 3.2.2 Application to an Ensemble of Spheres

We consider an ensemble of spheres whose diameters  $D$  are distributed according to known cumulative distributions  $F_n(D)$ . It has been established that the diameter and scale distributions of this system are related to each other as ((Dumouchel et al., 2008) and Ngo (2013)):

$$\begin{aligned}
 E_2(d) &= F_2(d) + 2\frac{d}{D_{21}} - \left(\frac{d}{D_{20}}\right)^2 (1 - F_0(d)) \\
 e_2(d) &= \frac{2}{D_{21}}(1 - F_1(d)) - 2\frac{d}{D_{20}^2}(1 - F_0(d))
 \end{aligned}
 \tag{3.39}$$

where  $D_{a,b}$  are the mean diameters defined by Eq. (3.16).

For illustration purposes, applications of Eq. (3.39) are presented. The first one concerns an ensemble of spheres of the same size (mono-dispersed distribution), the second one deals with an ensemble of spheres whose diameter distribution is equiprobable. Finally, a more general case is presented. It concerns an ensemble of spheres whose diameters are distributed according to a 3pGG function.

#### *Ensemble of Mono-Dispersed Spheres*

The ensemble of spheres considered in this application consists of spheres of the same diameter  $D'$ . In this case, it can be easily shown that the cumulative diameter distributions

$F_n(D)$  satisfy:

$$\begin{aligned} F_n(D) = 0 & \quad \text{if} \quad D < D' \\ F_n(D) = 1 & \quad \text{if} \quad D \geq D' \end{aligned} \quad n = 0, 1, 2, 3 \quad (3.40)$$

and the mean diameter series is given by:

$$D_{ab} = D' \quad (3.41)$$

Using Eqs. (3.39, 3.40 and 3.41), the cumulative and the scale distributions associated with this ensemble of spheres are expressed as:

$$\begin{aligned} E_2(d) &= 1 - \left(1 - \frac{d}{D'}\right)^2 \\ e_2(d) &= \frac{2}{D'} \left(1 - \frac{d}{D'}\right) \end{aligned} \quad (3.42)$$

As expected, since all spheres have the same diameter, the scale distribution  $e_2(d)$  is identical to the one of a single sphere (Eq. (3.38)). This first application validates Eq. (3.39).

### *Ensemble of Equi-Probable Spheres*

In this second application, an ensemble of spheres with an equi-probable number-based diameter distribution (i.e.,  $f_0(D) = \text{constant}$ ) is considered. If the sphere diameters range in the interval  $[0; D_{max}]$ , the number-based diameter distribution writes:

$$f_0(D) = \frac{1}{D_{max}} \quad (3.43)$$

Using Eqs. (3.16, 3.15 and 3.10), Eq. (3.43) allows expressing the cumulative and diameter distributions of all types:

$$\begin{aligned} F_n(D) &= \left(\frac{D}{D_{max}}\right)^{n+1} \\ f_n(D) &= \frac{(n+1)D^n}{D_{max}^{n+1}} \end{aligned} \quad n = 0, 1, 2, 3 \quad (3.44)$$

as well as the series of the mean diameters that is given by:

$$D_{ab} = \left( \frac{b+1}{a+1} \right)^{\frac{1}{a-b}} D_{max} \quad (3.45)$$

Finally, introducing Eqs. (3.44 and 3.45) in Eq. (3.39) reports the surface-based cumulative and scale distributions of an ensemble of equi-probable spheres:

$$\begin{aligned} E_2(d) &= 1 - \left( 1 - \frac{d}{D_{max}} \right)^3 \\ e_2(d) &= \frac{3}{D_{max}} \left( 1 - \frac{d}{D_{max}} \right)^2 \end{aligned} \quad (3.46)$$

The similarity of these distributions with those of the previous case (Eq. (3.42)) can be noted.

#### *Ensemble of 3pGG Distributed Spheres*

We finally consider a set of spheres whose diameters are distributed according to a 3pGG function. For such an ensemble, the diameter distributions of all types are given by Eq. (3.22). It can be shown that the cumulative diameter distributions are therefore given by (Dumouchel et al., 2008):

$$F_n(D) = 1 - \frac{\Gamma\left(\frac{\alpha+n}{q}, X\right)}{\Gamma\left(\frac{\alpha+n}{q}\right)}, \quad n = 0, 1, 2, 3 \quad (3.47)$$

where  $X = \frac{\alpha}{q} \left( \frac{d}{D_{q0}} \right)^q$ . Introducing this equation in Eq. (3.39) leads to the following expression for the surface-based scale distribution of an ensemble of spheres distributed according to a 3pGG function:

$$e_2(d) = \frac{2}{D_{q0}} \left( \frac{\alpha}{q} \right)^{(1/q)} \frac{\left( \Gamma\left(\frac{\alpha+1}{q}, X\right) - X^{1/q} \Gamma\left(\frac{\alpha}{q}, X\right) \right)}{\Gamma\left(\frac{\alpha+2}{q}\right)} \quad (3.48)$$

Once again, it is interesting to underline the ease of performing calculations with 3pGG functions.

### 3.2.3 Application to an Ensemble of Cylinders

We now consider ensembles of cylinders whose diameters are distributed according to known cumulative distributions  $F_n(D)$ . It has been shown that the surface-based cumulative and scale distributions of these ensembles are related to the diameter cumulative distributions as, (Ngo, 2013):

$$\begin{aligned} E_2(d) &= F_2(d) + \left(\frac{d}{D_{10}}\right)(1 - F_0(d)) \\ e_2(d) &= \frac{(1 - F_0(d))}{D_{10}} \end{aligned} \quad (3.49)$$

As in the previous subsection, these equations are applied to determine the surface-based scale distributions of an ensemble of mono-dispersed cylinders, an ensemble of equiprobable cylinders, and an ensemble of cylinders whose diameters are distributed according to a 3pGG function.

#### *Ensemble of Mono-Dispersed Cylinders*

In this first example, all cylinders have the same diameter  $D'$ . Equations (3.40 and 3.41) established for an ensemble of mono-dispersed spheres remain valid for the mono-dispersed ensemble of cylinders. Introducing these equations in Eq. (3.49) reports the following cumulative and scale distributions:

$$\begin{aligned} E_2(d) &= 1 - \left(1 - \frac{d}{D'}\right) \\ e_2(d) &= \frac{1}{D'} \end{aligned} \quad (3.50)$$

As expected, these expressions are the same as those established for a single cylinder (Eq. 3.37).

#### *Ensemble of Equi-Probable Cylinders*

The case of an equi-probable ensemble of cylinders is treated by considering that the diameters of the objects range in the interval  $[0; D_{max}]$ . As for the ensemble of equi-probable spheres, the number-based diameter distribution is given by Eq. (3.43). Using Eq.(3.20) along with the definition of the cumulative diameter distributions report the following expression for the cumulative distributions  $F_n(D)$  of an ensemble of equi-probable cylinders:

$$\begin{aligned} F_0(D) &= \frac{D}{D_{max}} \\ F_n(D) &= \left( \frac{D}{D_{max}} \right)^n \quad n = 2, 3 \end{aligned} \quad (3.51)$$

Remembering that  $F_1(D) = F_2(D)$  for any ensemble of cylinders and applying Eq. (3.51) in Eq. (3.49) lead to the following expressions for the cumulative and scale distributions of an ensemble of equi-probable cylinders:

$$\begin{aligned} E_2(d) &= 1 - \left( 1 - \frac{d}{D_{max}} \right)^2 \\ e_2(d) &= \frac{2}{D_{max}} \left( 1 - \frac{d}{D_{max}} \right) \end{aligned} \quad (3.52)$$

As for the ensembles of spheres, the proximity of writing of Eqs. (3.50 and 3.52) has to be noted. Furthermore, we see that the scale distributions of an equi-probable ensemble of cylinders are the same as those of a mono-dispersed ensemble of spheres. This important remark leads to the notion of Equivalent System that is presented in the last subsection of this chapter.

#### *Ensemble of 3pGG Distributed Cylinders*

We finally consider a set of cylinders whose diameters are distributed according to a 3pGG function. For such an ensemble, the diameter distributions of all types have to be rewritten from Eq. (3.22) by incorporating the specific feature of cylinder ensembles, i.e.,  $f_1(D) = f_2(D)$ . It comes:

$$f_n(D) = \frac{q}{\Gamma\left(\frac{\alpha+n-1}{q}\right)} \left(\frac{\alpha}{q}\right)^{\frac{\alpha+n-1}{q}} \frac{D^{\alpha+n-2}}{D_{q0}^{\alpha+n-1}} \exp(-X) \quad , \quad n = 2, 3 \quad (3.53)$$

Therefore, the cumulative diameter distributions are given by:

$$F_n(D) = 1 - \frac{\Gamma\left(\frac{\alpha+n-1}{q}, X\right)}{\Gamma\left(\frac{\alpha+n-1}{q}\right)}, \quad n = 2, 3 \quad (3.54)$$

Introducing this equation in Eq.(3.49) leads to the following expression for the surface-based scale distribution of an ensemble of cylinders distributed according to a 3pGG function:

$$e_2(d) = \frac{1}{D_{q0}} \left(\frac{\alpha}{q}\right)^{\frac{1}{q}} \frac{\Gamma\left[\frac{\alpha}{q}, \frac{\alpha}{q} \left(\frac{d}{D_{q0}}\right)^q\right]}{\Gamma\left(\frac{\alpha+1}{q}\right)} \quad (3.55)$$

where the  $\Gamma(a, b)$  is the upper-incomplete Gamma function.

### 3.2.4 Atomization Process Multiscale Description and Equivalent Systems

Although the multiscale description has been initially developed to provide a better description of non-spherical drop ensemble, it can be applied to describe any system of any shape, and, in particular, liquid system experiencing atomization. Such an application has been reported in the investigation of the atomization of deformed and stretched individual ligaments (Dumouchel et al., 2015a). In that study, the atomization of individual ligaments detaching from a turbulent sheet was followed by high frequency visualization. The scale distribution of the ligaments was measured as a function of time. The analysis of this evolution demonstrated that the size distribution of the drops results from a competition between the surface tension forces and the initial elongation the ligament is subjected to. When temporal resolution is not available, the atomizing flow is locally described from the nozzle exit down to the spray region. At each position, a local scale distribution averaged on a high number of realizations is measured, and the spatial scale distribution evolution is analyzed as a temporal evolution. This approach has been experimented on the atomization of highly perturbed liquid sheets ((Dumouchel and Grout, 2009), Vu and Dumouchel (2018)), of turbulent jets produced by car injectors (Dumouchel et al., 2015b), and of free viscoelastic jets submitted to a capillary instability (Tirel et al., 2017). These analyses demonstrated that the initial perturbations and the subsequent liquid structure development is controlled by the issuing flow dynamic whereas the deformation and breakup of these structures is a surface tension dominated process (Dumouchel et al., 2015b). This conclusion agrees with the one drawn from the fractal analysis of atomizing turbulent liq-

uid sheets (Grout et al., 2007). Furthermore, the multiscale analysis allowed differentiating the ligament production mechanisms and their impact on the spray drop size distribution in the atomization of such sheets (Vu and Dumouchel, 2018). Applied to viscoelastic capillary liquid jets, the multiscale analysis allows measuring the characteristic time of the elongational flows which are dominant in the atomization pattern of such liquids and that results in the production of numerous ligaments (Tirel et al., 2017). This time, known as the relaxation time, is an intrinsic property of the solution. The strength of this method is its ability to measure very small relaxation time (down to  $26 \mu\text{s}$  so far) and therefore to characterize very dilute polymer solutions for which no other technique is available.

As said in the previous chapter, textural atomization processes are local, rapid and involve very small structures. It is not intended, within the scope of this work, to perform a dynamic analysis of the process. The multiscale method will be applied to provide a description of the textural atomization process. Global scale distributions, averaged on many realizations, of the flow issuing from the nozzle will be measured. The behavior of these scale distributions in the small scale region will provide a description of the textural deformation of the liquid flow. Thus, a scale distribution describing the interface textural deformation will be obtained.

The mathematical formulation of the textural atomization process is also an objective of the work. To this end, the notion of Equivalent Systems can be used. It has been introduced from the observation that different systems may have the same scale distribution. This has been illustrated in the previous subsections where the surface-based scale distribution of a sphere has been found the same as the one of an ensemble of equiprobable cylinders. Equivalent systems are defined as follows:

TWO SYSTEMS ARE SAID EQUIVALENT IF AND ONLY IF THEIR RESPECTIVE  
SCALE DISTRIBUTIONS ARE EQUAL.

This notion has been used in previous investigations to derive mathematical expressions for measured scale distributions. For instance, the measured scale distributions of non-spherical drops produced from the atomization of stretched ligaments were successfully reproduced by those of ensemble of spheres distributed according to a 3pGG function (Dumouchel et al., 2015a). Therefore, the experimental scale distribution could receive a mathematical expression which is the one corresponding to its equivalent system of spherical elements.

However, an Equivalent System can not be constructed with any simple objects. For instance, it is impossible to determine an ensemble of spheres that would produce the surface-based scale distribution of a unique cylinder. On the other hand, in 2D, it can be demonstrated that an equivalent system of cylinders exists for any system.

From Eq.(3.49) it is possible to express the scale distribution of a cylinder ensemble as a function of its number-based diameter distribution  $f_{0c}(D)$ . It comes:

$$e_2(d) = \frac{1}{D_{10}} \left( 1 - \int_0^d f_{0c}(D) dD \right) \quad (3.56)$$

This equation can be used to determine the cylinder equivalent-system diameter distribution  $f_{0c}(D)$  from the scale distribution  $e_2(d)$  of the actual system. It comes:

$$f_{0c}(D) = -D_{10} \left[ \frac{de_2(d)}{dd} \right]_{d=D} \quad (3.57)$$

Since the scale distribution is always derivable, Eq. (3.57) says that  $f_{0c}(D)$  can always be calculated. In 2D, any system can be represented as an equivalent system of cylinders. The number-based diameter distribution of this system is given by Eq. (3.57). Furthermore, Eq. (3.57) allows establishing a mathematical formulation for the scale distribution  $e_2(d)$  if the diameter distribution  $f_{0c}(D)$  has one. In particular, if  $f_{0c}(D)$  is represented by a 3pGG function, the scale distribution takes the mathematical formulation reported by Eq. (3.55). In virtue of Eq. (3.57) and since the 3pGG function exhibits a single mode, Eq. (3.55) can represent scale distributions with a single inflexion point only. As for sphere ensembles, the parameters  $\alpha$  and  $q$  control the dispersion of the cylinder diameter distribution in the small and large regions, respectively. When applied to a set of deformed ligaments, the scale distribution  $e_2(d)$  contains information on the ligament size distribution in the large-scale region, and it contains information on the ligament deformation in the small-scale range. Therefore, when applying Eq. (3.55) to a set of deformed ligaments, the parameter  $q$  is sensitive to the ligament size distribution and the parameter  $\alpha$  to the distribution of scales associated with their deformation. To our knowledge, this is the first time an atomization process receives a mathematical expression based on these concepts.

# Chapter 4

## Experimental Setup and Optical Diagnostics

### 4.1 Hydraulic Circuit: Elements and Working Principle

The schematic of the hydraulic circuit is depicted in Fig. 4.1. The working fluid used is tap water (density  $\rho_l = 998.2 \text{ kg/m}^3$ , dynamic viscosity  $\mu = 0.001 \text{ Pa}\cdot\text{s}$ , surface tension with air  $\sigma = 0.07 \text{ N/m}$ ). This water is softened using a water lime-removal device then it is stocked in a non-pressurized 200 L reservoir at room temperature. The liquid is delivered by a centrifugal pump (Perollo PQM 2900 rev/min) that generates a fixed volume flowrate  $Q_{Tot} = 0.6 \text{ m}^3/\text{hr}$  at a pressure head of 7 bar. This flowrate is divided into  $Q_{Reg}$  that goes back to the reservoir and ( $Q_m = Q_{Tot} - Q_{Reg}$ ) that goes to the atomizer, see Fig. 4.1. The reservoir is automatically filled (a floating-valve is installed at the inlet of the tank) to ensure safe operational conditions for the pump. The backflow to the reservoir is filtered by a  $50 \mu\text{m}$  filter (Cuno) and is regulated by an electro-pneumatic globe-type flow control valve. The use of a bypass principle emanates from the inability of the pump along with the regulating valve to provide small flow rates. The bypass flow to the atomizer is regulated within a range of flowrates for  $Q_m$  from 20 to 170 ( $10^{-3} \text{ kg/s}$ ).

The flowrate  $Q_m = Q_{Tot} - Q_{Reg}$  in the bypass is controlled by a Coriolis-type mass flow meter (Micromotion IF9701R2N3B, 0-3400 range,  $\pm 4.2 \text{ kg/h}$  precision). The repeatability and reliability of flowrate measurements were controlled by a weighting procedure for the range of flowrates in this experiment. The pressure in the circuit is measured by a pressure sensor (Kistler PR23Y) placed after the flow meter. A shut-off electro-pneumatic ball valve (Parker 341N05) is installed to provide flexibility during the experiment, i.e. liquid injection

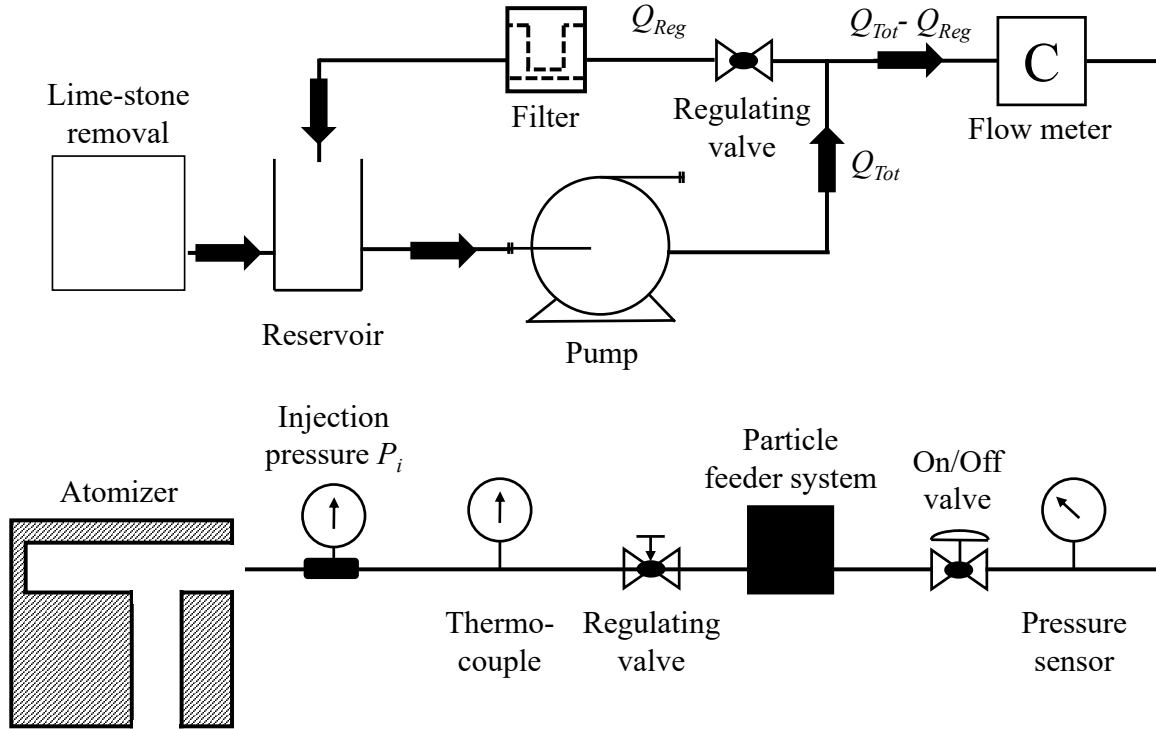


Figure 4.1: Schematic of the hydraulic circuit of the experimental test bench.

can be temporarily stopped by simply shutting off this valve without turning off the pump. A particle feeder-system is installed to add tracer particles to the water flow in order to enable velocity measurements inside the atomizer using laser Doppler velocimetry. The feeder system is detailed in §4.5.4. For very low flowrate ranges, an additional manual valve can be adjusted to precisely increase the pressure loss. This valve is placed between the feeder system and the atomizer. The water temperature is measured close to the atomizer inlet using a PT100 temperature sensor. Thanks to the automatic filling of the reservoir with fresh water, the water temperature remains at  $20 \pm 2^\circ\text{C}$  during the experiments. The liquid pressure (injection pressure  $P_i$ ) is measured just before the atomizer by a piezo-resistive pressure sensor (Kistler PR33X) connected to a 240 mL container where the liquid is quasi-static. The back-pressure at nozzle exit remains at atmospheric pressure  $P_{back} = P_{atm}$  for all the experiments. The differential pressure  $\Delta P_i = P_i - P_{back}$  is the reference pressure used to qualify the flow regimes (see section 4.4).

## 4.2 The Atomizer

The atomizer is a simplified large-scale model inspired from the internal path of a VCO Diesel nozzle (bounded by the red rectangle in Fig 4.2a). This atomizer has planar diopters

which facilitates visualizing the internal flow. Furthermore, the cavitation manifests itself at a relatively low velocity which also simplifies the optical measurements.

The schematic of the atomizer is presented in Fig. 4.2b. The internal flow is a 'T-shape' channel flow delimited using metallic and transparent plates. The cross-section is rectangular in each part of the flow with a thickness of 1 mm. The horizontal inlet channel is connected to the vertical nozzle orifice with an angle of  $90^\circ$ . The nozzle orifice has a rectangular shape whose dimensions are  $16 \text{ mm} \times 4 \text{ mm}$  in length ( $L_{ch}$ ) and width ( $w_{ch}$ ) respectively. The flow enters the nozzle along the horizontal  $x$  axis from right to left and exits the nozzle orifice along the vertical  $z$  axis.

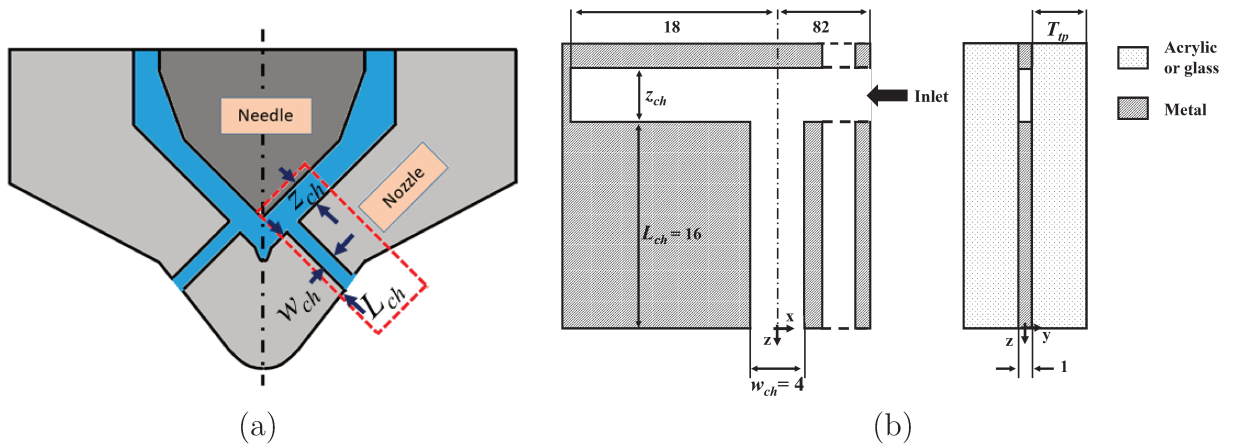


Figure 4.2: a) Schematic of a VCO injector (Sou et al., 2012) and b) schematic of the atomizer that is inspired from the internal path of a VCO atomizer, the red rectangle on Fig. a. Left is the front view and right is the side view. Dimensions are in mm.

Three atomizers with similar geometries but different inlet channel heights  $Z_{ch}$  are used. Two atomizers have a channel height  $Z_{ch} = 4$  mm and for the third one  $Z_{ch} = 2$  mm. The first atomizer body, named A1, is made of acrylic (thickness per plate  $T_{tp} = 25$  mm) and manufactured by Akira Sou, Kobe University, Japan. The other two atomizers, named G1 and G2, are made of BK7 glass (thickness per plate  $T_{tp} = 10$  mm). The motivation for manufacturing the glass atomizer was to provide transparent plates with a better optical quality and also with a smaller thickness, to improve the performances of velocity measurements of the internal flow using the LDV technique (see §4.5). The main characteristics of the atomizers are summarized in Table 4.1. We also take the opportunity to provide a full optical access to the nozzle outlet orifice for the glass atomizers, by removing any external part of the metallic plates from the transparent ones (see Fig. 4.3).

The atomizer is fixed on 3D linear displacement system (Zaber X-LSMS050A and X-LSMS200B). The travel distances are 200 mm for the vertical axis and 50 mm for the other axes. The repeatability of this system is less than  $1 \mu\text{m}$ .

Table 4.1: Characteristics of the atomizers.

Atomizer	Channel height $Z_{ch}$	Transparent thickness $T_{tp}$ (mm)	Body material
A1	4	25	acrylic
G1	4	10	glass BK7
G2	2	10	glass BK7



Figure 4.3: The atomizer with acrylic transparent material on the left (Sou et al., 2012), and BK7 glass on the right.

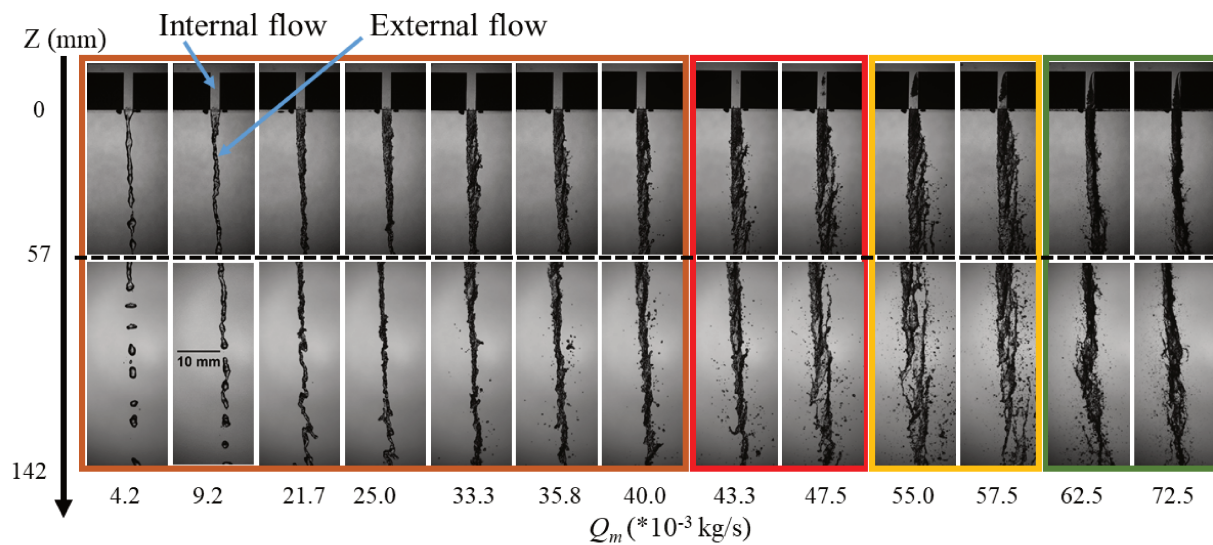
### 4.3 Identification of Flow Regimes

Identification of the flow regimes covered by the experiment is first done by visualizing the flow in the nozzle and in the near field of the nozzle orifice. Preliminary observations are performed simultaneously for the internal and external flow on A1 atomizer as a starting point.

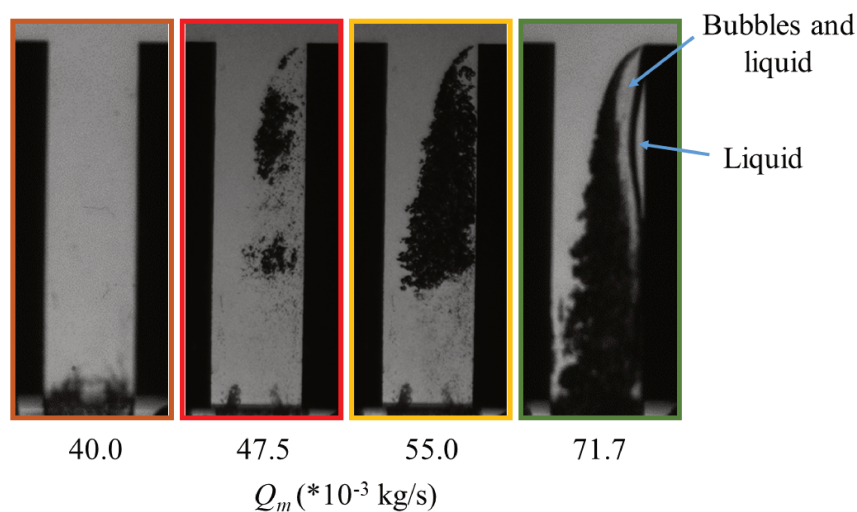
Visualization is performed by using a backlight configuration. The three essential components of this configuration, i.e. the light source, the object to be visualized and the camera are aligned along the optical axis. For the preliminary observations we employed a CCD camera (mvBlueCougar x125aG Matrix Vision) with a Cavitar 200 W as a light source (optical system No.I in Table 4.6). The details of this optical system are given in §4.6.

Front view visualizations are shown in Fig. 4.4: top row shows the internal and the near field external flow and bottom row shows the external flow farther downstream, i.e. at 57 mm from the nozzle-orifice exit. In Fig. 4.4 flow rate  $Q_m$  increases from left to right.

According to the internal flow and following the categorization of Sou et al. (2008), four regimes are identified. The first regime (bounded by the brown rectangle) is the one where there is no cavitation evidenced in the nozzle orifice. This regime is called *no-cavitation*



(a)



(b)

Figure 4.4: a) Preliminary front-view visualization using A1 atomizer: upper-row is the internal and external flow (the black pixels are cavitating structures for the internal flow and liquid for the external flow); bottom-row is the external flow captured at 57 mm downstream the nozzle-orifice exit. Brown-rectangle: no-cavitation flow regime; red-rectangle: cavitation inception flow regime; yellow-rectangle: super-cavitation flow regime; green-rectangle: partial-hydraulic flip regime; b) internal flow zoomed-in for representative operating conditions.

*flow Regime*. The second regime is the one where the cavitation starts to appear only in the first half of the nozzle orifice. This regime is called *cavitation inception flow Regime*. In the third regime the cavitation extends from the nozzle-orifice inlet to just above the orifice exit. This regime is referred to as *super-cavitation flow Regime*. When the cavitation cloud extends further downstream and goes out of the nozzle, the regime is called, in our case, *partial-hydraulic flip Regime* (Soteriou et al., 1995).

The preliminary observations reveal a modification of the atomization processes as the flow rate increases and as the cavitation inside the orifice evolves. We notice that the jet width in the near field increases as we move from no-cavitation to super-cavitation flow regime (as noticed by Arai et al. (1985), Sou et al. (2007, 2012)) and finally decreases for the partial hydraulic flip regime. We further notice the development of ligamentary deformations on, mainly, the right-side of the jet interface (Sou et al., 2008), i.e. on the side where the cavitation develops. Henceforth, we concentrate on the operating conditions corresponding to cavitating regimes, but starting from  $Q_m = 40 \cdot 10^{-3}$  kg/s which belongs to the non-cavitating flow regimes as shown in Fig. 4.4b.

## 4.4 Operating Conditions

In the experiment the mass flowrate  $Q_m$  is imposed and represents the control parameter of the study. The flowrate was varied to cover the different flow regimes in the nozzle from non-cavitating to partial-hydraulic flip regimes for the three tested atomizers. The injection pressure measured just upstream the atomizer is a consequence of the pressure losses for a given atomizer and a given flowrate.

The losses in the flow are characterized by the discharge coefficient (Gellales, 1931)  $C_D$  defined as the ratio of the actual flowrate to the theoretical one predicted by Bernoulli's principle, i.e. without pressure losses:

$$C_D = \frac{Q_m}{A_0 \sqrt{2\rho_l \Delta P_i}} \quad (4.1)$$

The discharge coefficients for the three atomizers shown in Fig. 4.5 as a function of  $\sqrt{\Delta P_i}$  exhibit nearly constant values for each atomizer, over the flowrate range of the study. For A1 atomizer,  $C_D \simeq 0.44$  and for G1 and G2 atomizers  $C_D \simeq 0.51$  and  $0.32$  respectively. Whereas the smallest value for G2 atomizer is expected, the difference between A1 and G1 was not awaited as the internal geometries of these atomizers are the same.

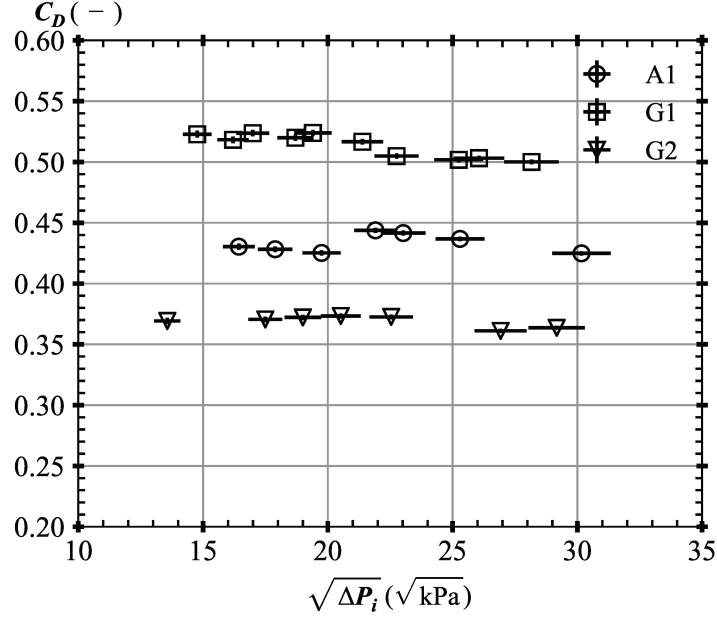


Figure 4.5: Discharge coefficient as a function of the injection differential pressure for A1, G1 and G2 atomizers.

Flow conditions in the three atomizers are characterized through the determination of Reynolds, Weber and cavitation numbers defined hereafter :

$$Re = \frac{U_b h_{noz}}{\nu} \quad (4.2)$$

$$We_g = \frac{\rho_g U_b^2 h_{noz}}{\sigma} \quad (4.3)$$

$$CN = \frac{p_{amb} - p_v}{0.5 \rho_l U_b^2} \quad (4.4)$$

where  $U_b = \frac{Q_m}{\rho_l A_0}$  is the bulk velocity in the orifice channel,  $\rho_l = 998.2 \text{ kg/m}^3$  is the water density,  $A_0$  is the cross-sectional area of the orifice exit,  $h_{noz} = 1 \text{ mm}$  is the nozzle-orifice thickness,  $\nu = 1 \times 10^{-6} \text{ m}^2 \cdot \text{s}^{-1}$  is the kinematic viscosity of water,  $\rho_g = 1.204 \text{ kg/m}^3$  is the air density,  $\sigma = 0.07 \text{ N/m}$  is the surface tension of water with air and  $p_v = 2339 \text{ Pa}$  is the vapor pressure of water at ambient temperature.

The operating conditions are summarized in Table 4.2, 4.3 and 4.4 for atomizers A1, G1 and G2 respectively.

The Reynolds ranges from  $5 \cdot 10^3$  to  $20 \cdot 10^3$  which suggests a sufficiently developed turbulence to trigger early perturbation of the issuing liquid flow.

Table 4.2: Operating conditions of A1 atomizer.

Condition No.	$Q_m$ ( $10^{-3}$ kg/s)	$\Delta P_i$ (kPa)	Regime	$U_b$ ( $m.s^{-1}$ )	$C_D$ (-)	$Re$ (-)	$CN$ (-)	$We_g$ (-)
A1-1	40.0	272	I	10.0	0.43	10000	1.98	1.7
A1-2	43.3	322	II	10.8	0.43	10800	1.69	2.0
A1-3	47.5	386	II	11.9	0.43	11900	1.40	2.4
A1-4	55.0	480	III	13.8	0.44	13800	1.05	3.3
A1-5	57.5	526	III	14.4	0.44	14400	0.96	3.6
A1-6	62.5	636	IV	15.6	0.44	15600	0.81	4.2
A1-7	72.5	914	IV	18.1	0.42	18100	0.60	5.7

Table 4.3: Operating conditions of G1 atomizer.

Condition No.	$Q_m$ ( $10^{-3}$ kg/s)	$\Delta P_i$ (kPa)	Regime	$U_b$ ( $m.s^{-1}$ )	$C_D$ (-)	$Re$ (-)	$CN$ (-)	$We_g$ (-)
G1-1	40.0	190	I	10.0	0.51	10000	1.98	1.7
G1-2	43.3	219	I	10.8	0.52	10800	1.69	2.0
G1-3	47.5	261	II	11.9	0.52	11900	1.40	2.4
G1-4	55.0	355	III	13.8	0.52	13800	1.05	3.3
G1-5	57.5	383	III	14.4	0.52	14400	0.96	3.6
G1-6	62.5	462	III	15.6	0.51	15600	0.81	4.2
G1-7	66.7	532	IV	16.7	0.51	16700	0.71	4.8
G1-8	75.8	705	IV	19.0	0.50	19000	0.55	6.2

Table 4.4: Operating conditions of G2 atomizer.

Condition No.	$Q_m$ ( $10^{-3}$ kg/s)	$\Delta P_i$ (kPa)	Regime	$U_b$ ( $m.s^{-1}$ )	$C_D$ (-)	$Re$ (-)	$CN$ (-)	$We_g$ (-)
G2-1	18.3	73	I	4.6	0.38	4600	9.42	0.4
G2-2	28.3	184	I	7.1	0.37	7100	3.95	0.9
G2-3	36.7	306	II	9.2	0.37	9200	2.36	1.4
G2-4	40.0	361	II	10.0	0.37	10000	1.98	1.7
G2-5	43.3	421	III	10.8	0.37	10800	1.69	2.0
G2-6	47.5	508	III	11.9	0.37	11900	1.40	2.4
G2-7	55.0	725	IV	13.8	0.36	13800	1.05	3.3
G2-8	60.0	851	IV	15.0	0.36	15000	0.88	3.9

The aerodynamic Weber number remains low enough ( $\lesssim 6$ ) to consider that the aerodynamic forces have a negligible effect on the atomization process.

The cavitation number  $CN$  is an indicator of the propensity of the internal flow to cavitate. The cavitation number chosen in this work is the one used by He and Ruiz (1995). This number accounts for the liquid vapor pressure in the expression of the pressure to be overcome to produce cavitation, and for the atomizer pressure-drop in the expression of the available pressure. A decrease of this number indicates an increasing propensity to cavitate.  $CN$  ranges from  $\simeq 0.5$  to  $\simeq 10$ , the lowest values being obtained for the highest flowrates, corresponding to cavitating regimes. The cavitation number value for which the cavitation starts to appear is about 1.7, 1.5 and 2.5 for A1, G1 and G2 atomizers respectively. The transition from developing cavitation to the super-cavitation regime is occurring for  $CN \simeq 1$  for A1 and G1 atomizers, and about 1.7 for G2 atomizers. Highest values of  $CN$  for G2 atomizer are consistent with the fact that cavitation propensity is significantly increased for this atomizer.

## 4.5 Punctual Optical Measurement Techniques

The velocity of the internal flow is measured using the Laser Doppler Velocimetry (LDV) technique. The velocity and diameter of droplets in the spray are measured by the Phase Doppler Particle Analyzer (PDPA) technique. These techniques are based on the light scattered by particles. Seeding particles were added to the liquid for internal flow-velocity measurements whereas droplets produced by atomization of the liquid served as probed particles. Both LDV and PDPA techniques share the same measurement principle. The basics of this measurement principle are underlined hereafter.

### 4.5.1 Velocity Measurement

LDV and PDPA measurements are based on the Doppler effect that is summarized here. The reader can refer to (Albrecht et al., 2013) for more details. Two coherent monochromatic laser beams of wavelength  $\lambda$  are intersecting with an angle  $\theta$  to constitute a cigar-like shape probe volume (see Fig. 4.6-left) constituted of fringes formed by the interference between the two beams. When a particle is traversing through the probe volume, it diffuses the light in all directions. This scattered light can be predicted by the generalized Lorenz-Mie Theory (Gouesbet et al., 1988). The light scattered by the traversing particle is received by photo-multipliers. The signal, called Doppler burst, is shown in Fig. 4.6-right. The frequency  $f_D$  of the light received by the photomultipliers depends on the velocity of

the traversing particle  $V_z$  and on the inter-fringe distance  $\delta_f$ , more precisely:

$$V_z = \delta_f f_D = \frac{\lambda}{2 \sin(\theta/2)} f_D \quad (4.5)$$

The measurement of the Doppler burst frequency  $f_D$  gives a rise to the determination of the particle velocity. As the burst frequency does not depend on the direction of the particle, the sign of  $V_z$  is not known a priori. This ambiguity is solved by introducing a frequency shift (40 MHz) thanks to a Bragg cell placed on one of the two beams that induces a fringe motion. A second velocity component is measured by using two additional laser beams of a different wavelength intersecting at the same location as the former.

### 4.5.2 Diameter Measurement

The light scattered by a particle depends on the size of this particle. Indeed, particles can be seen as spherical lenses, projecting an image of the fringes in the space whose size depends on the particle diameter. Using two sensors to record the Doppler burst will give the same velocity. However, the distance between these sensors and the magnification induced by the particle size will generate a time delay between the signals recorded by the two photomultipliers. The phase difference  $\Delta\Phi$  between the signals is linearly related to the diameter  $D$  of a spherical particle:

$$\Delta\Phi = C_\Phi D \quad (4.6)$$

where  $C_\Phi$  is the phase factor constant that depends on the sensor locations and the optical settings. The measurement of the time delay (phase difference) between the two Doppler bursts is used to determine the particle diameter by the PDPA measurement technique.

### 4.5.3 LDV and PDPA Setup

LDV and PDPA systems used in this work were both sharing the same optical configuration. It is composed of two pairs of monochromatic laser beams, transmitting optics (including Bragg cell) that makes the beams crossing with an angle  $\theta$ , receiving optics including lenses and photomultipliers and a signal processing unit, see Fig. 4.7.

The main characteristics of the settings are summarized in Table 4.5. The range of velocity for LDV setup is -187 to 263 m/s and -394 to 419 for PDPA setup. However, the registered velocity range is adapted to each operating condition.

The size of the probe volume, as shown in Table 4.5, is larger in the  $d_y$  direction due to the small value of  $\theta$  angle, compared to the other directions. A spatial filter is thus used to reduce the probe volume in this direction to about  $50 \mu\text{m}$ .

The diameter and velocity of drops in the spray are measured using the PDPA system in the dual mode configuration. In this mode the two photomultipliers pairs are incorporated in the same housing. Also, the off-axis scattering configuration is employed, characterized by the scattering angle  $\Phi_r$  of the collecting optics as shown in Fig. 4.7. Figure. 4.8 presents also the PDPA arrangement. Furthermore, the measurements were performed in the non-coincidence mode, i.e. the velocity and the diameter measurements are not necessarily performed on the same droplet.

Table 4.5: Characteristics of LDV and Phase Doppler Particle Analyzer (PDPA) setups.

	LDV		PDPA	
	Blue	Green	Blue	Green
Beam color	Blue	Green	Blue	Green
Wavelength (nm)	488	514	488	514
Number of fringes	21	21	21	21
Inter-fringe ( $\mu\text{m}$ )	2.025	2.133	3.989	4.201
Probe volume $dx$ ( $\mu\text{m}$ )	44.54	46.92	87.72	92.39
Probe volume $dy$ ( $\mu\text{m}$ )	367	386.6	1431	1507
Probe volume $dz$ ( $\mu\text{m}$ )	44.22	46.57	87.55	92.22
Beam half-angle $\theta/2$ (deg)	6.919	6.919	3.507	3.507
Scattering angle $\Phi$ (deg)	32	32	32	32
Receiver focal length [mm]	310	310	310	310
Scattering mode			Refractive	Refractive

#### 4.5.4 Seeding Particles

As indicated before, seeding particles were added to the liquid to trace the liquid flow and measure the liquid velocity in the nozzle. Seeding particles used are silver-coated hollow glass spheres (S-HGS) of mean diameter  $D_p = 10 \mu\text{m}$  and density  $\rho_p = 1.4 \text{ g.cm}^{-3}$ . The Stokes number  $St$  of the particles is used to evaluate their traceability relative to the fluid flow under consideration:

$$St = \frac{\rho_p D_p^2 U_b}{18\mu L_c} \quad (4.7)$$

where  $U_b$  is the velocity and  $\mu$  the dynamic viscosity of the liquid and  $L_c$  is a characteristic length of the flow. For  $L_c = 1 \text{ mm}$  and  $U_b = 20 \text{ m/s}$ , the Stokes number of S-HGS particles  $St = 0.13$ , indicating a good traceability (i.e.  $St < 1$ ) of the silver coated hollow glass sphere (S-HGS) particles in the present study.

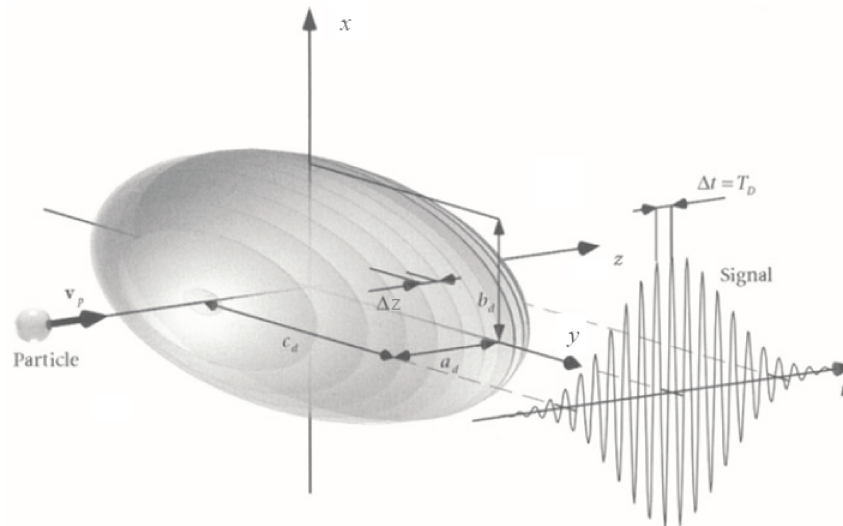


Figure 4.6: Example of a probe volume (on the left) and a Doppler burst (on the right) (Albrecht et al., 2013).

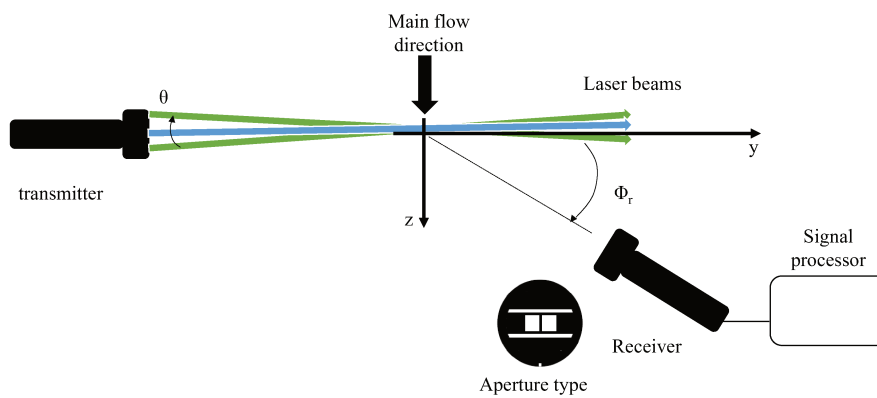


Figure 4.7: Schematic of the LDV and PDPA systems.

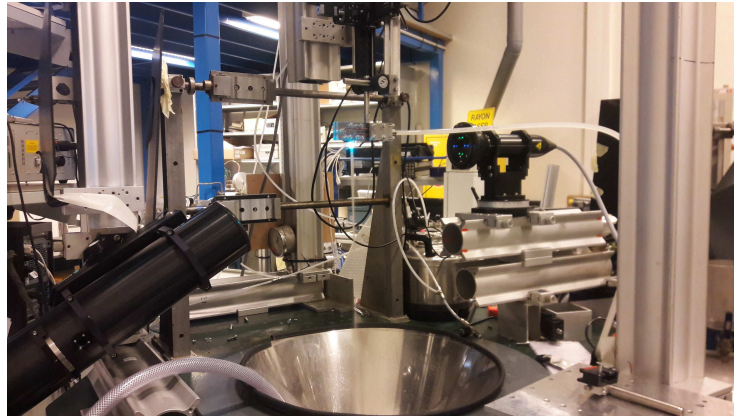
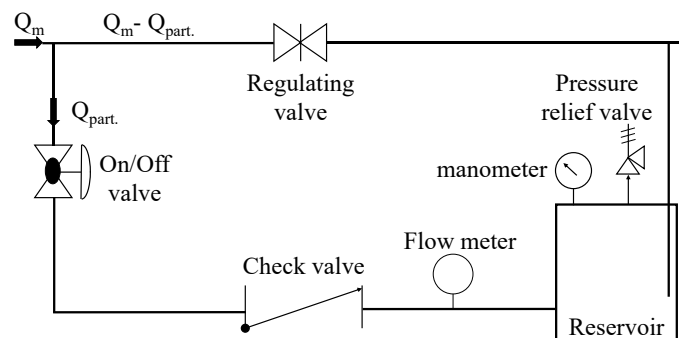


Figure 4.8: PDPA arrangement.

These particles were added to the liquid flow with a home-made seeding-particles feeder system whose schematic drawing is shown in Fig. 4.9. This system is a by-pass based-system, i.e. only part of the flow passes through the feeder system (particles flowrate  $Q_{part}$ ). The volume of the reservoir where seeding particles are placed is 5 liters. The liquid flows in the reservoir from the bottom to achieve an improved water-particle mixture. This mixture exits the tank by means of a pipe that extends from the top of the reservoir downstream to around 3-quarters of its length. This configuration is employed to alleviate the participation of the sedimented particles and to obtain a mixture between water and particles as homogeneous as possible. The activation of this circuit is achieved by opening an electrically-actuated on-off valve. The flow rate of the particle line is adjusted manually by means of the flow control valve to adjust the particle concentration. A pressure relief valve and a manometer are installed on the tank for security purposes.

Figure 4.9: Schematic of the seeding particles feeder system.  $Q_{part}$  is the flow rate in particles line.

## 4.6 Back-Light Imaging Measurement Techniques

### 4.6.1 Still Visualization

Visualization of the internal flow is only possible with an optical axis perpendicular to the width of the nozzle orifice, i.e. with an image plane parallel to  $(x, z)$ . This is called the 'front-view'. For the external flow, front-views and side-views have been made, the latter being obtained with an image plane parallel to  $(y, z)$  (see Fig. 4.2b). The two configurations are presented in Fig. 4.10.

For still images campaign, three different light sources are employed. Firstly, a Cavitar 200 W that is a high-power diode laser of variable pulse duration (down to 10 ns). This source has a wavelength of 640 nm and a maximum repetition rate of 100 kHz. The monochromatic nature with low degree of coherence make this source suitable when illumination with no speckle and no chromatic aberrations is desired. The light source consists in 4 components; namely, Cavilux control unit, laser unit, fiber optics and a collimating optics. The last can be manipulated for light optimization purposes. The collimating optics diameter is 25 mm which is smaller than the region of interest to be viewed (about  $80 \times 90 \text{ mm}^2$ ). Thus, a diffuser is inserted between this optics and the object in order to enlarge the back illumination.

Secondly, Cavitar 400 W that is identical to the 200 W Cavitar except for the power and the collimating optics which is 50 mm. The targeted region of interest using this light source delimits  $20 \times 13 \text{ mm}^2$ , and therefore, there is no need for a light diffuser.

Thirdly, a Quantel Ultra, frequency doubled Q-switched Nd: YAG laser ( $\lambda = 532 \text{ nm}$ ). This laser offers a short pulse duration ( 7 ns) and a repetition rate of 15 Hz providing a 30 mJ energy per pulse. We use light diffusers to cover the required field of view .

Two different cameras are used in the still images. The first one is a CCD camera (mvBlueCougar x125aG Matrix Vision) that provides a definition of  $2448 \times 2050$  pixels ( $3.45 \times 3.45 \mu\text{m}^2$ ) and a dynamics of 8 bits. The maximum obtainable frame rate is 10 Hz. Along with the camera, a 75 mm Avenir TV lens objective is used (magnification  $\gamma = 0.08$ ). The interrogation window (being suitable for the target of this study) delimits a region of interest of  $77 \times 87 \text{ mm}^2$  corresponding to  $1800 \times 2040$  pixels. The magnification leads to a pixel size in the object plane of  $43 \mu\text{m}$ .

The second camera is a CCD Dalsa Pantera 11M4 which offers a definition of  $2672 \times 4016$  pixels and a pixel size of  $9 \mu\text{m}$  as well as a dynamics of 8 bits. A Nikon objective (300mm f/4D IF-ED) with an extension tube of 36 cm length are used in order to obtain a magnification  $\gamma = 1.71$  and to achieve the required window of interrogation. One configu-

ration is made by combining this camera with the Nd: YAG source. In this case the spatial resolution is  $5.26 \mu\text{m}/\text{pixel}$  and the field of view is  $21.4 \times 14.2 \text{ mm}^2$ . Another configuration is used where the Cavitator 400 W source is associated to the Dalsa camera. In this latter case, a slightly higher magnification of  $\gamma = 1.84$  is obtained so that the spatial resolution is  $4.9 \mu\text{m}/\text{pixel}$  and the field of view is  $19.9 \times 13.2 \text{ mm}^2$ .

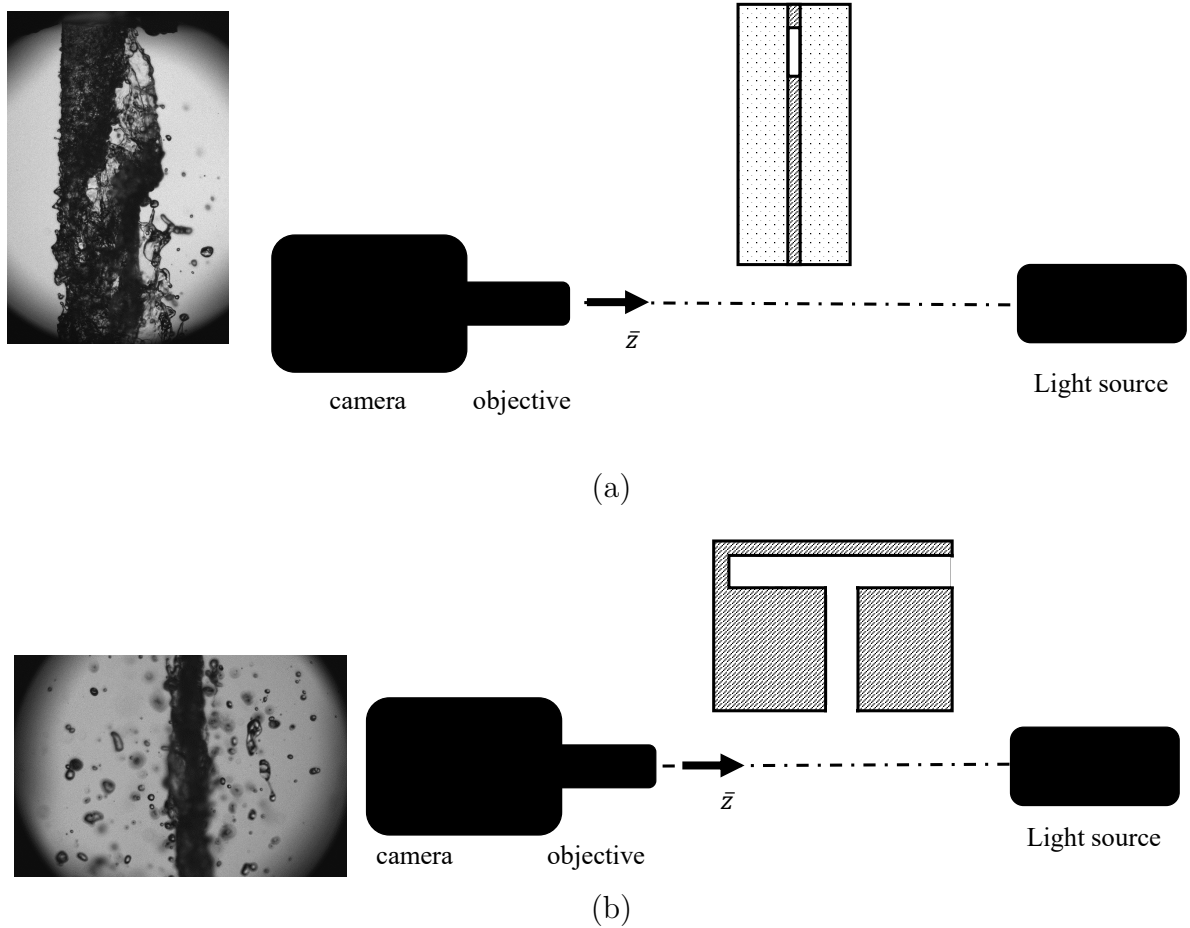


Figure 4.10: General schematic of the back-light illumination used in the present work for the visualization of: a) front view using the side view of the atomizer and b) side view using the front view of the atomizer (see Fig. 4.2b).  $\bar{z}$  is the optical axis.

Table 4.6 summarizes the visualization systems. The synchronization of the first and second systems are implemented as follows. The laser control unit and the camera are connected to the computer. We use an external synchronization mode, where the camera is triggered by a TTL signal originated from the laser control unit. This signal, whose duration is less than  $1 \mu\text{s}$ , might not be sufficient to trigger the camera. Therefore, the signal is directed to a delay generator (BNC model DG645) where the signal duration and delay are carefully adjusted. The produced signal then triggers the camera and an image

is captured.

Table 4.6: Summary of the visualization systems dedicated for capturing still images.

System No.	Light source	Camera	Diffuser No.	Objective (mm)	magnification ( $\gamma$ )
I	Cav. 200 W	mvBlue Cougar	1	75	0.08
II	Cav. 400 W	Dalsa	0	300	1.84
III	Nd: YAG	Dalsa	2	300	1.71

The third system is synchronized using a delay generator (BNC model DG645) that sends external TTL synchronization signals to trigger both the camera and the laser. The signal is sent to the camera through the computer and the camera opens its shutter for a relatively long time ( $1 \mu\text{s}$ ). The delay for the laser signals is adjusted to activate the laser pulse once camera shutter is completely opened. Considering the highest velocity in this experiment (20 m/s), the displacement of the jet during the laser pulse is  $0.14 \mu\text{m}$  which is much smaller than the resolution ( $5.26 \mu\text{m}/\text{pixel}$ ). This allows for a non-blurred image to be captured by the camera.

### 4.6.2 High-Speed Visualization

Back-light imaging is also employed for high-speed visualization experiments. High-speed visualization is used to track the evolution of the cavitation inside the nozzle as well as the evolution of the jet flow issuing from the atomizer. Figure 4.10 is still valid for the high-speed visualization. Two different optical diagnostics, that employ the same light source but two different cameras, are used. The systems employ a Xenon arc-based lamp with a power of 300 W (LSB530, LOT-Quantum Design) as a light source. It provides high intensity light with a luminous flux of 7000 lumens.

The first camera is a high-speed Vision Research CMOS Phantom V2640. It offers a maximum definition of  $2048 \times 1952$  pixels, and a pixel size of  $13.5 \mu\text{m}$ , which corresponds to a sensor size of  $27.6 \times 26.3 \text{ mm}^2$ . The maximum dynamics of this camera is 12 bits. A Nikon 300 mm f/4D IFED objective along with a 36 cm extension tube is associated to this camera to provide a magnification  $\gamma = 1.61$  corresponding to a resolution of  $8.4 \mu\text{m}/\text{pixel}$ . The maximum speed of the camera at full resolution is 6,600 fps and at a definition of  $1920 \times 1080$  pixels is 12,500 fps. For this definition, the window size in the object field is  $16 \times 17 \text{ mm}^2$ . This camera has several operating modes. In the standard mode, it has an exposure time of  $1 \mu\text{s}$  and this time can be decreased down to 142 ns in the high speed (HS) mode. The exposure time is set to 2-3  $\mu\text{s}$  to get enough illumination on the image sensor. The maximum displacement of the liquid elements for the highest

velocity ( $U_b = 20$  m/s) is thus around  $40 \mu\text{m}$  ( $\sim 5$  pixels), leading to some blurring effects in region of high velocity. The rate of frame per second utilized in the present work is 20000 fps at  $2048 \times 600$  pixels and 38000 fps at  $2048 \times 304$  pixels.

The second camera is a high-speed CMOS SA1.1 Photron. It offers a maximum definition of  $1024 \times 1024$  pixels, and a pixel size of  $20 \mu\text{m}$ , which corresponds to a sensor size of  $20.5 \times 20.5 \text{ mm}^2$ . Similarly, a Nikon 300 mm f/4D IFED objective along with a 15.5 mm extension tube is associated to this camera to provide a magnification  $\gamma = 0.97$  corresponding to a resolution of  $20.6 \mu\text{m}/\text{pixel}$ . The maximum speed of the camera at full resolution is 5,400 fps and at a definition of  $64 \times 16$  pixels is 675,000 fps. The exposure time is set to 12-83  $\mu\text{s}$ . The maximum displacement of the liquid elements for the highest velocity ( $U_b = 15$  m/s for G2 atomizer) is thus around  $180 \mu\text{m}$  ( $\sim 9$  pixels). Therefore, a blurring effect could be observed. Table 4.7 summarizes the systems of visualization.

Table 4.7: Summary of the visualization systems dedicated for capturing high-speed images.

System No.	Light source	Camera	Diffuser No.	Objective (mm)	magnification ( $\gamma$ )
I	Xenon	Phantom V2640	1	300	1.61
II	Xenon	Photron SA1.1	1	300	0.97

### 4.6.3 Image Pre-processing

Image analysis is applied to both still images and high-speed videos. High-speed videos can be seen as a set of successive still images that are individually processed with the same tools as for still visualization. A pre-processing must be applied to the images before making any measurement on an image. These treatments are explained just below.

Lets first recall what a numerical image is. It is a 2-dimensional matrix of pixels (picture element), each pixel physically corresponds to a photo-sensitive area on an image sensor. The amount of light reaching this area is translated in grey levels in the image. Thus, grey levels are positive by nature. The range of grey levels depends on the digitalization of the image; for instance, 8-bit image has a range of  $2^8 = 256$  levels from 0 to 255.

As we mentioned previously, back-light imaging techniques were used throughout this work. Liquid jet, droplets or cavitation bubbles are lit up by a lighting source. Light is refracted by liquid-gas interfaces of vapor bubbles or of liquid droplets and ligaments. Thus, in the internal flow the unaffected background corresponds to liquid. The attenuation of light indicates the presence of another phase. In fact, the existence of small bubbles

(gaseous or vapor) manifests by a darker grey level. In the flow emanating from the orifice, it is the liquid that appears in black over a white background corresponding to the air.

#### 4.6.3.1 Image Normalization

The light sources used in back-light configurations might produce heterogeneous background. As a consequence, pixels of the background might not all have the same illumination and this illumination can fluctuate from shot-to-shot. Therefore, normalization step is proposed to compensate this heterogeneity. This step is valid as far as the response of photo-sensor is linearly proportional to the light intensity, which is the case in the present work. To perform the normalization, two images have to be captured for each experiment:

1. Illuminated background without the liquid injection.
2. Obscurity image captured without the lighting source. The detected low gray-level in the obscurity image results from the electronic noise mainly due to the sensor temperature.

For both illuminating background and obscurity image, the mean over group of images is considered. Figure 4.11a represents the liquid jet (black color) issued from the acrylic atomizer (see fig 4.3), Fig. 4.11b resembles the background without injection and Fig. 4.11c is the obscurity. The intensity of the pixel  $(i, j)$  in the normalized image, shown in Fig. 4.11d, is calculated as follows:

$$I_n(i, j) = \alpha \frac{I_{im}(i, j) - I_{ob}(i, j)}{I_{bg}(i, j) - I_{ob}(i, j)} * N_F * GL_{max} \quad (4.8)$$

where the subscripts (im, ob, bg) refer to raw image, obscurity image, and background image, respectively;  $N_F$  is a normalization factor ( $N_F < 1$  to prevent overloaded grey levels);  $GL_{max}$  is the digitization-based maximum grey level (255 for the 8-bit digitization);  $\alpha$  is a shot-to-shot correction factor given by the ratio between the mean energy reference level of the source to the energy reference level of the image at the recording time:

$$\alpha = \frac{I_{bg}(Ref)}{I_{im}(Ref)} \quad (4.9)$$

The intensity references in Eq. (4.9) can be considered as: 1) the maximum grey level value in the images, 2) the mode (most populated grey level) of the grey level histogram searched in the background populations (see the arrows in Figs. 4.11f and 4.11e) or 3) the mean grey value of a region-of-interest (ROI) with no object. The temporal variation of

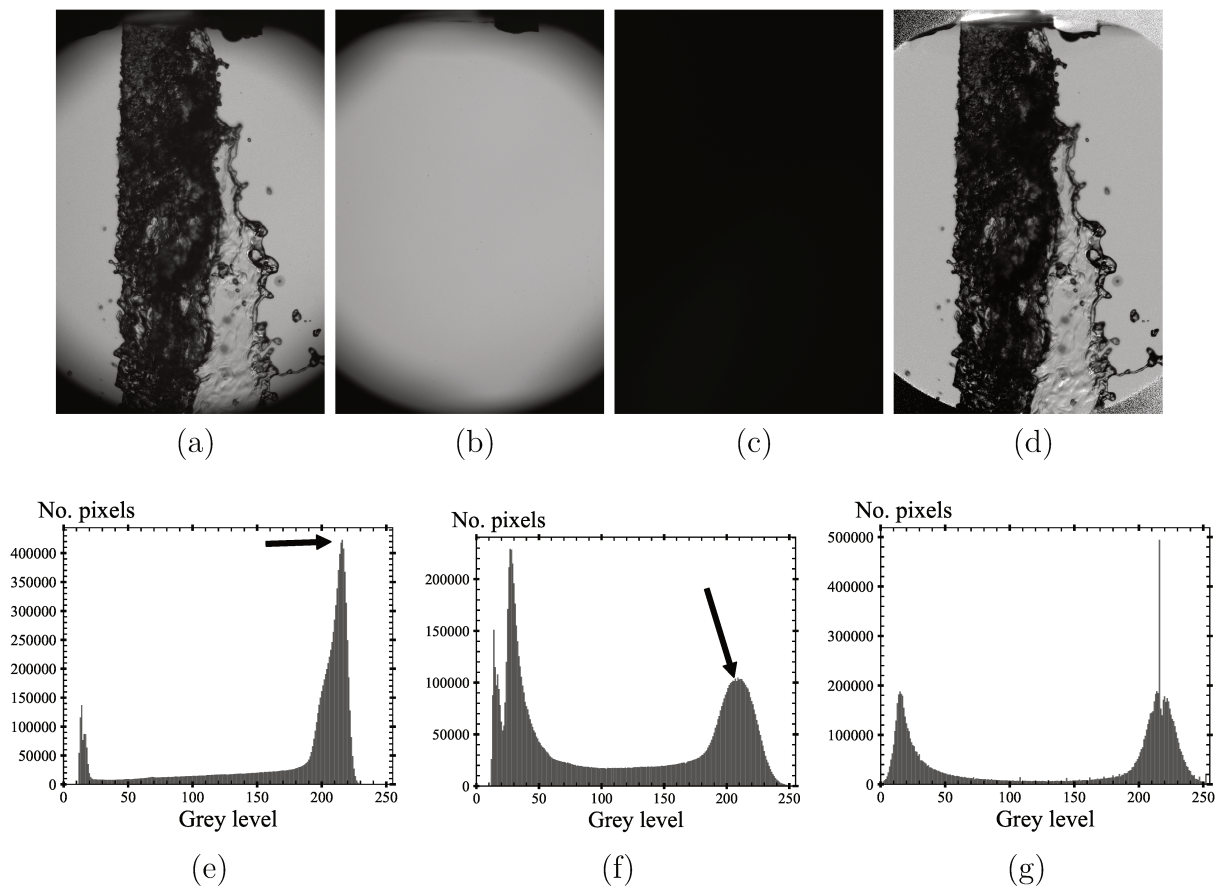


Figure 4.11: Illustration of the normalization process. a) raw image, b) background image, c) obscurity image, d) normalized image, e) grey level histogram of the background image, f) grey level histogram of the raw image and g) grey level histogram of the normalized image.

the background is compensated with this treatment, the efficiency being increased from option 1) to option 3). For jet or cavitation images where a region free of any black object can be defined, the third option is considered. For spray images with many droplet images covering the entire field of view, the second option is taken.

By looking at the grey level histogram of the raw and normalized images, Figs. 4.11f and 4.11g, respectively, we see that the background illumination of the normalized image is far less scattered than that of the raw image. We note that dark corner zones remain in the normalized image, because of the limited optical aperture (vignetting effect), that could not be treated in the normalization step. In this case, a suitable mask is applied to eliminate these zones.

#### 4.6.3.2 Image Segmentation

Image segmentation is an important task that implies the classification of pixels in sets corresponding to particular properties that can be identified by human beings. The objective here is to identify liquid or vapor phases on the images. The results are given in the form of a two-level (binary) image, one level corresponding to the liquid and the other to the gas or vapor. The normalized image (as we see in Fig. 4.11g) has a histogram of gray level values that exhibits substantially two populations, i.e. high intensity pixels resemble (in the present study) the illuminated background and low intensity pixels denote the object. Defining a threshold value that discriminates the object from the background leads to the binarization. Thus, in a binary image, the pixels are either 0 or 1 (where in the present work, 0 is the object and 1 is the background).

The threshold value  $N_{thresh}$  is very important as far as the size estimation of the object is concerned. However, for labeling operation the threshold value is not so essential since the objective is to identify as many object as possible. In the present work, a combination of two thresholding methods is used in the labeling process: global thresholding and wavelet thresholding.

##### *Global Threshold*

The global method considers the range of grey levels between the most populated grey-level value  $N_{max}$  and the minimum grey level  $N_{min}$ , and defines a relative threshold  $R_{thresh}$  fixed to 0.5 in the present work:

$$R_{thresh} = \frac{N_{thresh} - N_{min}}{N_{max} - N_{min}} \quad (4.10)$$

The global threshold method is based on global characteristics of the grey level histogram of the image (Blaisot and Yon, 2005) and mainly detects large objects and might neglects small ones.

### *Wavelet Transform*

Small objects that have low contrast need a second threshold step to be detected. It employs the wavelet transform that is capable of detecting the local gradient of the grey level at the border of the object. This method was developed in the PhD thesis of Yon (2003) and can be found also in Fdida and Blaisot (2009). The basic elements of this method are evoked here.

Wavelet transform can be seen as a spectral analysis that is spatially localized, unlikely to Fourier transform, for instance, that is concerned with the whole signal. The linear convolution of the normalized image  $I_n$  with a particular function called wavelet  $\psi$  leads to the coefficients of the wavelet  $W$  as expressed by:

$$W_{\Psi, I_n}(\vec{b}, a) = I_n(\vec{\chi}) \otimes \psi_{\vec{b}, a}(\vec{\chi}) \quad (4.11)$$

where the vector  $\vec{\chi}$  refers to a pixel in the image. The wavelet function  $\psi$  is an oscillating function with zero mean and given by:

$$\psi_{(\vec{b}, a)}(\vec{\chi}) = \frac{1}{\sqrt{a}} \Psi\left(\frac{\vec{\chi} - \vec{b}}{a}\right) \quad \text{where } a > 0 \quad (4.12)$$

where  $\vec{b}$  is the shifting parameter and  $a$  is the dilation parameter that controls the width of the function.  $\Psi$  is called the mother wavelet. The choice of this function depends on the application. For the drop localization the Mexican hat function is chosen:

$$\Psi(r) = \frac{2\pi}{\sqrt{3}}(1 - r^2)e^{-r^2/2} \quad (4.13)$$

where  $r$  is the radial coordinate of the pixel in the object plane. The Mexican hat function is the second derivative of a Gaussian function. Therefore, the convolution of the normalized image with the wavelet function can be interpreted as the second derivative of the grey-level of the image that is firstly convoluted with a Gaussian filter. Non-null wavelet coefficients  $W_{\Psi, I_n}(\vec{b}, a)$  correspond to the part of the image where concavity or convexity in the grey-level is found. As the dilation parameter  $a$  increases, the scale of the concavity or convexity increases. For detecting the interface of the droplet (or potentially any object),  $a$  has to be of the same order of magnitude of the blurred region width.

The application of the wavelet transform, for a fixed value of  $a$ , produces an image whose each pixel  $b$  is attached with a wavelet coefficient  $W(\vec{b}, a)$ . Positive coefficient values belong to pixels where the concavity in the grey-level is found, basically in the internal side of the drop (or object) interface. Negative values, however, correspond to pixels located in a convex grey-scale zone, principally in the external side of drop (or object) interface. Zero-values correspond to the background. A threshold on the convoluted image is then applied to determine the drop (or object) interface. This image is then combined with the global threshold image to constitute the binarized image. If the small out-of-focus droplets are targeted to be detected, one value of  $a$  is sufficient. However, for a larger depth-of-field, several wavelet transforms utilizing different values of  $a$  can be performed. The resulted binarized images from each wavelet transform operation are combined together with the one issued from the global threshold to constitute the final binarized image.

An additional step can be added which consists in labeling each object in the image, i.e. to give each object a unique grey level value that serves as a label.

### 4.6.3.3 Filling Holes

Refraction at liquid-gas interfaces can induce bright spots on liquid (black) objects in jet images that could be interpreted as background, i.e. as gas phase. Objects appear punctured in such cases. Figure 4.12a shows a raw image of a liquid jet with real holes and with parts, i.e. liquid membranes, that are low in contrast but are filled with liquid. These membranes can be interpreted as holes after segmentation as shown in Fig. 4.12b.

The misinterpretation of these parts of an image must be fixed for scale-distribution and statistical entropy analysis (see §4.7 & §4.9). For filling these holes, a program was developed in ImageJ V1.50i. The algorithm works as follows. The labeled image is binarized and then inverted so that all holes (including the background) appear as black (objects), see Fig. 4.12c. The "analyze particles" command in ImageJ V1.50i is used to list the objects with their characteristics (including the background that is embedded in object 1). Each object (hole) is then selected and the delimited area is projected on both the background and the raw images. The local grey level value of the raw image is compared to that of the background image. A higher local mean grey level in the raw image indicates a light refraction whereas a lower local mean value indicates light attenuation. A hole is filled if at least one of the following conditions is satisfied:

1. the mean grey value of the raw image is not within 5% of that of the background.
2. the maximum grey level of the raw image is not within 10% of that of the background.

3. the object area is less than 400 pixels (chosen as a trade-off) and the standard deviation of the raw image is larger than five-folds the one of the background.
4. the object area is larger than 400 pixels and the standard deviation of the raw image is larger than two and half-folds the one of the background.

However, these values might be adapted to the quality of the images to be treated. Fig. 4.13 illustrates processing of an image portion delimited by the red rectangle of Fig. 4.12b. This portion contains several holes and for illustration purposes let us consider the one delimited by the green contour. This hole satisfies the third condition and thus is filled. In Fig. 4.13d we notice that three holes remain. By inspecting these holes in Fig. 4.13b we notice that these holes are real gas and not misinterpreted. Therefore, these holes are not filled.

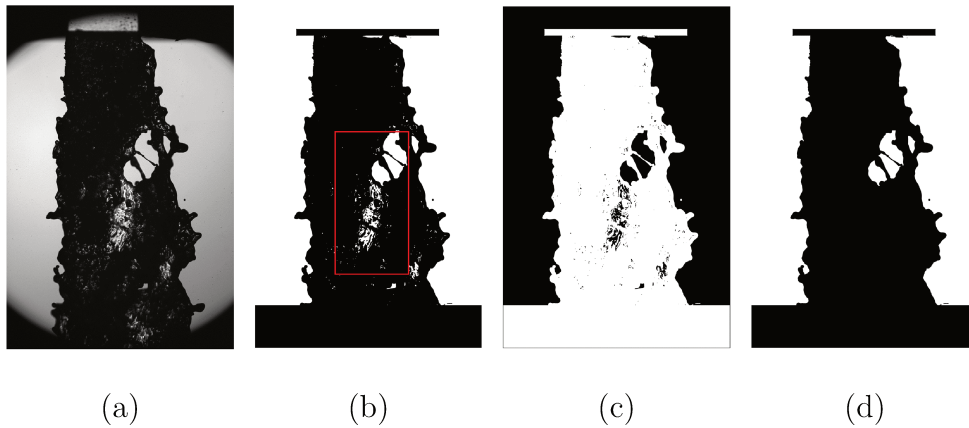


Figure 4.12: Illustration of the holes-filling process. a) raw image, b) labeled image with holes, c) inverted image and d) binarized image with holes-filled.

## 4.7 Scale Distribution Measurement Technique

The scale distribution analysis is an image analysis method that measures the scale distribution of a system whatever its shape. The images are first normalized, segmented and treated to fill holes as explained in §4.6.3. Note that all holes are filled in this case because it simplifies the analysis of the atomizing interface and also because not filling all holes (even the real holes in the jet) would result in a biased estimation of the separation of both sides of the jet (as we will see later). The objective being to characterize the deformation of the liquid-gas interface of the jet, droplets and detached liquid elements are discarded (see Fig. 4.14a.)

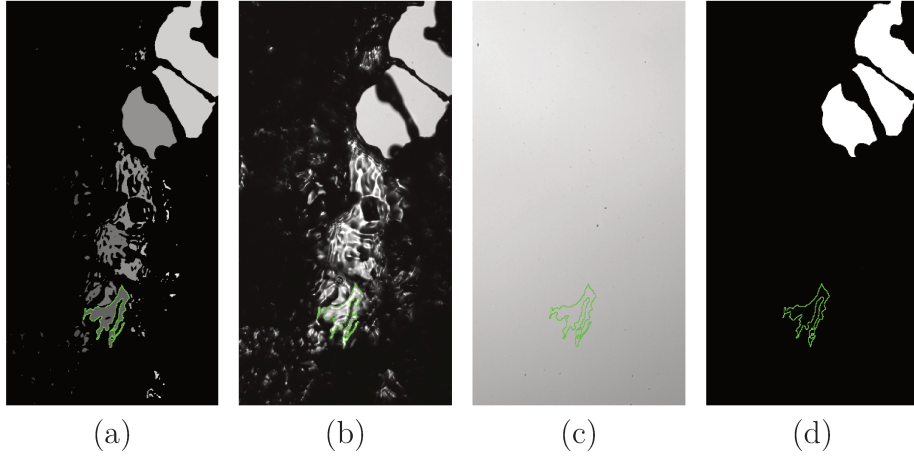


Figure 4.13: Example of the holes-filling process on a portion delimited by a red rectangle in Fig. 4.12b: a) selecting the hole as an object after image inversion, b) projecting the object onto the raw image, c) projecting the object onto the background image and d) projecting the object on the holes-filled image.

The scale distribution analysis is inspired from the Euclidean Distance Mapping (EDM) method applied to measure fractal dimension (Bérubé and Jébrak, 1999). The EDM function of ImageJ V. 1.50i is used in this work. An illustration is given in Fig. 4.14b.

The cumulative scale distribution  $E_2(d)$  is first measured from successive erosion operations with a circular structuring element of diameter  $d$  ranging from 0 to infinity (Soille 2004). The diameter  $d$  is referred to as the scale in the following.  $E_2(d)$  is the relative amount of surface area removed by the erosion operation at scale  $d$  (Dumouchel et al., 2017).

The atomization process is different on both sides of the jet as the right side of the jet revealed more changes related to the occurrence of cavitation in the nozzle. For the scale distribution analysis the jet is separated in two. The separation is given by the principal skeleton line of the jet (Soille, 2013), i.e. the longest skeleton path. The erosion operation at successive scales  $d$  is performed on the gray region only as illustrated in Fig. 4.15. For each value of  $d$ , the surface area lost by erosion is measured and the cumulative scale distribution  $E_2(d)$  is obtained. As shown in §3.2, the scale distribution  $e_2(d)$  is defined as the derivative of the cumulative scale distribution  $E_2(d)$  in the scale space. From a numerical point of view, this derivative is obtained by finite differences. The smallest possible scale increment in the successive erosion operations is one pixel. In the present measurement, we selected a scale increment step of 7 pixels in order to reduce the sensitivity to noise in the data by avoiding too small surface variations to be correctly measured between two consecutive scales. The scale step of 7 pixels corresponds to  $37 \mu\text{m}$  in the images of A1 atomizer and  $34 \mu\text{m}$  in those of G1 and G2 atomizers. The measurement of

the cumulative scale distribution is performed on each image and an area-weighted average for the cumulative distribution is obtained. The scale distribution  $e_2(d)$  is then derived: it represents the scale distribution of all textural structures that have been seen on the 500 proceeded images. It has been first checked that this number of images is far sufficient to get converged scale distributions.

Scale distribution examples corresponding to the image in fig. 4.14b are given in Fig. 4.16. For a single image Fig. 4.16a shows the cumulative distribution  $E_2(d)$ , Fig. 4.16b the scale distribution  $e_2(d)$  and averaged over 500 images Fig. 4.16c shows the scale distribution. The cumulative distribution is practically noise free but as  $e_2(d)$  is obtained from derivation of  $E_2(d)$ , it is very sensitive to small variation in  $E_2(d)$ , leading to the noisy results of the central plot in Fig. 4.16. Finally, averaging over 500 images gives the scale distribution a more regular shape.

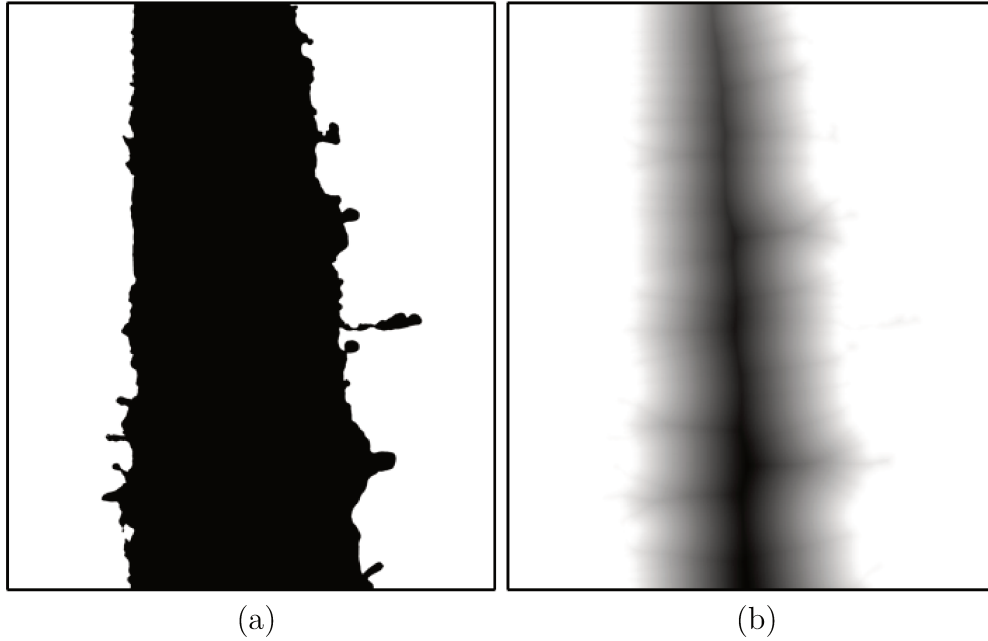


Figure 4.14: Image treatment steps for scale distribution measurement: a) image without the detached liquid and b) EDM image.

## 4.8 Drop Size and Shape Measurement Technique

Side view images are used to measure the size and shape of the spray droplets. The reason is that these images show a larger population of droplets than front view images. Normalization, segmentation and objects labeling steps are performed as can be seen in

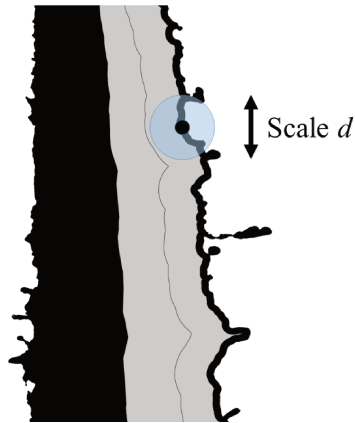


Figure 4.15: Scale distribution principle: erosion is performed on the region delimited by the principal skeleton line (the longest skeleton path) of the jet and the right interface, i.e. the grey region.

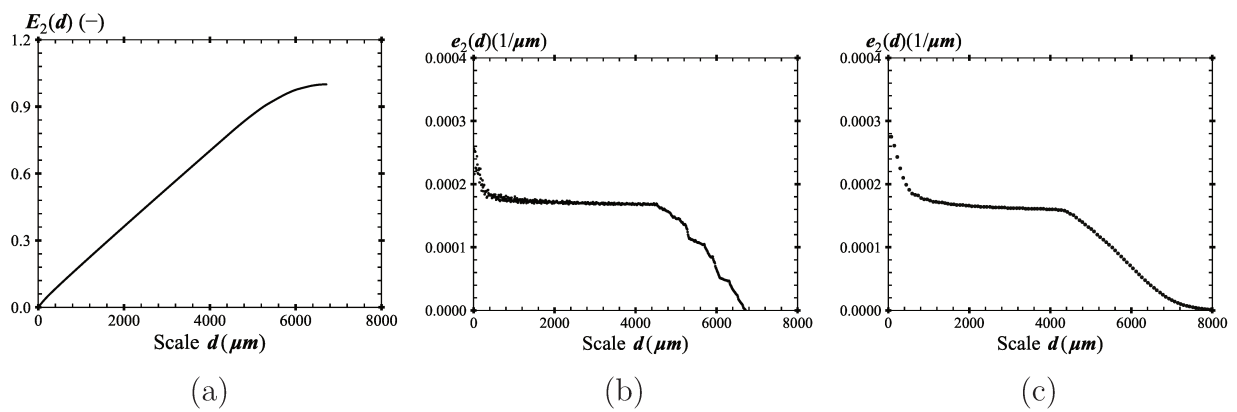


Figure 4.16: Scale distribution for the image shown in Fig. 4.14b: a) is the cumulative distribution  $E_2(d)$ , b) is the scale distribution  $e_2(d)$  and c)  $e_2(d)$  averaged over 500-images.

Figs. 4.17b and 4.17c, respectively.

The refraction of light can lead to bright spots in the droplet images, resulting in objects with a hole after segmentation. However, as the drop size measurement is based on the determination of the image contour, holes appearing inside the perimeter of the object does not affect the determination of the surface area delimited within this perimeter that serves for the droplet size measurement. The determination of the contour is of great importance for the accuracy of the size measurement. The contour of drop images is determined by using the imaging model developed in the spray team and presented hereafter .

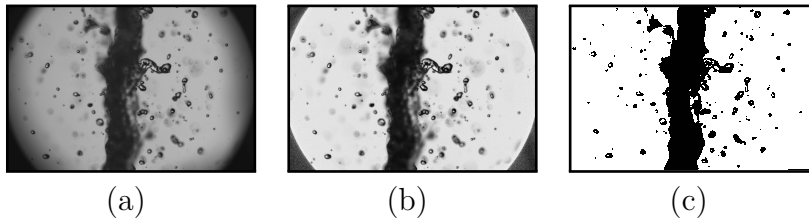


Figure 4.17: Illustration of the drop diameter measurement-steps: a) is the raw image, b) normalized image and c) labeled image.

### 4.8.1 Image Modeling

The image formation model developed by Blaisot and Yon (2005); Fdida and Blaisot (2009); Blaisot (2012) is recapitulated here. The aim of this modeling is to define objective parameters to get the liquid-gas interface from image analysis. As we mentioned previously, the back-light imaging system involving a non-coherent light source is employed. The illumination distribution in the image plane is written as the linear convolution between the object geometric image  $O_g(x, y)$  and the Point Spread Function of the imaging system  $PSF(x, y)$ . For a circular opaque or slightly light-transmitting object, the object function is given by:

$$O_g(x, y) = 1 - (1 - \tau)\Pi\left(\frac{-r^2}{2a_i}\right) \quad (4.14)$$

where contrast coefficient  $\tau$  is the amount of light transmitted by the object,  $r = \sqrt{x^2 + y^2}$  is the radial coordinate in the image plane,  $a_i = \gamma_0 a_0$  is the geometric object size;  $\gamma_0$  is the magnification factor; and  $a_0$  is the object real size. The rectangle function  $\Pi$  writes:

$$\Pi(t) = \begin{cases} 1 & \text{for } |t| < 0.5 \\ 0 & \text{Otherwise} \end{cases} \quad (4.15)$$

The Point-Spread Function (PSF) of an optical system can be seen as the response of the optical system to an infinitely small point in the object plane. It could result from different sources such as diffraction of the finite aperture, chromatic and geometric aberrations. The PSF for a poly-chromatic light source can be, according to Pentland (1987), approximated by a 2D Gaussian function as follows:

$$PSF(r) = s_0 \exp\left(-\frac{2r^2}{\chi^2}\right) \quad (4.16)$$

where  $\chi$  is the PSF half-width and  $s_0$  is a normalization constant. The PSF of an object varies according to the position of the object with respect to the focus-plane along the optical axis ( $\bar{z}$ ): the farther the object from this plane, the wider the PSF. It is assumed that the PSF is constant in the image plane (x,y) and, thus, it is a function of the distance from the focus plane only. In other words, the PSF half-width  $\chi$  is a function of  $\bar{z}$  only.

#### *Image Profile*

The linear convolution between  $O_g(r)$ , Eq. (4.14), and  $PSF(r)$ , Eq. (4.16) leads to the image profile  $\tilde{i}(\tilde{r})$ :

$$\tilde{i}(\tilde{r}) = 1 - 2(1 - \tau) \exp(-\tilde{r}^2) \int_0^{\tilde{a}} \rho \exp(-\rho^2) I_0(\tilde{r}\rho) d\rho, \quad (4.17)$$

where  $\tilde{r} = \sqrt{2}r/\chi$  designates the non-dimensional radial coordinate,  $\tilde{a} = \sqrt{2}a_i/\chi$  is the non-dimensional object radius and  $I_0$  is the modified Bessel function of the first kind. We note that the image profile is controlled by two parameters, i.e.  $\tau$  and  $\tilde{a}$ .

Figure 4.18 illustrates the dependence of the theoretical image profile  $\tilde{i}$  for different values of  $\tau$  and  $\tilde{a}$ . For a given object size  $a_0$ ,  $\tilde{a}$  is maximum for  $\chi$  minimum, i.e. when the object is in the focus plane. Furthermore, a given value for  $\tilde{a}$  can correspond to small in-focus object or a large out-of-focus object. For low  $\tilde{a}$ , i.e. when the geometrical object radius is comparable to the PSF half-width  $\chi$ , the image profile  $\tilde{i}$  exhibits V-shape with a minimum normalized value at the center with a value higher than  $\tau$  (see profiles for  $\tau = 0.2$  in Fig. 4.18). The profile tends to have U-shape as  $\tilde{a}$  increases with a minimum plateau reaching the value of  $\tau$ . For a given value of  $\tilde{a}$ , the image profile  $\tilde{i}$  depends on the contrast

coefficient  $\tau$ : lower  $\tau$  indicates a higher image contrast and vice-versa. We note that the minimum  $\tilde{i}_{min} = 0$  decreases as  $\tilde{a}$  increases and that  $\tilde{i}_{min} = \tau$  for  $\tilde{a} > 2.5$ .

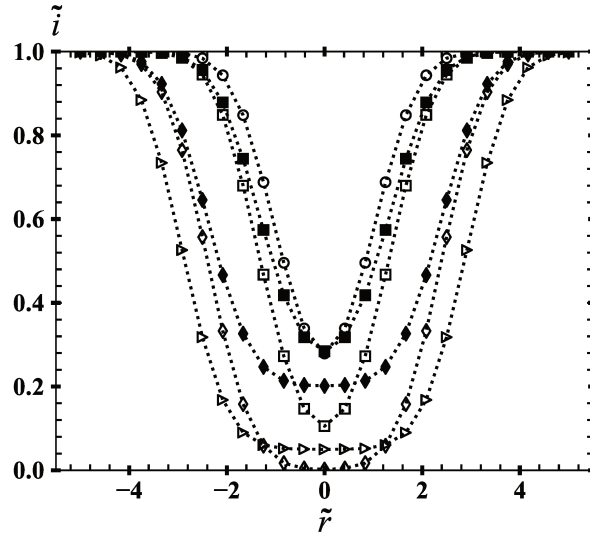


Figure 4.18: Theoretical image profile  $\tilde{i}(\tilde{r})$  as a function of  $\tilde{r}$  for:  $\tilde{a} = 1.13$  and  $\tau = 0$  (o);  $\tilde{a} = 1.5$  and  $\tau = 0$  ( $\square$ );  $\tilde{a} = 1.5$  and  $\tau = 0.2$  ( $\blacksquare$ );  $\tilde{a} = 2.5$  and  $\tau = 0$  ( $\diamond$ );  $\tilde{a} = 2.5$  and  $\tau = 0.2$  ( $\blacklozenge$ );  $\tilde{a} = 3$  and  $\tau = 0.05$  ( $\triangleright$ )

## 4.8.2 Image Parameters

Several image parameters are defined from the theoretical image profile. These parameters are essential in the droplet sizing and depth-of-field estimation and are introduced in Fig. 4.19.

The image contrast,  $C$ , is a non-dimensional parameter defined as:

$$C = \frac{\tilde{i}_{max} - \tilde{i}_{min}}{\tilde{i}_{max} + \tilde{i}_{min}} = \frac{1 - \tilde{i}_{min}}{1 + \tilde{i}_{min}} = \frac{(1 - \tau)(1 - \exp(-\tilde{a}^2))}{2 - (1 - \tau)(1 - \exp(-\tilde{a}^2))} \quad (4.18)$$

$C$  is bounded between  $[0:1]$  where  $C_{max} = 1$  is the contrast for a perfectly opaque object. In other situations  $C_{max}$  is given by:

$$C_{max} = \frac{1 - \tau}{1 + \tau} \quad (4.19)$$

For simplification reasons we consider in the following that  $\tau = 0$ , and thus  $C_{max} = 1$ .

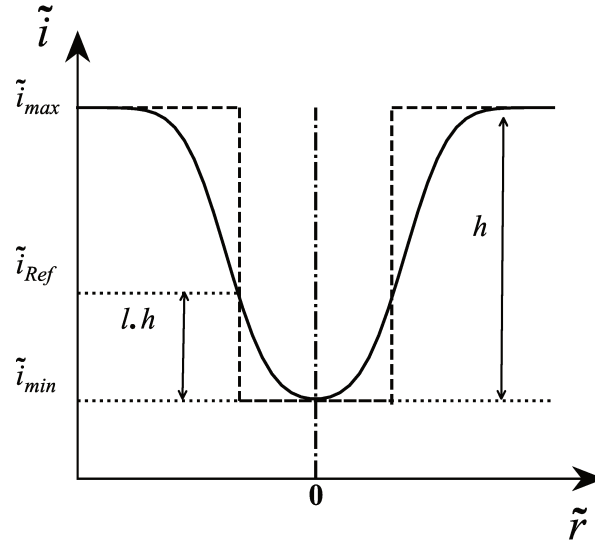


Figure 4.19: A theoretical image profile(line) and the object profile (dash-line).

The image half-width  $\tilde{r}$  is determined at the relative level ( $0 < l < 1$ ) of the image profile height  $h = i_{max} - i_{min}$ . Note that the reference level  $\tilde{i}_{Ref}$ , given by Eq. (4.20), lies between  $i_{min}$  and  $i_{max}$ .

$$\tilde{i}_{Ref} = \tilde{i}_{min} + l \cdot h \quad (4.20)$$

The image half-width is implicitly defined by:

$$\tilde{i}(\tilde{r}_l) = \tilde{i}_{Ref}(l) \quad (4.21)$$

As the reference level  $\tilde{i}_{Ref}$  is relative to the image profile height, it always exists even for out-of-focus objects. Thus, the image half-width is always defined whatever the object focusing.

### 4.8.3 Drop Diameter Estimation

The principle of the drop diameter estimation is based on defining a relative level  $\tilde{i}_{Ref}(l_m)$  from the measurement of the image parameters. The imaging model provides this information by evaluating Eq. (4.21) for  $\tilde{r}_l = \tilde{a}$ , i.e.  $\tilde{i}(\tilde{a}) = \tilde{i}_{Ref}(l_m)$ . Therefore, the reference level  $l_m$  can be expressed as:

$$l_m = 1 - \frac{2 \exp(-\tilde{a}^2) \int_0^{+\tilde{a}} \rho \exp(-\rho^2) I_0(2\rho\tilde{a}) d\rho}{1 + \exp(-\tilde{a}^2)} \quad (4.22)$$

Note that  $l_m$  is a function of  $\tilde{a}$  only. The contrast given by Eq. (4.18) is also a function of  $\tilde{a}$  only ( $\tau$  is set to zero). Therefore, a relation between  $C$  and  $l_m$  is established and shown in Fig. 4.20. Note that  $l_m$  is bounded between 0 and 0.63, and it increases as  $C$  increases and then slightly decreases as  $C \rightarrow 1$ . In practice, for each object in the image,  $C$  is calculated according to Eq. (4.18). From Fig. 4.20, the corresponding relative level  $l_m$  is found. After that, the threshold  $N_{thresh}$  expressed by Eq. 4.10 is calculated by setting the relative threshold  $R_{thresh} = l_m$ ;  $N_{max}$  and  $N_{min}$ , are defined locally in the object neighborhood. The object (binarized image) is locally defined from this threshold.

The measured radius  $r_{meas}$  given by Eq. (4.23) is deduced from the area inside the contour. For a better accuracy, a sub-pixel contour is computed at the relative level  $l_m$ , i.e. the sub-pixel location of contour points around contour pixels is estimated from a local interpolation of the grey level. The area  $A_{lm}$  is obtained from this sub-pixel contour.

$$r_{meas} = \sqrt{\frac{A_{lm}}{\pi}} \quad (4.23)$$

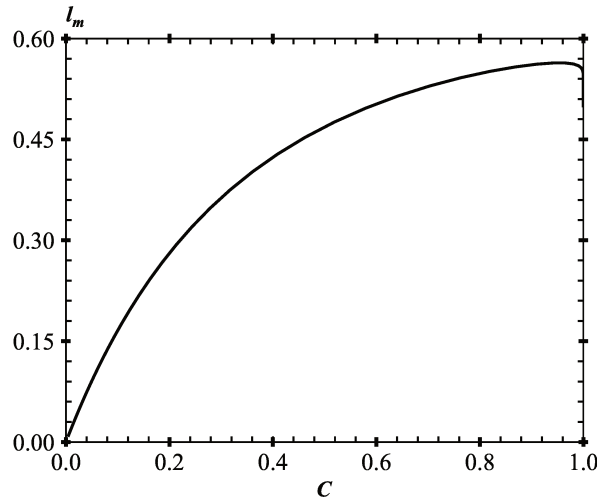


Figure 4.20: Reference level  $l_m$  as a function of the contrast  $C$ .

#### 4.8.4 Drop Size Distribution Estimation

Measuring a drop size distribution implies the definition of a control measurement volume for the counting. For image-based techniques, this requires the determination of a depth-of-field (DoF) criterion for the imaging system. Indeed, large droplets are visible for a farther distance from the focus plane than small drops. This necessitates a DoF criterion such that only the droplets within a given DoF are considered. In other cases the pdf would overestimate the large droplet population.

##### *Focus Selection*

The DoF criterion (focus selection) is based on the determination of the PSF half-width  $\chi$ . To this end, the gradient of the image profile at mid-level is considered, expressing the non-dimensional gradient  $\tilde{g}_{0.5}$  which is a function of  $\tilde{a}$  only. Mid-level is chosen as it is the location on the image profile that exhibits almost the largest slope. Remember that the contrast  $C$  is a function of  $\tilde{a}$  only as well. A relation between  $\tilde{g}_{0.5}$  and  $C$  is established, expressing  $\tilde{g}_{0.5} \equiv f(C)$  and presented in Fig. 4.21. From the experimental image, the gradient for each object is calculated at reference level  $l = 0.5$ . Expressing  $\tilde{g}_{0.5}$  as a function of  $g_{0.5}$  the relation obtained by Blaisot (2012) in Eq. (4.24) is used to determine the PSF half-width  $\chi$  for each object independently of its size:

$$\chi = \frac{\sqrt{2} \tilde{g}_{0.5}}{g_{0.5}} \quad (4.24)$$

Therefore, the DoF criterion is expressed by choosing a maximum value for  $\chi$ , i.e.  $\chi < \chi_{max}$ . Thus, every droplet with a PSF half-width  $\chi$  larger than the criterion  $\chi_{max}$  is discarded. In this way, over-estimation of the big droplets population is greatly reduced.

##### *PSF Calibration*

The DoF criterion that is based on PSF half-width estimation needs the calibration of the PSF of the imaging setup used to measure a drop size distribution. The calibration of the PSF half-width is performed by measuring the PSF half-width on images of a screen edge (actually a razor-blade) accurately positioned in the field of view. An example of PSF half-width measurement is illustrated in Fig. 4.22. The measurement of the PSF half-width is performed by considering the gradient at mid-level of screen edge image profiles. PSF calibration results for imaging setups No. II and III (see Table 4.6) are shown in Fig. 4.22. The minimum value for  $\chi$  is well defined and located on this calibration curves. This results from the fact that microscope-like optical configurations are used here, characterized by a magnification greater than one.

For the configurations No. II and III that were used for drop size measurements, the DoF criterion was fixed to  $\chi_{max} = 30 \mu\text{m}$ . This value is estimated from the largest out-of-focus location for which the smallest drop diameter are still visible. Indeed, the visibility, i.e. the contrast, of small drops rapidly decrease with out-of-focus. The contrast limit is fixed to  $C_{min} = 0.1$  which is considered to be just above the limit of noise in normalized images. The smallest diameter is fixed to  $10\mu\text{m}$  for these configurations. The maximum out-of-focus location of these  $10\mu\text{m}$  drops gives the value of the DoF criterion for all the drops in the spray. According the calibration of the PSF half-width shown in Fig. 4.22, the value for  $\chi_{max}$  yields to a DoF of around 1.2 mm. Thus, drop size distributions are built from droplets counted in a measurement volume of width given by the field of view (about  $20 \times 15 \text{ mm}^2$ ) and of depth about 1.2 mm.

### *Drop size distribution*

Drop size distributions are obtained by counting drops in images. The distributions delivered from image analysis are thus spatial frequency distributions. Typically, series of 500 images are considered. The droplet counting is based on the validation of several criteria. One is the DoF criterion presented just above. Another one is the size criterion. Typically, the range of diameter considered is from  $10\mu\text{m}$  to 2.5 mm. Another important criterion is the morphology criterion which allows selection of drops relatively to their shape. Typically, too deformed liquid elements are rejected, i.e. non spherical droplet, to construct a diameter distribution. More details on drop shape analysis are given in the section below.

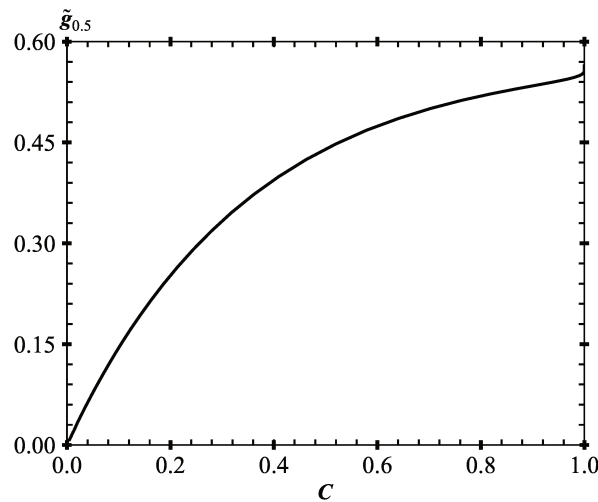


Figure 4.21: Gradient at the reference level  $l = 0.5$  as a function of the contrast  $C$ .

Depending on the operating point, the global number of counted droplets  $N_{glob}$  varied between 10000 and 150000 for series of 500 side view images in the near field of the nozzle. The shape criterion can lead to a rejection of a few percents up to 20% of the total number of counted droplets. But the stricter criterion remains the DoF criterion that can reject up to 70% of the drops. As explained above, this criterion is mandatory to prevent overestimation of the population of the biggest drops in a spray.

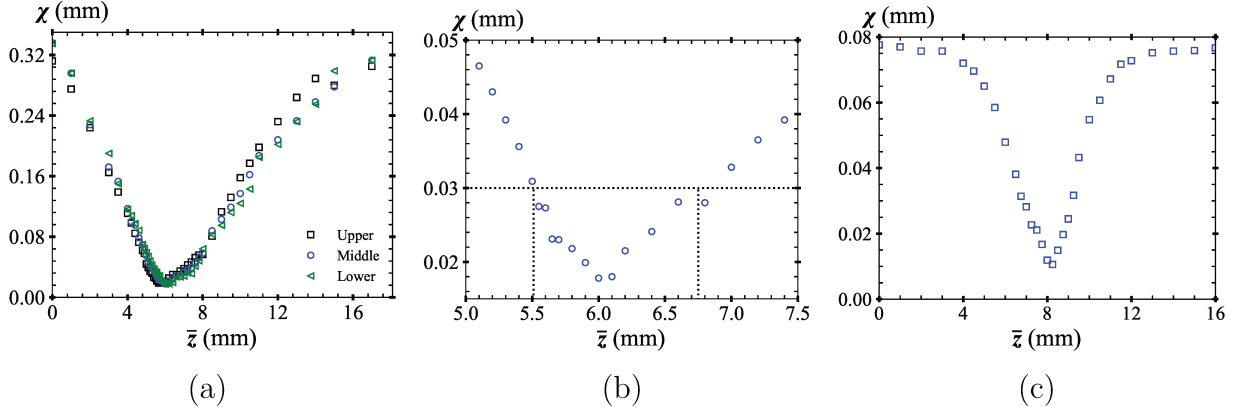


Figure 4.22: Experimental PSF half-width  $\chi$  determined at a reference level  $l = 0.5$  on a series of razor-blade images: a) at different height locations and b) zoomed-in at mid-height level using the optical diagnostic system No. III and c) using the optical system No. II (see Table 4.6).  $\bar{z}$  is the optical axis.

#### 4.8.5 Morphological Analysis

Primary atomization is characterized by largely deformed liquid elements that prevent using the spherical approximation to describe the droplets. With image-based drop sizing methods it is possible to qualify the shape of the liquid element, at least in 2D plane of projection given by the images. Several parameters are introduced to characterize the shape of the droplets:

1. Sphericity ( $S_p$ ) indicates the deviation of a droplet shape from the spherical shape. It compares the surface area of the symmetric difference between the object and a circle of same area and same barycenter (grey zone in Fig. 4.23a) to that of the object:

$$S_p = \frac{(S_{sph} \cup S_{obj}) - (S_{sph} \cap S_{obj})}{S_{obj}} \quad (4.25)$$

Sphericity varies from 0 for a completely spherical object to 2 for an elongated thin object.

2. Ellipticity ( $\epsilon_{ell}$ ) characterizes the stretching of the droplet. It is the ratio of the shortest side to the longest side of the smallest rectangle that encompasses the object (see Fig. 4.23b):

$$\epsilon_{ell} = \frac{l_{min}}{l_{max}} \quad (4.26)$$

Ellipticity varies between 0 for very elongated object and 1 for perfectly spherical object.

3. Irregularity ( $\phi_{irr}$ ) is defined as the ratio between the perimeters  $P_{cir}$  of the circle of same area to that of the object, more precisely:

$$\phi_{irr} = \frac{P_{cir}}{P_{obj}} \quad (4.27)$$

As  $\epsilon_{ell}$  does,  $\phi_{irr}$  values ranges from 0 to 1, where  $\phi_{irr} = 1$  refers to a perfectly regular sphere.

4. Uniformity ( $\eta_{unif}$ ) is defined as the difference between the longest distance ( $r_{max}$ ) and the shortest distance ( $r_{min}$ ) measured from the center-of-gravity of the object to the furthest and nearest contour point, respectively, divided by the measured radius  $r_{meas}$  (see Fig. 4.23c):

$$\eta_{unif} = \frac{r_{max} - r_{min}}{r_{meas}} \quad (4.28)$$

Uniformity is not bounded in the upper range. It varies between 0 for a perfect sphere and  $\infty$  as the object becomes less uniform.

5. Convexity ( $\zeta_{conv}$ ) is the ratio between the area of the object to that of its convex envelope  $S_{conv}$  which is the smallest shape that encompasses the object without any concave part in the contour (see Fig. 4.23d where concave part is drawn in grey):

$$\zeta_{conv} = \frac{S_{obj}}{S_{conv}} \quad (4.29)$$

As an object is included in its convex envelope,  $\zeta_{conv}$  is always less than or equal unity. The smaller the convexity, the larger the concavity parts for the object and the longer the interface for a given area.

According to these parameters, different families of droplets can be identified. Table 4.8 presents examples of shape parameter values for several objects. As far as constructing a drop diameter distribution is concerned, the sphericity parameter is important to count for the quasi-spherical droplets. In fact, to consider only quasi-spherical droplets in the construction of the drop diameter distribution we impose a sphericity  $S_p < 0.4$  (as a trade-off).

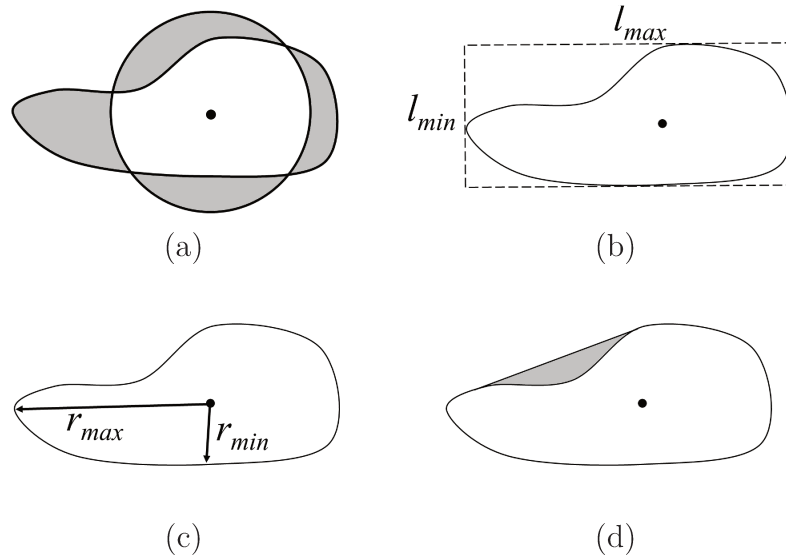


Figure 4.23: Definition of the object shape parameters: a) sphericity ( $S_p$ ), b) ellipticity ( $\epsilon_{ell}$ ), c) uniformity ( $\eta_{unif}$ ), d) convexity ( $\zeta_{conv}$ ).

Table 4.8: Example of liquid elements with their Shape parameters.

Object	Sphericity $S_p$	Ellipticity $\epsilon_{ell}$	Irregularity $\phi_{irr}$	Uniformity $\eta_{unif}$	Convexity $\zeta_{conv}$
	0.82	0.39	0.58	1.96	0.72
	0.05	0.92	0.99	0.12	1.00
	0.38	0.51	0.85	1.07	0.97
	0.83	0.46	0.73	1.77	0.80

## 4.9 Statistical Image Entropy

Each pixel in a segmented image refers to a physical state: for instance, for the external flow a black pixel refers to the liquid state  $s = L$  and a white pixel refers to the gas state  $s = G$  and for the internal flow a black pixel refers to the gas phase and a white one indicates the liquid. In the present study, the liquid state for the external flow is divided in two states, i.e. the liquid jet which is defined as the biggest black (liquid) object  $s = B$  and detached droplets that constitute the remaining objects. The gas state for the internal flow is also split in two parts; the cavitation cloud which is defined as the biggest cavitation bubble (biggest black object) and the detached bubbles. Therefore, three distinguishable physical states are defined for the internal flow; i.e. cavitation cloud, detached bubble and surrounding liquid and also for the external flows; i.e. liquid jet, detached droplets and surrounding gas. A statistical entropy tool based on the information theory of Shannon and developed by Blaisot and Yon (2003) is employed to characterize the internal and external flows. The entropy is calculated from the probability of occurrence of each state:

$$E = \sum_s \frac{-p_s \ln(p_s)}{\ln(3)} \quad (4.30)$$

where probabilities  $p_s$  refer to the three states mentioned above. It indicates how many states  $s$  did this pixel experience and what their relative probabilities  $p_s$  were. It can be seen as a measure of the variability of state of a pixel, i.e. entropy is zero as long as the pixel is experiencing the same state, regardless of the state. Entropy is maximum as far as the pixel is visited equally by the three states, i.e. the probability  $p_s = 1/3$  for each of the three states. This maximum entropy is used to normalize the entropy in Eq. 4.30.

A pixel is referred to as an active pixel ( $AP$ ) if it has non-null entropy value, i.e. if it has changed its state at least once. The number of active pixels  $N_{AP}$  increases monotonically with the number of images (or events). This number is used as an indication of the convergence of the amount of information contained by a set of images. The number of images required to statistically be representative is determined as soon as  $N_{AP}$  reaches a plateau. This is the criterion used to determine the number of images to be considered in the statistical analyses conducted in this work.

It is of interest to mention that the entropy is able to discriminate the regions that experienced three states. This discrimination is achieved by introducing the 3-state entropy criterion  $E_3$  where two of the states are equiprobable and the third one is zero, more precisely:

$$E_3 = \frac{\ln(2)}{\ln(3)} \approx 0.631 \quad (4.31)$$

---

For a pixel of entropy  $E > E_3$ , three states visited that particular pixel. For the external flow the three states region was called the primary atomization region in (Blaisot and Yon, 2003). This approach is also adopted here and is extended to the case of internal flows. In this latter case, the 3-state pixels belong to flow region presenting variable cavitation cloud and bubbles occurrence. The larger the 3-state region, the stronger the cavitation variability in the nozzle.

Because entropy is based here on the probability of occurrence of three different states, it is a more powerful tool than the standard deviation, for instance. Indeed, multi-state is not applicable in standard deviation computation and furthermore, the standard deviation results depend on the grey level values whereas entropy values do not.

# Chapter 5

## Results

### 5.1 Internal and External Flow Visualizations

This section presents a qualitative description of visualizations of the atomizer-orifice internal flow and of the flow issuing from the atomizer. As far as the internal is concerned, two optical diagnostics were used: the still visualization and the high speed configuration. The still images presented in this section were obtained with two optical systems according to the situation (see Table 4.6). The high-speed images were obtained with two optical systems according to the situation (see Table 4.7).

#### 5.1.1 Internal Flow

##### *Still Images*

Figure 5.1, Fig. 5.2 and Fig. 5.3 present typical images of the orifice internal flows for atomizer A1, G1 and G2 respectively. All images are orientated the same way: front view configuration with the upper flow coming from the right. The dark regions that are visible in the orifice flow are due to the presence of diopters that deviate the light. These diopters come from the presence of vapor resulting from liquid cavitation. These figures show a couple of images for all conditions excepting cases A1-1, G1-1 and G1-2 for which no cavitation has been observed at all time.

The first thing to be noted in the images is the dissymmetry of the cavitation region that is always on the right part of the flow and along the up-stream wall (right orifice wall). This, of course, is a direct consequence of the dissymmetry of the atomizer geometry. The second observation to be underlined is the dependence of the cavitation mechanism

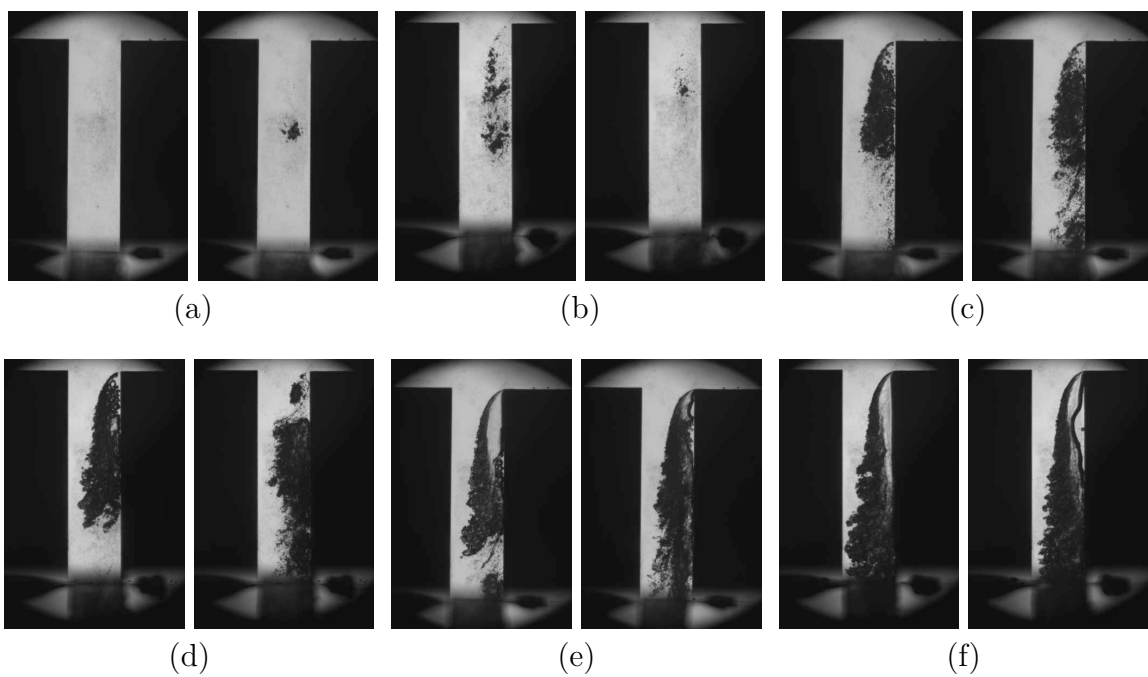


Figure 5.1: Still images of the internal flow of A1 atomizer using the optical system No. III: a to f presents A1-2 to A1-7 (Table 4.2). Flow enters from the upper-right and emerges downwards.

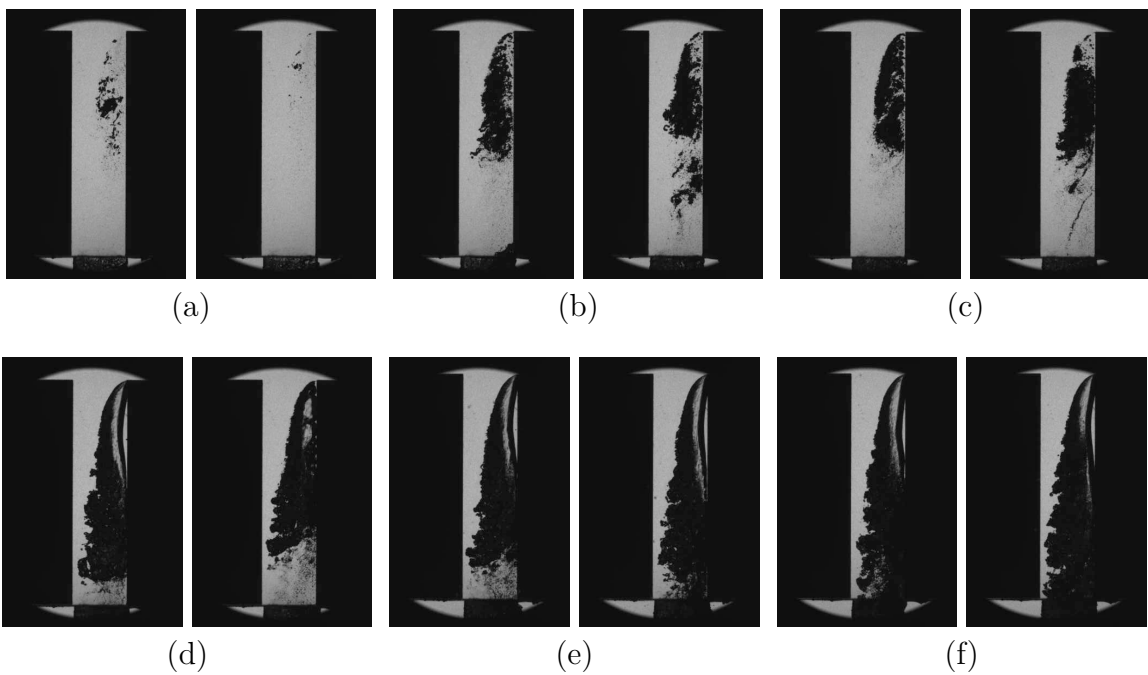


Figure 5.2: Still images of the internal flow of G1 atomizer using the optical system No. III: a to f presents G1-3 to G1-8 (Table 4.3). Flow enters from the upper-right and emerges downwards.

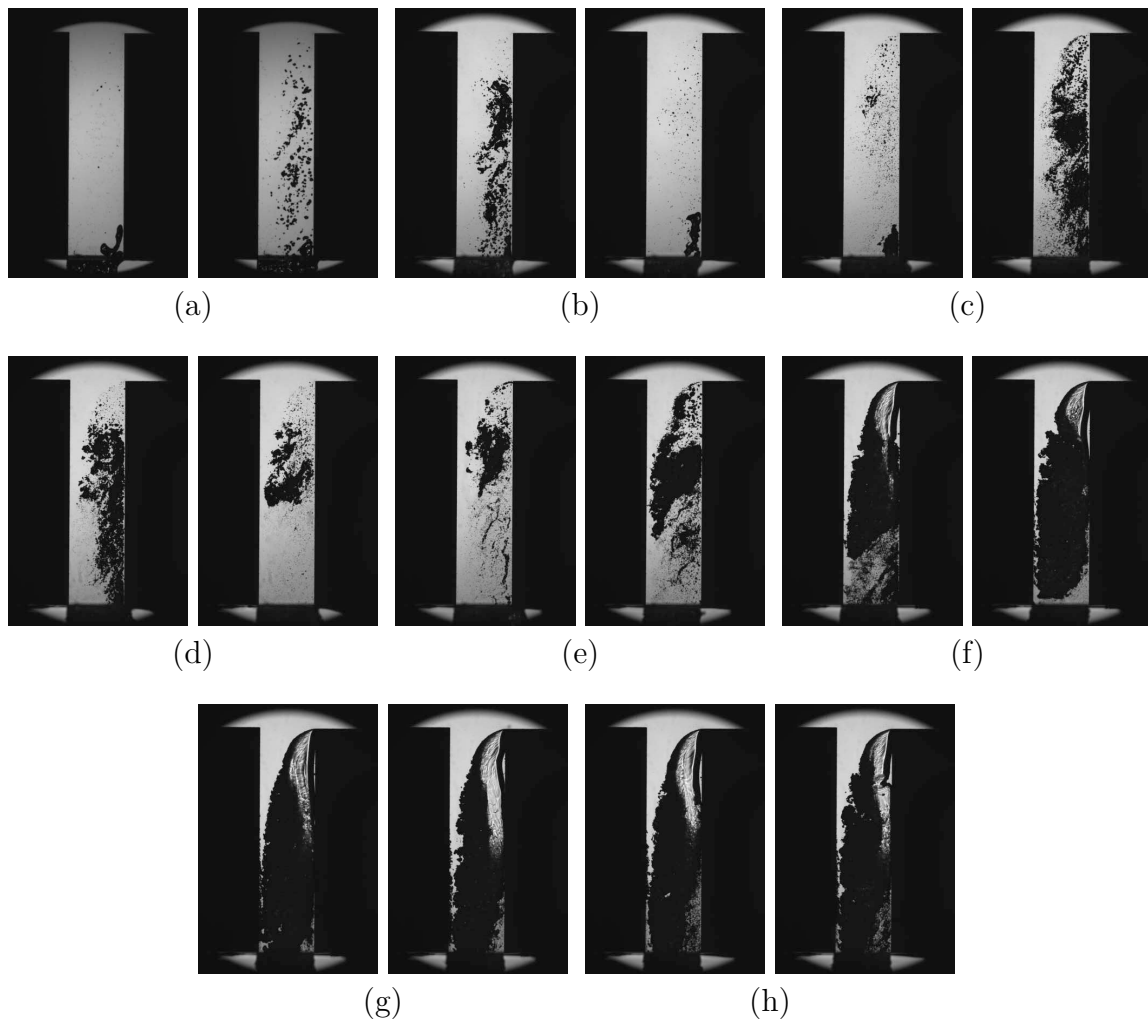


Figure 5.3: Still images of the internal flow of G2 atomizer using the optical system No. II: a to f presents G2-1 to G2-8 (Table 4.4). Flow enters from the upper-right and emerges downwards

on the flow rate. Four flow regimes are identified, they are similar to those reported in the literature (see Chap. 2). Flow Regime I corresponds to low flow-rates for which no cavitation is triggered in the orifice. They concerned cases A1-1, G1-1 and G1-2 and, sometime, the case G2-1 as seen in Fig. 5.3. This latter case will be discussed in more details later. The flow Regime II (developing cavitation) concerns cases A1-2,3; G1-3 and G2-3,4. This regime is characterized by the intermittent appearance of cavitating structures of moderate and variable sizes. The flow Regime III (super-cavitation) concerns cases A1-4,5; G1-4,5,6 and G2-5,6. In this regime, a large cavitation structure that seems attached to the orifice inlet is always visible. It is bounded by the boundary layer detachment wake and barely extends to the nozzle exit section. Smaller cavitation structures may detach from the main one and reach the nozzle exit before collapsing or collapse before reaching the nozzle exit. This behavior is known as the shedding mechanism. The flow Regime IV (partial-hydraulic flip) concerns cases A1-6,7; G1-7,8 and G2-7,8. Because of the dissymmetry of the atomizer, the hydraulic-flip regime is of the partial type (Soteriou et al., 1995). In this regime, a large and rather stable vapor structure develops from the orifice up-stream inlet corner and the long cavitation plume attached to it always reaches the nozzle exit section. A layer between the cavitation structure and the up-stream side wall is always observed. This layer is likely the liquid re-entrant jet reported by Ganippa et al. (2004) and Stanley et al. (2011). All these observations agree well with those reported by Sou et al. (2012).

Atomizers A1 and G1 report similar behaviors. We see for instance that the Regime III is associated with a  $CN$  number of the order of 1 for these two atomizers ( $CN$  values are given in Tables 4.2 and 4.3). The cavitating structures have similar shapes and reported similar variation in time. This variation is illustrated in Figs. 5.1 and 5.2 where two images are shown for each condition. For instance, in Regime II, cavitation always develops on the upper part of the orifice (A1-2,3; G1-3). In Regime III, the shedding mechanism reduces the length of the main cavitation structure (A1-4, G1-4). Sometimes, in this regime, the main cavitation structure detaches from the orifice inlet corner (A1-5, G1-5). In the hydraulic-flip regime, the left side of the main cavitation structure is subjected to the development of small perturbations. The main difference between these two atomizers that are identical in dimensions concerns cases for which a different flow regime is reported whereas the flow rate is the same. This is reported for cases A1-2 and G1-2 and for cases A1-5 and G1-5. This is, of course, a consequence of the level of pressure which is lower in atomizer G1 compared to atomizer A1. Having higher pressure levels, the flow in A1 is more incline to cavitate than the flow in G1. This difference indicates that the cavitation number  $CN$  used here is not able to fully classify the flow regimes.

The results reported by the third atomizer confirm this last remark. For this atomizer, the cavitation number  $CN$  of the order of 1 indicates a flow Regime IV. The flows in this atomizer show several differences with the two other atomizers. From a general point of

view, we could say that the cavitation structures fill the orifice space more than for the two other atomizers. In Regime II, the cavitation structures are wider. In flow Regimes III and IV, the shape of the cavitation structure at the up-stream inlet corner of the orifice is larger. In the hydraulic-flip regime, the cavitation structure occupies the orifice exit on its full width. However, the more noticeable difference is this appearance of gaseous bubbles in the orifice for cases with a high  $CN$  number for which cavitation is not expected. This behavior is explained thanks to the high-speed images presented in the following section.

### *High-Speed Images*

Figure 5.4 reproduces a sequence of images of the orifice flow for condition G2-1. The sequence describes how some external air can be sucked in the orifice and can spread up-stream. During the ascendant motion, the air structure breaks up into smaller bubbles. The resulting bubble cloud stagnates in the right part of the flow revealing a strong recirculation flow in this region. The bubbles collapse and the cloud becomes less and less dense until it disappears. Therefore, the gaseous structures reported by cases G2-1 and G2-2 in Fig. 5.3 are not due to cavitation and, in terms of flow dynamic, these cases well belong to the no-cavitation flow regime (Regime I) which agree with their low pressure level. The air-sucking mechanism shown in Fig. 5.4 denotes the existence of a long recirculation zone on the right part of the flow that extends down to the orifice exit and that is strong enough there to suck air in. This feature makes an important difference of behavior with the other atomizers. For atomizers A1 and G1, the recirculation zone in Regime 1 remains located in the upper part of the orifice as reported by the LDV measurements discussed later in this chapter. This difference reveals the importance of the needle position on the characteristics of the issuing flow.

The air-sucking mechanism may appear at other Regimes. Figure. 5.5 (A1-3) and Fig. 5.6 (G2-4) show two time-resolved image sequences of flow Regime II for atomizers A1 and G2, respectively. In atomizer A1, a cloud of cavitation bubbles is mainly located on the upper part of the orifice. The cloud varies in size, position, density. Some bubbles are caught by the downstream flow and collapse before reaching the orifice exit, while other are caught by the re-entrant jet along the up-stream side wall. In atomizer G2, the orifice appears filled with gaseous structures much more than that in atomizer A1. In fact, in this situation, the gaseous structures come from cavitation and air sucking mechanism as revealed by the image sequence. Therefore, the rate of gas in the orifice is higher for atomizer G2 than for the two others.

The air-sucking mechanism has been also observed with atomizer A1 but at a higher flow-rate. An example of this is presented in the image sequence shown in Fig. 5.7 (A1-6). At the beginning of this sequence, the long cavitating structure does not reach the nozzle exit at which the air-sucking mechanism is clearly visible from the third image. The air-sucking structures mix with the cavitating bubbles leading to the formation of a



Figure 5.4: Sequence of images of G2-1 from the left to right pictured over 13.92 ms (time delay between images  $480 \mu\text{s}$ ) using the optical system No. II in Table 4.7.

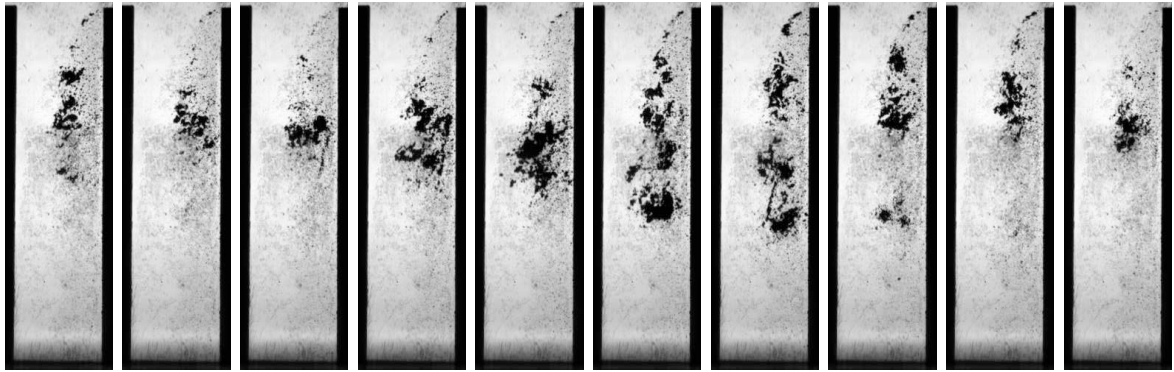


Figure 5.5: Sequence of images of A1-3 (Regime II) pictured over 1.35 ms (time delay between images  $150 \mu\text{s}$ ) using the optical system No. I in Table 4.7.

gaseous plume that extends down to the orifice exit section. This is why this case has been identified as Regime IV. According to this observation, identifying this case as a flow Regime III could have been more appropriate and would match better with case G1-6 classified in this regime. The sequence in Fig. 5.7 reveals sometimes the presence of big bubble between the large vapor structure and the wall in the upper part of the orifice. Probably detached from the main vapor body, these bubbles are rather stagnant. In the sequence shown, they appear to be destroyed by the up-stream re-entrant jet along the wall that is charged with the sucked air bubbles. This re-entrant jet reaches the upper-right inlet corner and perturbs the region where cavitation initiates. The main structure disconnects the inlet corner and the cavitation plume reduces in length as those of the flow Regime III. This demonstrates the important effect of the re-entrant jet and of the air-sucking mechanism.

Another manifestation of the re-entrant jet impact on cavitation is illustrated in Fig. 5.8. This figure presents an image sequence of the partial hydraulic-flip regime A1-7. The sequence shows how the large vapor structure attached to the orifice inlet corner gets perturbed and modified by the up-stream re-entrant jet. However, in this condition of high rate of cavitation, the re-entrant jet does not succeed in destroying the main structure of the cavitation process.

### 5.1.2 External Flow

Figure 5.9, Fig. 5.10 and Fig. 5.11 present still front-view images of the flow issuing from atomizer A1, G1 and G2, respectively. All working conditions are covered and two images are shown for each of them. (These images have the same orientation as those of the previous section.) The first point to be noted is that the strongly dissymmetric internal flows produce external flows with dissymmetric deformations. For every condition, the right

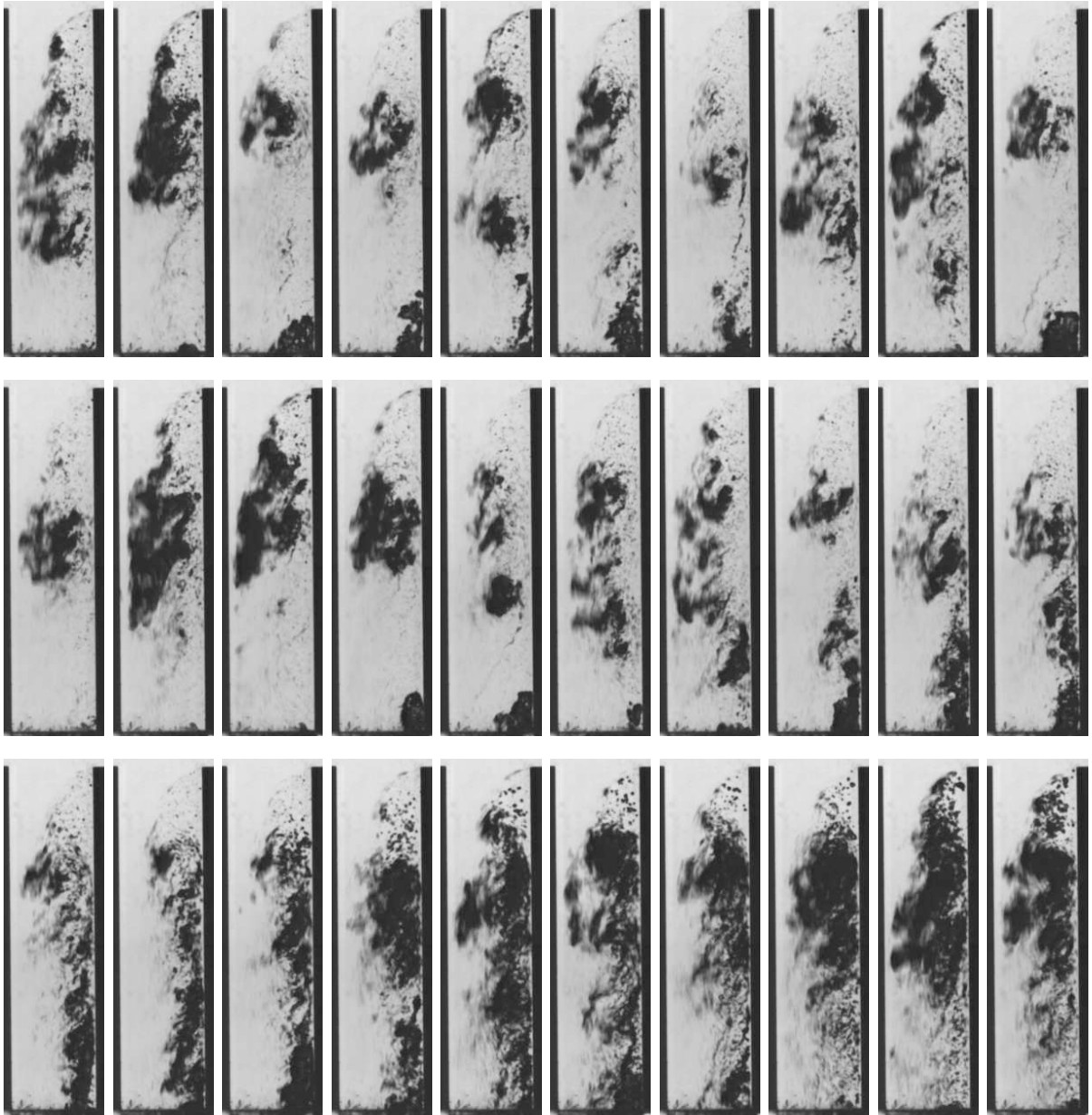


Figure 5.6: Sequence of images of G2-4 pictured over 13.92 ms (time delay between images  $480 \mu\text{s}$ ) using the optical system No. I in Table 4.7.

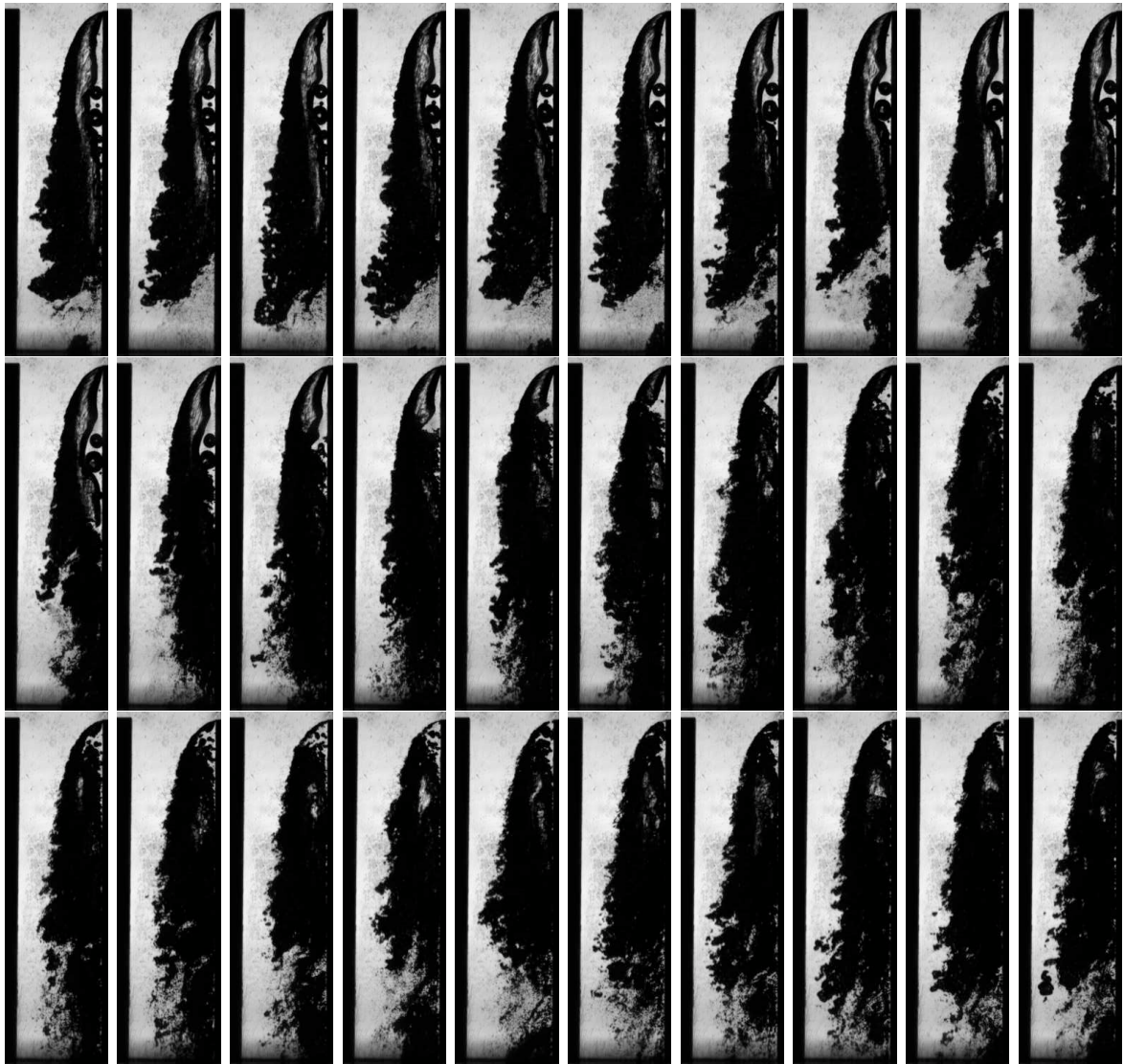


Figure 5.7: Sequence of images of A1-6 (Regime IV) pictured over 4.35 ms (time delay between images  $150 \mu\text{s}$ ) using the optical system No. I in Table 4.7.

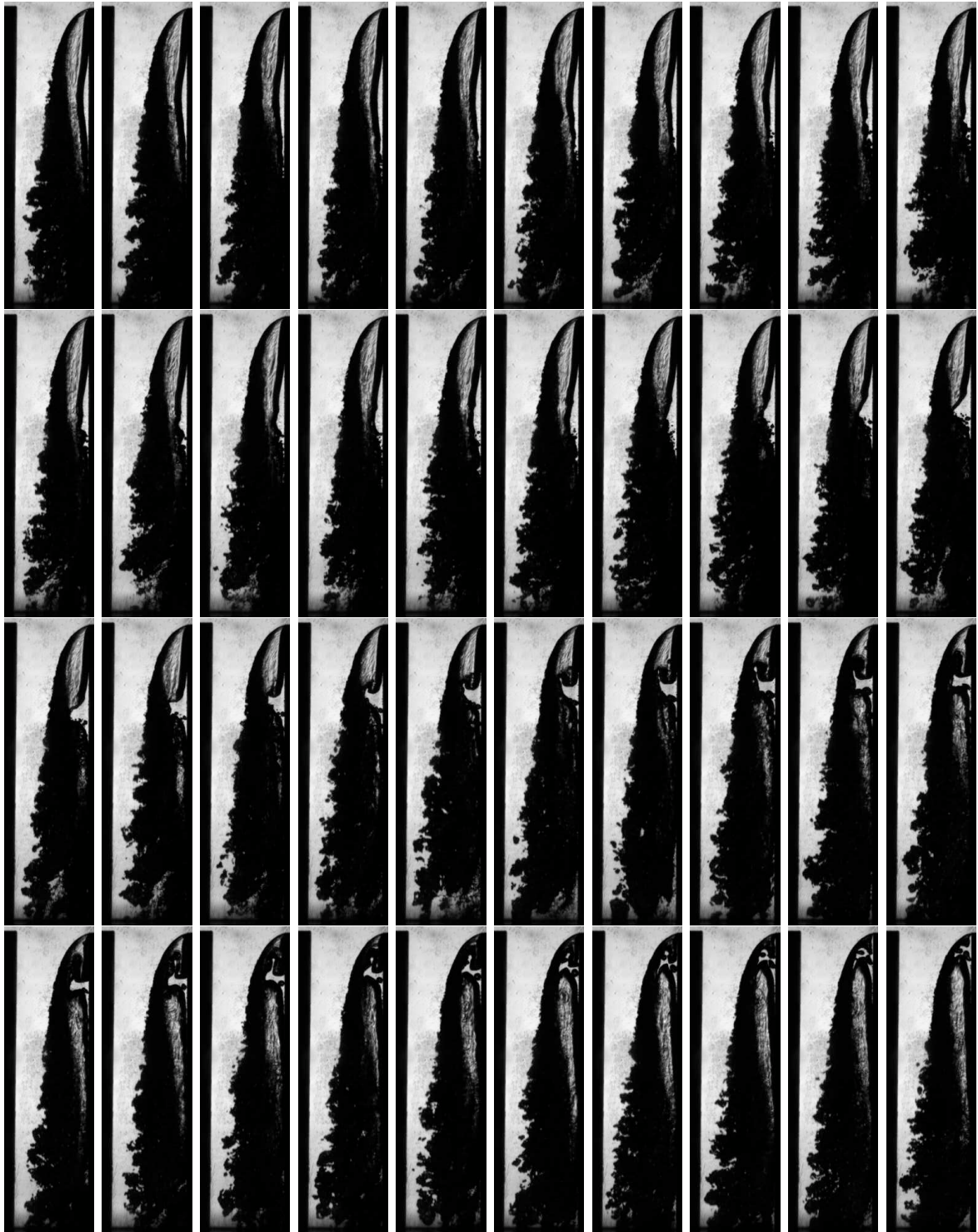


Figure 5.8: Sequence of images of A1-7 (Regime IV) pictured over 5.85 ms (time delay between images  $150 \mu\text{s}$ ) using the optical system No. I in Table 4.7.

interface, i.e., on the same side of the internal cavitation mechanism, is more perturbed and deformed than the left one. In agreement with many observations of the literature, this behavior is an illustration of the influence of cavitation on atomization since the imposed deformations lead to a textural atomization process. For every condition, a textural atomization process is observed on the right interface. It manifests by the development of ligaments whose size decreases and number increases as the flow rate increases. This is precisely this atomization process and the drops it produces that will be investigated and analyzed in the following.

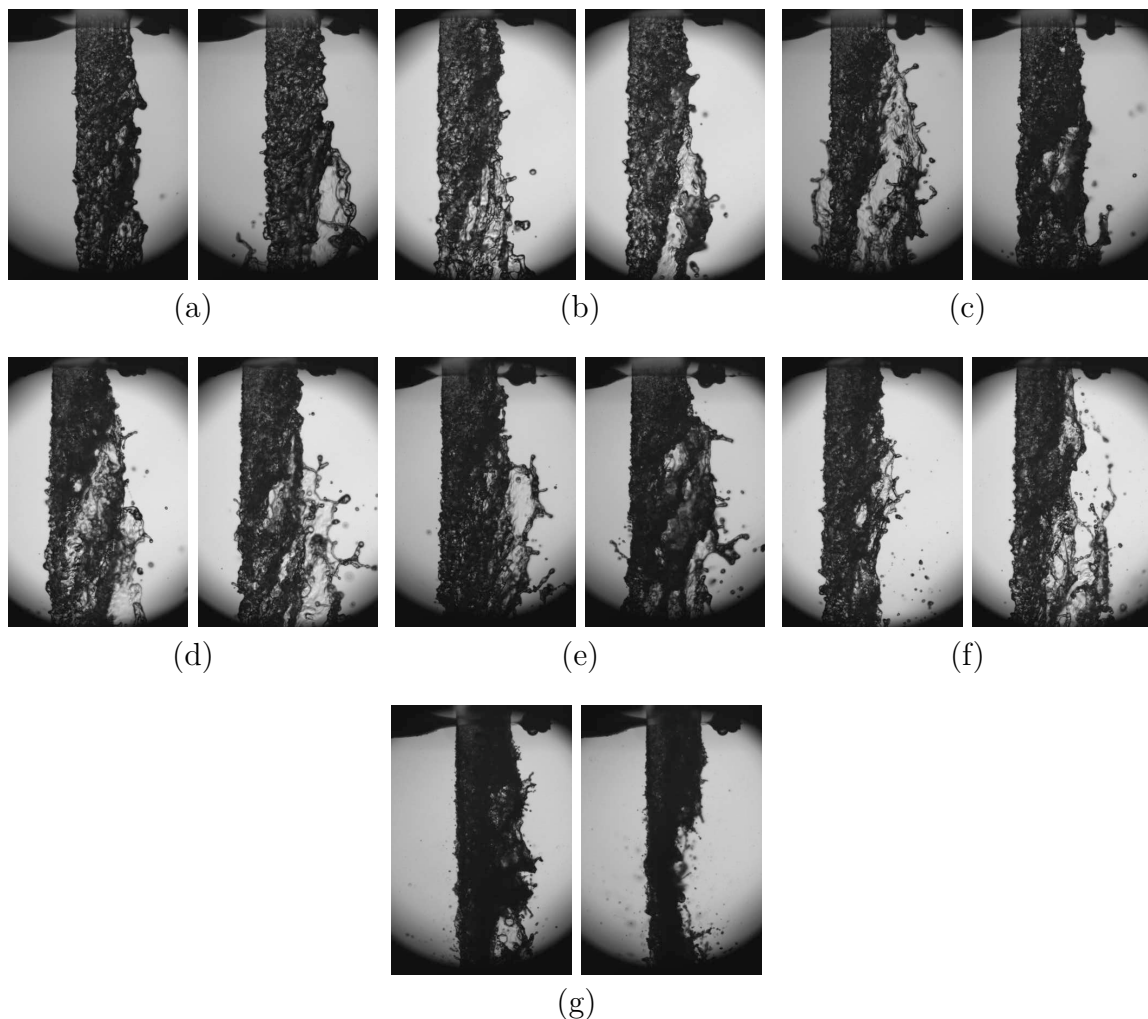


Figure 5.9: Still images of the external, front view of A1 atomizer using the optical system No. III: a to g presents A1-1 to A1-7.

Figure 5.9, Fig. 5.10 and Fig. 5.11 also show that Regimes I to III reveal a widening of the right side of the flow, behavior that has totally disappeared in Regime IV. For this regime, we note that the flows produced by the atomizers G1 and G2 are more symmetric

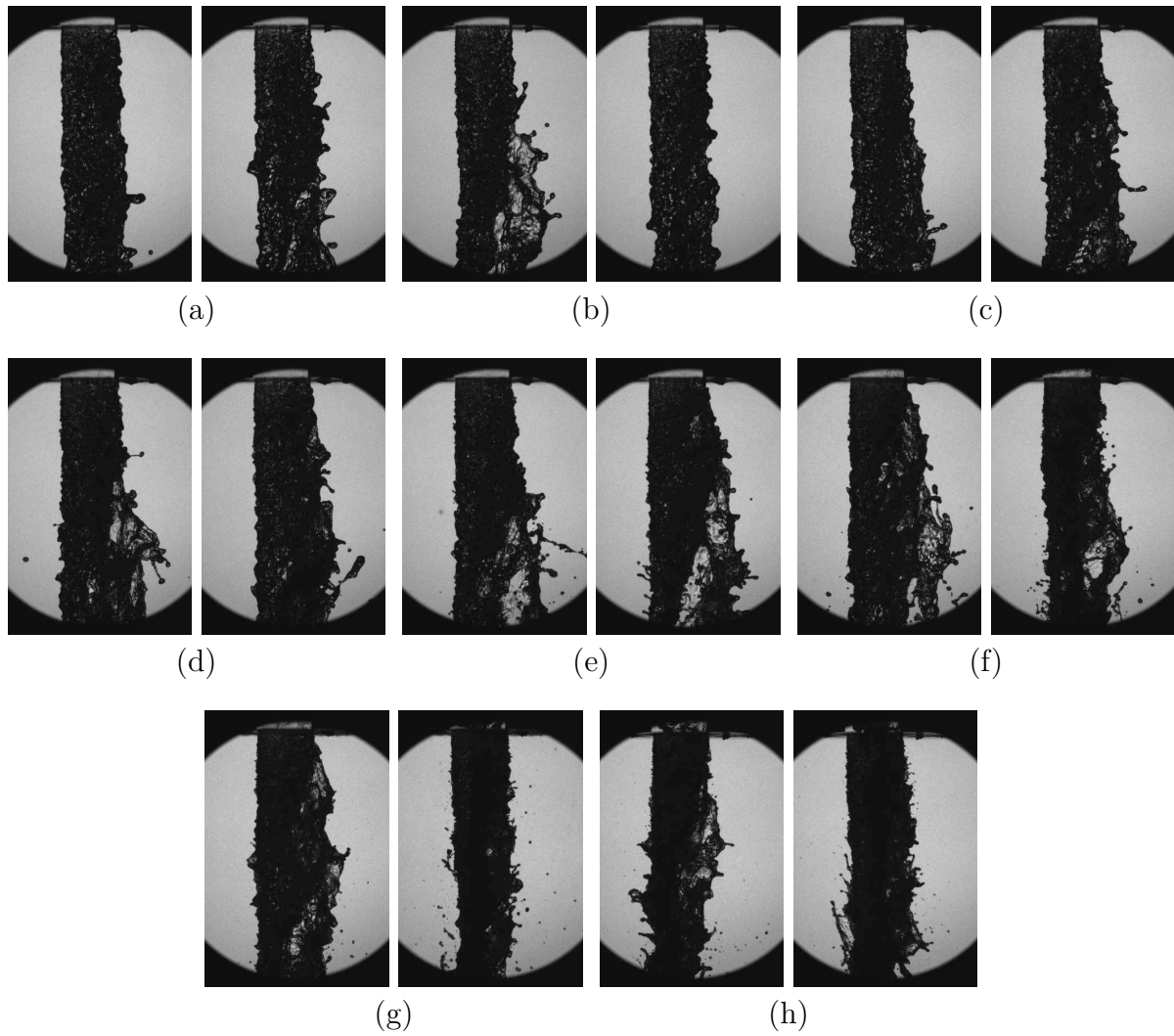


Figure 5.10: Still images of the external, front view of G1 atomizer using the optical system No. III: a to h presents G1-1 to G1-8.

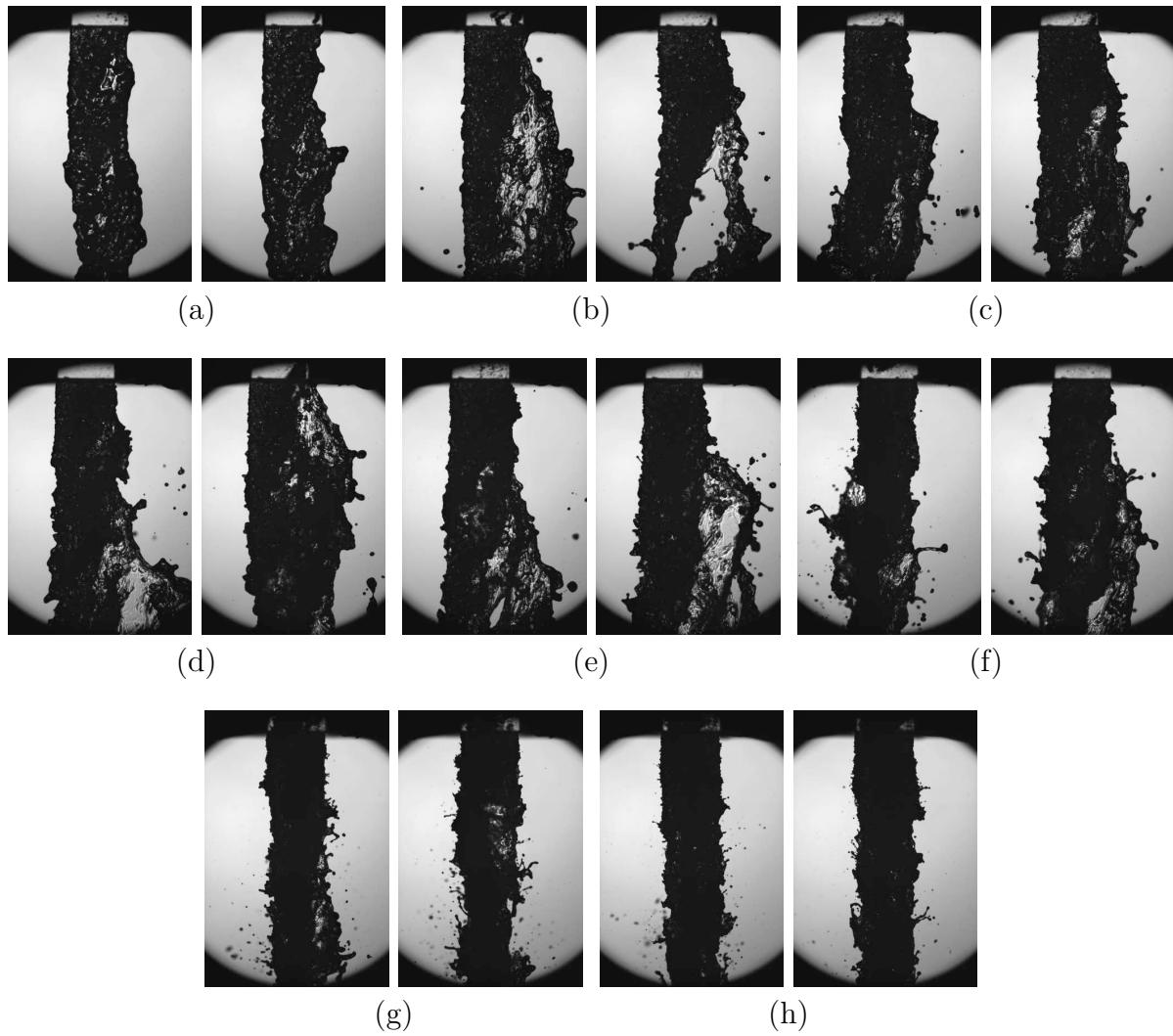


Figure 5.11: Still images of the external, front view of G2 atomizer using the optical system No. II: a to f presents G2-1 to G2-8.

and both interfaces are concerned with one textural atomization process.

In complement to the previous images, Figures 5.12 and 5.13 report side view images of the external flow, just at the nozzle exit, for atomizers G1 and G2, respectively. (Such images could not have been taken with atomizer A1 because the metallic plates exceed the transparent plates preventing seeing the atomizer exit section plane in the side view.) In this direction, we see that the external flow is rather symmetric for all conditions. At the nozzle exit, the flow is of course less wide than in the other direction. It expands radially, in equal measure on both sides, for Regimes III and IV. The deformation of these flow is mainly textural. The textural structures and their atomization are well visible in this direction. As observed previously, the textural structures are ligamentary and their number increases and their size decreases as the flow rate increases. The number of droplets also increases as the flow rate increases.

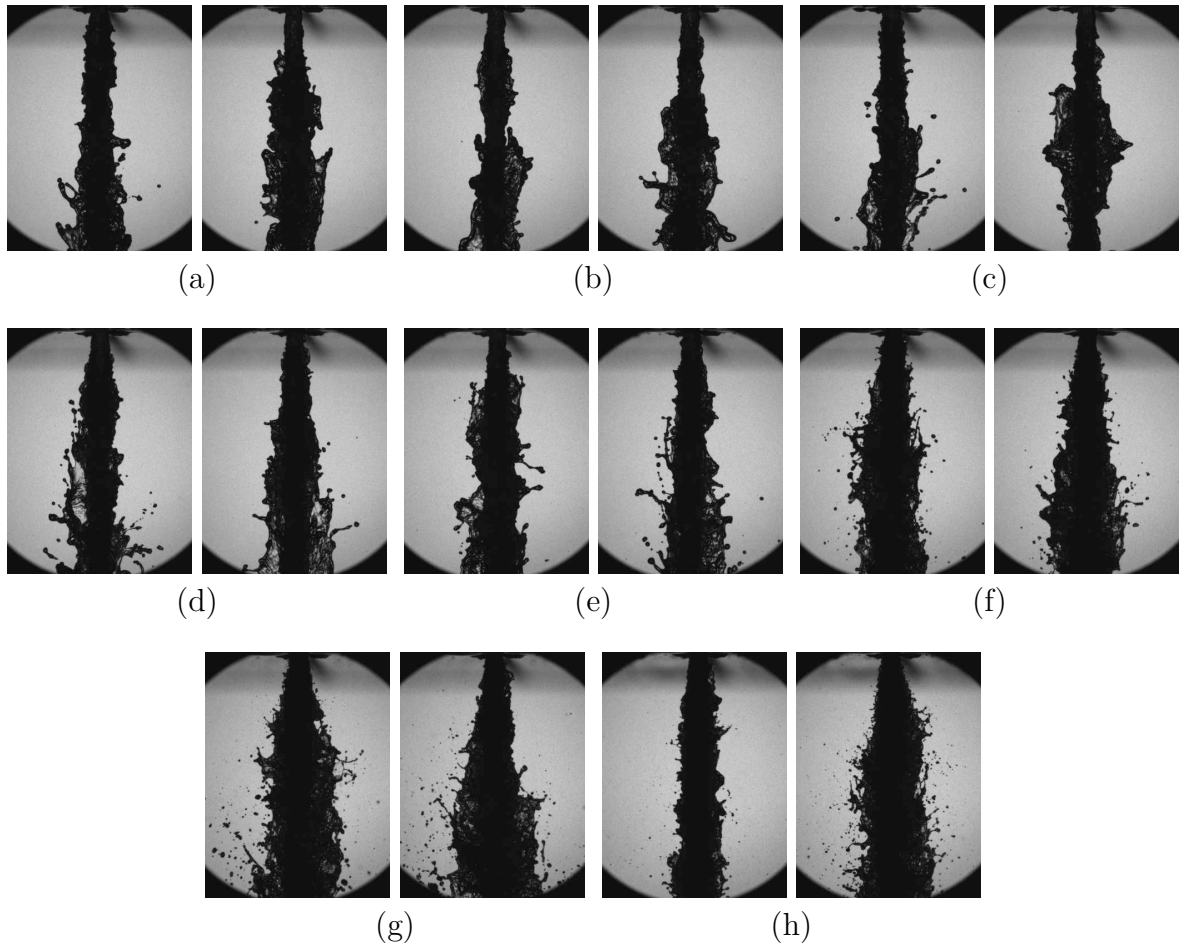


Figure 5.12: Still images of the side view of G1 atomizer at the nozzle-exit using the optical system No. III: a to h presents G1-1 to G1-8.

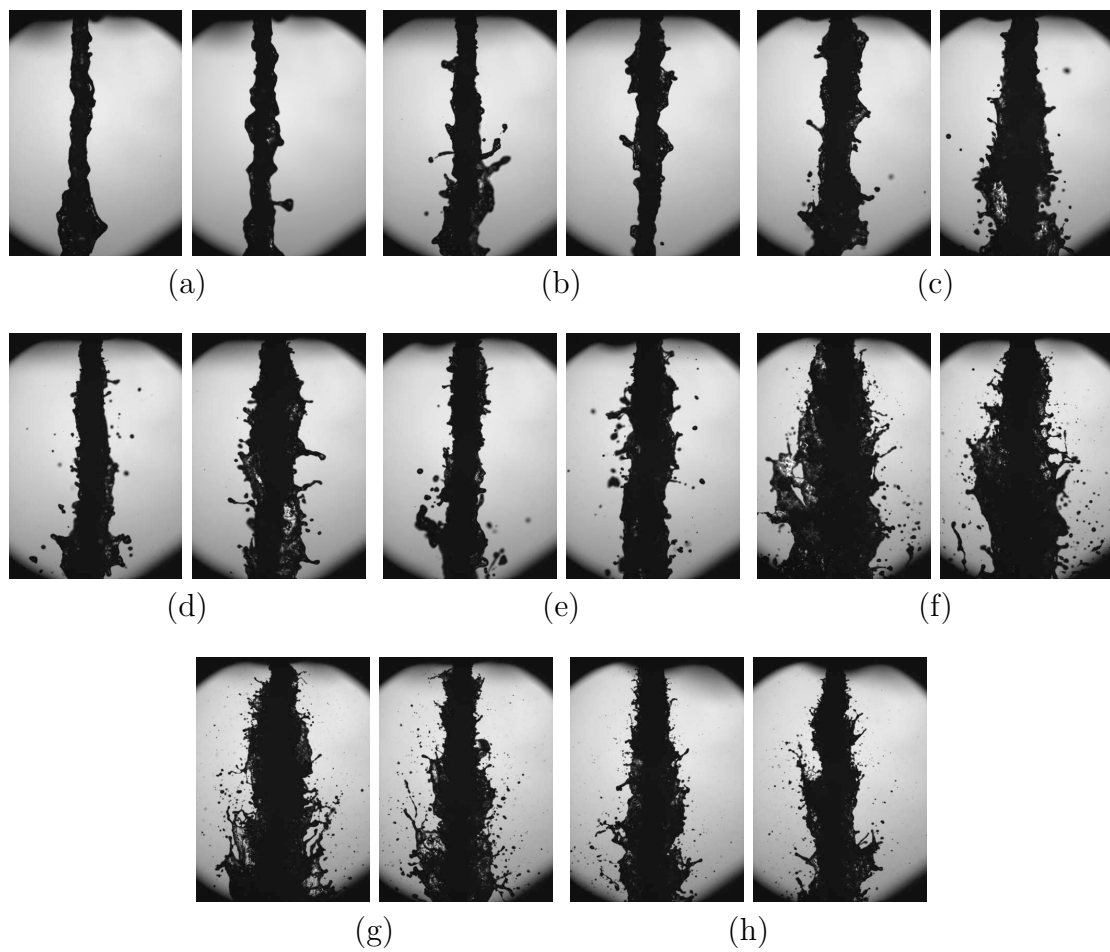


Figure 5.13: Still images of the side view of G2 atomizer at the nozzle-exit using the optical system No. II: a to h presents G2-1 to G2-8.

## 5.2 LDV Measurements

This section presents the Laser Doppler Velocimetry (LDV) measurements. The objective of these measurements is to characterize the flow in the atomizer orifice as well as the velocity distributions at the exit section. The measurements were performed for atomizer G1 at operating conditions G1-1 to G1-6 and G1-8. The smaller thickness of the transparent plates of this atomizer compared to A1 eases the implementation of the optical diagnostic. (Details of the optical arrangement are given in Sec. 4.5.3) The seeding-particle feeder-system was used to seed the flow with small particles.

Figure 5.14 gives the positions at which the measurements were performed. They are all located in the middle plane of the atomizer orifice ( $y = 0$ ). The results are presented in Fig. 5.15. The first row of this figure displays the map of the validation rate, defined as the percentage of events detected in the measurement volume that have led to the measurement of a velocity. The validation rates obtained for G1-1 are equal to 100% at all positions. This result demonstrates the correct implementation of the LDV diagnostic. The maps obtained for the other cases reveal a decrease of the validation rate in regions impacted by cavitation. As seen in the images shown above, the diopters due to the presence of bubbles deviate the light. This, of course, impacts the LDV measurements. We see that the validation rate decreases when the density of the bubble structures increases, i.e. when the flow-rate increases. At best, the representativeness of the velocities measured in the cavitation zone is of the order of the validation rate. However, the light diffused by collapsing bubbles may be caught and analyzed by the LDV providing velocities not at all representative of the flow. Therefore, the representativeness of the measured velocities might be lower than the validation rate. Furthermore, we note that no measurement was returned on both sides of the cavitation structure in the upper part of the orifice for the case G1-8. This case is identified as flow regime IV. The absence of measurement on the right side of the cavitation structure is expected since this region is occupied by a large and rather stable vapor structure that conveys no seeding particles. The absence of measurement on the left side of the cavitation structure is unexpected and suggests that the flow was not sufficiently seeded to perform measurements. This result suggests that the velocities that have been measured in the cavitation structure correspond to bubble interface displacement, that, as mentioned above, may not be representative of the flow. Therefore, a great care must be taken to interpret the measured velocity fields.

The second row of Fig. 5.15 presents the mean-velocity fields in the orifice. For the three first flow regimes (G1-1 to 6), a recirculation zone is visible in the discharge orifice. This zone is always close to the orifice right inlet corner and spreads along the upstream-side wall. At low flow rate, the recirculation zone is limited to a region that spreads down to the half of the orifice length. When the flow rate increases, the recirculation reinforces and its length increases. For cases G1-5 and G1-6, the recirculation occupies all the orifice

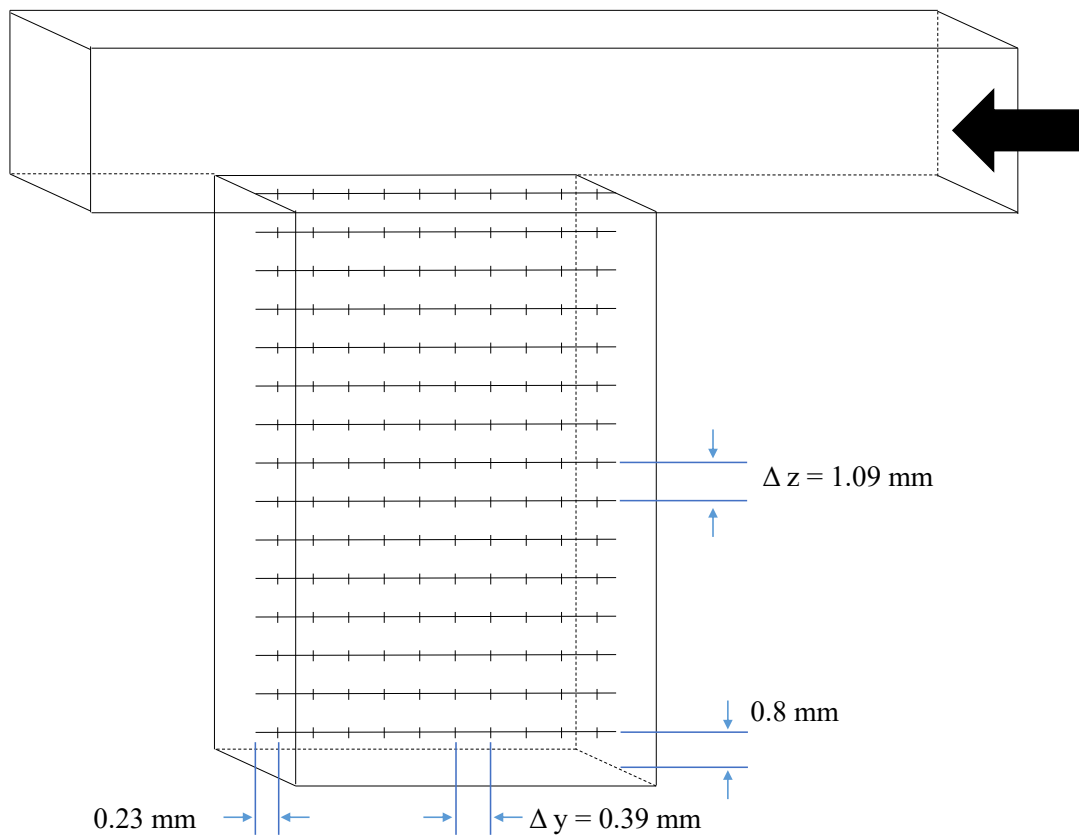


Figure 5.14: Working plan of the LDV measurements using G1 atomizer.

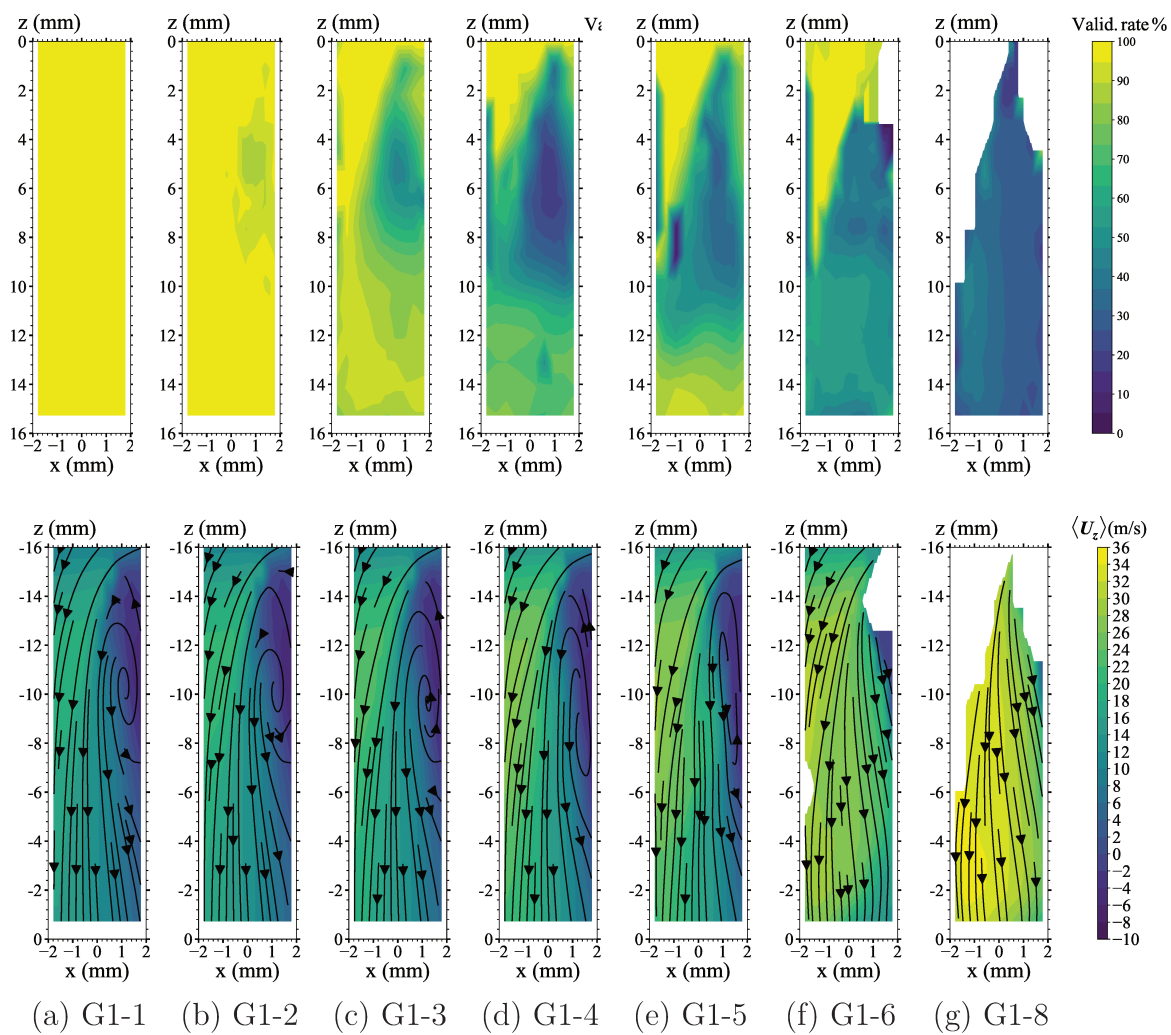


Figure 5.15: Experimental mean stream-wise velocity  $\langle U_z \rangle$  for G1 atomizer.

and extends almost to the orifice exit section. In the hydraulic-flip regime (G1-8), there is no trace of the recirculation in the orifice anymore and the flow seems to slide along the up-stream wall with a rather high velocity. Considering the comments made in the previous paragraph, this result has to be taken with care. Note that the velocity of the upstream re-entrant jet along the right orifice wall observed on the high-speed films in this flow Regime has not been measured. This is probably a consequence of the fact that the measurement volume could not be sufficiently approached to the wall to catch this flow. At the nozzle exit, we see for all conditions that the exit velocity profile is always strongly dissymmetric. The dissymmetry of the issuing flow deformations noticed above is of course directly correlated with this feature.

### 5.3 PDPA Measurements

This section presents the PDPA measurements. They have been performed for atomizer G1 and for conditions G1-1 to G1-6 and G1-8. The objectives of the measurements are to identify the textural spray drop-diameter distribution, its dependence on the spatial position, and to compare the velocity of the drops with the issuing flow mean velocity  $U_b$ . We remind here that the two optical probes are not in coincidence, i.e., they work independently: one measures the axial component of velocity and the other measures the diameter and the horizontal component of velocity in the  $(0, y)$  direction. Figure 5.16 shows the positions at which the measurements were performed. Note that the measurement points belong to the  $(0; y; z)$  plane at  $x = 0$ , since more droplets were visible in this orientation. The measurement points expand from  $z = 10$  mm to  $z = 60$  mm. At each  $z$  position, the measurements are performed between  $y = -13$  mm and  $13$  mm with a displacement step of  $0.5$  mm in the  $y$  direction except at  $z = 10$  mm where the positions range from  $y = -4.875$  to  $y = 4.875$  with a step of  $0.25$  mm.

Figure 5.17 shows the number of validated diameter measurements per unit time  $\dot{n}_p$  as a function of  $y$  and for several  $z$  distances. The  $\dot{n}_p$  signals are rather symmetric according to  $y = 0$  for all conditions. For the upper positions,  $\dot{n}_p$  is very small at  $y = 0$  because of the presence of the liquid flow at this position. On each side of  $y = 0$ ,  $\dot{n}_p$  shows a bell shape. The maximum height of the bell shape decreases and its width increases when the distance from the atomizer increases. This behavior indicates the spatial expansion of the textural spray. Considering all situations, we note that the maximum of  $\dot{n}_p$  varies between  $1500 \text{ s}^{-1}$  and  $400 \text{ s}^{-1}$ . This shows that the textural sprays contain a high number of droplets for the case G1-8. Figure 5.18 presents the local number-based drop diameter distributions at the maximum of  $\dot{n}_p$  for each  $z$  position. The validation rate of these measurements ranges from 30% to 70% according to the position, the smallest values being obtained at the closest atomizer positions for which the droplets had less time to get spherical. The local

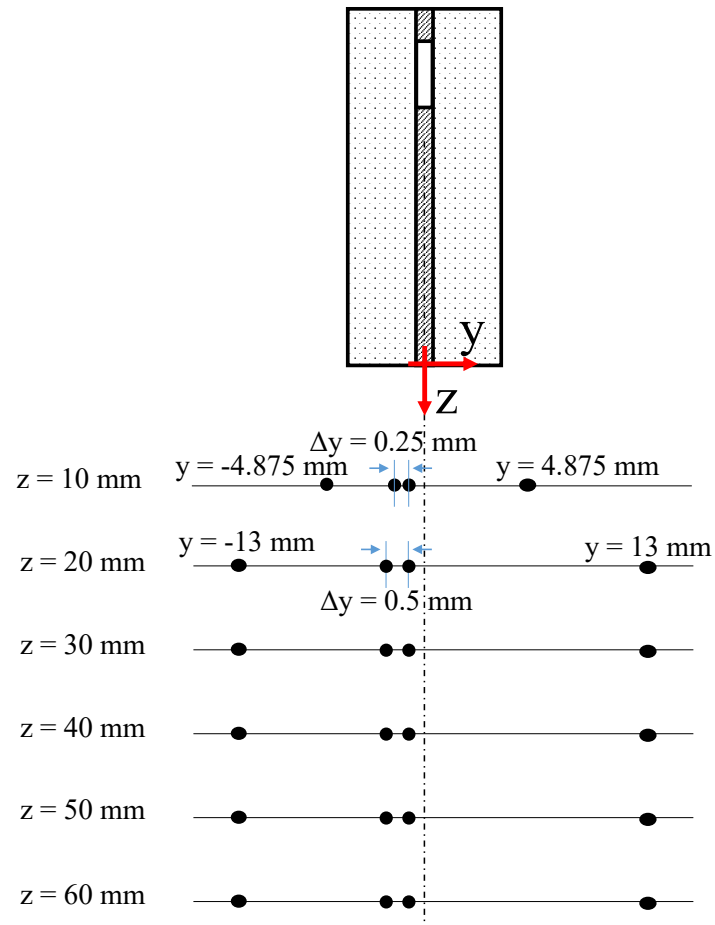


Figure 5.16: Schematic of the PDDPA measurement points performed at different distances from the nozzle exit; the measurements performed at  $x=0$  (middle of the injector in the front view); the grid coordination and distances are indicated on the figure.

number-based diameter distributions shown in Fig. 5.18 reveal the presence of a spray of fine droplets. The distributions are very much alike and show a population ranging from  $1 \mu\text{m}$  to  $200 \mu\text{m}$  with a peak located around  $D = 10 \mu\text{m}$ . Note that the left side (for diameters less than the peak diameter  $D_{p0}$ ) of the distributions are not smooth resulting probably from a lack of accuracy for this diameter range. It is worth recalling here that the PDPA instrument measures spherical drops only. In a spray, the most spherical drops are the small ones. Therefore, the diameter distributions of Fig. 5.18 characterize mainly the small drop population. At the closest distance from the orifice exit (position  $z = 10 \text{ mm}$ ), the axial velocity distributions of these drops are given in Fig. 5.19 for each G1 case. The peak velocity and distribution width both increase with the flow rate. For comparison, the mean velocities  $U_b$  of the orifice internal flows are indicated. As the flow rate increases, the ratio of this velocity on the maximum velocity of the distribution ranges from 0.83 to 0.63. This decrease is due to the fact that, close to the atomizer, the drop velocity is expected to be of the same order as the mean effective velocity of the issuing flow. However, in case G1-8, this mean effective velocity is higher than  $U_b$  since it occupies a portion of the exit section only because of the presence of cavitation structures in the orifice exit section. The droplets have therefore a velocity much higher than  $U_b$ .

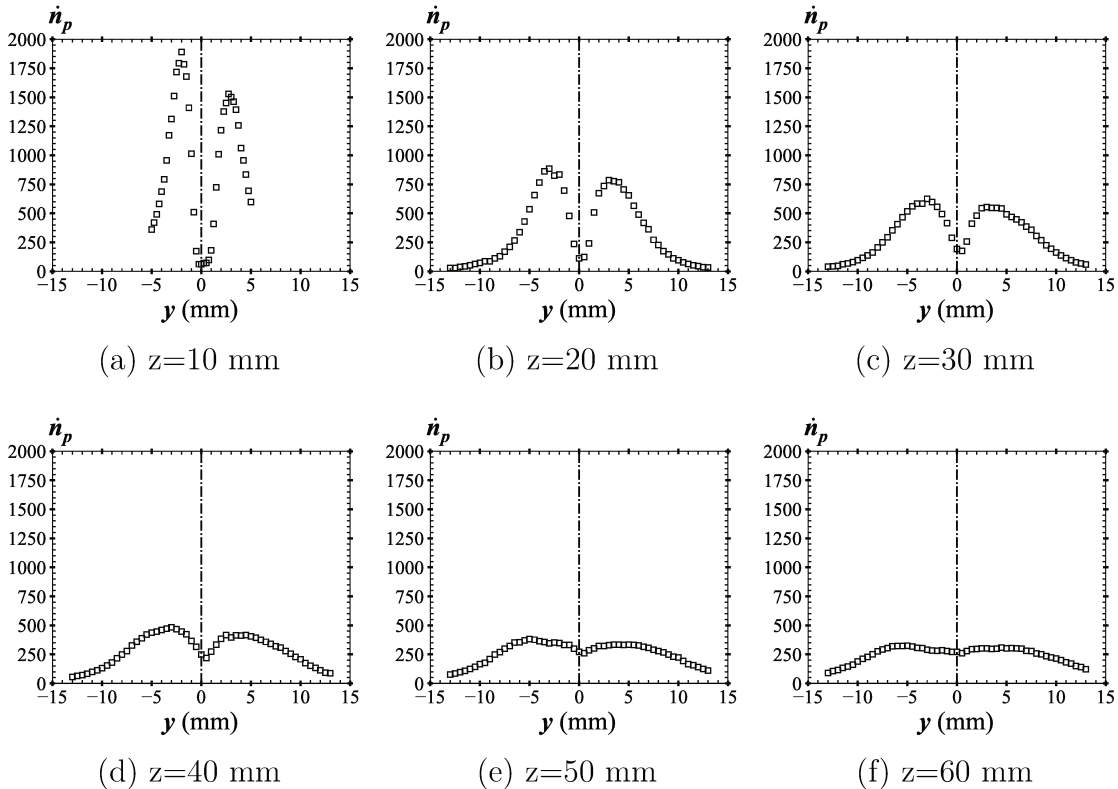


Figure 5.17: Validated data rate of the diameter-measurements for G1-8 as a function of the distance from the orifice axis for different distances  $z$  from the orifice exit.

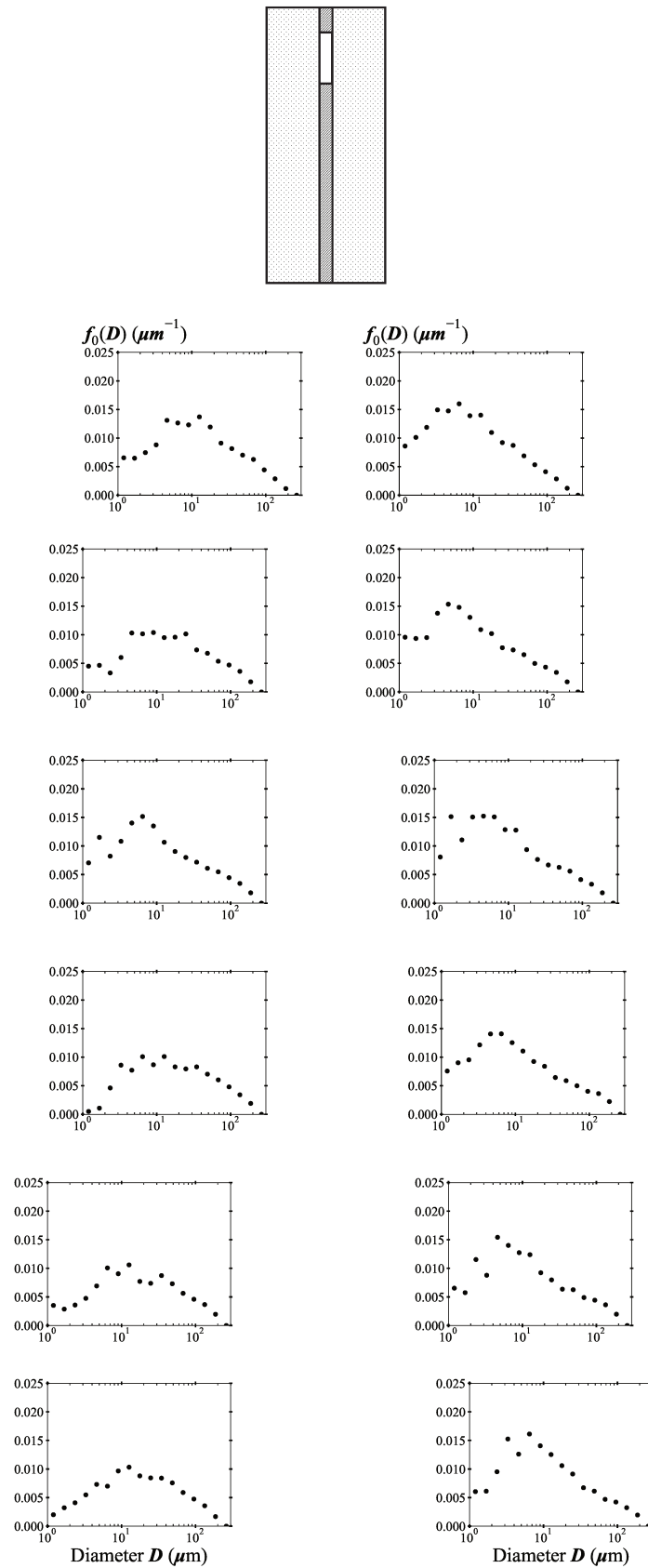


Figure 5.18: pdf of the drop diameter measured at the points of the highest and furthest from the atomizer axis at different distances (10 - 60 mm) from the nozzle orifice exit for G1-8.

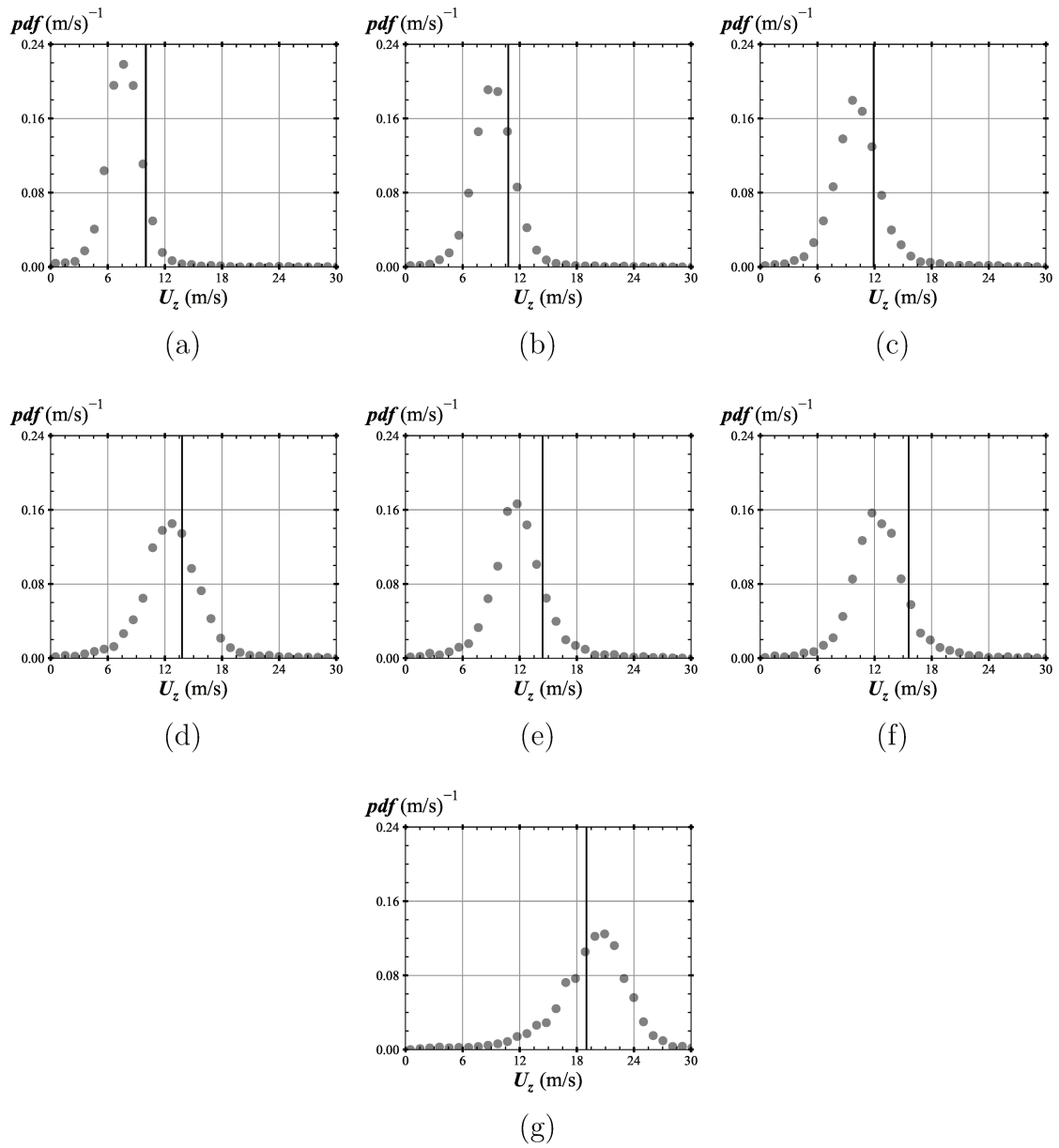


Figure 5.19: Droplet velocity at the highest validation rate of the PDPA measurements performed using G1 atomizer: a to f corresponding to operating conditions G1-1 to G1-6 and g to G1-8. The vertical line refers to the mean bulk velocity  $U_b$ .

## 5.4 Scale Distribution

This section presents the average scale-distribution characterizing the right side of the issuing flow front view. This side is the one that sustains the textural atomization of interest. The measurements were performed according to the protocol detailed in Sec. 4.7. The scale-distributions presented here and analyzed in the next Chapter are averaged on 500 images for every condition.

Figure 5.20, 5.21 and 5.22 present the scale-distributions for atomizer A1, G1 and G2, respectively. They all show the same shape: as the scale increases, the distributions first decrease, second reach a plateau, and third follow another decrease to reach the value zero at a specific scale  $d_{max}$  called the maximum scale. The decrease in the small scales ranges in a similar interval for all cases ( $[0, 1500\mu m]$ ). It is the signature of the textural atomizing ligaments. The decrease in the large-scale appears in a scale interval that depends on the case. It characterizes the structural deformation of the right side of the flow at the nozzle exit. At low flow rate, the decrease is rather stiff and is positioned around scale  $4000\mu m$  for atomizer A1 and G1, and around a slightly higher scale for atomizer G2. The sharpness of the decrease is a feature reported by the scale distribution of a rectangle (see Sec. 3.2.1). Therefore, the global shape of the flow is not deformed by large structures. When the flow rate increases, the maximum scale increases and the distribution decrease in the large scale region spreads on a wider scale interval. This behavior indicates that the shape of the flow is deformed by large structures of several sizes. This result agrees with the observations made on the still images in Sec. 5.1.2 concerning the enlargement of this flow side for the medium flow rates and for the three atomizers. When the flow rate again increases, the maximum scale decreases and the distribution decrease in the large scale region gets stiff again. Observed on the images, the disappearance of the large scale deformation results from the hydraulic flip flow regime that refrains the production of energetic large structures. These results show the influence of the atomizer flow regime on the structural deformation of the issuing flow.

As noted above, the scale-range of the textural deformation is similar for all conditions. The difference of  $e_2(0)$  between the cases is not representative of the textural atomization process only. The specific length  $e_2(0)$  is the perimeter per unit surface of the whole system. It depends both on the system perimeter and surface area, the later being not a textural atomization characteristic. Therefore, the first task in the analysis will consist in splitting the scale distribution to isolate the component representative of the textural atomization process.

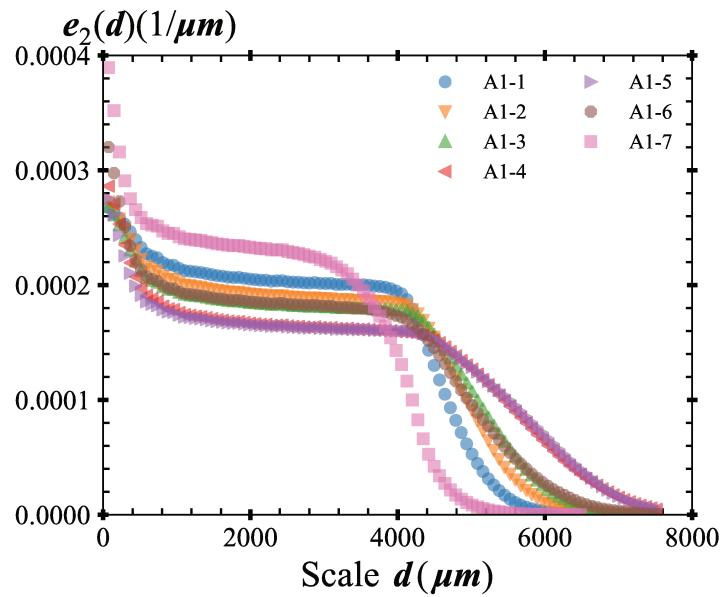


Figure 5.20: Measured scale distribution of A1-1 to A1-7. The scale step  $\Delta d = 7$  pixels ( $37 \mu\text{m}$ ).

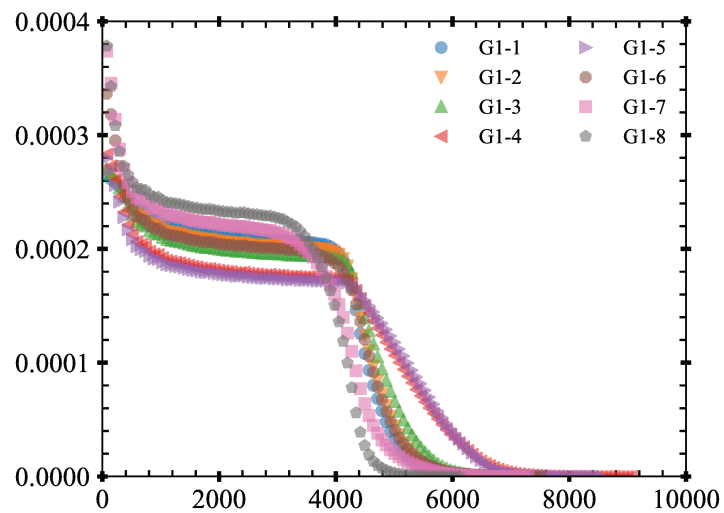


Figure 5.21: Measured scale distribution of G1-1 to G1-8. The scale step  $\Delta d = 7$  pixels ( $35 \mu\text{m}$ ).

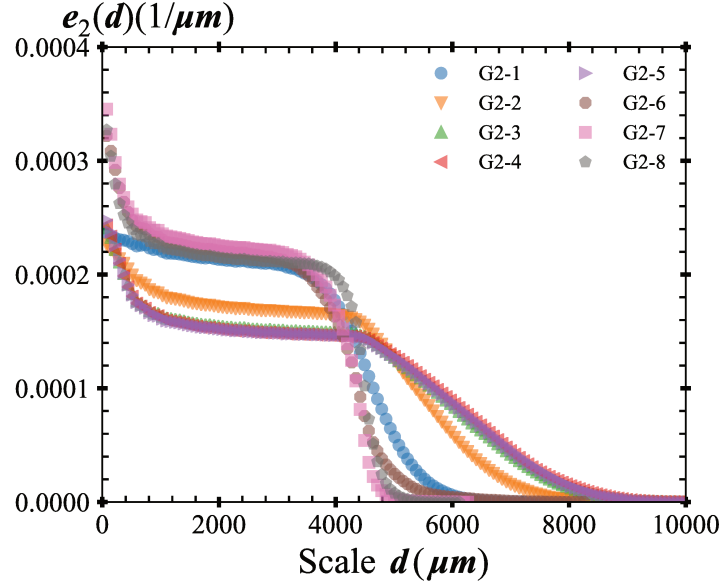


Figure 5.22: Measured scale distribution of G2-2 to G2-8. The scale step  $\Delta d = 7$  pixels ( $35 \mu\text{m}$ ).

## 5.5 Image-Based Drop Diameter Measurements

This section presents the drop diameter-distribution measured by image analysis. The measurement procedure is detailed in Sec.4.8. The measurements are performed for atomizers A1 (all conditions) and G2 (conditions 3 to 8, the number of drops for cases 1 and 2 was not high enough to produce reliable drop diameter distribution). We remind that the drop images have been taken in the lateral view configuration since droplets were more numerous in that direction. They covered the region extending from 40 mm to 54 mm from the atomizer. The distributions presented in this work are based on the analysis of 500 images for each case and the total number of measured drops  $N_T$  ranges from 2800 to 75000 according to the case (see Table 5.1). It is important to highlight that  $N_T$  is the total number of droplets after applying the DoF criterion explained in Sec. 4.8.4. Beside the diameter, the image analysis reported a series of shape parameters introduced in Section 4.8.5. Among these parameters, the sphericity parameter  $S_p$  quantifies the deviation from circularity of each element (see Sec. 4.8.5). It varies from 0 to 2, 0 being the case of a circle. The elements reporting a high  $S_p$  are very deformed droplets or ligamentary structures whose atomization is not over. These elements must be excluded from the spray drop diameter distribution. The distributions were built by considering droplets with  $S_p < 0.4$  only. According to the situation, the number of selected droplets varies from 1800 to 67600 and corresponds to 69% and 90% of the total number of measured drops, respectively (see Table 5.1).

Table 5.1: Number of droplets for each operating condition of A1 and G2 atomizers:  $N_T$  is the total of measured droplets and  $N_{valid}$  is the validated number of droplets.

Cond No.	A1		G2	
	$N_T$	$N_{valid}$	$N_T$	$N_{valid}$
1	2600	1800	-	-
2	3800	3000	-	-
3	6700	4600	8400	7900
4	10700	7400	11700	11100
5	12500	8600	16100	14900
6	17200	13600	38300	25100
7	47000	32900	61600	49500
8	-	-	75400	67600

Since the measurement of the drop diameter distribution is based on detection and measurements of surface areas, the surface-based diameter distribution  $f_2(D)$  is the more appropriate function type to represent the results. This distribution is related to the number-based distribution  $f_0(D)$  (see Eq. (3.15)):

$$f_2(D) = \left(\frac{D}{D_{20}}\right)^2 f_0(D) \quad (5.1)$$

The surface-based drop-diameter distributions  $f_2(D)$  are presented in Fig. 5.23 for atomizer A1 and G2. This figure shows that the drop diameter distribution of the textural sprays exhibits two modes. The right mode is the main one: it shows a peak diameter  $D_{peakR}$  that decreases when the flow rate increases. The peak diameter  $D_{peakL}$  of the left mode appears not affected by the mass flow rate but the drop population does: it increases with the flow rate. The left mode appears clearer in the number-based diameter distribution shown in Fig. 5.24. Considering that the textural atomization process consists of the rupture of ligaments, this kind of bimodal distribution could have been expected. Indeed, it is known that ligaments have a propensity to produce two drop categories, i.e., main droplets whose diameter is of the order of the initial ligament size, and satellite droplets whose diameter is far less than the main-droplet one (Vassallo and Ashgriz, 1991). The number and size of the satellite drops depend on the initial shape of the ligament and on the physical mechanisms in play, and more, specifically, on the ratio between surface tension and elongation effects if any (Dumouchel et al., 2015a).

The diameter distributions obtained for A1-1 and A1-2 are a bit noisy because of the low number of drops they include for such wide distributions. They however fit well with the distributions obtained for the other cases. When the flow rate increases, the main-drop peak slides towards the small diameter direction. As far as the satellite-drop peak

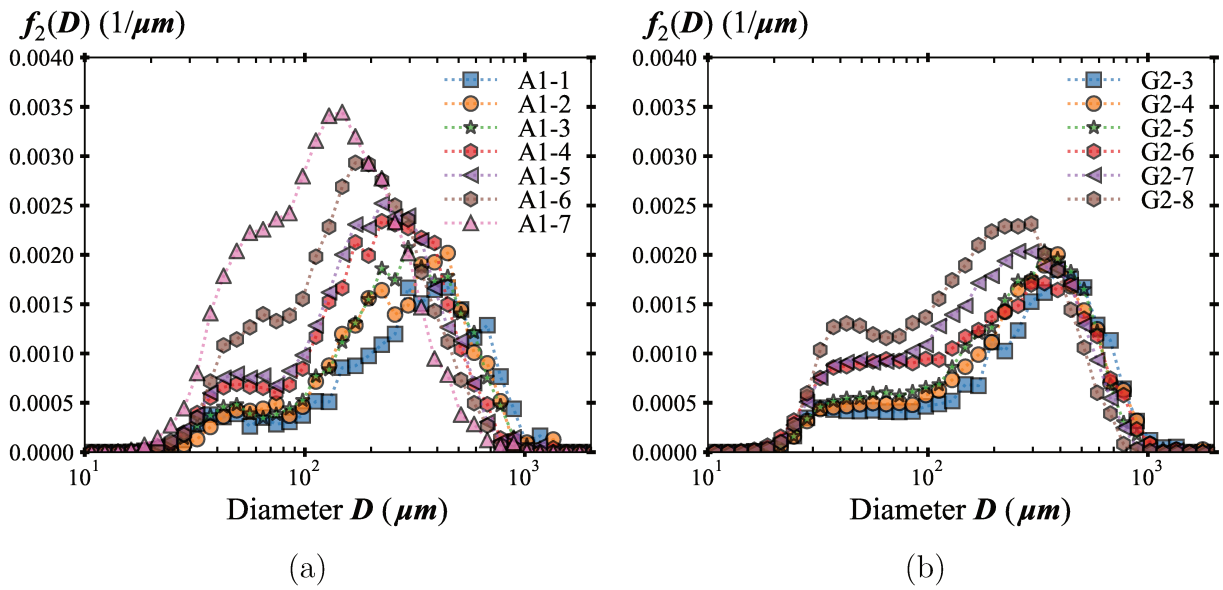


Figure 5.23: Experimental surface-based drop diameter distribution  $f_2(D)$  for the atomizers: a) A1 and b) G2.

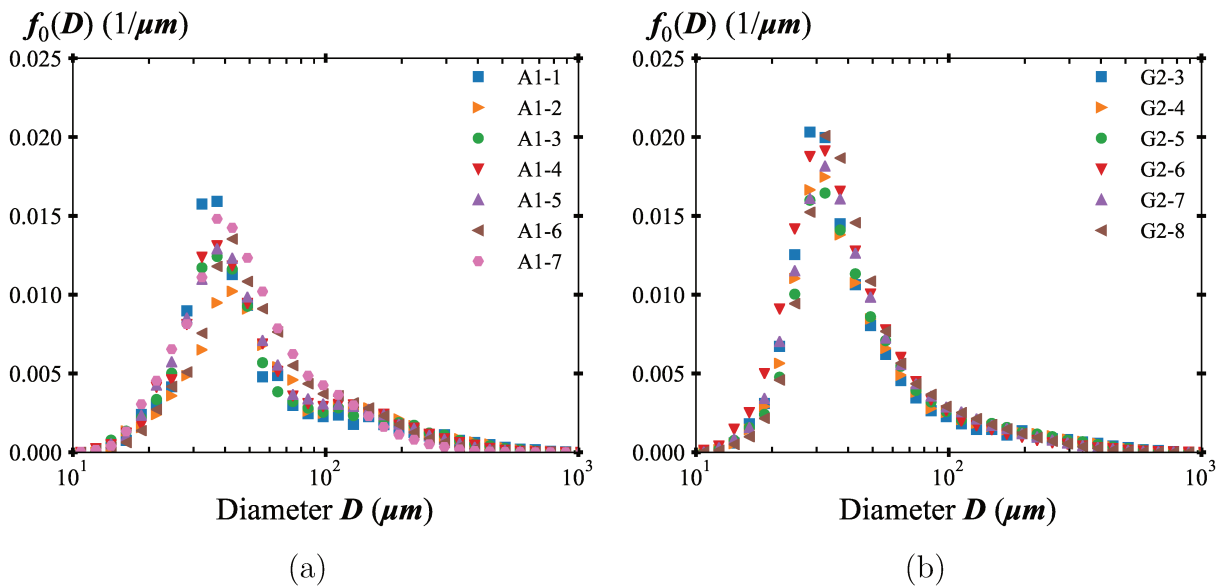


Figure 5.24: Experimental number-based drop diameter distribution  $f_0(D)$  for the atomizers: a) A1 and b) G2.

is concerned, we mainly see an increase of this population proportion when the flow rate increases.

The distribution obtained for case A1-7 (see Fig. 5.23a and 5.24a) is interesting to consider since it can be globally compared with PDPA diameter distributions measured with atomizer G1 presented in Fig. 5.18 (penultimate and ante-penultimate rows) as these two atomizers have the same internal geometry. The PDPA measures droplets of diameters from 1 to 200  $\mu\text{m}$  with a peak in the distribution around 5-10  $\mu\text{m}$  whereas image-based diameter measurements range from 10 to 1000  $\mu\text{m}$  with a peak around 40  $\mu\text{m}$  for number-based distribution (Fig. 5.24a). It is obvious that image analysis is not able to measure the left part of the PDPA distribution (to the left of the peak) as it is below the minimum limit of the image analysis. However, PDPA distributions on the left of Fig. 5.18 clearly present an extension of the peak up to  $\sim 40 \mu\text{m}$  corresponding to the peak of image analysis. We could conclude that it is difficult to measure drop size distribution below  $\sim 40 \mu\text{m}$  by image analysis whereas PDPA seems more efficient in this range, For diameter over 200  $\mu\text{m}$  it is guessed that shape deformation starts to be significant enough for the PDPA to be unable to measure these drops whereas image analysis considers them. Indeed, the criterion  $S_p < 0.4$  is flexible enough to accept a bit deformed droplets. It must be mentioned that the sampling region in both techniques could be different.

The distributions obtained for atomizer G2 report the same evolution with the flow rate. However, the main peak height does not increase as much as that for atomizer A1. This is due to the fact that cases A1-6 and A1-7 correspond to higher flow rate than case G2-8. Figure 5.25 presents the evolution of the Sauter mean diameter  $D_{32}$  with the flow rate. The results for the two atomizers are shown. As expected, the mean diameter decreases when the flow rate increases. At low flow rates, atomizer G2 sprays have mean diameters smaller than those of atomizer A1 sprays. For a given flow rate, the pressure level in G2 is higher than in A1, and these two atomizers do not report the same flow regime. Therefore, we see an impact of the flow regime on the drop size distribution of the textural spray when the flow rate is low. For higher flow rates, both atomizers report the same mean diameters  $D_{32}$ . To have a better perception of this behavior, Fig. 5.26 compares the diameter distributions of the two atomizers for two flow rates, i.e.,  $40 \cdot 10^{-3} \text{ kg/s}$  (A1-1 and G2-4) and  $55 \cdot 10^{-3} \text{ kg/s}$  (A1-4 and G2-7). For both cases, we see that the distributions are very much alike. For the low flow rate ( $40 \cdot 10^{-3} \text{ kg/s}$ ) we note that the main-drop population for atomizer G2 is slightly shifted to the left of the main-drop population obtained for the other atomizer. Furthermore, the satellite drop population shows a higher peak for G2 than for A1. These two observations explain the reduction of the  $D_{32}$  observed for atomizer G2. For the second flow rate ( $55 \cdot 10^{-3} \text{ kg/s}$ ), the two distributions show some differences. This time, the main-drop population is slightly wider for atomizer G2 and the satellite drop population remains higher for this atomizer. However, for this case, these differences have a negligible impact on the value of the Sauter mean diameter because of their opposite influences on this

diameter annihilate.

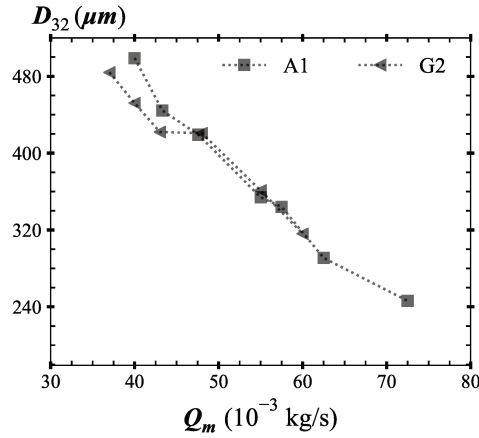


Figure 5.25: Sauter mean diameter  $D_{32}$  as a function of the flow rate  $Q_m$  for both A1 and G2 atomizers.

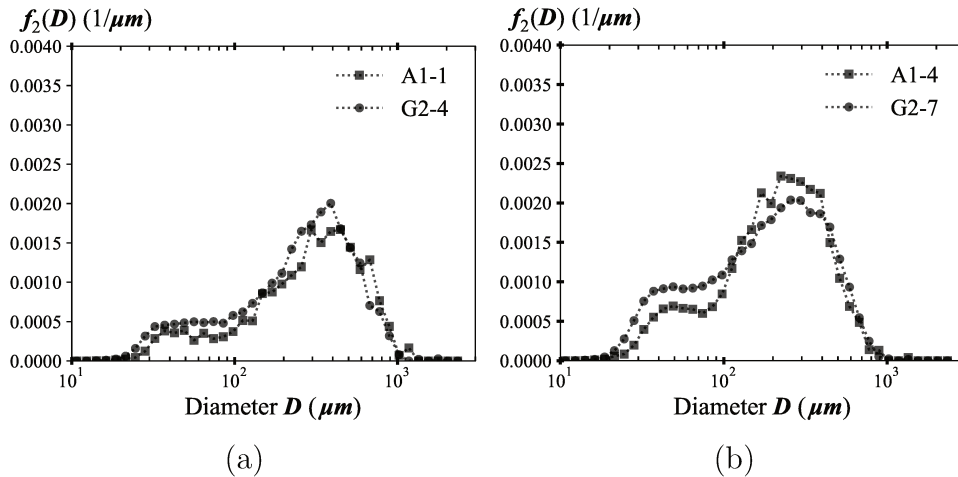


Figure 5.26: Surface-based drop size distribution  $f_2(D)$  for: a) A1-1 and G2-4, b) A1-4 and G2-7.

The differences between A1 and G2 spray drop size distributions are very small in every situation and could be of the order of magnitude of the reproducibility of the measurement. It seems therefore reasonable to conclude that both atomizers A1 and G2 report very similar textural spray drop diameter distribution for a given flow rate. The closeness between the distributions will be quantified in the next chapter. The only difference that may be considered is the fact that the satellite drop population is always a higher proportion of the spray for atomizer G2. Apart from that, it should be concluded here that the reduction of the height of the atomizer inlet section has a rather negligible effect on the drop size distribution of the textural spray produced just at the nozzle exit.

# Chapter 6

## Analysis

This chapter presents analyses that have been performed on the experimental results exposed on the previous chapter. These analyses are presented in three sections. The first one considers the question of the influence of cavitation on the internal orifice flow characteristics. This point will be approached by using numerical simulations of the internal flow. The second section proposes an analysis of the temporal variability of the cavitation structures and of the atomization region. The influence of this variability on the textural atomization process will be approached by considering the standard deviation of the scale distribution. Finally, the last section addresses the question of the mathematical representation of the textural-atomization process scale-distribution and of the spray drop size distribution, as well as the connection between these two characteristics.

### 6.1 Influence of Cavitation on Orifice Flow

In this section we intend to get an idea on the influence of the cavitation on the liquid flow characteristics, and more specifically, at the outlet of the atomizer orifice. To achieve this, the velocity fields in the orifice of the atomizer measured with LDV and presented in the previous chapter, are going to be compared with velocity fields resulting from numerical simulations. The simulation work has been conducted by Aqeel Ahmed, PhD student involved in the HAoS project. Highly resolved LES (Large Eddy Simulation) is performed within the framework of open-source tool box OpenFOAM. Based on the Taylor length scale, the average mesh size is determined and found equal to  $50 \mu\text{m}$  in the nozzle area and reduces down to  $5 \mu\text{m}$  as walls are approached. Special treatment of inlet boundary condition is required for initializing fully developed turbulent flow. This has been achieved using the synthetic turbulent inlet generator. The pressure is set to zero gradient at the

inlet. At the outlet, zero gradient boundary condition is used for the velocity and a fixed pressure value is specified. In this case, the value is 0 since in incompressible simulation, the pressure difference is of interest instead of the absolute static pressure. The simulation tool is not equipped to make the liquid cavitate. Therefore, at a given flow rate, it reports the characteristics of the non-cavitating flow. Comparing these characteristics with those resulting from the LDV measurements allows identifying the impact of cavitation on the liquid flow dynamics. This work has been conducted with atomizer G1 only, since LDV measurements are available for this atomizer only. The cases considered are G1-1, G1-4 and G1-8, which correspond to flow Regime I, III and IV respectively.

Figure 6.1 show the mean axial velocity maps  $\langle U_z \rangle$  in the orifice for case G1-1 reported by the experiments (LDV) and the simulations (LES). Remind that this case belongs to the non-cavitation flow regime and therefore, we expect an agreement between simulation and experiment. At first glance, this agreement is good. Its quality is confirmed in Fig. 6.2 that compares several profiles at several positions in the orifice. From left to right, this figure shows the radial profile of the ratios  $\langle U_z \rangle / U_b$ ,  $\langle U_{z,rms} \rangle / U_b$ ,  $\langle U_x \rangle / U_b$ ,  $\langle U_{x,rms} \rangle / U_b$ , where  $U_{k,rms}$  is the root mean square of the velocity component in the k direction. For each case, the line is the result provided by the simulation whereas experimental results are shown by dots. The two first images show a very good correspondence for the axial component of velocity  $\langle U_z \rangle$ : LDV and LES mean axial velocity profiles are the same. At the nozzle entrance, we remark that  $\langle U_z \rangle$  passes from 0 to a constant value at a specific radial position where a strong velocity gradient appears. The rms velocity of this component shows a peak at the position of this gradient. At the other positions, we note the  $\langle U_z \rangle / U_b$  profiles are very dissymmetric and the rms are higher in the right side, where the axial component is the smallest. At position  $z = -7.5$  mm,  $\langle U_z \rangle / U_b$  seems to be negative along the upstream side wall. This corresponds to the re-entrant jet that was visualized in the high speed film sequences.

As far as the radial component is concerned, the agreement between the simulation and the experiment is not as good as for the axial component. A slight disagreement is visible on the mean radial velocity profile at the positions  $z = -4.1$  mm and  $-7.5$  mm. Note however that the values of the radial velocity are very small. For the other positions, the results are rather good for the radial mean velocity and rms-velocity. Note that the gradient of the axial velocity noticed at the orifice entrance is also observed for the radial component of velocity. The agreement underlined in Fig. 6.2 gives credit to the measurement and to the simulation results.

Figure 6.3 shows the same four images as Fig. 6.2 but for the case G2-4 (Regime III). We see that the profiles (either measured or calculated) are rather similar to those shown in the Fig. 6.2. Note here, that the radial velocity gradient at the orifice inlet aligns with the main cavitation structure that develops in this region. It is rather unexpected to see that LES and LDV report very similar results which would mean that the cavitation has

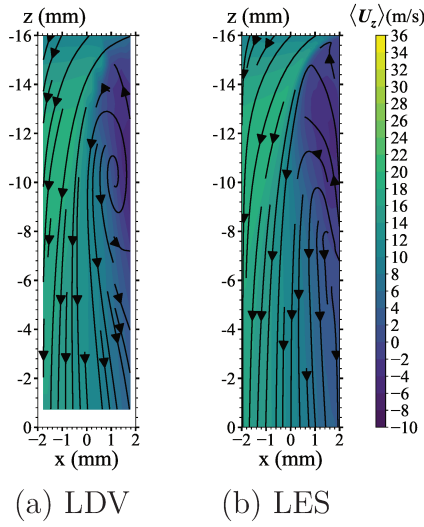


Figure 6.1: Comparison between the LDV and LES for the mean stream-wise mean velocity  $\langle U_z \rangle$  of G1-1.

a rather limited influence on the mean velocity component and on the rms velocity. This seems to be particularly the case at the nozzle exit section.

Finally, Fig. 6.4 proposes the results for case G1-8 (Regime IV). In this case, we see strong differences between the LDV and LES results. It seems that cavitation increases the local axial component of velocity as well as the rms of the radial velocity component at the nozzle exit. However, as explained in the previous Chapter, the representativeness of the measured velocity may be very low. Furthermore, the differences obtained here in the cavitation structure were not found in the previous case (Fig. 6.3) where a good agreement was found everywhere, even at positions where the cavitating structure was apparent.

It is rather difficult to bring a strong conclusion on the results presented in this section. Considering the results for the case G1-4, we can say that whatever the influence of the cavitation on the flow characteristics  $\langle U_z \rangle / U_b$ ,  $\langle U_{z,rms} \rangle / U_b$ ,  $\langle U_x \rangle / U_b$  and  $\langle U_{x,rms} \rangle / U_b$ , this influence has disappeared at the orifice exit section. This behavior appears to be related to the specific geometry of the atomizer. In particular, its very small thickness could impose a strong control on the flow that is mainly function of this geometrical characteristics. Of course, the work presented here does not allow concluding on the possible influence of cavitation on the turbulence at the nozzle exit. This turbulence might be also affected by the orifice thickness. Based on the current observations, the cavitation influences the flow characteristics at the exit section when the cavitation reaches the nozzle exit (Regime IV).

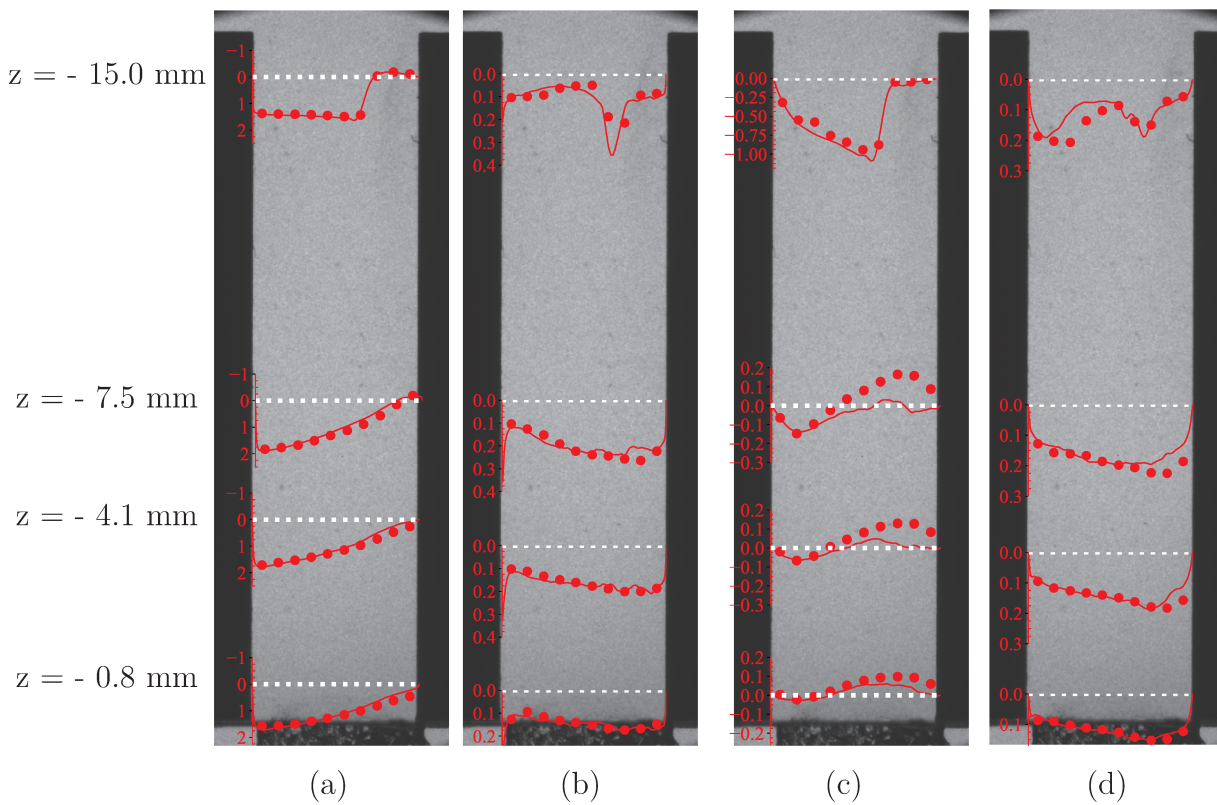


Figure 6.2: a) Normalized mean stream-wise velocity profile  $\langle U_z \rangle / U_b$ ; b) fluctuations  $\langle U_{z,rms} \rangle / U_b$ ; c) normalized span-wise velocity  $\langle U_x \rangle / U_b$ ; d) fluctuations  $\langle U_{x,rms} \rangle / U_b$  for G1-1.  $U_b = 10.0$  m/s. White dashed-line is the position where the velocity profile is probed. Red-dot is the LDV measurement and the red-line is the LES simulation.

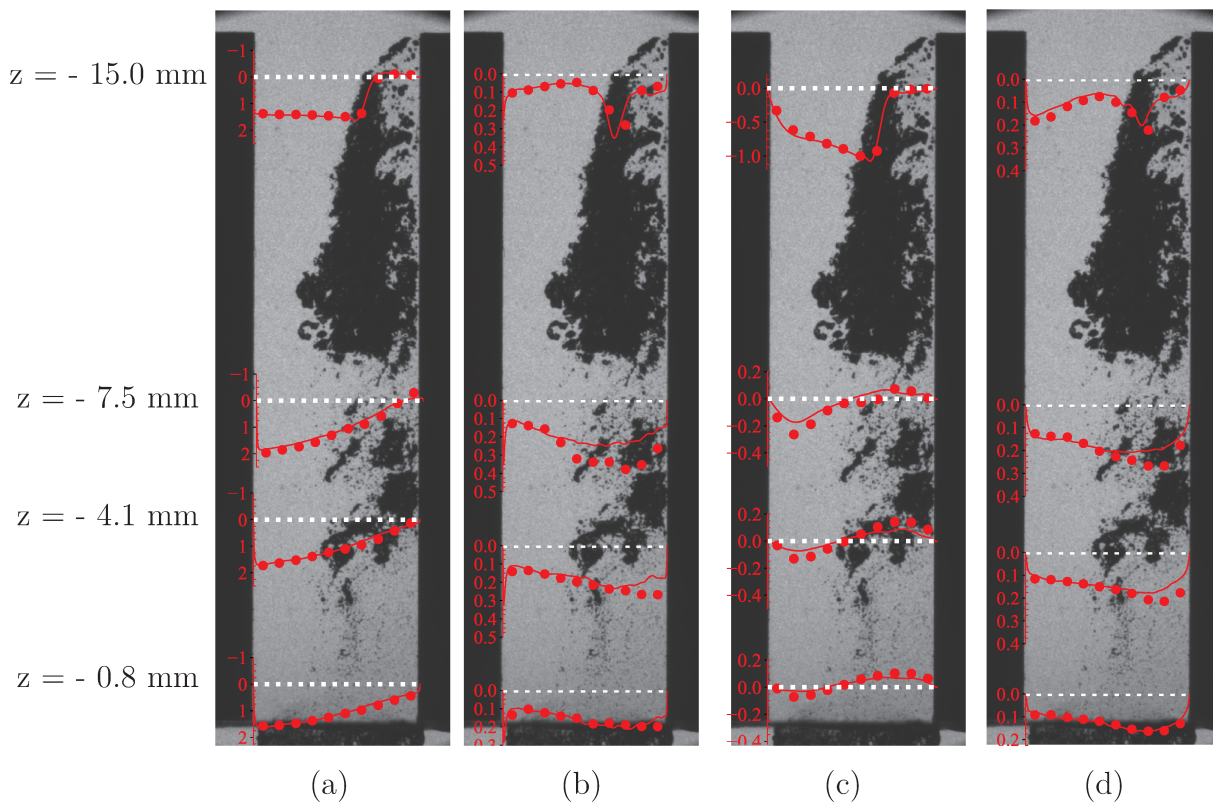


Figure 6.3: a) Normalized mean stream-wise velocity profile  $\langle U_z \rangle / U_b$ ; b) fluctuations  $\langle U_{z,rms} \rangle / U_b$ ; c) normalized span-wise velocity  $\langle U_x \rangle / U_b$ ; d) fluctuations  $\langle U_{x,rms} \rangle / U_b$  for G1-4.  $U_b = 13.8$  m/s. White dashed-line is the position where the velocity profile is probed. Red-dot is the LDV measurement and the red-line is the LES simulation.

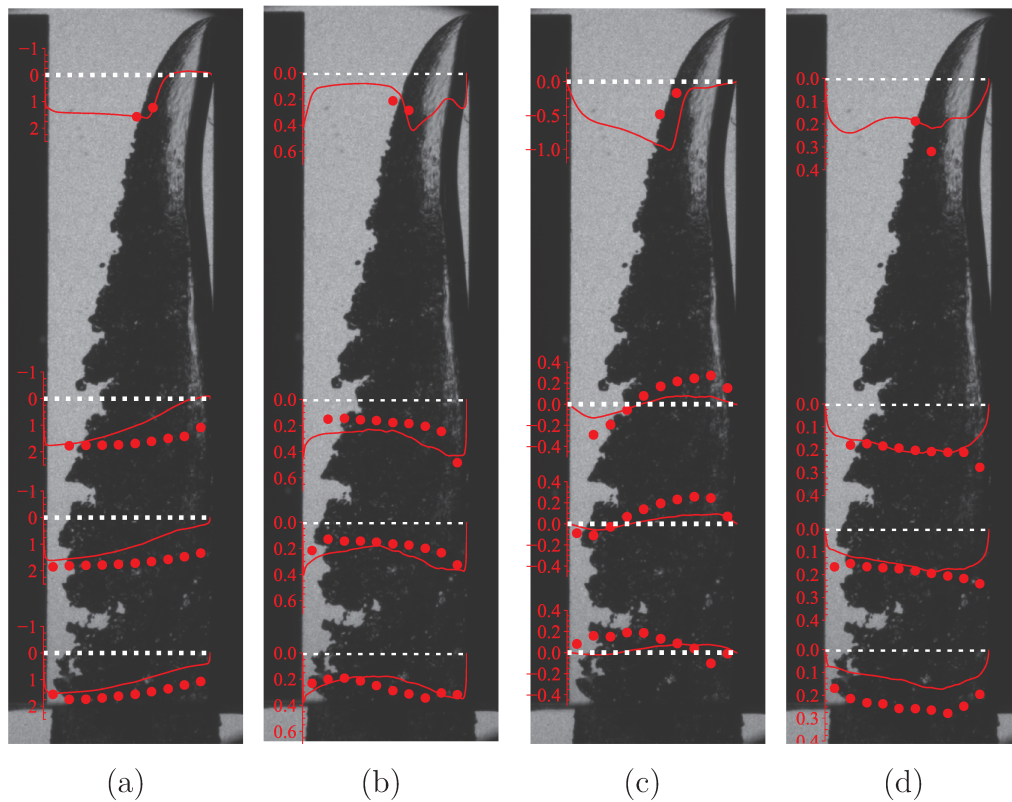


Figure 6.4: a) Normalized mean stream-wise velocity profile  $\langle U_z \rangle / U_b$ ; b) fluctuations  $\langle U_{z,rms} \rangle / U_b$ ; c) normalized span-wise velocity  $\langle U_x \rangle / U_b$ ; d) fluctuations  $\langle U_{x,rms} \rangle / U_b$  for G1-8.  $U_b = 19.0$  m/s. White dashed-line is the position where the velocity profile is probed. Red-dot is the LDV measurement and the red-line is the LES simulation.

## 6.2 Internal and External Flow: Entropy Analyses

This section presents the analysis of the temporal variability of cavitation in the internal flow and of atomization in the external jet flow. This analysis is based on the determination of local entropy. We recall here that three states are allocated to pixels of the internal flow images which correspond to liquid and vapor phases where the latter is split into detached bubbles and cavitation cloud (the biggest vapor 'bubble'). For the external flow three states are also defined. They are the surrounding gas, the liquid jet and the detached liquid elements, i.e. ligaments and droplets. The local entropy is calculated from the probability of these three states (see §4.9). An entropy value is given to each image pixel, giving rise to entropy maps. A pixel having seen only one state get a null entropy value. The maximum entropy is reached when the three states are equiprobable. The highest the entropy value, the highest the cavitation variability for the internal flow or the highest the atomization activity for the external flow.

We will distinguish two kinds of entropy value range to analyze the entropy maps. The first one is the *active region* corresponding to non-null entropy pixels, i.e. to pixels being visited by at least two states. The second one is the *3-state region* corresponding to pixels visited by each of the three states at least one time.

### *Internal Flow*

Entropy maps for the three atomizers are presented in Figs 6.5-6.7 for the internal flow. The colormap used to represent entropy values goes from black to yellow color for entropy values from 0 to 0.631 corresponding to the limit of the 3-state entropy and from white to red color for entropy values greater than 0.631, corresponding to the *3-state region*. The delimiting zone is marked by a blue line on the entropy maps. The extent and the shape of the entropy distribution is a mark of the 'activity' of cavitation in the nozzle.

It is worth noting that the shape of the *active region* at nozzle entrance is particularly reproducible. Indeed, whatever the flow rate and the cavitation regime, the upstream delimitation of this region is always the same for a given atomizer. This shows the direct link between cavitation activation and the hydrodynamic flow geometrical properties. We notice that atomizer A1 and G1 sharing the same geometry present similar *active region* shapes at nozzle entrance whereas for atomizer G2 this region is a bit larger.

As expected, at low flow rates the *active region* is reduced. In cavitation inception regime, this region extends to half the orifice length downstream nozzle entrance for A1 and G1 atomizers but cover the entire nozzle length for G2. Indeed, for atomizer G2, not only cavitation participates to the two-phase flow in the nozzle but also air bubbles sucked in at the nozzle orifice exit as a result of the large recirculation zone (see §5.1).

This results in a long active region covering all the nozzle length for this atomizer, even in no-cavitation regime (see Figs 6.7a). We can also notice that as soon as flow regime III (*super-cavitation*) is reached, the entropy *active region* is hollow (see Figs 6.5c, 6.6b and 6.7d). This hollow zone is induced by the permanent presence of the cavitation cloud at this location for these conditions. Atomizer G2 is a particular case also as the *active region* extends down to the orifice exit whereas it does not for the other two. This is due to the air bubbles sucked in the liquid flow.

For the end of *super-cavitation* regime and for the *partial-hydraulic flip* regime, the *active region* is hollow with thin boundaries, and it covers practically the entire nozzle length. This can be seen in Figs 6.5d-6.5f for atomizer A1, Figs 6.6d-6.6f for atomizer G1, and Figs 6.7e-6.7g for atomizer G2. This indicates a particular reproducible shape of the cavitation cloud over image series. Indeed, the very thin boundary of the *active region* on the left side of the internal flow clearly shows that the boundary of the cavitation cloud is unchanged on this side.

It is also of interest to consider the shape and the extent of the *3-state region* (in red on the entropy maps). This region is at the center of the active region. For low cavitation activity, i.e. for *cavitation inception* regime, the cavitation cloud is not developed and varies in shape and location over the series. In that case the *3-state region* delimits the common area for all the cavitation clouds over time. As soon as the cavitation cloud develops and is attached to the right upper corner of the internal geometry, the *3-state region* mainly appear upstream at this upper right corner or at the downstream end of the cavitation cloud. The behavior is different for these two regions.

The occurrence of the *3-state region* upstream is linked to the detachment of the flow in this region, accompanied with a recirculation zone that brings detached bubbles near the cavitation cloud. The images often evidences the presence of liquid in this region. The three states are thus encountered in the region.

The occurrence of the *3-state region* downstream is related to the variation over time of the length of the cavitation cloud. At the downstream end of it, detached droplets and liquid coexist together with the cavitation cloud, leading to this *3-state region*. This particular region is a place of high cavitation variability, meaning that large vapor bubbles, small bubbles and liquid are visiting this location. We observe that this downstream region disappears for the last operating point for each atomizer, meaning that the cavitation cloud permanently reached the nozzle exit in this condition. We also notice that for G2 atomizer, the cavitation cloud occupies the whole nozzle width in the second half of the nozzle length. This is linked to the wider *active region* at nozzle entrance for this atomizer, as noticed above.

To quantify these results, the *3-state region* area was estimated. This area is normalized

by the area of the nozzle ( $16 \times 4 \text{ mm}^2$  for the three atomizers). The results are reported in figure 6.8 as a function of the flow rate. Here again the trend is practically the same for atomizers A1 and G1 and differs for atomizer G2 principally at low flow rates. In fact, the *3-state region* area increases with the flow rate to reach a maximum about 20% when *super cavitation* regime is reached. Still increasing the flow rate, the area progressively decreases down to a few percents when the cavitation cloud is very stable over time. The first four points for atomizer G2 are clearly detached from the other points. This is due to sucked in air bubbles that strongly participate to the flow. This is especially evident for low flow rates although for higher flow rates this contribution can remain important but air bubbles cannot be identified in those cases.

### *External Flow*

Entropy maps of the external flow for the three atomizers are presented in Figs 6.9-6.11. The same colormap as for the internal flow is used. The *3-state region* has a particular signification for the external flow. Indeed, the location where the jet, the detached droplets and the gas coexist is considered to correspond to the location where primary atomization occurs. This region was actually called the primary atomization zone by Blaisot and Yon (2003).

For the external flow, the *active region* and the *3-state region* are of similar shapes, the latter being a bit smaller than the former. We thus focus mainly on the *3-state region*, i.e. the primary atomization region.

The first observation comes from the dissymmetry of the jet already mentioned in the previous chapter, which clearly appears on entropy maps. Indeed the primary atomization region is far more thinner on the left side of the jet. We can notice that for atomizers A1 and G1 the primary atomization region remains practically the same for all flow rates. Only for the highest flow rate does this region spread a little bit more. For G2 atomizer the primary atomization region becomes very thin for *cavitation inception* regime and also at the beginning of *super-cavitation* regime.

We consider now the right part of the jet. If we consider only atomizers A1 and G1, the trend is expanding of the primary atomization region when the flow rate increases. This is accompanied by a change of orientation of this region. Indeed, the deviation, i.e. the spray angle, is small with *no cavitation* regime, it becomes larger for *super-cavitation* regime and finally tends to zero in *partial-hydraulic flip* regime and the entire external flow becomes rather symmetric for high flow rates. The behavior is mainly the same for G2 atomizer except that deviation is more pronounced. Also, the spreading of the primary atomization region is wider in *no cavitation* regime. Symmetrization of the external flow for G2 in *partial-hydraulic flip* regime is also particularly noteworthy. This is not surprising, given

that the cavitation cloud fills the entire nozzle width in this regime.

The primary atomization region area was quantified for the external flow the same way as that for the *3-state region* for the internal flow. As the spray is not bounded, this area  $A_a$  is normalized here by the area of a rectangle of same length as that of the spray and of width equal to that of the nozzle (4 mm for the three atomizers). The results are reported in figure 6.12 as a function of the flow rate. Left and right side of the image, i.e. downstream and upstream part of the spray, are considered separately. If we just consider the cavitation regimes, the same trend is observed for the three atomizers. The primary atomization region area  $A_a$  first increases with the flow rate and reaches a maximum about 20% between *super cavitation* regime and *partial-hydraulic flip* regime. When the maximum is passed,  $A_a$  decreases to about 10%. As already mentioned, the two sides of the spray cannot be compared. The values for  $A_a$  on the downstream side are far below those for the upstream side and the total area finally matches with the results for the upstream side.

The internal flow entropy images highlight a certain degree of variability of the flow characteristics at the nozzle exit. The influence of this variability on the textural atomization process is investigated as follows. A mean entropy is calculated in the orifice bottom region defined by  $0 \leq x \leq 2$  mm and  $-1\text{mm} \leq z \leq 0$ . This mean entropy quantifies the variability of the right part of the issuing flow. For the external flow the scale distribution at the minimum resolved scale  $e_2(d_{min})$  is considered. In fact, this quantity resembles the perimeter length per unit surface area. The variability of the textural atomization process is quantified by calculating the standard deviation  $\sigma$  for  $e_2(d_{min})$ , more precisely:

$$\sigma_{e_2(d_{min})} = \sum_{i=1}^{500} \sqrt{(e_2(d_{min}) - e_{2,i}(d_{min}))^2} \quad (6.1)$$

where  $e_2(d_{min})$  is the scale distribution at the minimum resolved scale  $d_{min}$  averaged over 500 images and  $e_{2,i}(d_{min})$  is the one for the  $i^{th}$  image. Figure 6.13 shows  $\sigma_{e_2(d_{min})}$  as a function of the mean entropy. This figure reports a certain trend when the variability at the nozzle exit-section is mainly induced by cavitation and does not show any specific trend when the variability at the nozzle exit is due to air-sucking mechanism.

### 6.3 Textural Atomization and Sprays

This section presents the analysis of the textural scale distributions and of the spray drop diameter distributions. Several objectives are pursued. Mathematical formulation wants to be obtained both for the scale distribution of the textural-atomization process and the spray drop diameter distribution. The similarity of textural spray drop diameter distribution wants to be quantified. The connection between the atomization process and the spray

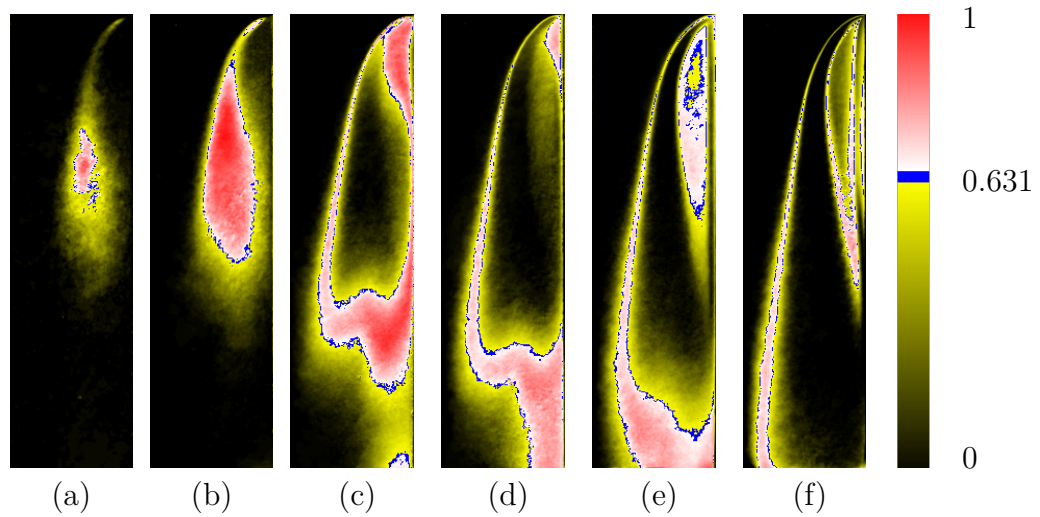


Figure 6.5: Entropy maps for the internal flow of A1 atomizer: a to f presents A1-2 to A1-7.

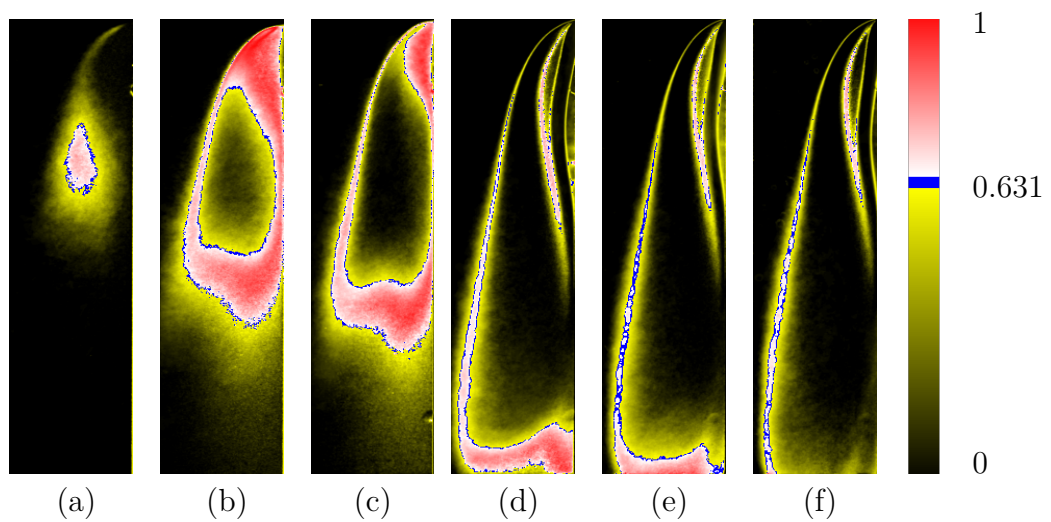


Figure 6.6: Entropy maps for the internal flow of G1 atomizer: a to f presents G1-3 to G1-8.

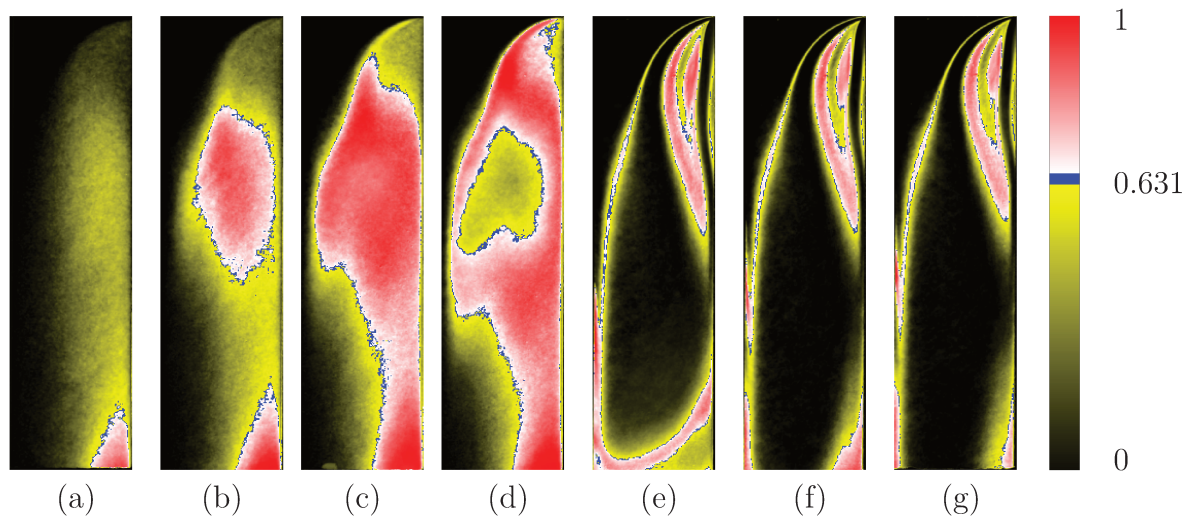


Figure 6.7: Entropy maps for the internal flow of G2 atomizer: a to g presents G2-2 to G2-8.

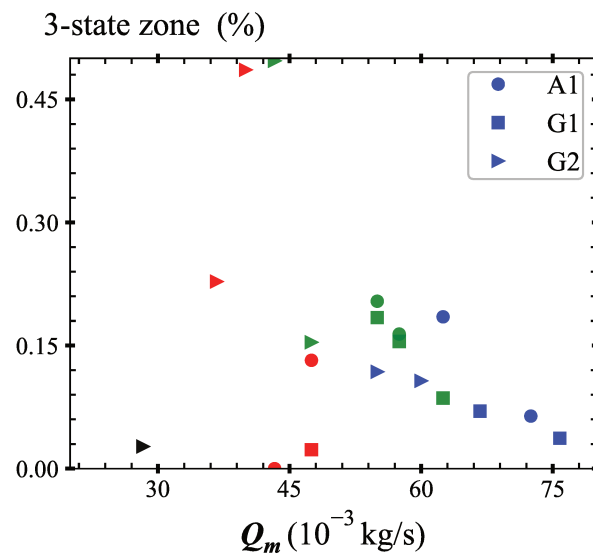


Figure 6.8: Normalized 3-state region area for internal flow of atomizers A1, G1 and G2.

Colors indicate the cavitation regime: black for regime I (*no cavitation*), red for II (*cavitation inception*), green for III (*super cavitation*) and blue for IV (*partial-hydraulic flip*).

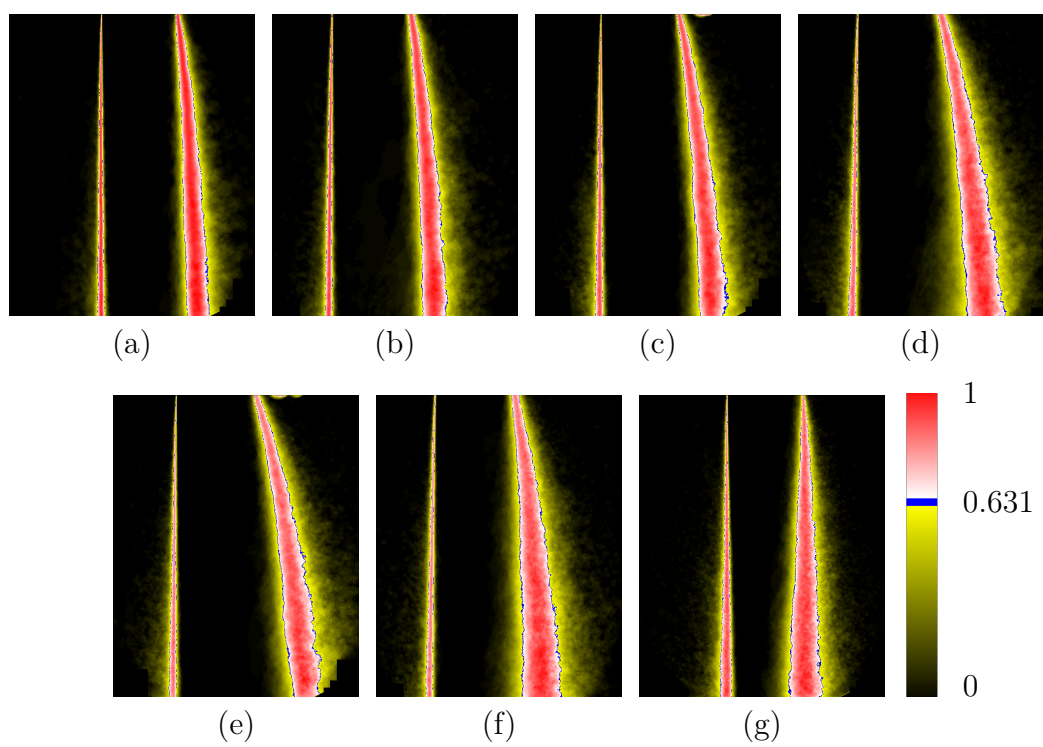


Figure 6.9: Entropy maps for the external flow of A1 atomizer: a to g presents A1-1 to A1-7.

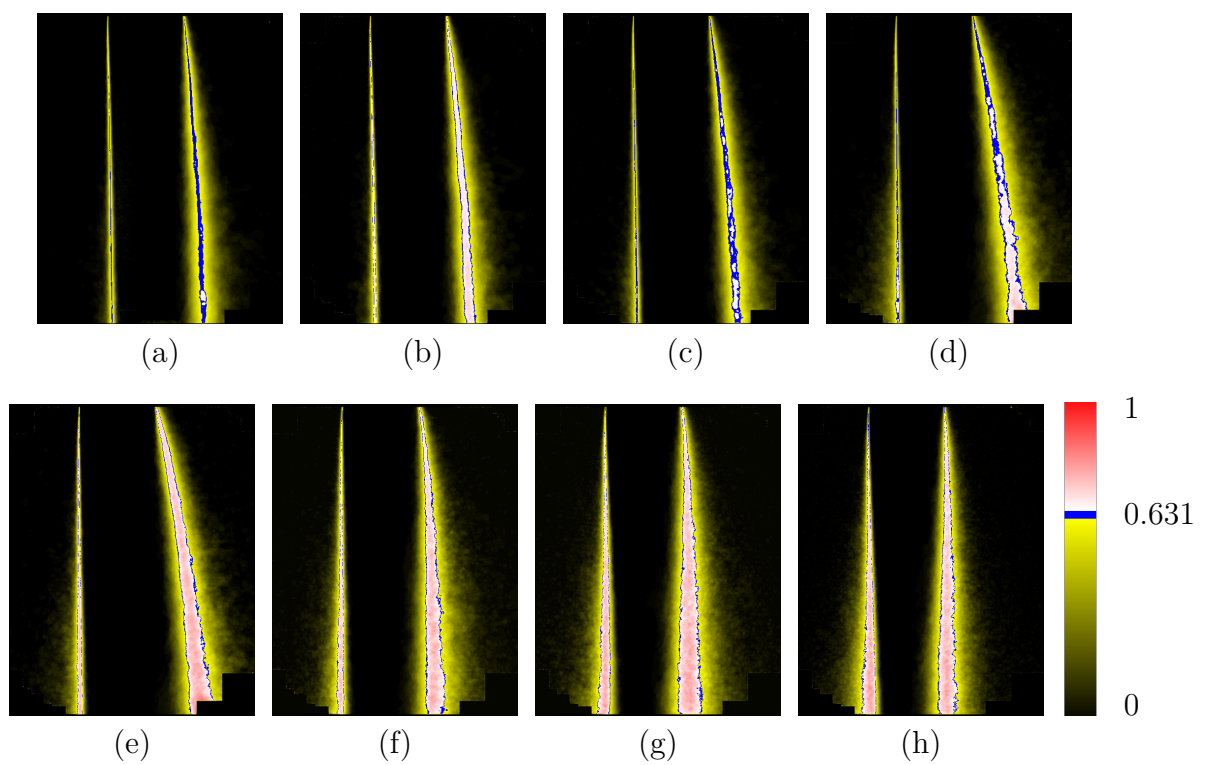


Figure 6.10: Entropy maps for the external flow of G1 atomizer: a to h presents G1-1 to G1-8.

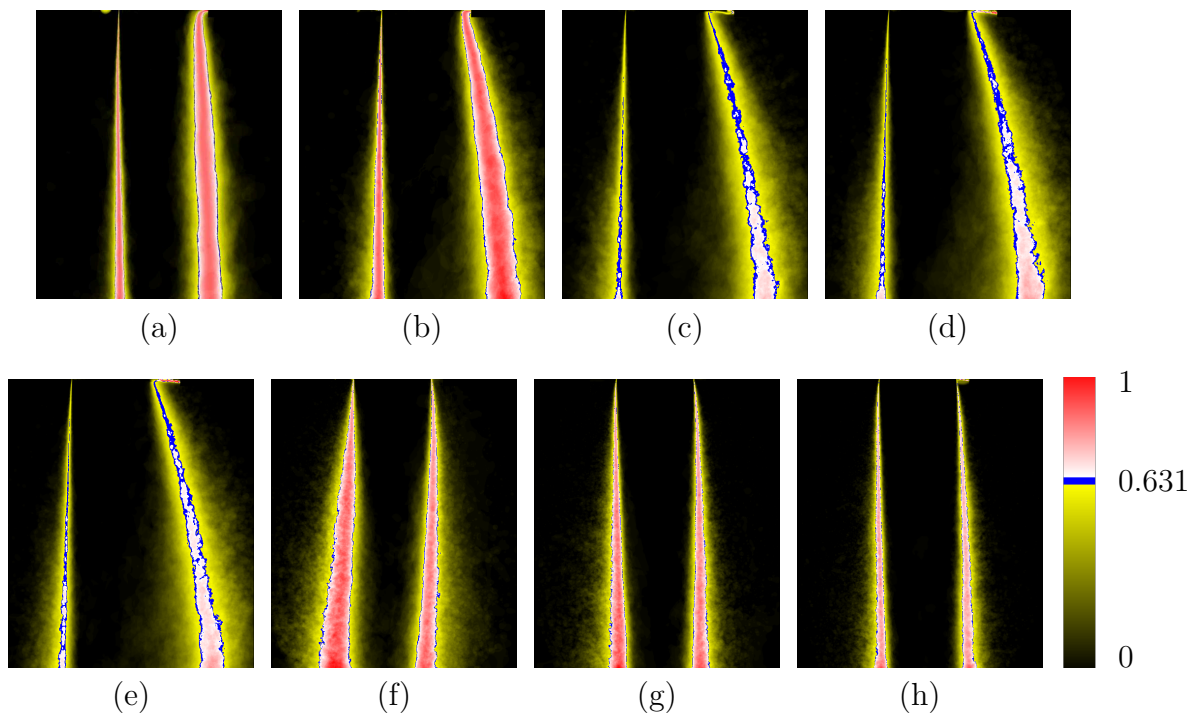


Figure 6.11: Entropy maps for the external flow of G2 atomizer: a to h presents G2-1 to G2-8.

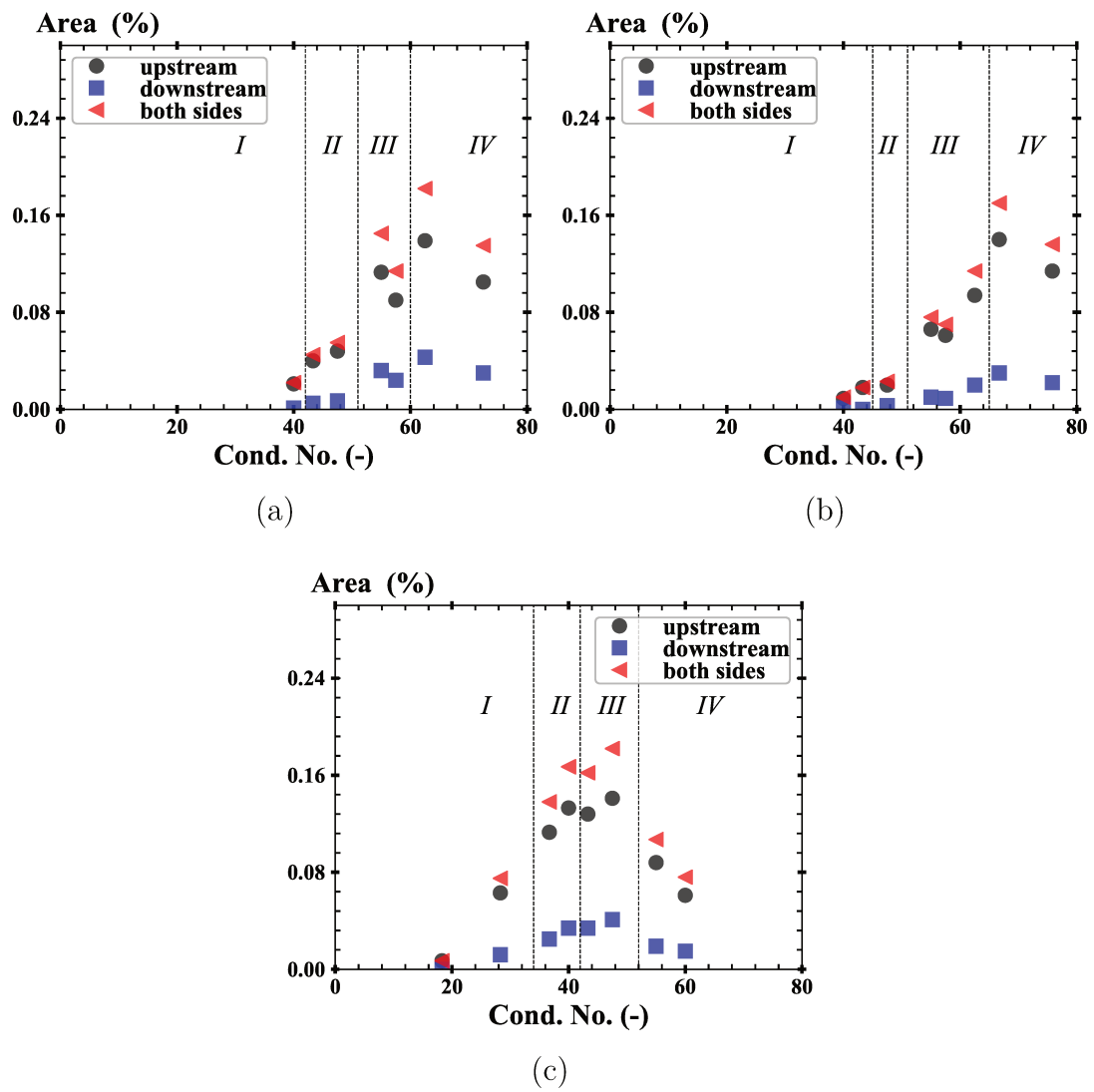


Figure 6.12: Primary atomization region normalized area for: a) A1, b) G1 and c) G2 atomizers.

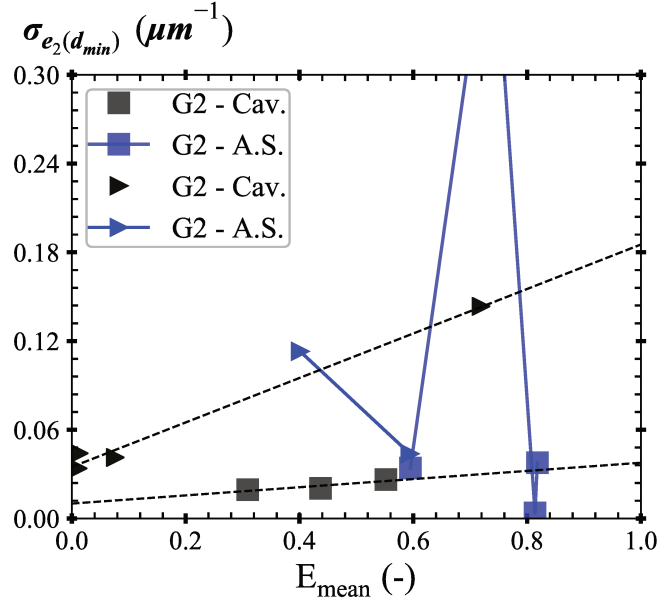


Figure 6.13: Standard deviation of the scale distribution at the smallest scale  $e_2(d_{min})$  as a function of the mean entropy at the nozzle exit for mainly cavitation-induced variability (Cav.) and mainly air sucking-induced variability (A.S).

wants to be studied by finding correlation between the mathematical characteristics of their respective distributions. The section is divided in two subsections. The first one presents the determination of the mathematical formulation for the spray drop diameter distribution and investigates the closeness of the distributions obtained for atomizers A1 and G2. The second one presents the determination of the mathematical formulation for the textural atomization process scale distribution. Two applications of this analysis will be presented: one to correlate the textural atomization process characteristics with those of the sprays (atomizer A1) and a second one to compare the textural atomization process scale distribution obtained with atomizers A1 and G2.

### 6.3.1 Spray Drop Diameter Distribution Analysis

The experimental surface-based drop diameter distribution  $f_2(D)$  of the droplets of the textural sprays have been measured by image analysis for atomizer A1 and atomizer G2. These distributions have been presented in the previous Chapter (see Fig. 5.23) and the first task consists in establishing a mathematical formulation for these distributions. The 3pGG distribution (Eq. (3.22)) is used for this purpose. As reported in Fig. 5.23, the experimental drop-diameter distributions show two peaks. Since the 3pGG distribution is a mono-modal function, a combination of two 3pGG distributions is required to fit the

experimental results. The following decomposition is adopted:

$$f_2(D) = \beta_f f_{2L}(D) + (1 - \beta_f) f_{2R}(D) \quad (6.2)$$

Seven parameters have to be determined: three for the left component  $f_{2L}(D)$  characterizing the distribution of the satellite drops, three for the right component  $f_{2R}(D)$  characterizing the distribution of the main drops, and the weighting parameter  $\beta_f$ . Two conditions are imposed in the parameter determination procedure. First, the two dispersion parameters  $\alpha$  and  $q$  that must have the same sign (Dumouchel, 2006) are both taken positive for every component. Thus, the parameter  $\alpha$  characterizes the dispersion in the lower-diameter range of the distribution, whereas the parameter  $q$  controls the dispersion in the upper-diameter range of the distribution. Second, for each component, the experimental peak diameter ( $D_{peakL}$  or  $D_{peakR}$ ) is imposed to the mathematical distribution. Using Eqs. (3.22, 3.30 and 3.31), it can be shown that each component writes:

$$f_{2*}(D) = \frac{q_*}{\Gamma\left(\frac{\alpha_*+2}{q_*}\right)} \left(\frac{\alpha+1}{q_*}\right)^{\frac{\alpha_*+2}{q_*}} \frac{D^{\alpha_*+1}}{D_{peak*}^{\alpha_*+2}} \exp\left(-\frac{\alpha_*+1}{q_*} \left(\frac{D}{D_{peak*}}\right)^q\right) \quad * = L \text{ or } R \quad (6.3)$$

The peak diameters  $D_{peakL}$  and  $D_{peakR}$  obtained for both atomizers and for all conditions are shown in Fig. 6.14 as a function of the cavitation number  $CN$ .

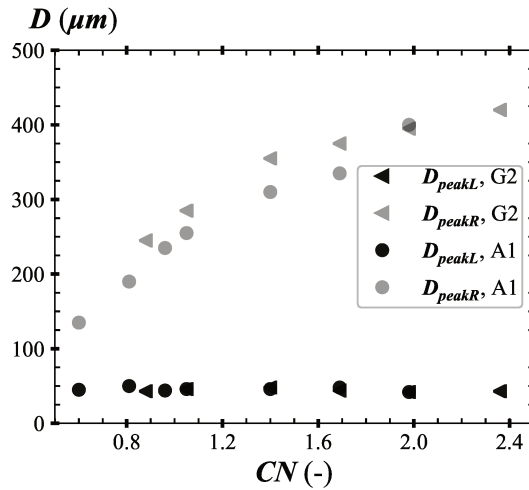


Figure 6.14: Correlation between the  $D_{peak}$  left and right for A1 and G2 atomizers as a function of  $CN$ .

As already noticed,  $D_{peakR}$  decreases as  $CN$  decreases while  $D_{peakL}$  remains rather the

same. We see also that both atomizers report very similar peak diameters. The use  $D_{peakL}$  and  $D_{peakR}$  reduces the number of parameters to be determined to 5:  $\alpha_L$  and  $q_L$  for the satellite peak,  $\alpha_R$  and  $q_R$  for the main drop peak, and the weighting parameter  $\beta_f$ . For every condition, the determination of the parameters that ensure the best fit of the measurements is performed with a Scilab routine written for this purpose. For each condition, the mathematical fit provides a very good representation of the measured drop-diameter distribution. An illustration of that is given in Fig. 6.15. The resulting parameters are listed in Table 6.1 and Table 6.2

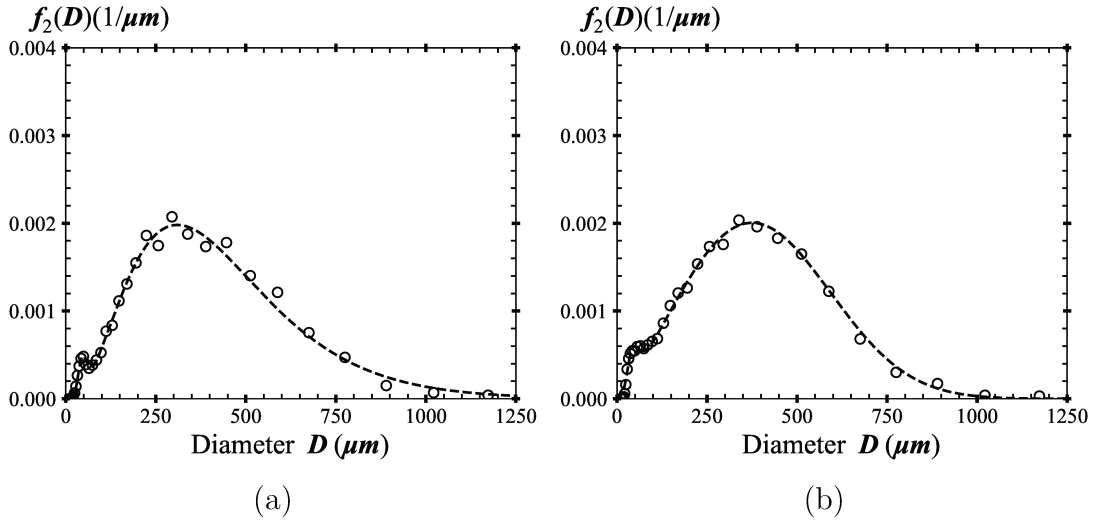


Figure 6.15: Example of the  $f_2(D)$  fit for: a)A1-3 and b)G2-5. Good fit was obtained for the other conditions.

Table 6.1: Peak diameters of the drop diameter distribution and parameters of the mathematical fit for A1 atomizer.

Cond. N <sup>o</sup>	$D_{peakL}$ ( $\mu\text{m}$ )	$D_{peakR}$ ( $\mu\text{m}$ )	$\alpha_L$ (-)	$q_L$ (-)	$\alpha_R$ (-)	$q_R$ (-)	$\beta_f$ (-)
1	42	400	8.93	1.50	0.69	1.54	0.0077
2	48	335	9.67	1.66	0.79	1.37	0.0063
3	46	310	9.39	1.40	1.86	0.92	0.011
4	46	255	9.49	1.23	2.21	0.84	0.017
5	44	235	10.4	1.00	3.36	0.61	0.020
6	50	190	11.2	0.94	11.8	0.21	0.035
7	45	135	14.8	1.14	14.8	0.13	0.024

The comparison of the distributions  $f_2(D)$  for A1 and G2 presented in Chap. 5 revealed that the only difference between them concerns the proportion of the satellite drop popula-

Table 6.2: Parameters of the mathematical fit of the drop diameter distribution  $f_2(D)$  for G2 atomizer.

Cond. N <sup>o</sup>	$D_{peakL}$ ( $\mu\text{m}$ )	$D_{peakR}$ ( $\mu\text{m}$ )	$\alpha_L$ (-)	$q_L$ (-)	$\alpha_R$ (-)	$q_R$ (-)	$\beta_f$ (-)
3	43	420	11.6	0.42	0.64	2.01	0.0179
4	42	395	11.5	0.64	0.28	2.37	0.0123
5	44	375	11.8	0.64	0.21	2.58	0.0136
6	48	355	14.2	0.32	0.08	2.05	0.0360
7	46	285	14.9	0.46	0.33	1.62	0.0248
8	43	245	15.5	0.67	0.47	1.47	0.0294

tion. The weighting parameter  $\beta_f$  is a quantification of this since it is equal to the surface proportion represented by  $f_L(D)$ , i.e., by the satellite droplets. Figure 6.16 compares the weighting parameters obtained for A1 and G2.

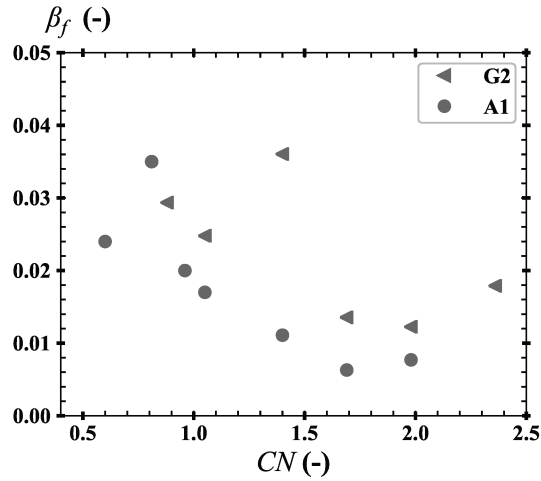


Figure 6.16:  $\beta_f$  as a function of  $CN$  for A1 and G2 atomizers.

This figure confirms that the surface of satellite drops represents a higher proportion of the surface of the whole spray for G2 than for A1. It seems that this distinction vanishes at high flow rates (low  $CN$ ). The parameters of each distribution component (Tables 6.1 and 6.2) allow quantifying the width of each peak by using the non-dimensional variance  $\Delta_2$  of the surface-based diameter distribution introduced by Sowa (1992) and defined as:

$$\Delta_2 = \left( \frac{D_{42}^2 - D_{32}^2}{D_{32}^2} \right) \quad (6.4)$$

In virtue of Eq. (3.30),  $\Delta_2$  can be expressed as a function of the parameters  $\alpha$  and  $q$ . It comes:

$$\Delta_2 = \frac{\Gamma\left(\frac{\alpha_R+4}{q_R}\right)\Gamma\left(\frac{\alpha_R+2}{q_R}\right)}{\Gamma^2\left(\frac{\alpha_R+3}{q_R}\right)} - 1 \quad (6.5)$$

The parameter  $\Delta_2$  is determined for each component ( $\Delta_{2L}$  and  $\Delta_{2R}$ ) and plotted in Fig. 6.17 as a function of the cavitation number.

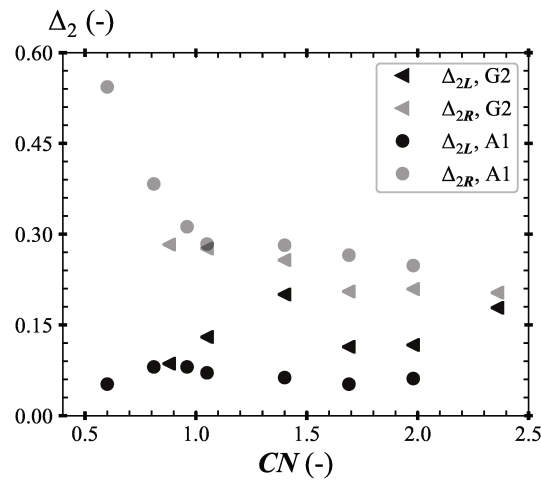


Figure 6.17:  $\Delta_2$  as a function of  $CN$  for A1 and G2 atomizers.

When  $CN$  decreases,  $\Delta_{2R}$  increases continuously. This effect is due to the persistence of a rather extended distribution tail when the flow rate increases. We note that the sprays produced by the two atomizers report the same  $\Delta_{2R}$ . The variation of  $\Delta_{2L}$  with the cavitation number is less obvious. However, it appears that the satellite drop distribution is wider for atomizer G2 sprays than for atomizer A1 sprays. Again, this behavior seems to vanish when the flow rate increases. The origin of the difference in width between A1 and G2 satellite drop population can be approached by considering the parameters of this peak. Figure 6.18 presents the parameters  $\alpha_L$  and  $q_L$  as a function of the cavitation number for the two atomizers.

Globally, the parameters shown in Fig. 6.18 do not vary much with the cavitation number. (An increase seems to take place when  $CN$  decreases below 1.) However, the differences between the results obtained for the two atomizers reveal that the composition of the satellite population is different. The parameter  $\alpha_L$  is higher for G2 than for A1: the satellite sizes disperse less in the lower diameter range for G2 than for A1. At the opposite, the parameter  $q_L$  is less for G2 than for A1: the satellite sizes disperse more in

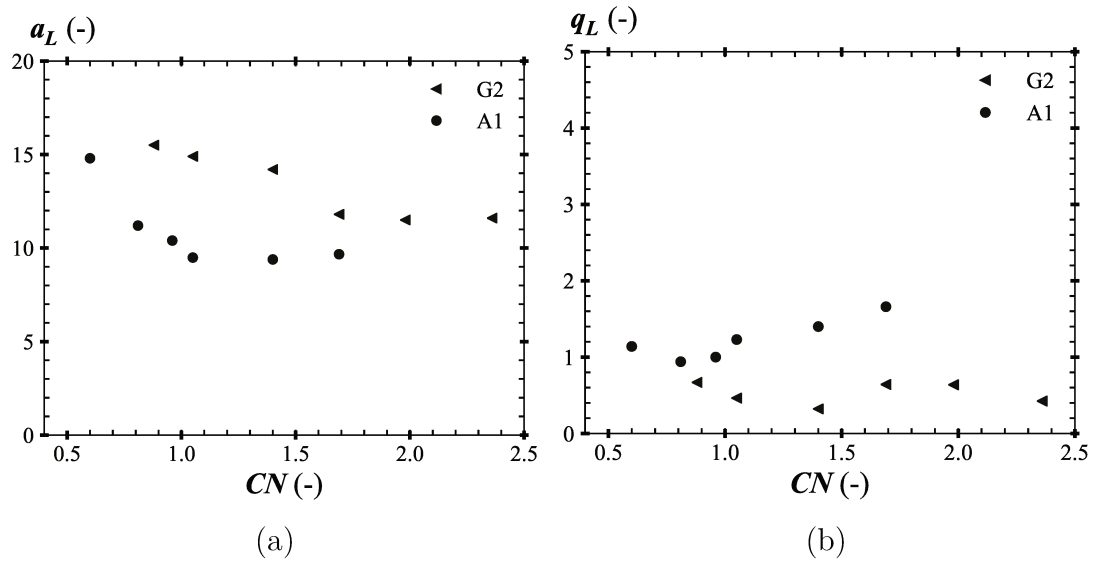


Figure 6.18: a)  $\alpha_L$  and b)  $q_L$  as a function of  $CN$ .

the upper diameter range for G2 that for A1. Therefore, although the satellite populations for A1 and G2 have the same peak diameter, the distribution around this peak is slightly different for the two atomizers: G2 satellite sprays disperse more in the upper-size range and less in the lower-size range.

In conclusion, this section shows that the 3pGG function is very appropriate to mathematically represent the drop diameter distribution of the textural sprays. It was confirmed that both atomizers A1 and G2 produce very similar textural sprays in terms of size distribution for a given flow rate. The only difference is rather weak: it says that G2 satellite sprays are more dispersed in size, represent a higher surface proportion of the whole spray, and are differently distributed around the peak diameter. It has to be kept in mind that these atomizers work at different pressure level. Therefore, if the injection pressure is fixed, atomizer G2 will produce larger droplets than atomizer A1 since the pressure drop is higher in G2.

### 6.3.2 Textural Atomization Analysis

*Mathematical scale-distribution:*

The first step of the analysis is to isolate the scale distribution of the textural atomizing structures from the measurements presented in Figs. 5.20 to 5.22. This is achieved with the help of the mathematical formulation established for the scale distribution in Chap. 3

and given by Eq. (3.55), i.e.:

$$e_2(d) = \frac{1}{D_{q0}} \left( \frac{\alpha}{q} \right)^{\frac{1}{q}} \frac{\Gamma \left[ \frac{\alpha}{q}, \frac{\alpha}{q} \left( \frac{d}{D_{q0}} \right)^q \right]}{\Gamma \left( \frac{\alpha+1}{q} \right)} \quad (6.6)$$

This expression corresponds to the scale distribution of an ensemble of cylinders whose diameters are distributed according to a 3pGG function with the three parameters  $\alpha$ ,  $q$  and  $D_{q0}$ . It has been demonstrated in Chap. 3 that, in 2D, any system has an equivalent system of cylinders, which is a cylinder set that has the same scale distribution as the actual system. Referring to Chap. 3, the number-based diameter distribution  $f_{0c}(D)$  of the equivalent system of cylinders can be deduced from the measured scale distribution  $e_2(d)$  by Eq. (3.57), i.e.;

$$f_{0c}(D) = -D_{10} \left[ \frac{de_2(d)}{dd} \right]_{d=D} \quad (6.7)$$

Thus, Eq. (6.7) is first applied to determine  $f_{0c}(D)$ , and second, the distribution  $f_{0c}(D)$  will be fitted by a 3pGG function. As explained in Chap. 3, Eq. (6.6) suits scale distributions with one single inflexion point whereas those measured in this work report two inflexion points (Figs. 5.20 to 5.22). To reproduce this characteristic, the scale distribution is decomposed as the sum of two components:

$$e_2(d) = \beta_e e_{2,1}(d) + (1 - \beta_e) e_{2,2}(d) \quad (6.8)$$

In this equation,  $e_{2,1}(d)$  and  $e_{2,2}(d)$  are two scale distributions represented by Eq. (6.6): they both depend on three parameters and they are both normalized. Since the experimental scale distribution is normalized also, the weighting parameter  $\beta_e$  ranges from 0 to 1. (This parameter actually represents the relative surface area of the ligament structures of the textural atomization process.) The application of Eq. (6.8) to fit the measured scale distributions requires the determination of seven parameters:  $(\alpha_i, q_i, D_{q0i})$  for each component and  $\beta_e$ . The fitting process is performed on the first derivative  $e'_2(d)$  of the scale distributions. The calculation of these derivatives is completed by the condition  $e'_2(0) = 0$  imposed for each case. The scale distribution derivatives report two modes, each of them being associated with a derivative  $e'_{2,i}(d)$ :  $e'_{2,1}(d)$  for the small scale mode, and  $e'_{2,2}(d)$  for the large scale mode. Each mode is fitted with the derivative of Eq. (6.6) and the last parameter  $\beta_e$  is obtained from the surface area of each mode.

A Scilab routine was written to determine the set of parameters that provides the best fit of the measured scale distribution. The routine was applied for each condition, the solution for one condition being used as initial point to find the solution of the next condition. The distribution component  $e_{2,1}(d)$  resulting from this process is the scale distribution of the textural atomization process. It expresses as Eq. (6.6) and can be calculated thanks to the values of the parameter triplet  $(\alpha_1, q_1, D_{q01})$ .

*Application I: the atomizer A1:*

This procedure is first applied on the results provided by atomizer A1. The scale distributions obtained for this atomizer are shown in Fig. 5.20. The derivatives of the scale distribution show two bell-shape peaks: one in the small scale range and one in the large scale range. According to Eq. (6.7), these peaks represent the number-based diameter distributions of cylinder equivalent system of each peak. They are separated at a specific scale  $d_{sep}$ . In this first application,  $d_{sep}$  is identified as the scale in the range  $]0; d_{max}/2]$  for which  $e'_2(d)$  is minimum.

As said above, the condition  $e'_2(0) = 0$  is imposed in the fitting process. For cases A1-1 to 5, this condition reasonably agrees with the measurements but could not be verified for A1-6 and A1-7 because of a lack of spatial resolution (limited to  $37 \mu\text{m}$ ) in the scale analysis. Although the Scilab succeeded in getting results in most situations, the determination of the parameters  $\alpha_1$  and  $q_1$  was proved difficult for A1-6 and A1-7 for which a specific determination protocol has been followed. First, the parameter  $q_1$  was evaluated from the correlation between the mass flow rate  $Q_m$  and the parameter  $q_1$  obtained for A1-2 to A1-5 (Regime I condition is not considered here). Second, the parameter  $\alpha_1$  is determined as the best fit provider conditioned by the constraint  $e'_2(0) = 0$ . For all conditions, this analysis returned very good fits of the experimental scale distributions. An illustration of this fit is shown in Fig. 6.19.

The parameter triplets  $(\alpha_1, q_1, D_{q01})$  are listed in Table 6.3 and used with Eq. (6.6) to calculate the scale-distributions of the textural atomization processes. These distributions are plotted in Fig. 6.20 for all A1 working conditions.

The scale distributions in Fig. 6.20 spread to scales of the order of  $1500 \mu\text{m}$  with a rather extended tail in the large-scale range. When the flow rate increases (from A1-1 to A1-7), the scale distribution squeezes in the small scale range and its width decreases, but the distribution tails remain extended in the large scale range. These two behaviors combine in an increase of  $e_{2,1}(0)$  when  $CN$  decreases and indicate that the ligament size-distribution shifts towards the small-size region, inducing an increase of the interface length per unit surface area. The three parameters of the distributions  $e_{2,1}(d)$  correlate with the cavitation number  $CN$  (see Fig. 6.21) expressing the dependence between the flow regime and the textural atomization process. We first note that the values of  $D_{q01}$  are rather high

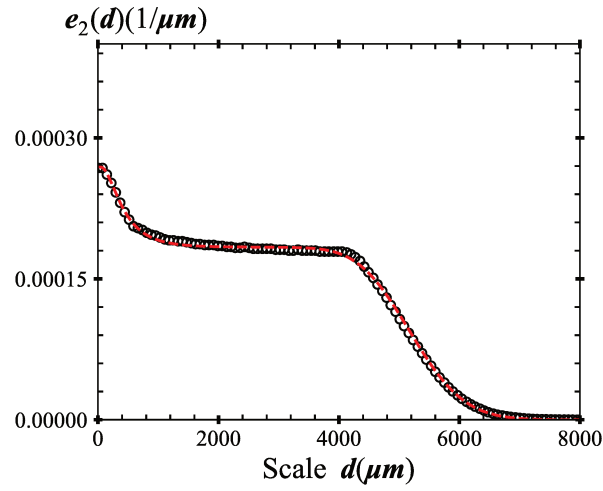


Figure 6.19: Example of the mathematical fit of the scale distribution: circle is the experimental data and the dashed line is the mathematical fit. Good agreement is obtained also for the other conditions.

Table 6.3: Parameters of the mathematical fit of the scale distributions for A1 atomizer.

Cond. N <sup>o</sup>	$\alpha_1$ (-)	$q_1$ (-)	$D_{q01}$ ( $\mu\text{m}$ )	$d_p$ ( $\mu\text{m}$ )	$-e'_{2,1}(d_p)$ ( $10^{-6}\mu\text{m}^{-2}$ )	$d_{p2}$ ( $\mu\text{m}$ )	$-e''_2(d_{p2})$ ( $10^{-8}\mu\text{m}^{-3}$ )
1	3.69	0.53	550	304	4.39	70	1.35
2	7.54	0.24	453	250	6.32	72	2.22
3	10.00	0.21	418	253	6.98	86	2.68
4	10.09	0.20	348	205	10.2	67	4.68
5	11.71	0.19	329	204	11.1	72	5.45
6	12.20	0.17	295	179	13.9	63	7.57
7	14.93	0.15	236	150	21.3	57	14.7

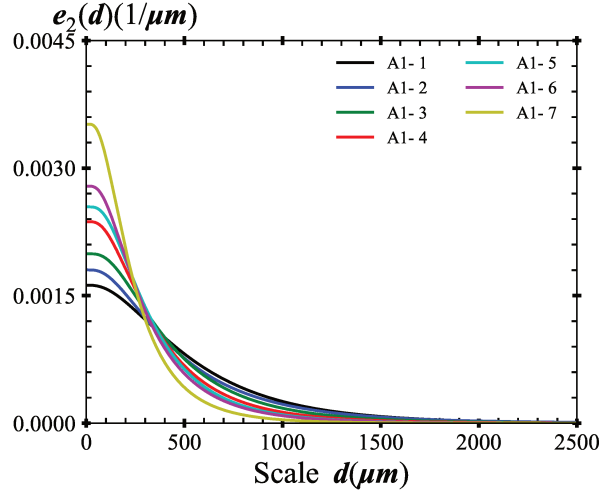


Figure 6.20: Textural atomization process for A1 atomizer.

considering the low order of this mean diameter (order being equal to the value of  $q_1$ ). This, of course, is a consequence of the long tail in the large scale region noticed in Fig. 6.20. Therefore, being sensitive to the scale distribution tail,  $D_{q_01}$  appears to be representative of the ligament size distribution, and its decrease with the cavitation number  $CN$  illustrates the production of finer and finer ligaments as the flow rate increases.

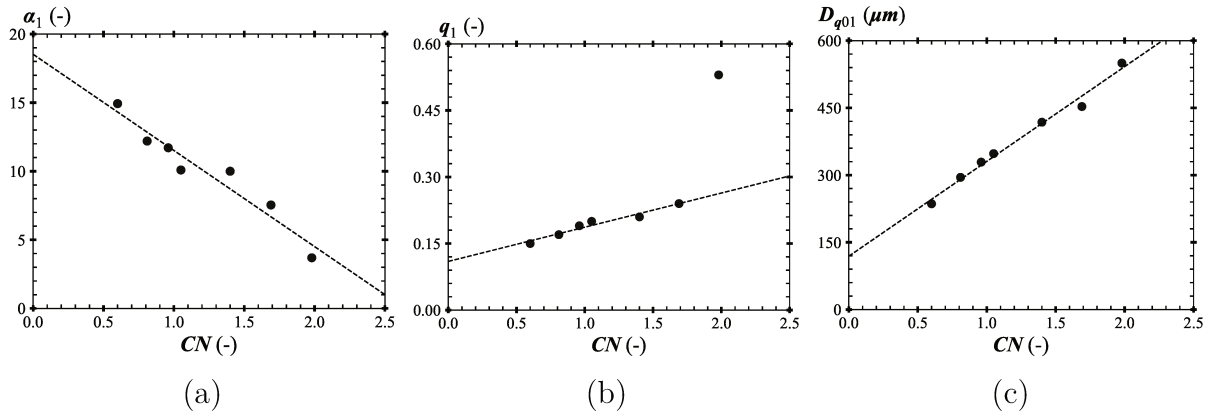


Figure 6.21: a)  $\alpha_1$ , b)  $q_1$  and c)  $D_{q_01}$  as a function of  $CN$ .

Second, Fig. 6.21 shows that the dispersion parameters  $\alpha_1$  and  $q_1$  show opposite variations. As explained in Chapter 3, the parameter  $q_1$  is sensitive to the ligament size-distribution and the parameter  $\alpha_1$  to the distribution of scales associated with their deformation. The variations reported in Fig. 6.21 explain that, as  $CN$  decreases, the dispersion of the ligament size-distribution increases ( $q_1$  decreases) whereas the dispersion of their deformation scales decreases ( $\alpha_1$  increases). This last behavior is associated with the de-

crease of the mean diameter  $D_{q01}$  illustrated in Fig. 6.21: the deformation-scale range shrinks because the ligaments are thinner.

The scale distributions of the textural atomization process (Fig. 6.20) all show one inflexion point, i.e., for one specific scale, called  $d_p$ ;  $e_2''(d_p) = 0$ . According to Eq. (6.7), we see that the scale  $d_p$  is also the modal diameter  $D_{p0}$  of the number-based diameter distribution of the cylinder equivalent-system. Therefore, in virtue of Eq. (3.21), it comes:

$$d_p = D_{q-1,-1} \quad (6.9)$$

The values of the scale  $d_p$  are given in Table 6.3 for all conditions. This scale is of the order of the half of  $D_{q01}$  and reports a similar correlation with the cavitation number as this mean diameter. This specific scale is therefore representative of the size distribution of the ligaments involved in the textural atomization process. Another characteristic of the inflexion point is the derivative of the scale distribution at this scale,  $e_{2,1}'(d_p)$  which is given by the following expression:

$$-e_{2,1}'(d_p) = \alpha_1 \left( \frac{\alpha_1}{q_1} \right)^{\frac{1}{q_1}} \left( \frac{\alpha_1 - 1}{q_1} \right)^{\frac{(\alpha_1 - 1)}{q_1}} \frac{\exp\left(\frac{1 - \alpha_1}{q_1}\right)}{D_{q01}^2} \quad (6.10)$$

Considering Eq. (6.7),  $-e_{2,1}'(d_p)$  is proportional to the peak height of the cylinder equivalent-system number-based diameter distribution and, therefore, informs on the stiffness of this peak. The values are given in Table 6.3. They were found to correlate with the cavitation number as  $-e_{2,1}'(d_p) \propto CN^{-1.35}$ . This correlation indicates that, although the size distribution of the ligaments remains very much extended in the large scale region, the peak width of this distribution narrows on the diameter  $d_p$  when  $CN$  decreases. It appears therefore that the three parameters ( $q_1$ ,  $d_p$ ,  $-e_{2,1}'(d_p)$ ) provide relevant properties of the ligament size-distribution including, its position in the size space ( $d_p$ ), the dispersion around this peak ( $-e_{2,1}'(d_p)$ ) and the dispersion in the upper size domain ( $q_1$ ).

The parameters produced by the mathematical fit procedures applied on the textural atomization scale distributions and on the spray drop-diameter distributions are characteristics of the same system in two different states. They should therefore correlate. At this stage, it is pertinent to remark that the scale distribution  $e_{2,1}(d)$  and the diameter distribution  $f_2(D)$  spread in the same scale interval. As shown above, the droplet diameter distributions show two peaks. The correlation is established on the idea that the main-drop population (right peak of the distribution) is associated with the size distribution of the textural atomization ligaments, whereas the satellite population (left peak of the distribution) is associated with the deformation of these ligaments.

As far as the main drop population is concerned, the correlations obtained between the parameters  $(q_1, d_p, -e'_{2,1}(d_p))$  and the parameters  $(\alpha_R, q_R, D_{peakR})$  validate this approach (Figs. 6.22, 6.23 and 6.24).

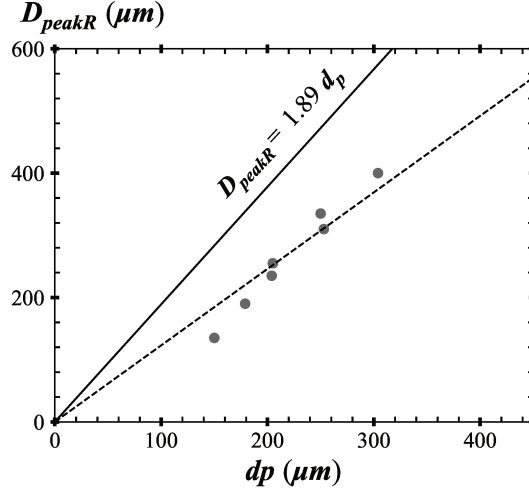


Figure 6.22:  $D_{peakR}$  VS  $d_p$ .

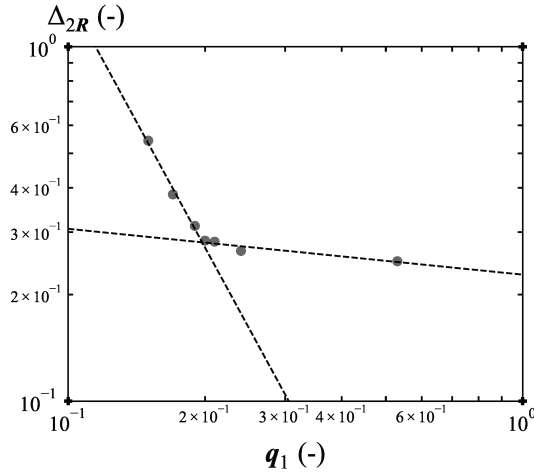


Figure 6.23:  $\Delta_{2R}$  VS  $q_1$ .

First, Figure 6.22 shows that  $d_p$  and  $D_{peakR}$  are of the same order of magnitude:

$$D_{peak,R} \approx 1.23d_p \quad (6.11)$$

This result confirms that  $d_p$  is a characteristic size of the ligaments. The coefficient 1.23 is less than the theoretical coefficient 1.89 reported by Rayleigh (1878) for the breakup of

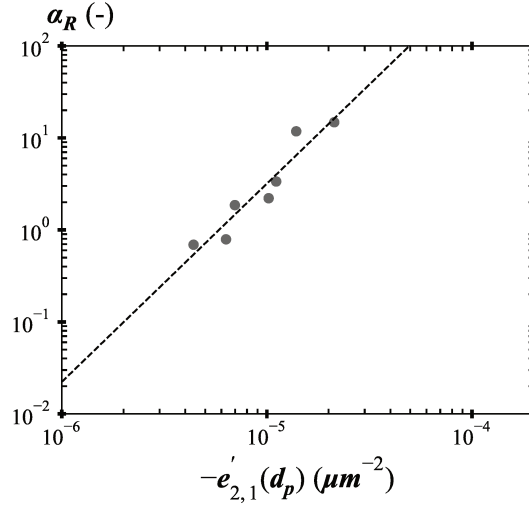


Figure 6.24:  $\alpha_R$  VS  $-e'_{2,1}(d_p)$ .

a cylindrical smooth ligament due to capillary instability, probably because, being initially deformed, the ligaments are prompt to produce smaller drops as well as satellite droplets, the last point being attested by the measured drop diameter distributions. These considerations and results evidence the major contribution of the surface tension effects, and, therefore, the negligible influence of the aerodynamic forces in the ligament breakup. Second, Fig. 6.23 reports a strong correlation between the dispersion parameter  $q_1$  and the relative width of the main droplets diameter-distribution  $\Delta_{2R}$ . As expected, an increase in the dispersion ligament size-distribution ( $q_1$  decreases) induces an increase of the relative width of the main-drop diameter-distribution. Two tendencies, represented by the dash lines in Fig. 6.23, appear: as  $q_1$  decreases, the first tendency corresponds to the flow Regimes I and II and the second one corresponds to the flow regimes III and IV. This observation could constitute a proof of a direct influence of the cavitation on textural atomization processes. Finally, Fig. 6.24 displays the correlation between the parameters  $\alpha_R$  and  $-e'_{2,1}(d_p)$ . The positive derivative of this correlation says that the main-drop population disperses less in the small diameter range when the peak of the ligament size-distribution gets narrower.

The second peak of the drop-size distribution (left peak in Fig. 5.23) represents the satellite population. The number and size of these droplets depend on the deformation of the ligaments and should therefore correlate with the dispersion parameter  $\alpha_1$  of the atomization process scale distribution. It has to be mentioned here that the measurement of the left peak is less accurate than the one of the right peak. However, two interesting observations deserve to be presented. First, taking inspiration from the previous analysis, we suggest introducing the first inflexion point of the function  $-e'_{2,1}(d)$  (by first we mean the one obtained for the smallest scale). The scale at which this inflexion point is found is called  $d_{p2}$ :  $-e'''_{2,1}(d_{p2}) = 0$ . By using Eq.(6.6) it can be shown that:

$$e''_2(d) = -\frac{q}{\Gamma\left(\frac{\alpha+1}{q}\right)} \left(\frac{\alpha}{q}\right)^{\left(\frac{\alpha+1}{q}\right)} \left[ \alpha \left(1 - \left(\frac{D}{D_{q0}}\right)^q\right) \right] \frac{D^{\alpha-2}}{D_{q0}^{\alpha+1}} \exp\left(-\frac{\alpha}{q} \left(\frac{D}{D_{q0}}\right)^q\right) \quad (6.12)$$

$$d_{p2} = \left( \frac{q + 2\alpha - 3 - \sqrt{q^2 + 2(2\alpha - 3)q + 1}}{2\alpha} \right)^{(1/q)} D_{q0} \quad (6.13)$$

These characteristics are calculated for all conditions and listed in Table 6.3. It appears that  $d_{p2}$  is almost constant such as the second diameter peak  $D_{peakL}$  (see Tables 6.1 and 6.3). Furthermore,  $-e''_{2,1}(d_{p2})$  correlates with the cavitation number  $CN$  in a similar way as  $-e'_{2,1}(d_p)$ :  $-e''_{2,1}(d_{p2}) \propto CN^{-1.93}$ . It correlates also with the parameter  $\alpha_L$  again in a similar way as  $-e'_{2,1}(d_p)$  with  $\alpha_R$  (Fig. 6.24). (The parameter  $\alpha_L$  characterizes the dispersion in the small-diameter range of the satellite droplets.) We understand that the successive inflexion points of the scale distribution and its derivatives identify representative scales as far as the drop diameter distribution is concerned.

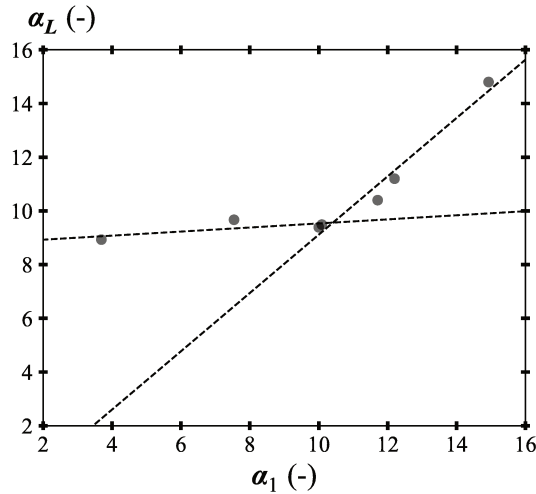


Figure 6.25:  $\alpha_L$  VS  $\alpha_1$  for A1 atomizer.

The second observation concerns the correlation between  $\alpha_1$  and  $\alpha_L$  (Fig. 6.25) which globally indicates that the dispersion in the small-diameter range of the satellite population increases with the one in the small-scale range of the ligament deformation. Two parts are identifiable in the figure:  $\alpha_1$  and  $\alpha_L$  are of the same order of magnitude when  $\alpha_1 > 10$ , otherwise, the dispersion  $\alpha_L$  varies far less than  $\alpha_1$ .

The cases  $\alpha_1 > 10$  correspond to the high flow rates for which the textural atomizing

ligaments are thin. This thinness imposes structural deformation and atomization only: the satellite droplet sizes disperse in the diameter space in the same way as the small-deformation scales disperse in the scale space. This manifests by  $\alpha_1 \approx \alpha_L$ . The cases  $\alpha_1 < 10$  correspond to the low flow rates for which the textural atomizing ligaments are coarser and their deformation (characterized by  $\alpha_1$ ) is mainly textural and is less involved in the production of drops. Thus, the parameter  $\alpha_L$  becomes less dependent on  $\alpha_1$ . This behavior reveals that, if the deformation scale is far less than the size of the ligament, it will not participate to the atomization process. This also explains that the amount of satellite droplets is less for these cases.

The result presented in Fig. 6.25 therefore indicates that, as far as the drop production is concerned, the knowledge of the system deformation over the whole scale range is not always necessary, and precisely in the case where the ligament deformation scales are far smaller than the ligament size. It occurs that the scale  $d_{p2}$  is a characteristic of the ligament deformation and the scale  $d_p$  is a characteristic of the ligament size. Therefore, the ratio  $d_{p2}/d_p$  should be appropriate to delimit the two behaviors found in Fig. 6.25. Figure 6.26 plots this ratio versus the ratio  $\alpha_1/\alpha_L$ . When  $d_{p2}/d_p > 0.32$  (A1-3 to A1-7) the satellite population depends on the ligaments deformation ( $\alpha_1/\alpha_L \approx 1$ ). When  $d_{p2}/d_p < 0.32$  (A1-1 and A1-2), the satellite population is far less dependent on the ligament deformation. This result is another demonstration of the importance of the scales  $d_p$  and  $d_{p2}$ .

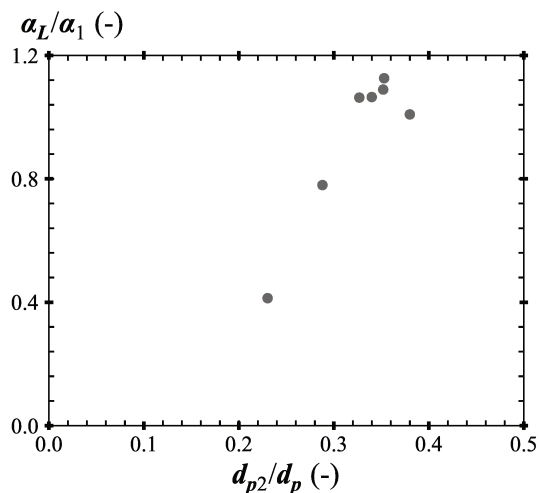


Figure 6.26:  $\alpha_1/\alpha_L$  VS  $d_{p2}/d_p$  for A1 atomizer.

*Application II: Atomizers A1 and G2:*

The second application involves the atomizers A1 and G2. The scale distributions measured for A1 and G2 are given in Figs. 5.20 and 5.22, respectively. The objective is to compare the textural atomization processes of these two atomizers that produced sprays

with very similar drop-diameter distributions. We recall here that the only difference between these textural spray drop-size distributions is weak and concerns the satellite drop population: G2 satellite sprays are more dispersed in size, represent a higher surface proportion of the whole spray, and are differently distributed around the peak diameter than the A1 satellite sprays. It is therefore decided to focus the analysis on the small scale region. To achieve this, the separation scale  $d_{sep}$  at which the separation of the two peaks of  $-e'_2(d)$  is performed, is now determined in the interval  $]0; 900\mu m]$  instead of  $]0; d_{max}/2]$  as in the previous application. This modification returns smaller scales  $d_{sep}$  for all cases: the large scales of the textural atomization process are omitted. This difference eases the determination of the parameters  $(\alpha_1; q_1; D_{q01})$ . This last point has been another motivation to introduce this modification. Indeed, a distribution tail showing a long extension in the upper scale region constitutes a difficulty in the determination of the parameter  $q_1$ . (The difficulty in obtaining this parameter for A1-6 and A1-7 in application I was because of that.) The reduction of the scale  $d_{sep}$  minimizes this difficulty. In consequence, the determination of the fitting parameters was easier in the second application. However, it must be kept in mind that the scale distribution  $e_{2,1}(d)$  determined in this second application provide a description of a part of the textural atomization process only.

The analysis is performed for conditions A1-1 to A1-7 and for conditions G2-2 to G2-8. For each condition, the mathematical fit was good. Tables 6.4 and 6.5 list the parameters for the scale distributions  $e_{2,1}(d)$  and Fig. 6.27 shows these distributions.

Table 6.4: Parameters of the mathematical fit of the textural atomization process for A1 atomizer - application II.

Cond. N <sup>o</sup>	$\alpha_1$ (-)	$q_1$ (-)	$D_{q01}$ ( $\mu m$ )	$d_p$ ( $\mu m$ )	$-e'_{2,1}(d_p)$ ( $10^{-6}\mu m^{-2}$ )	$d_{p2}$ ( $\mu m$ )	$-e''_2(d_{p2})$ ( $10^{-8}\mu m^{-3}$ )
1	1.54	9.12	490	437	5.10	-	-
2	1.81	2.21	441	307	6.26	-	-
3	2.18	1.93	417	303	6.95	67	2.82
4	2.95	0.96	341	222	10.6	61	5.32
5	3.61	0.83	321	218	11.7	73	6.19
6	6.43	0.38	270	173	16.5	61	10.1
7	15.5	0.18	217	151	24.5	64	19.2

These figures show scale distributions with maximum scales no greater than  $900 \mu m$ . The scale distributions and their evolution appear similar to what was reported in Fig. 6.20 which makes us think that they cover a large part of the textural atomization process. To compare the results between the two atomizers, Figs. 6.28a 6.28b and 6.28c plot their parameters  $q_1$ ,  $\alpha_1$  and  $D_{q01}$ , respectively, as a function of the cavitation number  $CN$ . The conclusions of the first analysis are convoked to interpret the results. Figure 6.28a reports similar values and a similar behavior for the parameter  $q_1$ . For all cases,  $q_1$  are less for G2

Table 6.5: Parameters of the mathematical fit of the textural atomization process for G2 atomizer - application II.

Cond. N <sup>o</sup>	$\alpha_1$ (-)	$q_1$ (-)	$D_{q01}$ ( $\mu\text{m}$ )	$d_p$ ( $\mu\text{m}$ )	$-e'_{2,1}(d_p)$ ( $10^{-6}\mu\text{m}^{-2}$ )	$d_{p2}$ ( $\mu\text{m}$ )	$-e''_2(d_{p2})$ ( $10^{-8}\mu\text{m}^{-3}$ )
2	1.4	3.31	550	385	3.57	-	-
3	2.3	1.40	401	267	5.40	53	3.34
4	2.6	1.17	379	249	5.79	62	3.88
5	2.3	1.33	390	256	5.62	47	3.69
6	5.0	0.54	309	204	7.61	72	6.85
7	8.3	0.34	245	169	12.0	68	13.6
8	15.5	0.18	230	158	13.1	67	16.2

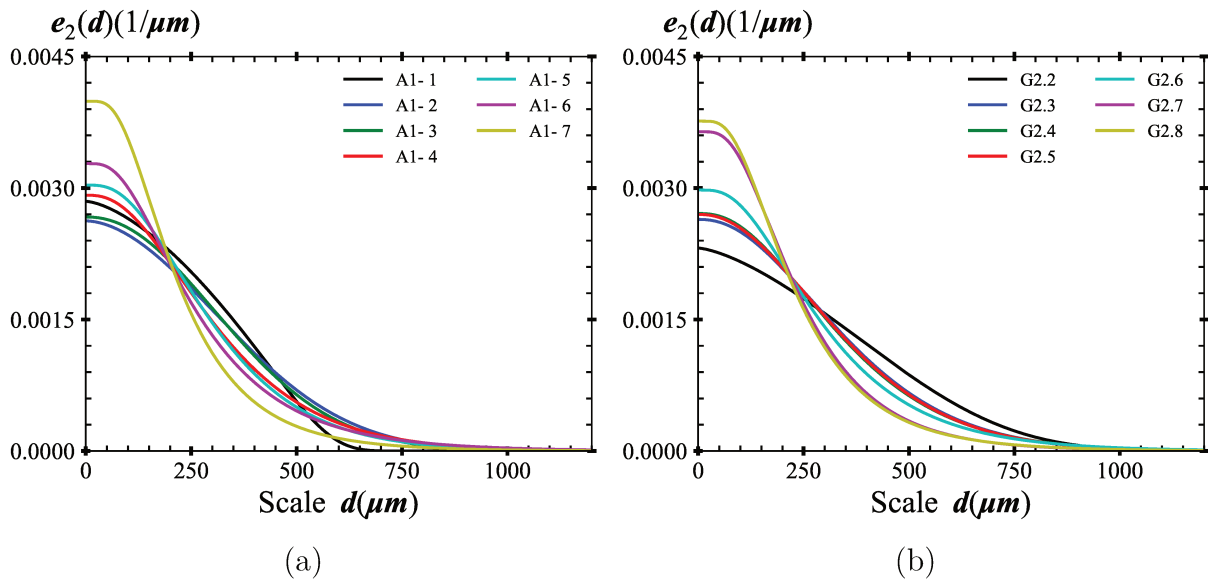


Figure 6.27: Textural atomization process extracted using following method II for: a) A1 and b) G2 atomizers.

than for A1. The parameter  $q_1$  is an indicator of the dispersion in the upper scale: even if the whole textural atomization process is not covered in the present application, this parameter is indicative of the dispersion in the upper-scale range of the textural ligament size. Another information on the textural ligament size distribution is given by the mean diameter  $D_{q01}$ . Fig. 6.28c shows that  $D_{q01}$  evolves with the cavitation number  $CN$  in a similar way for both atomizers. We however note that the ligament mean size is smaller for atomizer G2 than for atomizer A1, but that the ligament size distribution disperses more in the upper-size range for G2 than for A1. These results say that atomizer G2 produced slightly thinner ligaments than atomizer A1, but with greater dispersion in the upper-size range. These two behaviors conjugate to produce very similar main-drop population. The third parameter ( $\alpha_1$ , Fig. 6.28b) again reports similar value and variation with the parameter  $CN$ . For a given  $CN$ , we see that  $\alpha_1$  is always greater for G2: the ligament deformation scales disperse less in the lower-scale range for G2 than for A1. This suggests that the textural ligaments produced by atomizer G2 may be less deformed than those produced by atomizer A1.

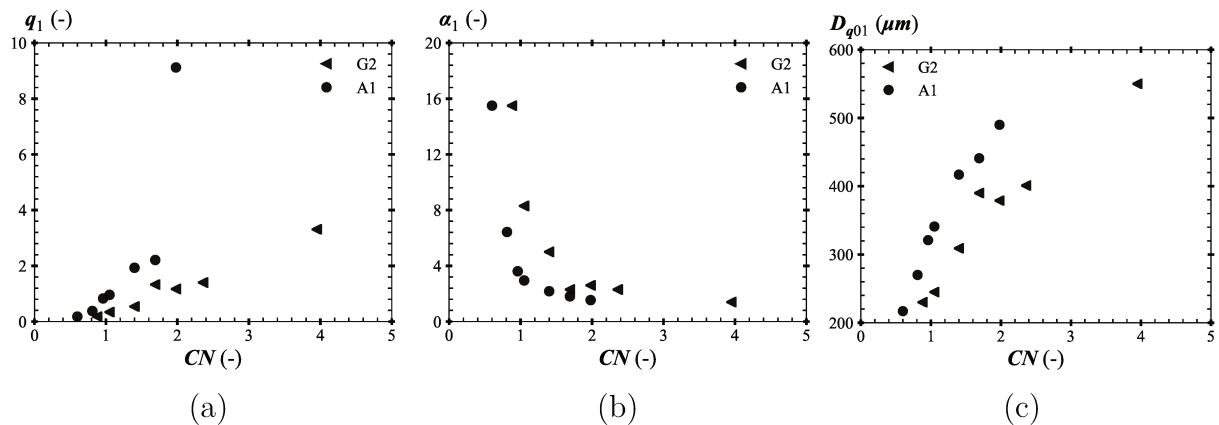


Figure 6.28: a)  $q_1$ , b)  $\alpha_1$  and c)  $D_{q01}$  as a function of  $CN$ .

This first set of comparisons demonstrates that atomizers A1 and G2 exhibit a rather similar textural atomization process. Some differences have been noted, but they seem marginal to impact the diameter distribution of the produced drops. The strong similarity between the atomization process agrees with the strong similarity noticed between the drop size distribution.

Finally, taking advantage from the results of the first application, we investigate the correlation between the scale distribution parameters and those of the drop-diameter distribution for the two atomizers. For instance, Fig. 6.29 shows the main-drop peak diameter  $D_{peakR}$  as a function of the scale  $d_p$  (the values of this scale are given in Tables 6.4 and 6.5). For both atomizers, Fig. 6.29 shows a rather linear dependence between  $D_{peakR}$  and  $d_p$ . We note that  $d_p$  is greater for G2 than for A1. Furthermore, for G2, the dependence

between  $D_{peakR}$  and  $d_p$  is close to the theoretical behavior also shown in the figure. This pleads to less deformed textural ligaments for G2 than for A1 and agrees with the remark made above. The characteristics of scale  $d_{p2}$  are also calculated and listed in Tables 6.4 and 6.5. Figure 6.30 shows the parameter  $\alpha_L$  as a function of  $-e_2''(d_{p2})$ . It is interesting to note that a strong and almost unique dependence between these two parameters. This indicates that  $-e_2''(d_{p2})$  is well representative of the dispersion of the satellite sizes in the lower scale range: it contains information on the ligament deformation scale dispersion. Finally, Fig. 6.31 shows the ratio  $\alpha_1/\alpha_L$  versus the ratio  $d_{p2}/d_p$ . Note that a unique behavior is obtained. This result demonstrates that the ratio  $d_{p2}/d_p$  contains an information on the capacity of the small deformation to produce satellite droplets. If  $d_{p2}/d_p$  is high,  $\alpha_1/\alpha_L$  is around 1 meaning that the satellite size and the ligament deformation disperse the same way in the lower scale range: small droplets directly result from the ligament deformation. If  $d_{p2}/d_p$  is low,  $\alpha_1/\alpha_L$  is low: the deformation scales of the ligament are less involved in the satellite drop production. The scales  $d_p$  and  $d_{p2}$  are important scales of the atomization process. Furthermore, the ratio  $d_{p2}/d_p$  is a very good indicator of the implication of the small scale in the drop production process. If this ratio is too small, the small deformation will not be at the origin of drop production.

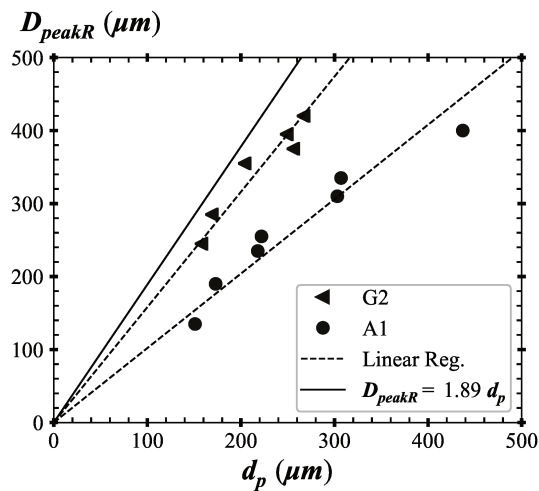


Figure 6.29: Correlation between the parameter  $D_{peakR}$  and the parameter  $d_p$  for A1 and G2 atomizers.

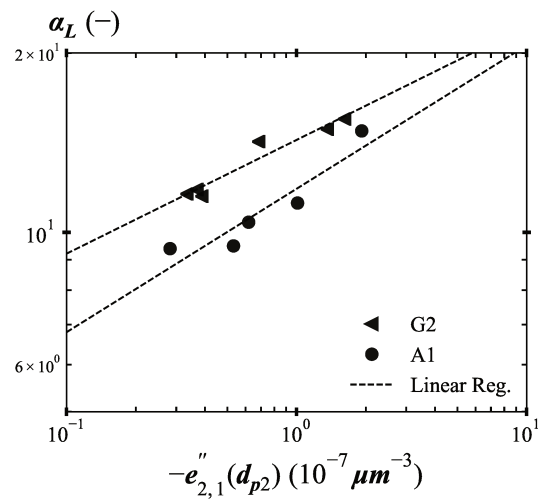


Figure 6.30: Correlation between  $\alpha_L$  and  $-e''_{2,1}(d_{p2})$  for A1 and G2 atomizers.

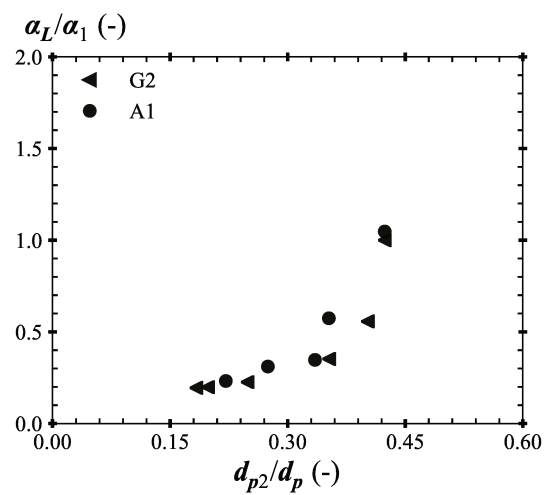


Figure 6.31: Ratio of  $\alpha_1/\alpha_L$  as a function of  $d_{p2}/d_p$  for A1 and G2 atomizers.

# Chapter 7

## Conclusions and Perspectives

The experimental investigation on the textural atomization process reported in this thesis provides interesting conclusions on the physics of this process as well as on the original methods developed to analyze the experimental results.

From the physical aspect, it has to be first mentioned that investigating textural atomization process is a rather new proposition. The studies of the literature on this topic are almost inexistent. However, such atomization processes produce very small droplets arranged in a spray that, according to the situation, may be very dense. Within the scope of this work, the textural atomization processes on flows issuing from an atomizer in which cavitation takes place have been considered. Part of the work has been dedicated to the development of the cavitation structures in the atomizer. The general conditions of cavitation appearance and the flow regimes it triggers have been identified and are in agreement with the results of the literature on this topic. However, we have found that the gas inclusions in the orifice of the atomizer do not result all from cavitation. Indeed, because of specific atomizer geometry, a large recirculation in the orifice may sometimes extend down to the exit section and suck air in the orifice. Being caught by the re-entrant jet (ascendant part of the recirculation zone) the sucked air mixes with the cavitation structures. The air-sucking mechanism appears dependent on the atomizer geometry. In particular, it is enhanced if the entry channel height is reduced. Therefore the air-sucking mechanism seems more prone to appear for low needle lift. The influence of cavitation on the issuing flow characteristics has been questioned. Coupling experimental and numerical approaches has led us to the conclusion that when the cavitation does not reach the exit section, it has no influence on the mean and rms velocity profiles at the nozzle exit. This result is believed to be related to the small thickness of the atomizer orifice: the flow is mainly controlled by this geometrical characteristic feature. Therefore, the cavitation has probably no influence on the atomization process in this case. However, when the cavitation structures reach the atomizer exit section, a sudden evolution of the atomization process has been observed. In

this case, the role of cavitation on atomization is indisputable. A specific analysis of the internal cavitation structures demonstrates that cavitation may generate a large variability of the exit flow characteristics. When this variability is due to cavitation, a clear trend is observed for the variability of the textural deformation of the interface. When this variability is due to the air-sucking mechanism, no specific variability trend of the interface deformation is noticed. Another connection between cavitation and textural atomization process has been evidenced from a fine analysis of this process. This analysis is based on a multiscale method. The scale distribution it provides describes the atomizing ligamentary structures and includes information on the size distribution and on the deformation of these structures. To our knowledge, this is the only approach ensuring such a complete description. It has been found that when cavitation reaches the orifice exit section, the main-drops of the spray disperse more in size as a consequence of the increase of the ligament size dispersion. The analysis of the atomization process and of the spray has led to the proposition of the following model: the drop-size distribution of the textural sprays presents a main-population mainly associated with the size distribution of the textural ligaments and a satellite population associated with the deformation of these ligaments. The atomization process and the resulting spray drop size distribution appear quite independent of the atomizer inlet channel height when the flow rate is fixed. The main (and only) influence of this geometrical parameter is to increase the number of satellite drops. These conclusions have to be taken with care since the work has been conducted at a constant flow rate. If one is working at a given injection pressure (which is actually often the case), reducing the inlet pipe height will consume more energy and decrease the flowrate: the resulting textural atomization process will produce a coarser spray. As far as the analysis is concerned, it is worth mentioning that the image entropy analysis is a powerful instrument to visualize and quantify the variability zones of a mechanism. Furthermore, the multiscale method convoked to describe the textural atomization appears to be very appropriate. The scale distribution it provides defines the concept of equivalent systems on which a mathematical representation of the atomization-process scale-distribution can be established. For the first time, an atomization process has received a mathematical expression. It is obtained from the mathematical diameter distribution of a set of cylinders that has the same scale distribution as the actual system. This approach is particularly adapted here since the atomization ligaments are rather cylindrical structures. The chosen mathematical distribution, i.e., the 3pGG function, was found very appropriate for this purpose as well as to represent the spray drop-size distribution. As far as the use of the 3pGG function is concerned, it is worth mentioning that three parameters are necessary to successfully represent the scale distribution and the drop size distribution. They allow dissociating the drops produced by the larger ligaments from those produced by the more numerous. In the present study, these two populations evolved differently and required their own indicator ( $q$  or  $\alpha$ ) to be correctly taken into account. The physical relevance of this mathematical expression has been evidenced by the correlations found between the three parameters it

involves and the cavitation number of the flow on one hand, and the parameters of the diameter distribution of the drops on a second hand. The atomization model mentioned above has been derived from these correlations that demonstrate the possibility of evaluating the drop diameter-distribution from the textural atomization scale distribution. In this exercise, the scales at which the scale distribution and its derivative show an inflexion point are important. They inform on the typical size and dispersion in small diameter range of each drop diameter-distribution mode. Furthermore, their ratio gives an information of the implication of the small deformation on the satellite production.

This work proposes new tools and a different way of describing atomization processes and sprays. One of the main contributions of the method is the ability to establish a mathematical description of the atomization process and the spray. This aspect should be very much appreciated in a community often short in approaches to predict drop diameter distribution from a ruffled interface. The present work validates the appropriateness of the tools developed in this thesis and suggests exploring their use in more details. For instance, the application of the equivalent system concept could be refined in order to better treat the case of very deformed ligament. A better spatially-resolved optical equipment should allow improving the present analysis in the small scale and drop regions, a domain where models are very much wanted.

To establish a further connection between the internal and external flows one has to compute the turbulence-related quantities inside the orifice and particularly at the exit-section from the data issued from the LDV measurement. The hypotheses upon-which this kind of computations are built have to be taken with precautions. The connection that could be established would enhance understanding the influence of the internal flow characteristics and particularly the cavitation on the issuing flow characteristics.

# Bibliography

- Abderrezzak, B. and Huang, Y. (2016). A contribution to the understanding of cavitation effects on droplet formation through a quantitative observation on breakup of liquid jet. International Journal of Hydrogen Energy, 41(35):15821 – 15828. 4th International Conference on Energy Engineering and Environment Engineering (ICEEEE2016), 15-16 April 2016, Hong Kong, China.
- Albrecht, H.-E., Damaschke, N., Borys, M., and Tropea, C. (2013). Laser Doppler and phase Doppler measurement techniques. Springer Science & Business Media.
- Andriotis, A. and Gavaises, M. (2009). Influence of vortex flow and cavitation on near-nozzle diesel spray dispersion angle. Atomization and Sprays, 19(3).
- Andriotis, A., Gavaises, M., and Arcoumanis, C. (2008). Vortex flow and cavitation in diesel injector nozzles. Journal of Fluid Mechanics, 610:195–215.
- Arai, M. (1988). Break-up length and spray formation mechanism of a high speed liquid jet. In Proceedings of the 4th International Conference on Liquid Atomization and Spray Systems.
- Arai, M., Shimizu, M., and Hiroyasu, H. (1985). Breakup length and spray angle of high speed jet. In Proceedings of the 3rd International Conference on Liquid Atomization and Spray Systems, volume 1, pages 1–10.
- Arcoumanis, C., Gavaises, M., Flora, H., and Roth, H. (2001). Visualisation of cavitation in diesel engine injectors. Mécanique & industries, 2(5):375–381.
- Babinsky, E. and Sojka, P. (2002). Modeling drop size distributions. Progress in energy and combustion science, 28(4):303–329.
- Badock, C., Wirth, R., Fath, A., and Leipertz, A. (1999a). Investigation of cavitation in real size diesel injection nozzles. International journal of heat and fluid flow, 20(5):538–544.

- Badock, C., Wirth, R., and Tropea, C. (1999b). The influence of hydro grinding on cavitation inside a diesel injection nozzle and primary break-up under unsteady pressure conditions. Proc. 15th ILASS-Europe, 99:5–7.
- Bergwerk, W. (1959). Flow pattern in diesel nozzle spray holes. Proceedings of the Institution of Mechanical Engineers, 173(1):655–660.
- Bérubé, D. and Jébrak, M. (1999). High precision boundary fractal analysis for shape characterization. Computers & Geosciences, 25(9):1059–1071.
- Blaisot, J. (2012). Drop size and drop size distribution measurements by image analysis. Heidelberg, Germany.
- Blaisot, J. and Yon, J. (2003). Entropy based image analysis for the near field of direct injection diesel jet. In ILASS.
- Blaisot, J. and Yon, J. (2005). Droplet size and morphology characterization for dense sprays by image processing: application to the diesel spray. Experiments in fluids, 39(6):977–994.
- Chaves, H., Knapp, M., Kubitzek, A., Obermeier, F., and Schneider, T. (1995). Experimental study of cavitation in the nozzle hole of diesel injectors using transparent nozzles. SAE transactions, pages 645–657.
- Dabiri, S., Sirignano, W., and Joseph, D. (2007). Cavitation in an orifice flow. Physics of Fluids (1994-present), 19(7):072112.
- Desantes, J., Payri, R., Salvador, F., and De la Morena, J. (2010). Influence of cavitation phenomenon on primary break-up and spray behavior at stationary conditions. Fuel, 89(10):3033–3041.
- Desantes, J. M., Payri, R., Pastor, J. M., and Gimeno, J. (2005). Experimental characterization of internal nozzle flow and diesel spray behavior. part i: Nonevaporative conditions. Atomization and sprays, 15(5).
- Dumont, N., Simonin, O., and Habchi, C. (2000). Cavitating flow in diesel injectors and atomization: a bibliographical review. In Proceedings of ICLASS.
- Dumouchel, C. (2006). A new formulation of the maximum entropy formalism to model liquid spray drop-size distribution. Particle & Particle Systems Characterization, 23(6):468–479.
- Dumouchel, C. (2008). On the experimental investigation on primary atomization of liquid streams. Experiments in fluids, 45(3):371–422.

- Dumouchel, C. (2009). The maximum entropy formalism and the prediction of liquid spray drop-size distribution. Entropy, 11(4):713–747.
- Dumouchel, C., Aniszewski, W., Vu, T.-T., and Ménard, T. (2017). Multi-scale analysis of simulated capillary instability. International Journal of Multiphase Flow, 92:181–192.
- Dumouchel, C., Blaisot, J.-B., Abuzahra, F., Sou, A., Godard, G., and Idlahcen, S. (2019). Analysis of a textural atomization process. Experiments in fluids.
- Dumouchel, C., Blaisot, J.-B., Bouche, E., Ménard, T., and Vu, T.-T. (2015a). Multi-scale analysis of atomizing liquid ligaments. International Journal of Multiphase Flow, 73:251–263.
- Dumouchel, C., Cousin, J., and Grout, S. (2008). Analysis of two-dimensional liquid spray images: the surface-based scale distribution. Journal of Flow Visualization and Image Processing, 15(1):pp. 59–83.
- Dumouchel, C., Cousin, J., and Triballier, K. (2005a). Experimental analysis of liquid–gas interface at low weber number: interface length and fractal dimension. Experiments in fluids, 39(4):651–666.
- Dumouchel, C., Cousin, J., and Triballier, K. (2005b). On the role of the liquid flow characteristics on low-weber-number atomization processes. Experiments in fluids, 38(5):637–647.
- Dumouchel, C. and Grout, S. (2009). Application of the scale entropy diffusion model to describe a liquid atomization process. International Journal of Multiphase Flow, 35(10):952–962.
- Dumouchel, C., Leboucher, N., and Lisiecki, D. (2013). Cavitation and primary atomization in real injectors at low injection pressure condition. Experiments in fluids, 54(6):1–17.
- Dumouchel, C., Ménard, T., and Aniszewski, W. (2015b). Towards an interpretation of the scale diffusivity in liquid atomization process: An experimental approach. Physica A: Statistical Mechanics and its Applications, 438:612–624.
- Evers, L. W. (1994). Characterization of the transient spray from a high pressure swirl injector. Technical report, SAE Technical Paper.
- Fdida, N. and Blaisot, J.-B. (2009). Drop size distribution measured by imaging: determination of the measurement volume by the calibration of the point spread function. Measurement Science and Technology, 21(2):025501.

- Fdida, N., Mauriot, Y., Ristori, A., Vinger, L., Chevalier, P., and Theron, M. (2018). Primary atomization of a cryogenic lox/n<sub>2</sub> and lox/he jet in a coaxial rocket injector. In 14th Triennial International Conference on Liquid Atomization and Spray Systems, ICLASS, 23-26 July.
- Ganippa, L. C., Bark, G., Andersson, S., and Chomiak, J. (2004). Cavitation: a contributory factor in the transition from symmetric to asymmetric jets in cross-flow nozzles. Experiments in Fluids, 36(4):627–634.
- Gavaises, M., Andriotis, A., Papoulias, D., Mitroglou, N., and Theodorakakos, A. (2009). Characterization of string cavitation in large-scale diesel nozzles with tapered holes. Physics of fluids, 21(5):052107.
- Gellales, A. (1931). Effect of length diameter ratio on fuel sprays, etc. Technical report, NACA Tech. Report.
- Gouesbet, G., Maheu, B., and Gréhan, G. (1988). Light scattering from a sphere arbitrarily located in a gaussian beam, using a bromwich formulation. JOSA A, 5(9):1427–1443.
- Grout, S., Dumouchel, C., Cousin, J., and Nuglisch, H. (2007). Fractal analysis of atomizing liquid flows. International Journal of Multiphase Flow, 33(9):1023–1044.
- Guildenbecher, D., López-Rivera, C., and Sojka, P. (2009). Secondary atomization. Experiments in Fluids, 46(3):371.
- Guo, G., He, Z., Zhang, Z., Duan, L., Guan, W., Duan, X., and Jin, Y. (2018). Visual experimental investigations of string cavitation and residual bubbles in the diesel nozzle and effects on initial spray structures. International Journal of Engine Research, page 1468087418791061.
- He, L. and Ruiz, F. (1995). Effect of cavitation on flow and turbulence in plain orifices for high-speed atomization. Atomization and Sprays, 5(6).
- Hiroyasu, H. (1991). Break-up length of a liquid jet and internal flow in a nozzle. In Proc. 5th. ICLASS, pages 275–282.
- Kapur, J. (1983). Twenty-five years of maximum-entropy principle. Journal of Mathematical and Physical Sciences, 17:103–156.
- Karasawa, T., Tanaka, M., Abe, K., Shiga, S., and Kurabayashi, T. (1992). Effect of nozzle configuration on the atomization of a steady spray. Atomization and Sprays, 2(4).
- Kaye, B. H. (1994). A random walk through fractal dimensions. VCH.
- Kim, J., Nishida, K., and Hiroyasu, H. (1997). Characteristics of the internal flow in a diesel injection nozzle. International Journal of Fluid Mechanics Research, 24(1-3).

- Knapp, R., Daily, J., and Hammitt, F. (1970). Cavitation,(1970). Institute of Hydraulic Research, University of Iowa.
- Laonual, Y., Yule, A., and Walmsley, S. (2001). Internal fluid flow and spray visualization for a large scale valve covered orifice (vco) injector nozzle. ILASS-Europe 2001, Zurich, 2–6 Sept.
- Lecompte, M. and Dumouchel, C. (2008). On the capability of the generalized gamma function to represent spray drop-size distribution. Particle & Particle Systems Characterization, 25(2):154–167.
- Lefebvre, A. H. (1989). Atomization and sprays. Hemisphere Publishing Corporation.
- Lindgren, R. and Denbratt, I. (2000). Modelling gasoline spray-wall interaction-a review of current models. SAE transactions, pages 2365–2382.
- Marmottant, P. and Villermaux, E. (2004). On spray formation. Journal of fluid mechanics, 498:73–111.
- Mauger, C., Méès, L., Michard, M., Azouzi, A., and Valette, S. (2012). Shadowgraph, schlieren and interferometry in a 2d cavitating channel flow. Experiments in fluids, 53(6):1895–1913.
- Mitroglou, N., Gavaises, M., Nouri, J., and Arcoumanis, C. (2011). Cavitation inside enlarged and real-size fully transparent injector nozzles and its effect on near nozzle spray formation. In Proceedings of the DIPSI Workshop 2011. Droplet Impact Phenomena & Spray Investigations, pages 33–45. Dip. Ingegneria industriale. Università degli studi di Bergamo.
- Mugele, R. and Evans, H. (1951). Droplet size distribution in sprays. Industrial & Engineering Chemistry, 43(6):1317–1324.
- Ngo, V.-D. (2013). Etude de la morphologie des éléments d’un spray liquide et de leur production. PhD thesis, Rouen.
- Nurick, W. (1976). Orifice cavitation and its effect on spray mixing. Journal of fluids engineering, 98(4):681–687.
- Ohrn, T., Senser, D. W., and Lefebvre, A. H. (1991a). Geometrical effects on discharge coefficients for plain-orifice atomizers. Atomization and Sprays, 1(2).
- Ohrn, T., Senser, D. W., and Lefebvre, A. H. (1991b). Geometrical effects on discharge coefficients for plain-orifice atomizers. Atomization and Sprays, 1(2).

- Payri, F., Bermudez, V., Payri, R., and Salvador, F. (2004). The influence of cavitation on the internal flow and the spray characteristics in diesel injection nozzles. Fuel, 83(4):419–431.
- Payri, F., Payri, R., Salvador, F. J., and Martínez-López, J. (2012). A contribution to the understanding of cavitation effects in diesel injector nozzles through a combined experimental and computational investigation. Computers & Fluids, 58:88–101.
- Payri, R., Garcia, J., Salvador, F., and Gimeno, J. (2005). Using spray momentum flux measurements to understand the influence of diesel nozzle geometry on spray characteristics. Fuel, 84(5):551–561.
- Pearce, I. and Lichtarowicz, A. (1971). Discharge performance of long orifices with cavitating flow. In Proceedings of Second Fluid Power Symposium, Guildford, UK.
- Pentland, A. P. (1987). A new sense for depth of field. IEEE transactions on pattern analysis and machine intelligence, (4):523–531.
- Rayleigh, L. (1878). On the instability of jets. Proceedings of the London mathematical society, 1(1):4–13.
- Reitz, R. and Bracco, F. (1982). Mechanism of atomization of a liquid jet. The physics of Fluids, 25(10):1730–1742.
- Sato, K. and Saito, Y. (2001). Unstable cavitation behavior in a circular-cylindrical orifice flow, fourth int. Sym. on Cavitation-CAV2001, pages 1–8.
- Shavit, U. and Chigier, N. (1995). Fractal dimensions of liquid jet interface under breakup. Atomization and Sprays, 5(6).
- Soille, P. (2013). Morphological image analysis: principles and applications. Springer Science & Business Media.
- Soteriou, C., Andrews, R., and Smith, M. (1995). Direct injection diesel sprays and the effect of cavitation and hydraulic flip on atomization. SAE transactions, pages 128–153.
- Soteriou, C., Andrews, R., Torres, N., Smith, M., and Kunkulagunta, R. (2001). Through the diesel nozzle hole—a journey of discovery. ilass americas. In 14th Conference on Liquid Atomization and Spray Systems, Dearborn, MI.
- Sou, A., Hosokawa, S., and Tomiyama, A. (2007). Effects of cavitation in a nozzle on liquid jet atomization. International journal of heat and mass transfer, 50(17):3575–3582.
- Sou, A., Hosokawa, S., and Tomiyama, A. (2009). Dimensionless numbers on cavitation in a nozzle of pressure atomizers. In ICLASS.

- Sou, A., Maulana, M. I., Hosokawa, S., and Tomiyama, A. (2008). Ligament formation induced by cavitation in a cylindrical nozzle. Journal of Fluid Science and Technology, 3(5):633–644.
- Sou, A., Pratama, R. H., Tomisaka, T., and Kibayashi, Y. (2012). Cavitation flow in nozzle of liquid injector. In Proceedings of the 12th triennial international conference on liquid atomization and spray systems.
- Sou, A., Tomiyama, A., Hosokawa, S., Nigorikawa, S., and Maeda, T. (2006). Cavitation in a two-dimensional nozzle and liquid jet atomization (ldv measurement of liquid velocity in a nozzle). JSME International Journal Series B, 49(4):1253–1259.
- Sowa, W. (1992). Interpreting mean drop diameters using distribution moments. Atomization and Sprays, 2(1):pp. 1–15.
- Stanley, C., Barber, T., Milton, B., and Rosengarten, G. (2011). Periodic cavitation shedding in a cylindrical orifice. Experiments in fluids, 51(5):1189–1200.
- Tamaki, N., Shimizu, M., Nishida, K., and Hiroyasu, H. (1998). Effects of cavitation and internal flow on atomization of a liquid jet. Atomization and Sprays, 8(2).
- Tirel, C., Renoult, M.-C., Dumouchel, C., Lisiecki, D., Crumeyrolle, O., and Mutabazi, I. (2017). Multi-scale analysis of a viscoelastic liquid jet. Journal of Non-Newtonian Fluid Mechanics, 245:1–10.
- Vassallo, P. and Ashgriz, N. (1991). Satellite formation and merging in liquid jet breakup. Proc. R. Soc. Lond. A, 433(1888):269–286.
- Villermaux, E. (2007). Fragmentation. Annu. Rev. Fluid Mech., 39:419–446.
- Vu, T.-T. and Dumouchel, C. (2018). Analysis of ligamentary atomization of highly perturbed liquid sheets. International Journal of Multiphase Flow.
- Wu, P.-K., Miranda, R., and Faeth, G. (1995). Effects of initial flow conditions on primary breakup of nonturbulent and turbulent round liquid jets. Atomization and sprays, 5(2).
- Yon, J. (2003). Jet Diesel haute presssion en champ proche et lointain: Etude par imagerie. PhD thesis, Université de Rouen.



## Abstract

Textural atomization designates the mechanism of drop peeling from the interface of a free liquid flow. This mechanism is controlled by the characteristics of the flow issuing from the injector and manifests at its vicinity. Almost uninvestigated, textural atomization is a rapid phenomenon, implies very small ligamentary structures and produces a mist of fine droplets. The work of this thesis is an experimental investigation of a textural atomization process observed on flows issuing from cavitating injector. Three academic transparent atomizers are used and optical diagnostics are implemented: LDV (Laser Doppler Velocimetry) and PDPA (Phase Doppler Particle Analyzer) to describe the internal flow and the spray, respectively, and still imaging at high spatial resolution or high-speed imaging for the internal and external flows. A first observation reveals a strong link between the cavitation regime and the textural atomization process. An analysis implying the measurement of the variability of the internal flow and of the atomization process quantifies this link. Here, the atomization process is described by the measurement of its scale distribution. Associated with the concept of equivalent system, this multi-scale analysis returns a mathematical expression for the investigated atomization process. This result is unprecedented. Completed by a mathematical description of the spray drop-diameter distribution, it offers a new support to build a model of ligamentary atomization processes presented in this work and that connects ligament size and deformation to the drop populations. These fine analyses provide a better knowledge of the investigated atomization process. For instance, we learn that, at fixed flow rate, the height of the inlet pipe feeding the orifice has no influence on the atomization process. Furthermore, a criterion has been established to identify the smallest ligament deformation scale implied in the drop production.

Key words: atomization, spray, cavitation, image analysis, multi-scale analysis

## Résumé

L'atomisation textuelle désigne le mécanisme d'arrachage de gouttes à l'interface d'un écoulement liquide libre. Ce mécanisme est contrôlé par les caractéristiques de l'écoulement au sortir de l'injecteur et se manifeste dans son champ proche. Peu étudiée, l'atomisation textuelle est un phénomène rapide, impliquant de très petites structures ligamentaires et produisant un brouillard de très fines gouttes. Le travail de cette thèse est une étude expérimentale d'un processus d'atomisation textuelle observé sur des écoulements produits par des injecteurs cavitants. Trois atomiseurs académiques transparents sont utilisés et des diagnostics optiques sont mis en œuvre : la LDV (vélocimétrie doppler laser) et le PDPA (Phase Doppler Particle Analyzer) pour décrire l'écoulement interne et le spray, respectivement, et l'imagerie fixe à forte résolution spatiale ou à haute-cadence pour les écoulements interne et externe. Une première observation montre un lien important entre le régime de cavitation et le processus d'atomisation textuelle. Une analyse impliquant la mesure de variabilité de l'écoulement et du processus d'atomisation textuelle quantifie ce lien. Ici, le processus d'atomisation est décrit par la mesure de sa distribution d'échelle. Associée au concept de système équivalent, cette analyse multi-échelle permet de produire une écriture mathématique du processus étudié. Ce résultat est sans précédent. Complété par une description mathématique de la distribution de taille des gouttes produites, il offre un appui nouveau pour construire un modèle d'atomisation ligamentaires présenté dans ce travail et qui relie taille et forme des ligaments aux populations de gouttes formées. Ces analyses fines amènent une meilleure connaissance du mécanisme d'atomisation étudié. Par exemple, on apprend qu'à débit fixé, la hauteur du canal d'alimentation de l'orifice de décharge n'influence pas les processus d'atomisation textuelle. Par ailleurs, un critère est établi pour identifier la plus petite échelle de déformation des ligaments impliquée dans la production des gouttes.

Mots clef : atomisation, spray, cavitation, analyse d'image, analyse multi-échelle